NASA Conference Publication 2488

58th Shock and Vibration Symposium

Volume II

Proceedings of a symposium held in
Huntsville, Alabama
October 13-15, 1987

DEPARTMENT OF DEFENSE
UNITED STATES OF AMERICA

NASA Conference Publication 2488

58th Shock and Vibration Symposium

Volume II

Compiled by
Walter Pilkey and Barbara Pilkey
University of Virginia
Charlottesville, Virginia

Proceedings of a symposium sponsored by
the Department of Defense and
the National Aeronautics and Space Administration
and held in Huntsville, Alabama
October 13-15, 1987

National Aeronautics
and Space Administration

**Scientific and Technical
Information Division**

1988

Symposium Management

Host Representatives

Jess H. Jones - Marshall Space Flight Center
James W. Daniel - U.S. Army Missile Command

Administrative Management

William W. Wassmann - Naval Surface Weapons Center

Contract Support

Advanced Technology & Research, Inc.
Laurel Technology Center
14900 Sweitzer Lane
Laurel, MD 20707

Project Manager

Henry C. Pusey, ATR, Inc.

58th Symposium Program Committee

James D. Cooper
Defense Nuclear Agency
SPSS
Washington, DC 20305

James W. Daniel
U.S. Army Missile Command
AMSMI-RD-TE-C
Redstone Arsenal, AL 35898

Jess H. Jones
NASA Marshall Space Flight Center
Structural Analysis Division
Huntsville, AL 35812

John H. Wafford
U.S. Air Force
ASD/ENF
Wright-Patterson AFB, OH 45433

William W. Wassmann
Naval Surface Weapons Center
Environments Branch Code H14
Silver Spring, MD 20902-5000

Proceedings Compilers

Walter D. Pilkey
Mechanical and Aerospace Engineering
University of Virginia
Charlottesville, VA 22901

Barbara F. Pilkey
Mechanical and Aerospace Engineering
University of Virginia
Charlottesville, VA 22901

Table of Contents

CONTRIBUTORS

Carl A. Anderson
Naval Surface Warfare Center
Dahlgren, Virginia

Gilbert J. Bastien
Environmental Engineering Department
Hughes Aircraft Company
Ground Systems Group
Fullerton, California 92634

Philip B. Bogert
Director, Structural Dynamics Division
NKF Engineering, Inc.
Reston, Virginia

David L. Brown
Structural Dynamics Research Laboratory
Department of Mechanical and Industrial Engineering
University of Cincinnati
Cincinnati, Ohio 45221-0072

J. H. Cowles
BBN Laboratories Incorporated
Union Station
New London, Connecticut 06320

Thomas J. Dwyer
General Electric Company
P.O. Box 8555
M4018/Building 100
Philadelphia, Pennsylvania 19101

R. C. Haberman
BBN Laboratories Incorporated
Union Station
New London, Connecticut 06320

Jeffrey M. Komrower
NKF Engineering, Inc.
Reston, Virginia

Avivi Lev
Consultant, NKF Engineering, Inc.
Reston, Virginia

George F. McDonough
Director, Structures and Dynamics Laboratory
George C. Marshall Space Flight Center
National Aeronautics and Space Administration
Huntsville, Alabama

Barton W. McPheeters
Engineer, NKF Engineering, Inc.
Reston, Virginia

S. Mittal
General Electric Company
Valley Forge Space Center
RCA Astro Space Division
P.O. Box 8555
Philadelphia, Pennsylvania 19101

M. Pakstys
NKF Engineering, Inc.
Reston, Virginia

Mario Paz
Carrier Vibrating Equipment
3400 Fern Valley Road
Louisville, Kentucky 40213

Robert W. Rost
Structural Dynamics Research Laboratory
Department of Mechanical and Industrial Engineering
University of Cincinnati
Cincinnati, Ohio 45221-0072

Rudolph J. Scavuzzo
Professor, Department of Mechanical Engineering
University of Akron, Akron, Ohio

M. L. Soni
University of Dayton Research Institute
Dayton, Ohio 45469

A. L. Stiehl
Department of Mechanical Engineering
Pennsylvania State University
McKeesport, Pennsylvania 15135

J. C. Strain
General Electric Company
Valley Forge Space Center
RCA Astro Space Division
P.O. Box 8555
Philadelphia, Pennsylvania 19101

Robert B. Tarn
Rockwell International/Rocketdyne Division
Canoga Park, California

Mitsuhiro Tsuchiya
Environmental and Structural Test Department
Tsukuba-Space-Center
National Space Development Agency of Japan
Niihari-Gun, Ibaraki-Ken, 305, Japan

Douglas S. Wright
NKF Engineering, Inc.
Reston, Virginia

FEATURED PAPERS

Challenges in Structures and Dynamics

George F. McDonough

Giving a keynote address is one of the pleasures which usually comes with advanced age and experience. It is particularly welcome in that some of the other pleasures diminish somewhat with time. The main thing a keynote speaker is asked to do is to share whatever insight and perspective he has managed to gain from the events he has witnessed and, possibly had some role in shaping. Furthermore, he need not defend a position against others who may see differently from their different perspectives. My first purpose in this address, in addition to making a transition from the warm glow of the welcoming addresses to getting down to the business of this symposium, is to put the symposium in the context of the flow of activities here in NASA at the George C. Marshall Space Flight Center. I want to show you some of the things we are doing and show how they fit with the work to be reported here later. Based on our work, I would like to suggest some approaches to future development and some possible pitfalls which I foresee in the development of technology. But, before I get into that, I want to urge you to make the most of this opportunity to share your knowledge and experience with your fellow workers. At the time of the last symposium there was considerable doubt that we would be able to carry on because of dwindling support. Had this occurred it would have been a great loss, so I am very pleased that NASA and the Marshall Space Flight Center were able to continue their support and to co-sponsor with the U.S. Army Missile Command this Fifty-Eighth Shock and Vibration Symposium. We believe that this is an important forum in which to discuss important issues in Dynamics but that it can only provide the forum; the ideas and the search for knowledge must come from you who are participating in this symposium. So I urge a lively exchange of ideas and even the expression of some conflict of opinions to give life to this meeting. Without that, attending any symposium is not a great deal superior to reading the papers given at the symposium. This has not been a passive forum, which is one of its greatest strengths, and I urge you now to participate fully to make the most of this opportunity.

Now for the challenges. There is no shortage of challenges in shock and vibration. Some have been with us unchanged for many years, others have developed over the years and very few

PRECEDING PAGE BLANK NOT FILMED

are really new. I want to cover a few of these challenges from the point of view of the work which is done in my organization within NASA and the other groups with whom we collaborate. Since we are space-oriented we may not have the best perspective on many earthbound problems, but yet we must build, transport and launch our space vehicles. We also are a civilian agency, yet we have used military vehicles in our launches and are now participating in the Strategic Defense Initiative flight experiments and other military projects. When I look over such things as the broad application of NASA-developed computer programs such as NASTRAN throughout industry and at the infusion of analytical and experimental techniques either developed for space use or adapted to space use from industrial use, it appears to me that our window on dynamics offers a reasonably clear view of where the challenges and opportunities lie. Today, I have chosen a few of these as examples to show a pattern of challenges. It is good to see, in looking over the program, that some of these same areas and even the same examples will be described in detail.

One challenge which never changes because it is the heart of how we solve problems is the gathering of field or experimental data and its use either directly as a basis of design or in the verification of models which are in turn the basis of design. This includes the development of better test and instrumentation methods to permit gathering data in locations or environments we have not been able to measure before. It also includes simpler and less expensive tests and measurements so that our programs can afford to include them. An example of a test which permitted large programmatic savings in both facilities and test expense was the use of impedance testing on the Hubble Space Telescope (HST), an exploded view of which is shown in Figure 1. The Space Telescope had a somewhat restricted modal test program primarily due to funding constraints. Figure 2 shows a summary of the modal test; some elements of recognized significance were not included in the test, particularly the interfaces with the Orbiter; however, the test was generally successful in that it provided the data called out in the test plan. Furthermore, adequate finite element models were established based on test results, as shown in Figure 3. After the test program had been completed, it was determined that additional tests were required to verify some of the missing interfaces, such as the Orbiter/HST interface and determine attached solar array frequencies. There was no suitable way to perform the standard fixed-base modal test which was the standard approach. For one thing, the Hubble Space Telescope was in a clean room area to prevent contamination of the optics. It could not be removed, therefore, testing would have to take place in that facility. The facility contained no suitable mounting base upon which to place the Telescope so one would have to be constructed in the area at high cost because of construction problems and cleanliness requirements. These considerations prevented conventional testing. The answer to our dilemma came in the form of impedance testing, which could readily be done in place without facility construction or potential contamination. There were, however, many doubters since none of us had experience with impedance testing of a structure as complex as the Space Telescope. We all agreed there was no choice but to try and, if results were unsatisfactory, to reconsider other testing. A summary of the test techniques is shown in Figure 4 and typical results in Figure 5. The comparisons generally were excellent, and the required characteristics were obtained. This success leads to a further challenge to establish this technique as a fully alternative approach to model verification of large, complex structures rather than one to be called upon only when circumstances prevent the usual fixed-base testing. There are many large payloads on our horizon for which impedance testing can be a major factor and we shall seek applications of this technique wherever it is the best approach for the application. Its use will depend not only on how well it meets our needs but also on how well we can convince the flight safety and other review boards that the results are comparable with those from better established techniques.

Another Hubble Space Telescope challenge which has arisen because of the extended storage of the Telescope in Sunnyvale is monitoring its environment for dynamic transient inputs due to earthquakes. The system was developed inhouse at MSFC, both hardware and software, and was adapted from test monitoring systems. The system is triggered automatically by any seismic signal to record acceleration levels. Records are analyzed at MSFC for assessment of possible damage to the Space Telescope. We are pleased to report that the recent earthquake in the Los Angeles area was not felt by these instruments so it had no effect on the Space Telescope. This effort is typical of the many, sometimes small but important, problems which occur in our programs. Their solutions require a knowledge of the techniques and equipment of dynamic environment monitoring.

While on the subject of innovative techniques of testing, I would like to switch to another of our major programs, the Space Shuttle Main Engine (SSME). The internal environment of this or any other engine is difficult to instrument thoroughly because of potential structural weakening by wall penetrations at key locations and other similar constraints. Therefore, the location of much of the instrumentation we have is predicated on safety and ease of servicing rather than optimum location for environment determination. We have had good results from these measurements in providing adequate redlines to shut down a malfunctioning engine before it fails catastrophically and also as a diagnostic tool. Yet test anomalies still occur and we are still searching for additional diagnostic internal environment monitoring tools. One which looks promising, particularly for ground testing, is a non-intrusive examination of the engine plume by remote sensing using optical methods. Of course, we have for many years used the simplest optical detector, the eyes of the test observers who can terminate the test.

The concept is simple: to perform spectral analysis of the engine plume to detect engine failure in real-time. The system also provides indicators of engine wear and provides new information on the characteristics of the plume which can yield clues on engine operating efficiency. What caused the interest in this system was that examination of ordinary film and video imagery of engine anomaly incidents showed that eight of twenty-seven major engine test failures exhibited anomalous behavior in this imagery. An example is shown in Figure 6, a case in which the anomaly was traced to a failure of a main injector. Spectral characteristics of SSME failures never had been measured but there was clear indication that additional information could be gained from measurements beyond the visible spectrum. Our approach has been to study the phenomena occurring in the plume, which includes some preliminary plume measurements, then to develop and operate a prototype Optical Plume Anomaly Detector (OPAD). We now have a set of instruments installed on an SSME test stand at the National Space Technology Laboratories (NSTL); a layout of this system is shown in Figure 7. As shown, the equipment includes, in addition to the test stand cameras, an instrument table which holds a visible and an ultraviolet optical multispectral analyzer, an ultraviolet camera, two spectrometers in different ranges and a set of radiometers. Some typical results for a test in which an anomaly occurred are shown in Figures 8 and 9. Figure 8 shows the radiance of the plume in the various wavelengths at a single time point. Each peak is associated with the presence of a particular element or compound in the exhaust by-products. Potassium and sodium are of particular interest here. Figure 9 is an isoplot of data for the same test and shows the time variance of the data. The time at which the anomaly occurred is clearly shown by the appearance of the radiance in the potassium wavelength (770 nm) and the large increase in radiance at the sodium wavelength (589 nm). This test was terminated by redline cutoff seven-tenths of a second later. The cause of the problem was found to be a weld failure in the nozzle which allowed the escape of hydrogen which was ignited external to the engine. The optical system showed that it could have shut down the engine a significant time earlier than was done by the thermocouple which caught the out of tolerance temperature.

Other anomalies detected include bearing wear and the presence of copper tape inadvertently left in the combustion chamber from a nozzle plug. Burning copper is frequently noted in the plume as green streaks; it often indicates wear of rubbing surfaces. The status of the development of the system is that a multispectral analyzer is being procured for one test stand and that the prototype OPAD will be fabricated early next year. This OPAD will have cutoff capability but will be used in an open-loop mode until sufficient confidence is built to use it as a cutoff device. Finally, we are making arrangements to incorporate spectral data into the existing engine data banks. The next challenge will be to correlate this new data with strain gages, accelerometers and other internal data sources which also indicate engine health degradation or wear. Then we can consider further uses, potentially as a flight instrument.

Another tool which is contributing to the definition of environments in the SSME, is our rapidly improving capability of using computational fluid dynamic (CFD) methods to analyze the flow within the engine. Just a few years ago we were unable to solve any but the most simplified cases of axisymmetric flow with highly constrained geometries and fluid properties. Today, we are making substantial progress on realistic problems, thanks to the availability of computer systems such as the Engineering Analysis Data System (EADS) here at the Marshall Space Flight Center. This system has at its core a four-processor CRAY X-MP. We also are using the even larger National Aerodynamic Simulator, based on a CRAY II, at the Ames Research Center, as well as other supercomputers throughout NASA, other government agencies, the universities and industry.

Figure 10 shows the layout of the SSME with the hot gas flow areas indicated in red. Hydrogen and oxygen are mixed and ignited in the preburner, pass through the turbines into the turnaround ducts and transfer ducts, then are injected into the main combustion chamber, where additional liquid oxygen (LOX) is added through LOX posts, and burned. Areas which have been or are being analyzed include the flow through turbopump bearings, turbine turnaround ducts and transfer ducts, injectors and the nozzle. Some of the design concerns, in addition to the efficiency of flow through the system, include turbine blade loads, fatigue of the bellows shield and the response stability and fatigue of the LOX posts located at the injection plate to the main combustion chamber. Actually, several of these concerns are coupled, for example, the turbulence and unevenness of flow in the transfer ducts is a major driver of unsteady response of the LOX posts and a subsequent cause of their failure in fatigue.

The pictorials of Figure 11 are representations of the output of CFD analysis which show the contours of flow velocity in these tubes for the current three-duct design and the proposed two-duct design. Red indicates the highest velocity while, at the other end of the spectrum, indigo indicates the lowest velocity. As can be seen, the flow in the outer tubes of the three-tube configuration shows wide variations of velocity and the flow in the center tube is very low. This is an inefficient design compared with the two-tube case shown below it in which the flow velocity can be seen to vary over a much narrower range.

We at the Marshall Space Flight Center do not have primary responsibility for the development of the CFD models, within NASA that job belongs to the research centers. But we, together with the SSME developer, Rocketdyne, do have the responsibility to verify these codes through benchmark tests and to develop them into useful design tools. Where no suitable code exists or where alternate approaches are needed, we utilize industry and university capabilities directly to develop what is needed. This cooperative split of responsibility has worked well for the program although developing the proper balance of activities among the participants has been a challenge in itself.

To show how we answer the challenge of verifying and comparing existing or newly developed programs, we can examine the example of the turnaround duct. Figure 12 shows a summary of four CFD codes used for the analysis of the hot gas manifold showing the basic algorithm, turbulence model and number of grid points. As can be seen, the INS3D model has an order of magnitude more grid points than the other models. Figure 13 shows how the results vary for these codes in terms of outer wall static pressure coefficients and how each compares with data from an air flow test. In this case, three of the codes compare fairly well, the fourth less so. Also, the number of grid points does not appear to make a great deal of difference. Of course, for other situations the relative accuracy of codes sometimes differs. As with all flow or structural models, the comparison with the test data is the best basis of validation. The hot gas manifold was an excellent benchmark problem because it brought out the strengths and weaknesses in these codes. Also, because this part of the engine was subject to redesign, we were able to mount an extensive series of cold gas and hot fire tests at full scale and water flow tests at one-half scale. These latter were especially useful in visualizing the flow patterns. A typical one-half scale water flow model test is shown in Figure 14. This combination of tests allows us to verify flow scaling as well as to make maximum use of the cheaper and simpler air and water flow tests, reserving hot fire tests for final verification. Similar approaches have been used in studying the Solid Rocket Motor redesigned field and nozzle-to-case joints and have contributed greatly to our confidence in the ability of the redesign to operate safely.

Another area of intensive CFD activity is in turbine flow. A typical CFD analysis of pressure distributions on the high pressure fuel turbopump turbine blades is shown in Figure 15. This analysis has been extended to an animation showing the variation of pressure and thermal loads on the rotor blades as they pass the stator blades. Results of these analyses were used as inputs, along with centrifugal forces, to a combined stress and thermal analysis of the blades. The blades were modeled structurally using the ANSYS program. A two-dimensional analysis used nonlinear material properties and bilinear gap elements connecting the blade and disk structures. The three-dimensional models used linear-orthotropic properties, a substructured disk and bilinear gap elements. Geometry of the blade is shown in Figure 16; the lower part, which fits into the wheel, is called the fir tree because of its shape.

Some typical results are shown in Figures 17 and 18. Figure 17 shows results from a two-dimensional analysis of a blade/disk model with nonlinear material properties. The boundaries include frictionless bilinear gap elements with uniform contact on all mating surfaces. The loading is generated by centrifugal force and power bending stresses at full power level steady-state conditions. The results, zoomed in on a local area for detail, show a highly localized region of high stress in the fir tree area of contact with the disk, shown in red, spreading through a yellow area denoting lower stress and then to a relatively uniform stress field. Figure 18 is the big picture from which the blow-up of Figure 17 was taken; this figure shows slices through the entire area of the second stage fir tree from trailing edge (lower left) to leading edge (upper right). These results are based on a three-dimensional blade/substructured disk model using linear-orthotropic material properties. The boundaries include bilinear gap elements with uniform contact on all mating surfaces. The loading includes centrifugal forces, power bending pressures and thermal gradients at full power level steady-state. The contour plots depict the principal strain levels on each slice. The pattern of reduction of strain in the body of the fir tree as one progresses from the trailing to leading edge is apparent. The strains shown here are driven largely by thermal loads and, hence, show a substantial decrease generally from left to right in the figure, which corresponds to going from the highly heated trailing edge toward the less heated leading edge. The area in which the cracks have been occurring is at the root of the fir tree notch as shown by the red. This corresponds to the blow-up shown earlier. These patterns of strain give useful clues to explain the cracks which have occurred in the blades during test. The fine-grain strain definition is particularly useful in determining gradients.

As can be seen from the SSME program, and it is increasingly true for all our programs, extremely large amounts of data are being stored. And the statistical information contained within that data often is the key to establishing the allowable time between replacement of key parts as well as the vibration levels to which components must be qualified. Particularly in the SSME, where many parts are subjected to a severe combination of high temperatures and high mean stress plus fluctuating stress, we can only continue to operate the engines for multiple use by relying on a data base of flight and ground test data. The data system we have developed, a paper on which will be given later in the symposium, first connects the Rocketdyne and National Space Technology Laboratories (NSTL) test data acquisition systems with the MSFC data evaluation through high-rate (1.544MB) satellite links. The two main uses of the system are as a quick turnaround scheme for reduction and evaluation of engine test data and as a storage and retrieval system for the entire archives of engine test data. The former use allows us to reduce the spacing between tests by speeding up the process of evaluating the data from the last test. The latter capability allows us to manipulate data and evaluate trends for individual engines or components or families of engines. The types and uses of the data are shown in Figure 19; each type of data is useful for a particular aspect of analysis. Statistical information can be obtained as well through analysis of the data. Without such a large efficient data system, there simply would be no way to fully utilize the data base which contains many channels of data from hundreds of engine tests and is growing rapidly. The remaining challenge is to bring out the full potential of the system and to seek better display and manipulation methods for the system. In doing so, we will lean on the experience gained with other data bases such as our computerized vibroacoustic data bank. This data bank is used to predict structural response to acoustics for payloads and launch vehicle elements by similarity with elements of Saturn V, Titan III and Shuttle. Figure 20 shows how the data bank is used to develop acoustic scaling factors by comparing the measured environment of the reference vehicle with the model test acoustic environment of the new vehicle. Comparison of the structural and mass configurations similarly produces structural scale factors. Using these scale factors and the measured random vibration of the reference vehicle, the random vibration of the new vehicle can be predicted. The prediction is calculated and displayed as a response spectrum. This system has been an outstanding success, both in increased productivity and in producing a product the precision of which is superior to that from previous manual techniques.

For the final challenge, I would like to shift subjects somewhat to the area of control-structure interaction. This is becoming a discipline in itself, as opposed to a separation of structural dynamics and control dynamics, because of the intensive interaction between the two disciplines. The Hubble Space Telescope and even more so the Space Station are flight projects in which pointing control interacts critically with structural motion or attitude control reaction wheels. In the case of the Telescope, special isolators were used to reduce the feed-through of vibration from the reaction wheels. This was a problem somewhat different from the normal narrow-band isolation of large forces in that the forces were quite small (e.g., the noise for a carefully selected bearing). A similar generic large space structure concept has been developed at MSFC to use obtrusive sensors and effectors for rigid body and vibrational control; it is shown in Figure 21. The test specimen is a 20 meter deployable mast a four meter cruciform mounted on control gimbals. The effector or elements are linear momentum exchange devices with accelerometers as sensors. The results shown in Figure 22 indicate the improved damping of motion when the control loop is closed. The system which was tested had 15 modes below 2.5 Hz and damping of these modes was 1.5 percent or less. More advanced techniques than these are under development including the use of unobtrusive effectors; in our first experiments a piezo-electric polymer was used. A 0.1 ounce effector was able to quickly damp out the response of a cantilever beam with a 4 lb mass attached at the tip. We have been building a laboratory with expanded capabilities for larger space structures to test new concepts and also will be using a flat floor facility to permit unrestrained motion in the horizontal plane. This laboratory will help us meet the challenge of using closed loop control techniques to supply the damping required for many applications we can foresee.

SUMMARY

These example challenges represent only a small fraction of the problems facing our programs, because we in the space program, just as other members of the dynamics community, seek to push the boundaries of our capabilities outward to accomplish things that have not been done before. We run turbopumps at higher speeds and thus produce higher stresses which require new materials, and so on. We are building even larger space vehicles, geostationary platforms and a space station, and creating new structural concepts, even exotic materials, in order to meet all the challenges these structures produce. Adding damping to a structure through active control brings yet another aspect to structural properties. We have been able to succeed because of the experience we have gathered from earlier work. But for this work to be as useful as possible, we have to organize the results and analyze them. That is why we can expect to see even more emphasis on data bases and automated analysis, as well as increased statistical inference. We need to plan these data base systems carefully so that they become the tools we need because the expense of maintaining them will be great if they are unwieldy and there will be extreme difficulties in modifying a system that does not give us the needed output.

The area of testing of models and prototypes is getting even more interesting for us than it has been because of the combination of zero-gravity environment and large structure (e.g., space station). The difficulty and expense of using standard methods precludes the complete modal survey that traditionally has been used. Impedance testing is only one of the alternate techniques under consideration; there also are new measurement techniques such as lidars which must be included in our thinking. And some testing must be done in space because this is the first time that large structures such as the space station will exist as a total system.

New instrumentation for internal flow and combustion processes in engines is beginning to yield more accurate and much finer grained pressure and temperature inputs for analysis of dynamic response and stress. The development of finer grained structural analysis has paralleled that of CFD because both are constrained by the same limitation: available computer capacity. As the turbine blade analysis showed, we are able to utilize the new data with reasonable facility. This is largely because we have developed pre- and post-processing programs which eliminate the labor-intensity of more traditional methods of analysis. Two aspects of this approach are of concern to me, however. The first is that we tend to use our capabilities to the limit, and there are probably analyses being run which go well beyond what is needed to get the required answer in terms of depicting areas which are not of concern or showing detail in areas where stress or forces are nearly constant. The other concern is that these tools allow us to obtain results without fully understanding what we are doing. This always has been possible, but the temptations get stronger as the equipment gets automated. Many of us older engineers are beginning to long for the sight of a free-body diagram and to wonder whether some of the younger ones know what one is. The challenge is to keep our grip on what really is happening as well as on trying to understand what is happening in the microstructure of materials now that we are in the age of single crystal turbine blades, for example.

And this brings me to a final point. It appears that the day of the narrow specialist is waning. More and more, a good dynamicist must learn something about the other specialties with which he comes in contact: materials, control systems, flow dynamics, data management, statistics, and other specialties we haven't touched upon. We increasingly can't solve our problems based on inputs from one group and then pass our results on to someone else. Although this cross-fertilization will complicate our work somewhat, it will help us immensely to see the big picture and in so doing will give us insights and understanding far beyond that we would have as specialists. We will be the richer for it.

ORIGINAL PAGE IS
OF POOR QUALITY

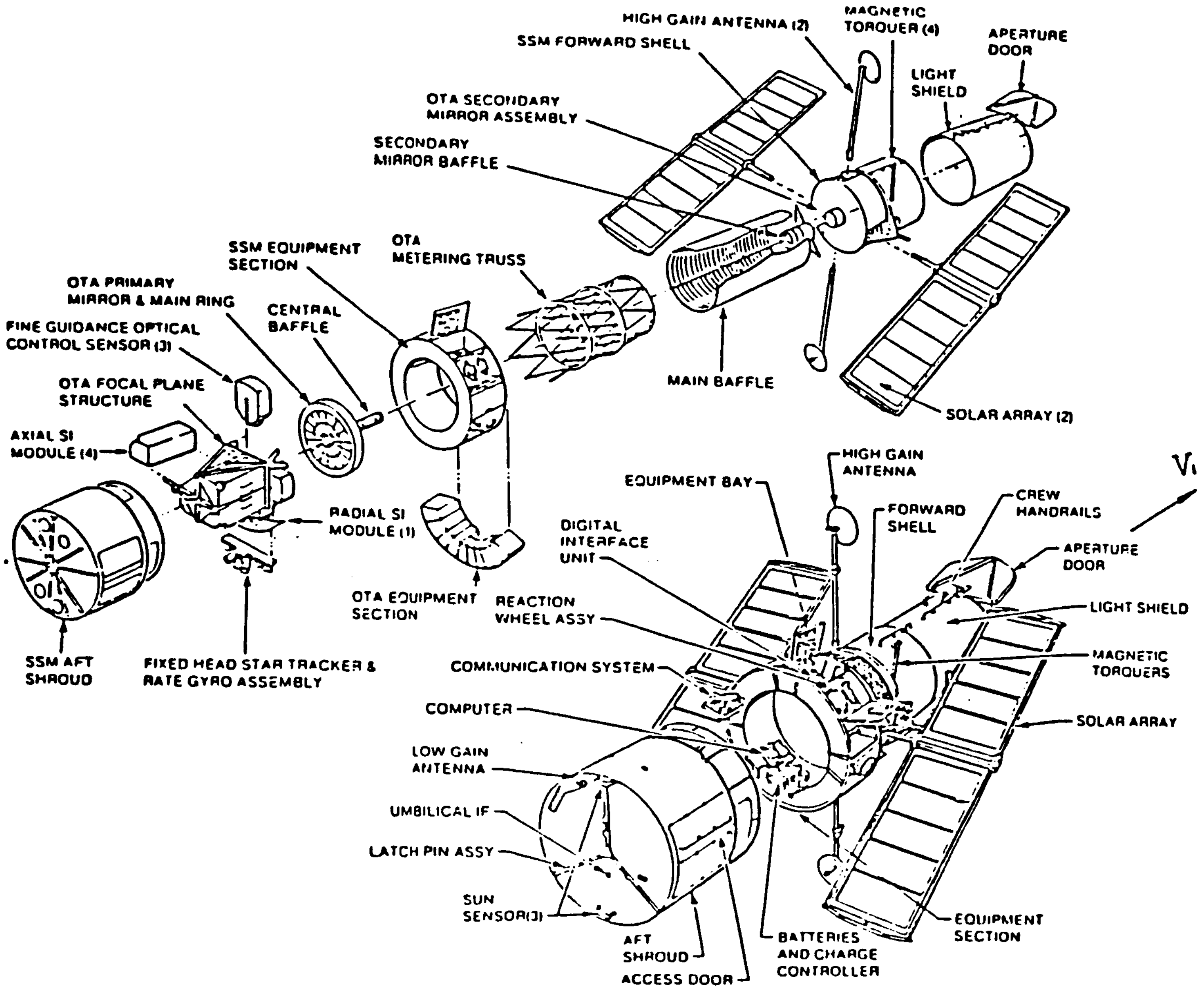

FIGURE 1 EXPLODED VIEW OF THE HST

MODAL SURVEY TEST

- 0 OBJECTIVE: DYNAMIC MODEL VERIFICATION
- 0 SINE DWELL USING LOCKHEED AUTOMATIC TEST CONTROL AND DATA ACQUISITION SYSTEM
- 0 WIDE BAND SWEEPS FOR OVERALL FREQUENCY RESPONSE
- 0 NARROW BAND SWEEPS FOR MODAL PROPERTIES
- 0 MODES OF INTEREST
  - OTA/SSM "SCISSORS" (SIGNIFICANT FOR LOADS AND JITTER)
  - SSM AFT SHROUD (SIGNIFICANT FOR LOADS)
  - PRIMARY AND SECONDARY MIRROR (SIGNIFICANT FOR JITTER)
  - RWA ISOLATOR MODES (SIGNIFICANT FOR JITTER)
  - OTHER JITTER PRODUCING MODES
  - SUSPENSION SYSTEM MODES (FOR FIXTURE CONTRIBUTIONS)

FIGURE 2

SAMPLE MODE SHAPE COMPARISON: V3 AFT SHROUD

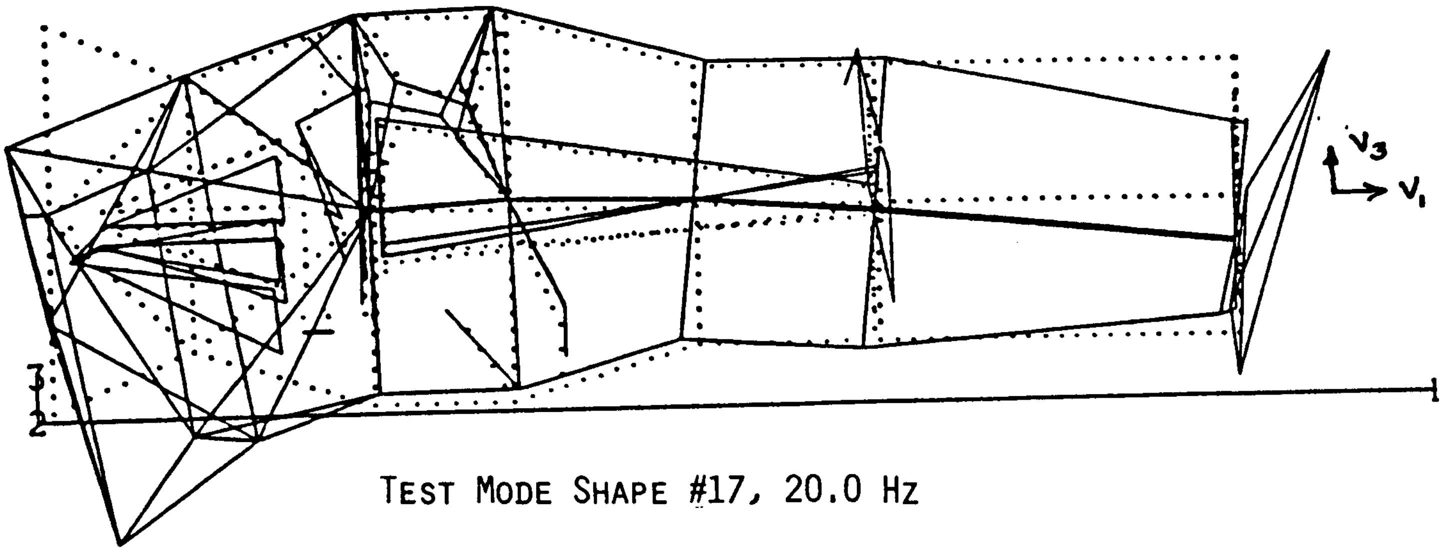

TEST MODE SHAPE #17, 20.0 Hz

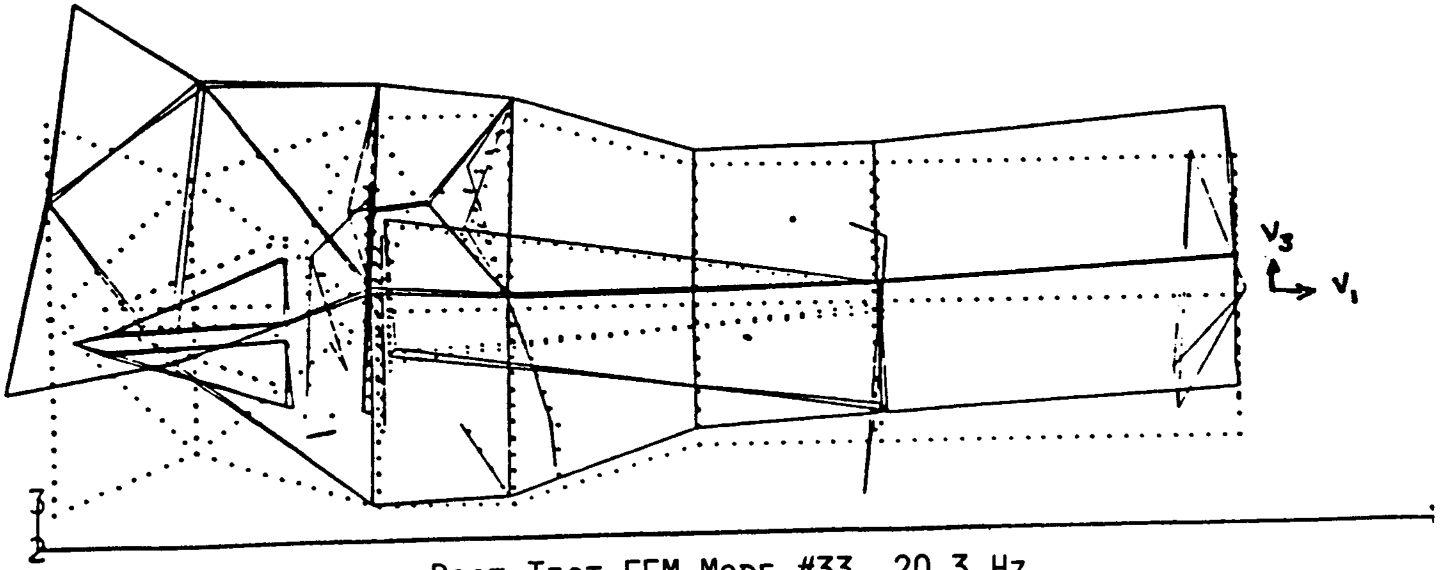

POST-TEST FEM MODE #33, 20.3 Hz

FIGURE 3

IMPEDANCE TEST TECHNIQUES

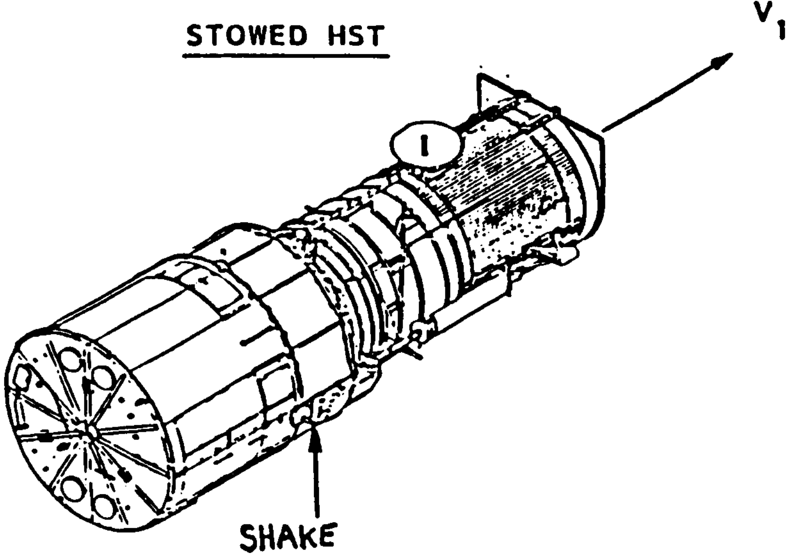

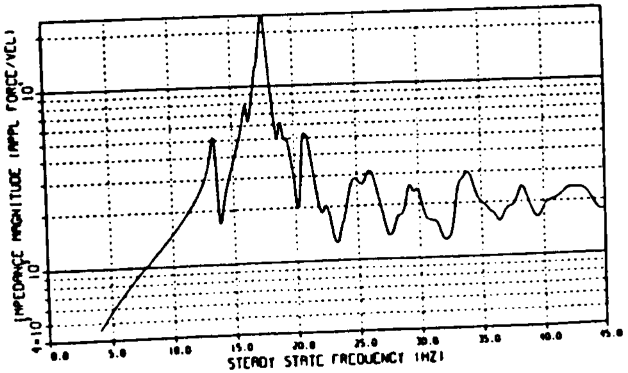

IMPEDANCE TESTING

- SINGLE SHAKER STEADY STATE SINE SWEEP FOR EACH INTERFACE DEGREE OF FREEDOM (6 FOR HST)
- IMPEDANCE = (APPL FORCE) - (RESPONSE VEL)
- IMPEDANCE PEAK IDENTIFIES MODE OF STRUCTURE FIXED AT SHAKEN POINT
- IMPEDANCE PEAK IS THE PRIMARY CONTRIBUTOR TO FUNDAMENTAL STOWED VEHICLE MODES AND VICE VERSA
- IMPEDANCE PEAKS AND TRANSFER FUNCTION MINIMA OCCUR AT SAME FREQUENCY POINT

TRANSFER FUNCTION TESTING

- SINGLE SHAKER STEADY STATE SINE SWEEP
- TRANS FN = H (W) = (RESPONSE ACC) - (APPL FORCE)
- RESPONSE PEAKS IDENTIFY CRITICAL MODES
- TRANSFER FUNCTION MINIMA ARE GENERALLY IGNORED

FIGURE 4

HST POST-TEST ANALYSIS
-V2 AFT TRUNNION, V3
INTERFACE ACCELEROMETER (94")

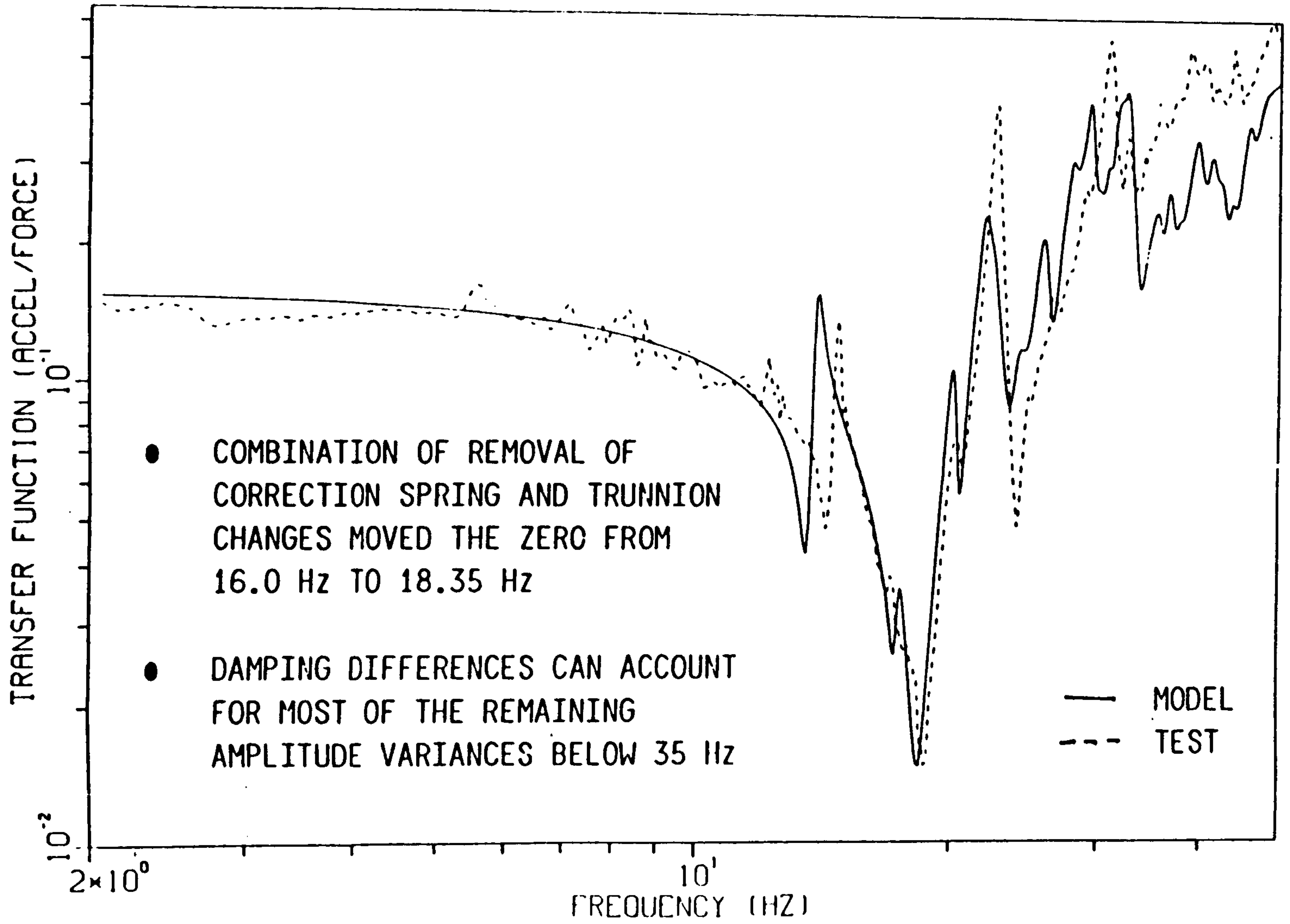

- COMBINATION OF REMOVAL OF CORRECTION SPRING AND TRUNNION CHANGES MOVED THE ZERO FROM 16.0 Hz TO 18.35 Hz
- DAMPING DIFFERENCES CAN ACCOUNT FOR MOST OF THE REMAINING AMPLITUDE VARIANCES BELOW 35 Hz

FIGURE 5

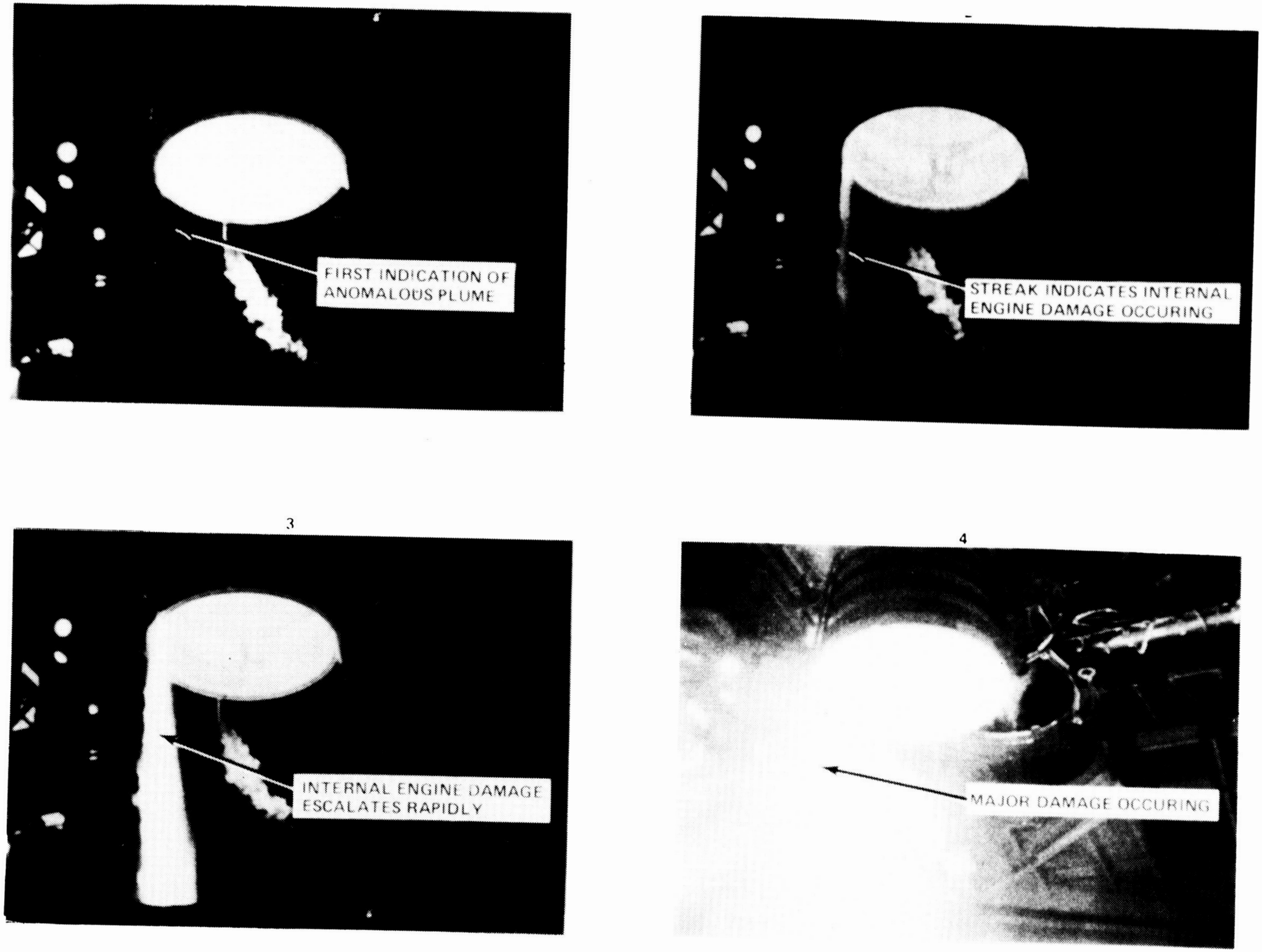

3

4

FIRST INDICATION OF ANOMALOUS PLUME

STREAK INDICATES INTERNAL ENGINE DAMAGE OCCURING

INTERNAL ENGINE DAMAGE ESCALATES RAPIDLY

MAJOR DAMAGE OCCURING

SEQUENTIAL FILM FRAMES OF FAILURE - 400 f/sec

FIGURE 6

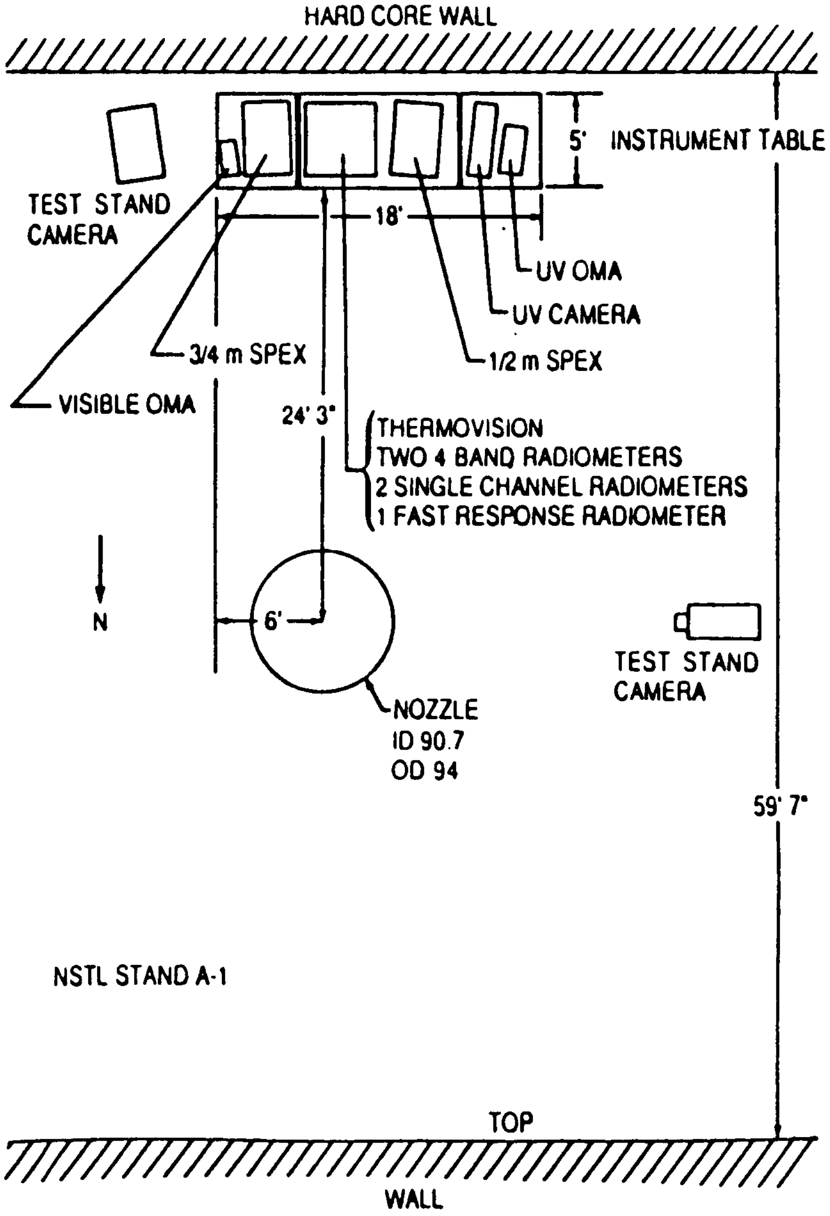
HARD CORE WALL
5'
INSTRUMENT TABLE
TEST STAND CAMERA
18'
UV OMA
UV CAMERA
1/2 m SPEX
3/4 m SPEX
VISIBLE OMA
24' 3"
THERMOVISION
TWO 4 BAND RADIOMETERS
2 SINGLE CHANNEL RADIOMETERS
1 FAST RESPONSE RADIOMETER
N
6'
NOZZLE
ID 90.7
OD 94
TEST STAND CAMERA
59' 7"
NSTL STAND A-1
TOP
WALL

FIGURE 7

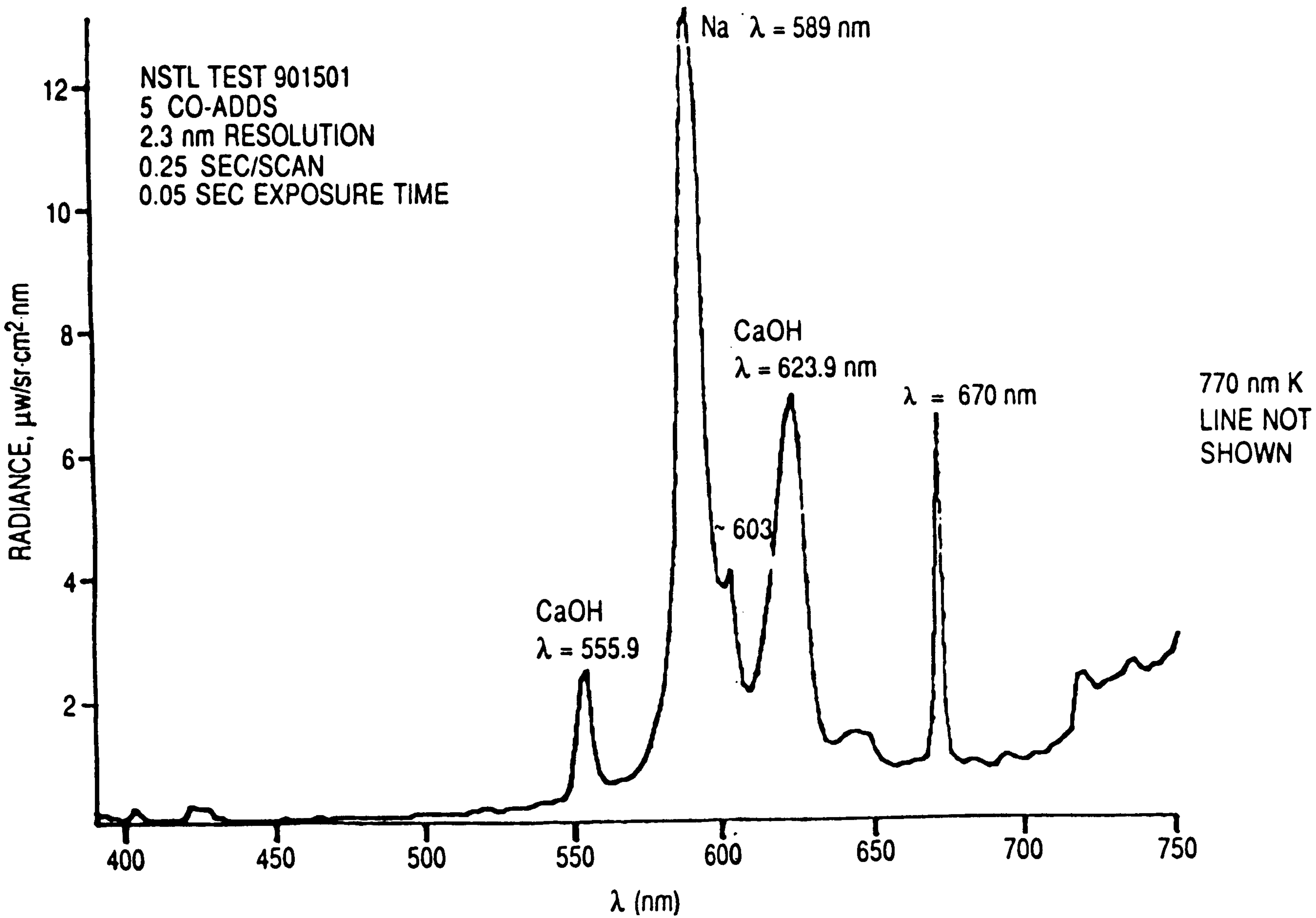
NSTL TEST 901501
5 CO-ADDS
2.3 nm RESOLUTION
0.25 SEC/SCAN
0.05 SEC EXPOSURE TIME
Na λ = 589 nm
CaOH
λ = 623.9 nm
λ = 670 nm
770 nm K
LINE NOT
SHOWN
~ 603
CaOH
λ = 555.9
RADIANCE, μw/sr·cm²·nm
12
10
8
6
4
2
400
450
500
550
600
650
700
750
λ (nm)

FIGURE 8

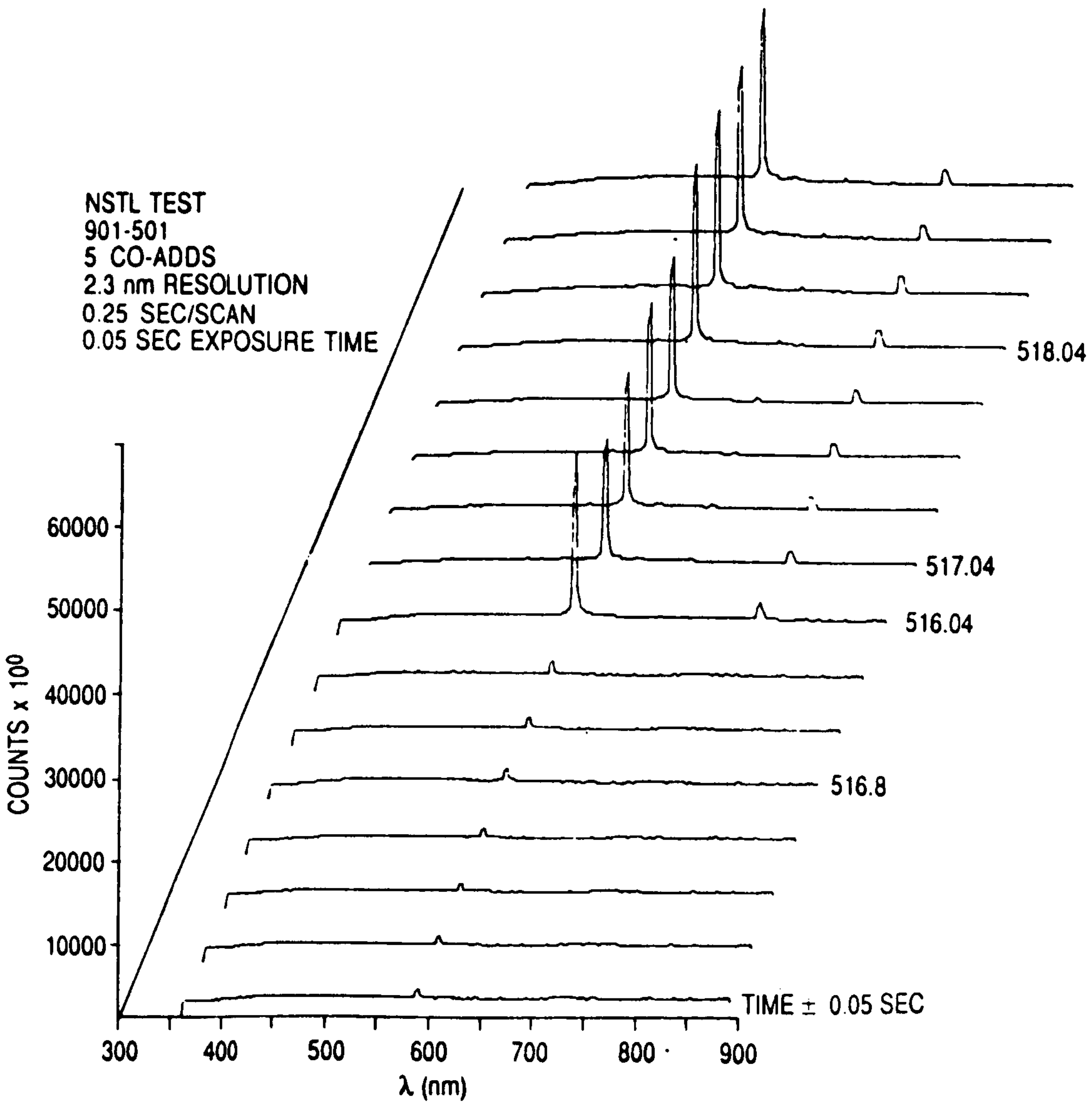NSTL TEST
901-501
5 CO-ADDS
2.3 nm RESOLUTION
0.25 SEC/SCAN
0.05 SEC EXPOSURE TIME
COUNTS x 100
60000
50000
40000
30000
20000
10000
300
400
500
600
700
800
900
λ (nm)
518.04
517.04
516.04
516.8
TIME ± 0.05 SEC

FIGURE 9

VALIDATION OF HOT GAS FLOW PATH DESIGN METHODS

P = 3600 PSIA
T = 1675°R
$\dot{m}$ = 169 #/SEC

P = 3600 PSIA
T = 1475°R
$\dot{m}$ = 73 #/SEC

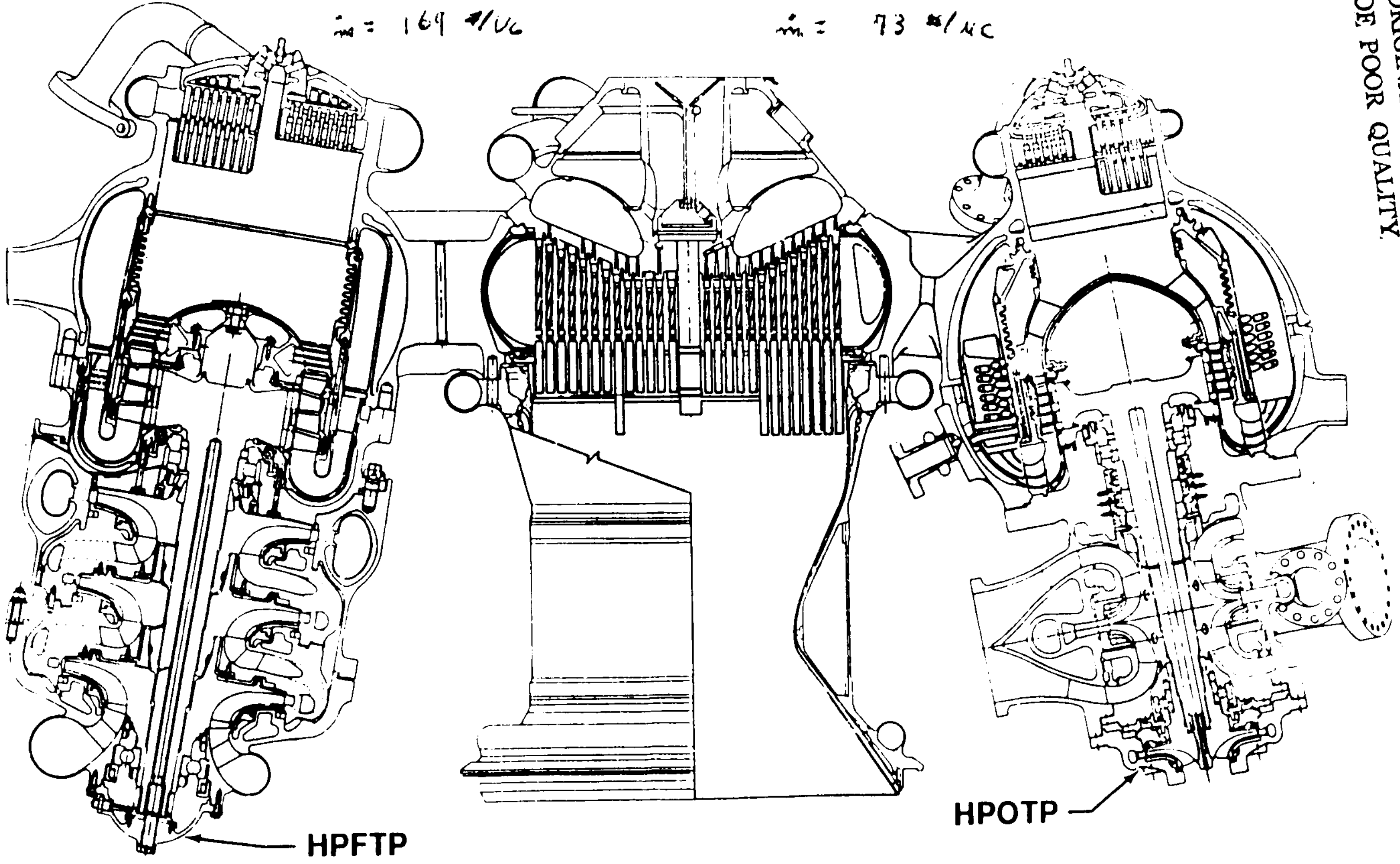

FIGURE 10

Velocity Magnitude Contours In The Transfer Tubes Of The SSME Hot Gas Manifold Are Calculated By CFD

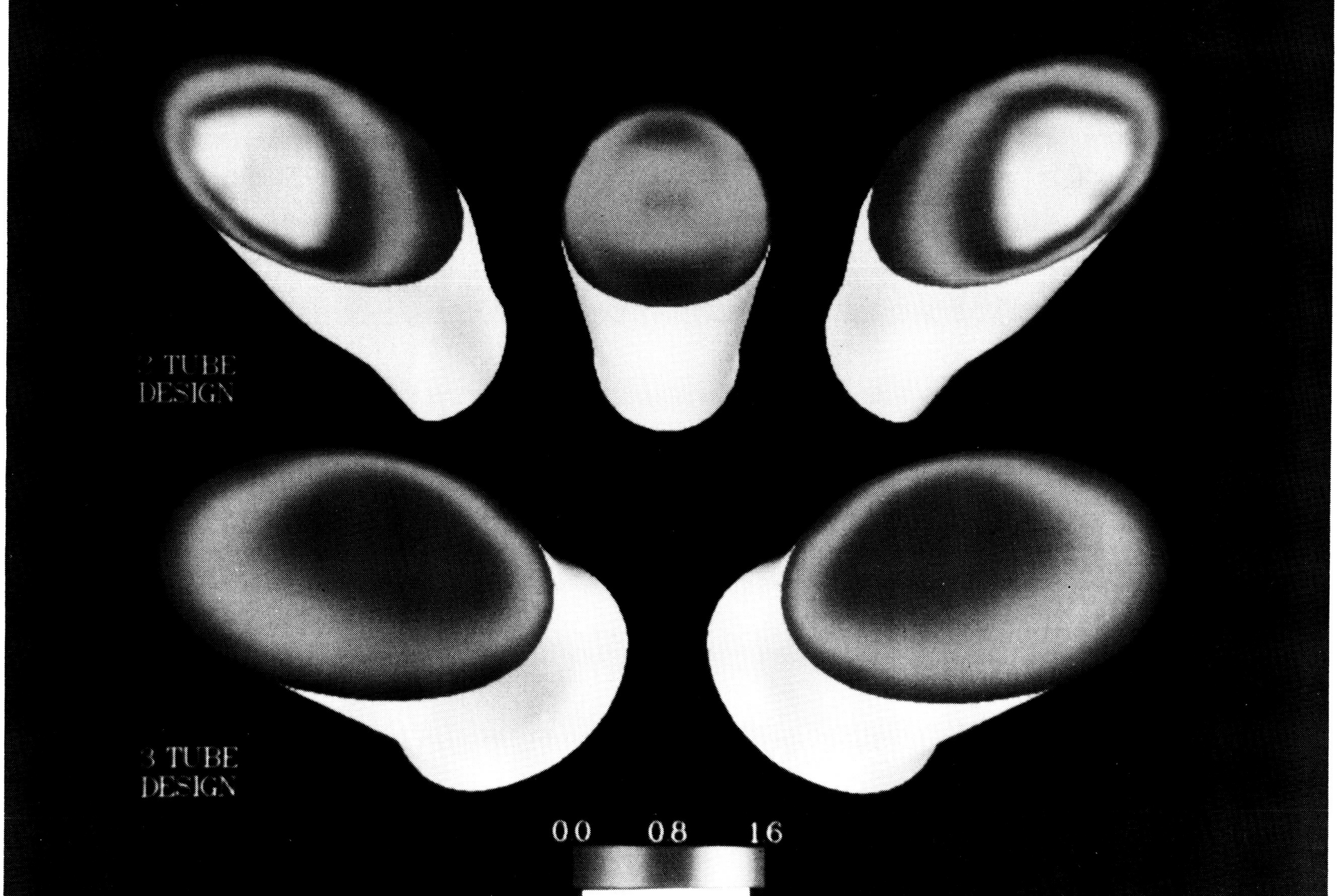

FIGURE 11

ORIGINAL PAGE IS
OF POOR QUALITY

OBJECTIVES:

- COMPARE ANALYSES OF PHASE II+ HGM COMPLETED OVER LAST 2 YEARS TO AIR FLOW DATA
- SUMMARIZE RUN HISTORIES FOR THE CODES CONSIDERED

CODE	ALGORITHM	TURBULENCE MODEL	NO. OF GRID POINTS (II+)
INS3D	BEAM-WARMING PSEUDO-COMPRESSIBILITY	ALGEBRAIC MIXING LENGTH	185088*
PAGE	TWO-STEP EXPLICIT MACCORMACK	PRANDTL- VAN DRIEST	21059
PHOENICS	SIMPLE TYPE	K-ε	10076
VAST	DYNAMICALLY DIFFERENCED EXPLICIT	ALGEBRAIC MIXING LENGTH	10724

*NO STRUTS, NO VARIATION IN TURBINE EXIT CIRCUMFERENTIAL PRESSURE, RACETRACK INCLUDED

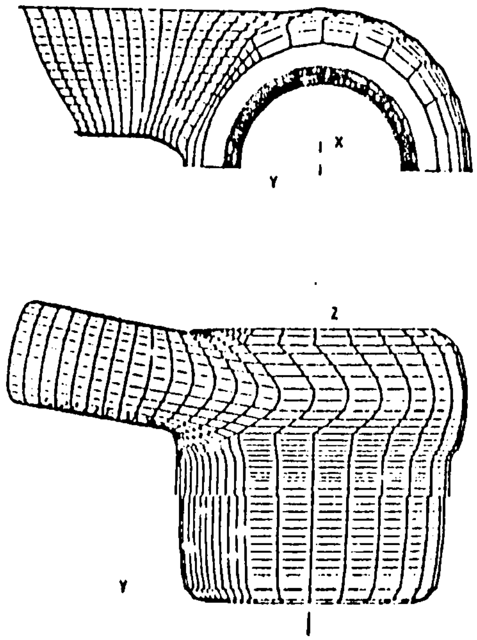

FIGURE 12 COMPARISON OF HOT GAS MANIFOLD ANALYSES TO AIR FLOW DATA

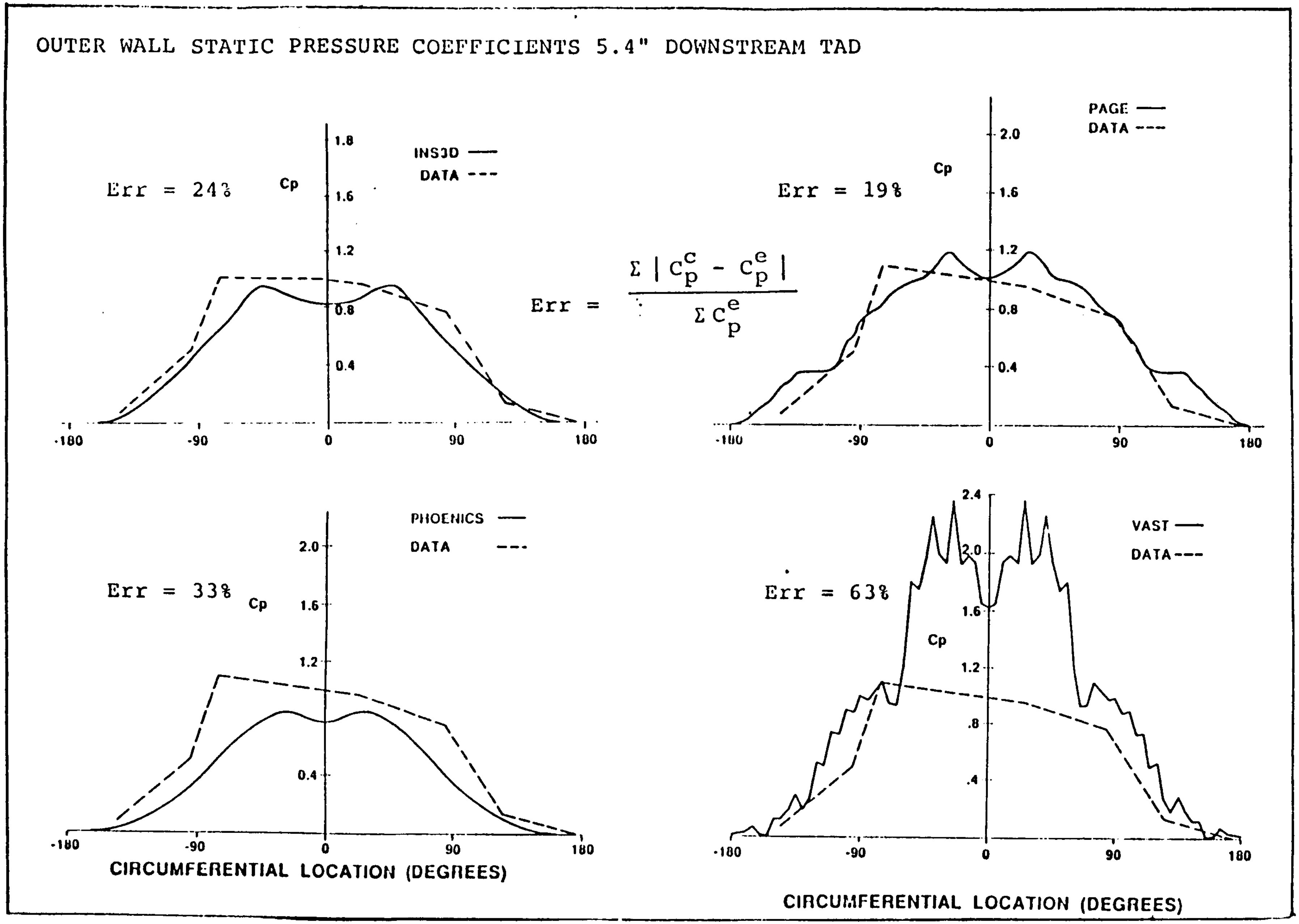
OUTER WALL STATIC PRESSURE COEFFICIENTS 5.4" DOWNSTREAM TAD

$$Err = \frac{\Sigma \left| C_p^c - C_p^e \right|}{\Sigma C_p^e}$$

FIGURE 13 **COMPARISON OF HOT GAS MANIFOLD ANALYSES TO AIR FLOW DATA**

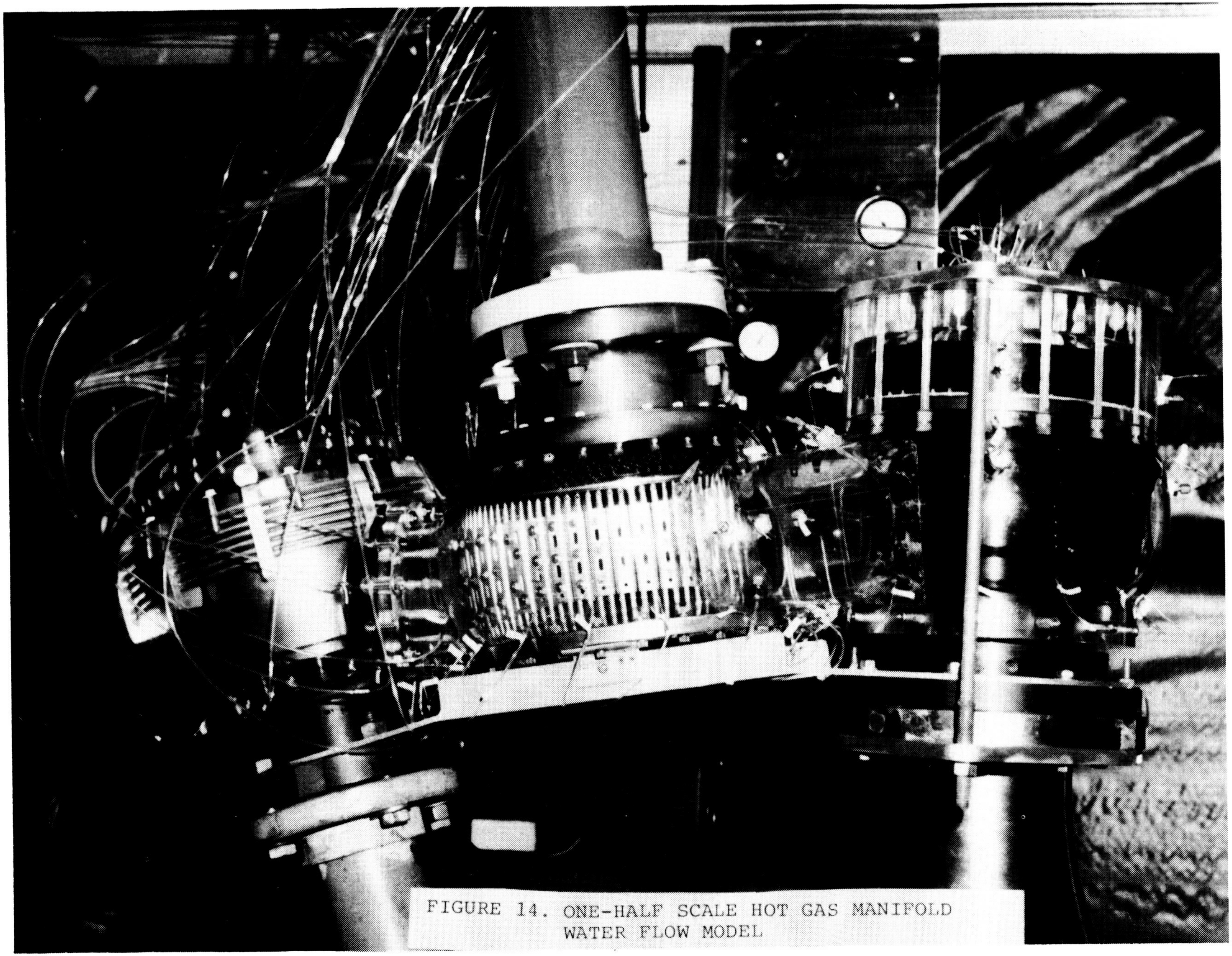

FIGURE 14. ONE-HALF SCALE HOT GAS MANIFOLD
WATER FLOW MODEL

ORIGINAL PAGE IS
OF POOR QUALITY

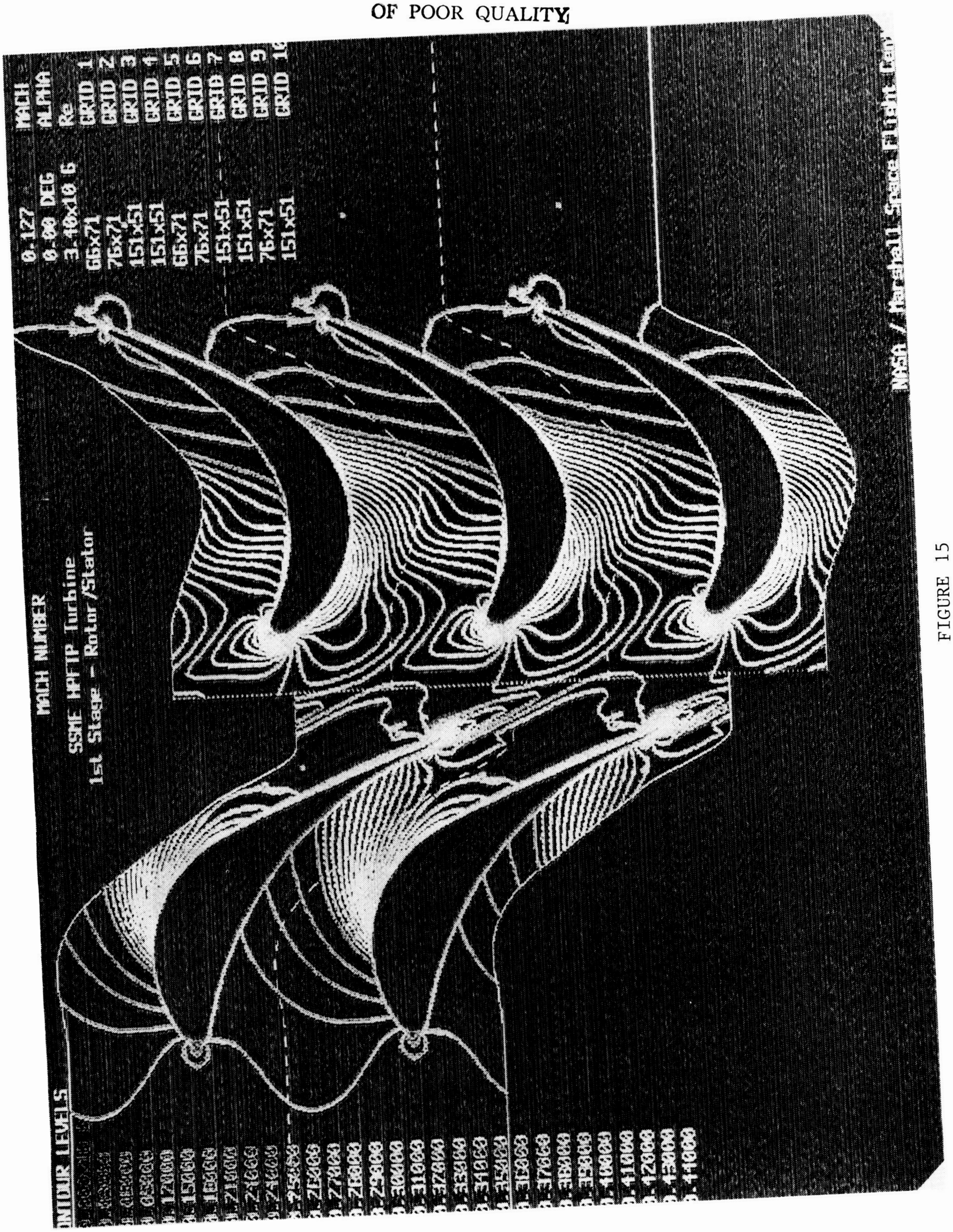

FIGURE 15

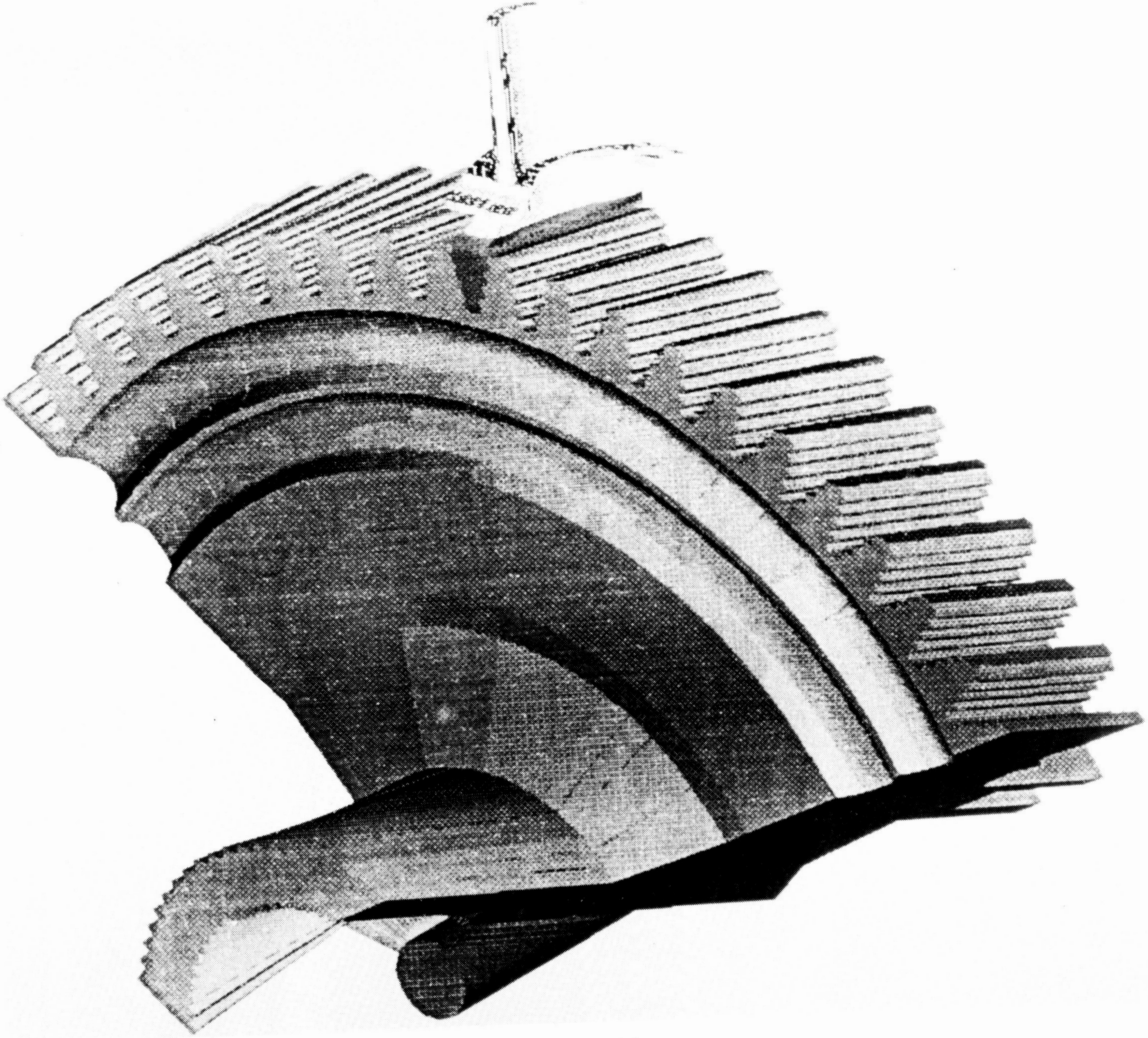

FIGURE 16

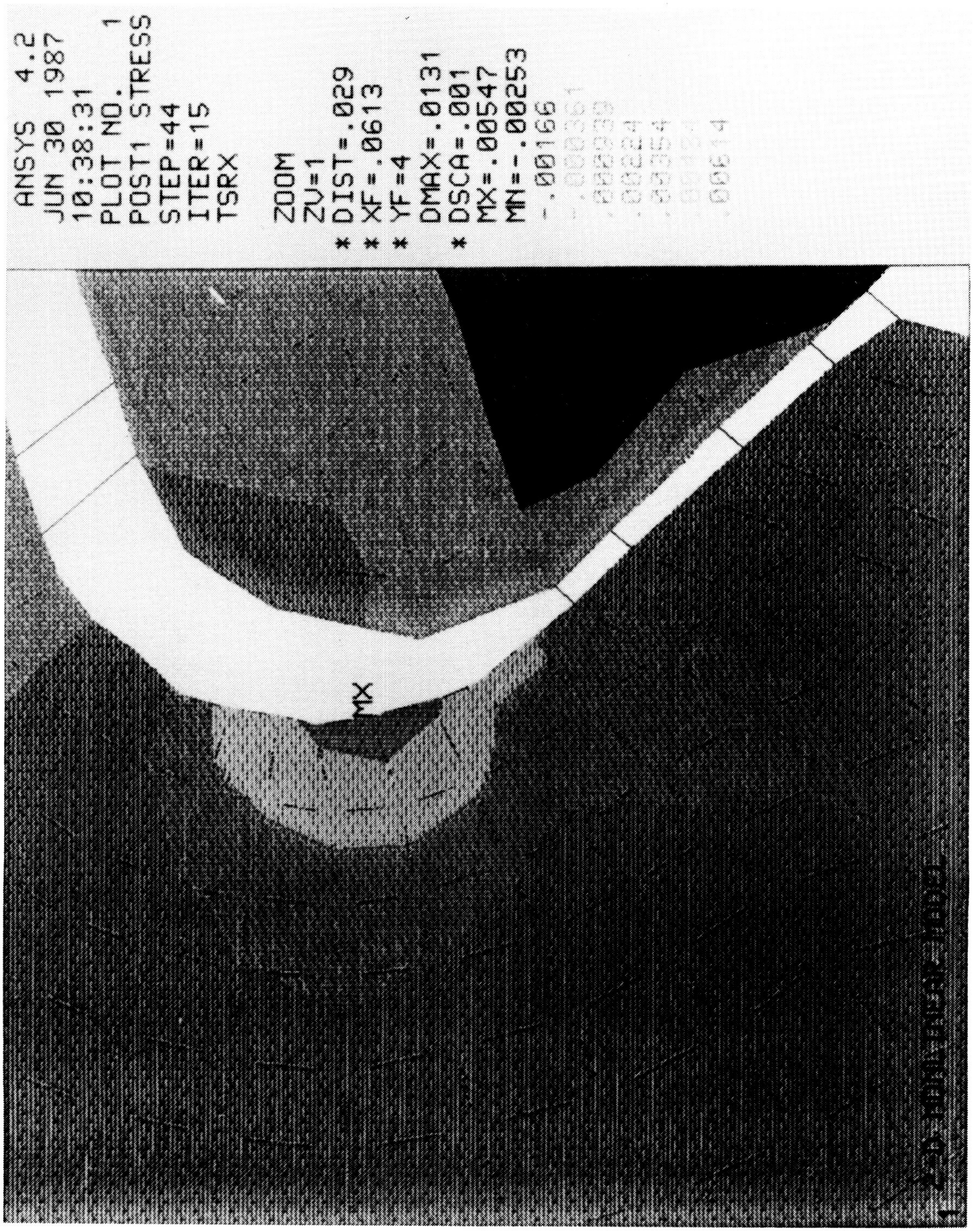
ANSYS 4.2
JUN 30 1987
10:38:31
PLOT NO. 1
POST1 STRESS
STEP=44
ITER=15
TSRX
ZOOM
ZV=1
*DIST=.029
*XF=.0613
*YF=.4
*DMAX=.0131
*DSCA=.001
MX=.00547
MN=-.00253
-.00166
-.000361
.000939
.00224
.00354
.00484
.00614
MX

FIGURE 17


ANSYS 4.2
AUG 12 1987
11:08:12
PLOT NO. 23
POST1 STRESS
STEP=2
ITER=15
SP1
ZV=1
DIST=.55
XF=.601
YF=.4
ZF=3.98
MX=.0043
MN=.000211
.000257
.000757
.00126
.00176
.00226
.00276
.00426
.00476
SECOND STAGE FIRTREE FACE 1,8,15,23,30
*T.E.
L.E.
(FPL SS PRESSURE+SPEED+THERMAL)

FIGURE 18

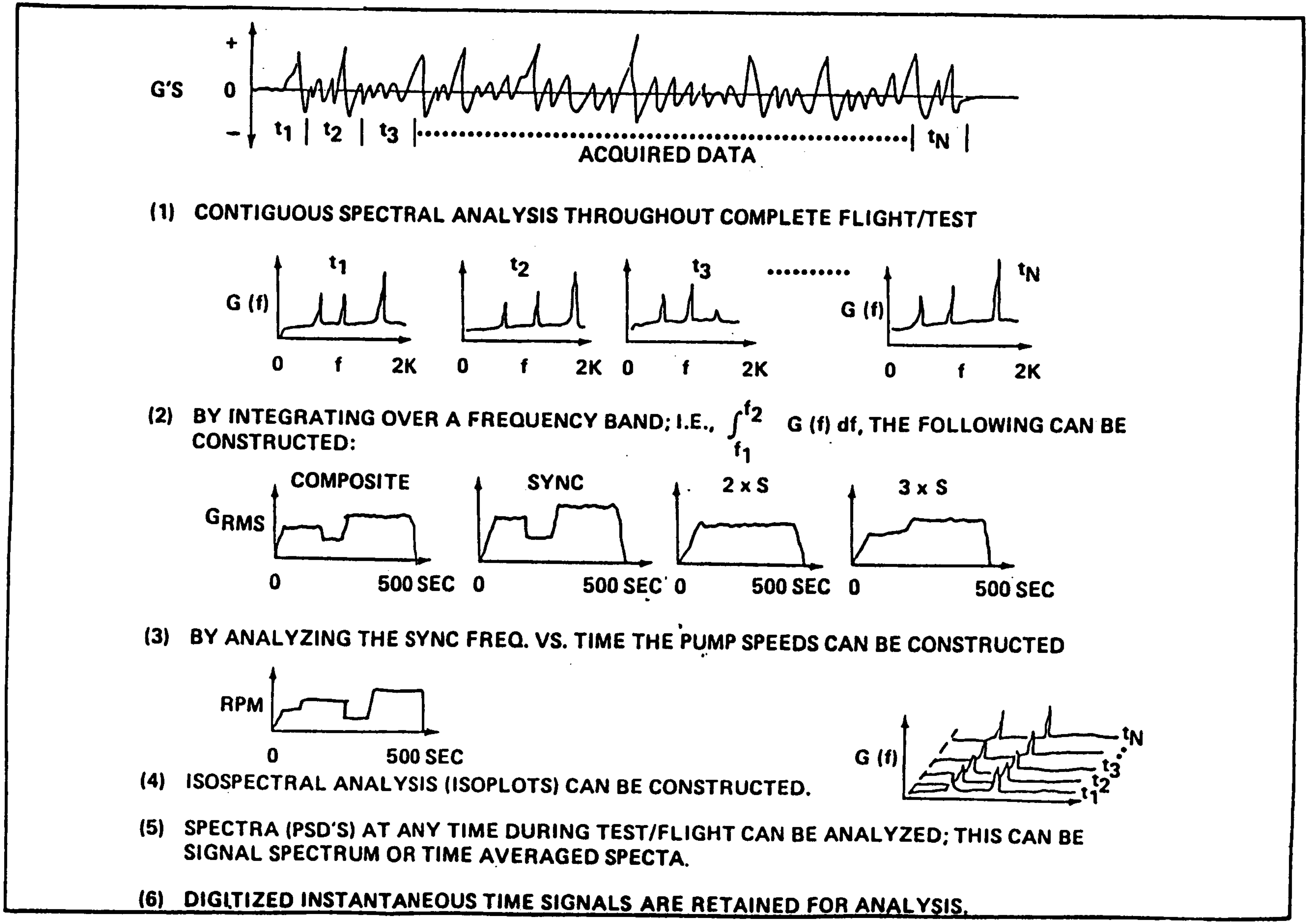

(1) CONTIGUOUS SPECTRAL ANALYSIS THROUGHOUT COMPLETE FLIGHT/TEST

(2) BY INTEGRATING OVER A FREQUENCY BAND; I.E., $\int_{f_1}^{f_2} G(f)\,df$, THE FOLLOWING CAN BE CONSTRUCTED:

(3) BY ANALYZING THE SYNC FREQ. VS. TIME THE PUMP SPEEDS CAN BE CONSTRUCTED

(4) ISOSPECTRAL ANALYSIS (ISOPLOTS) CAN BE CONSTRUCTED.

(5) SPECTRA (PSD'S) AT ANY TIME DURING TEST/FLIGHT CAN BE ANALYZED; THIS CAN BE SIGNAL SPECTRUM OR TIME AVERAGED SPECTA.

(6) DIGITIZED INSTANTANEOUS TIME SIGNALS ARE RETAINED FOR ANALYSIS.

FIGURE 19 ACQUISITION AUTOMATED HIGH SPEED SPECTRAL

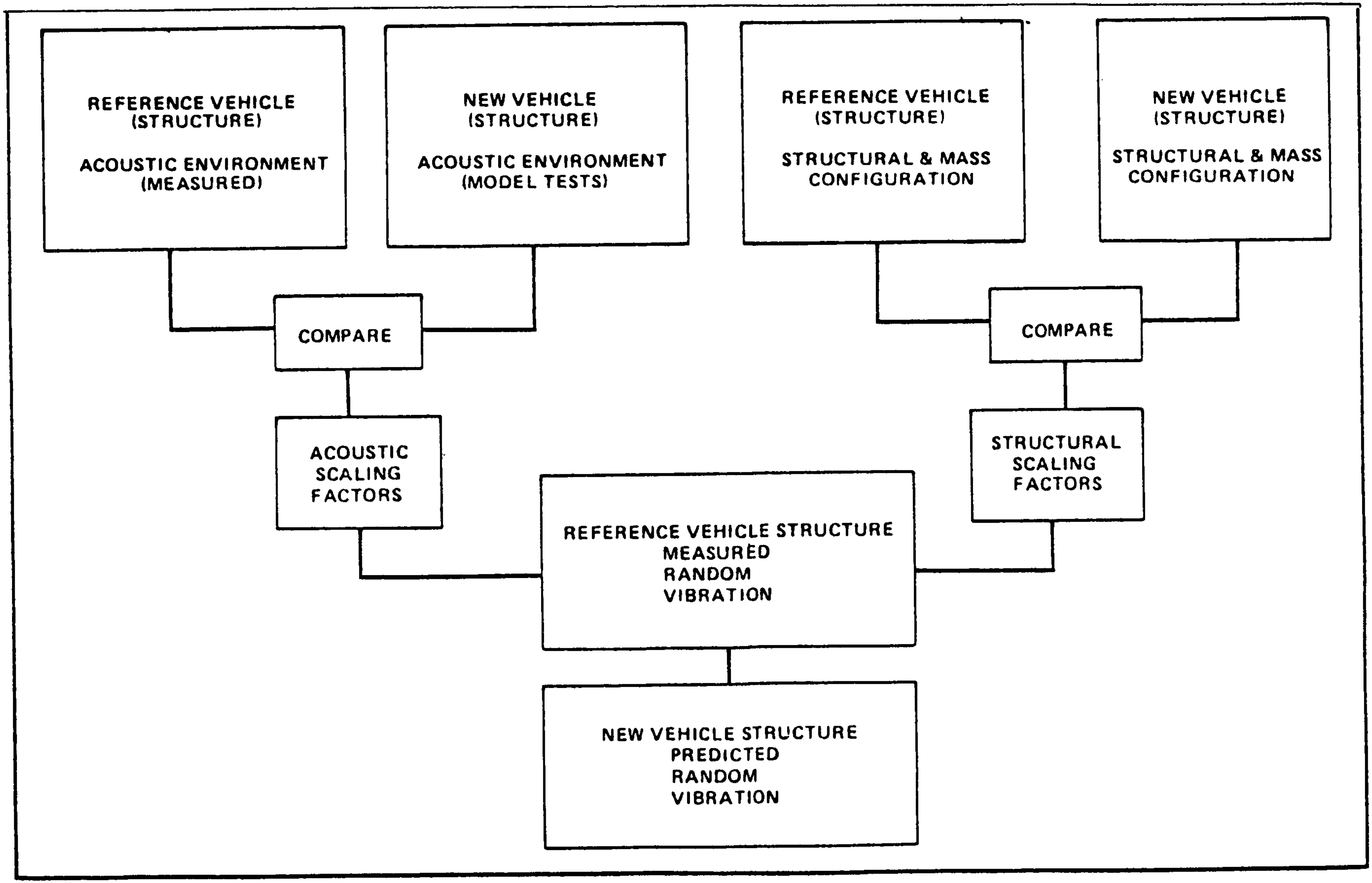

FIGURE 20 RANDOM VIBRATION CRITERIA DEVELOPMENT

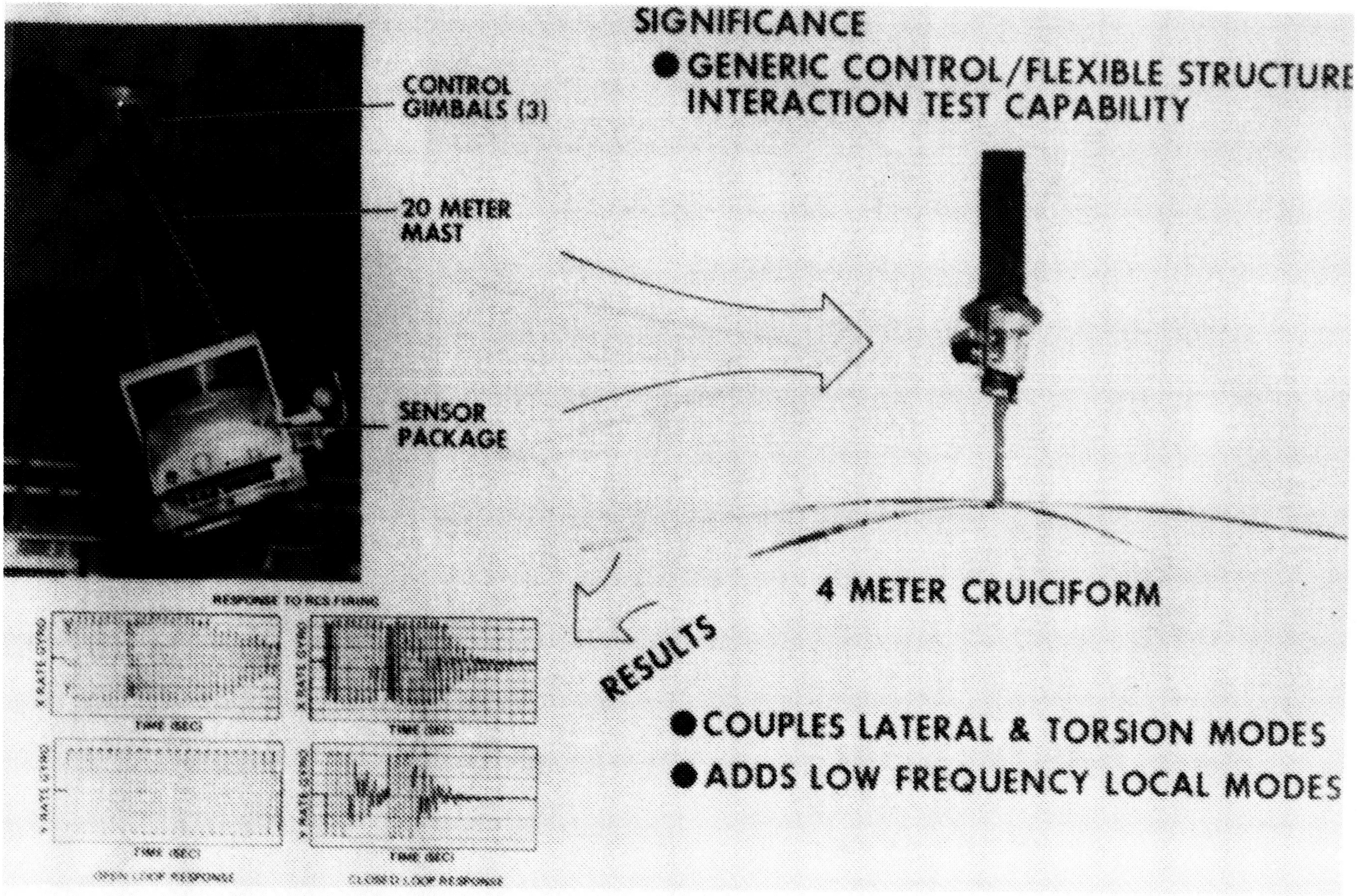

SIGNIFICANCE

- ●GENERIC CONTROL/FLEXIBLE STRUCTURE INTERACTION TEST CAPABILITY

RESULTS

- ●COUPLES LATERAL & TORSION MODES
- ●ADDS LOW FREQUENCY LOCAL MODES

Figure 21. LSS control for configuration 1.

A Commanding Officer's Perspective of Ship Shock Trials

Carl A. Anderson

Captain Anderson served as Commanding Officer, USS YORKTOWN (CG 48), an AEGIS guided missile cruiser, from July 1983 to June 1986. He received the Legion of Merit for displaying "extraordinary leadership and professionalism in guiding USS YORKTOWN through commissioning, predeployment workups, and an eight-month Mediterranean and Black Sea deployment," described by the Chief of Naval Operations as a modern-day odyssey. Captain Anderson has been Commander, Naval Surface Warfare Center, since August 1986.

TEXT OF ADDRESS

It is indeed a pleasure to be with you today. Your Shock and Vibration Symposium has a long and distinguished record of building technical excellence into many diverse and critical systems. Once again, you are bringing together people from DOD, industry, and the universities; fostering cooperation on the international level; and considering mutual objectives in modern technology. I hope this unique forum will continue for many years to come.

Your theme today, "New Horizons in Dynamics," is most appropriate to an era that's bringing rapid changes to our products and our methodology. We in the Navy refer to this as the "Revolution at Sea." It is, in effect, revolutionizing our combat system and platform design, manufacturing, and testing. But more significantly, it is revolutionizing the nature of surface warfare. With sophisticated systems such as AEGIS now in the fleet, the Navy no longer thinks in terms of individual weapons, but rather in terms of integrated weapons systems and platforms. The concept of the battle group also affects these systems and the ways in which they are employed.

ONE COMMANDING OFFICER'S OUTLOOK ON SHOCK TESTING HIS SHIP

The shock trials of USS YORKTOWN in 1984 illustrate several aspects of this revolution at sea. YORKTOWN was the second of a new class of cruisers. Its AEGIS combat system is capable of detecting, classifying, and tracking multiple targets in the air, on the surface, and under the sea. In short, this is a new kind of ship with revolutionary interaction among combat systems, the platform, and the battle group. As the first ship of its class to undergo shock trials, YORKTOWN'S performance would have critical implications for the entire ship class.

As far as I was concerned, being Commanding Officer of YORKTOWN was the best job in the Navy. In fact, when I got the word about the forthcoming shock trials, my immediate reaction was: If my ship gets blown up I might have to spend my entire operational command in the shipyard! But I soon realized there were two approaches I could take in preparing for the trials. The first option was the passive approach, in which the measurement of success is confined to engineering considerations (principally, identification of failures). Or on the other hand, I could take the active approach: adding measurements of readiness and crew response--bringing in the human element.

Underwater shock tests provide an experience very close to actual warfare. You get the same effect as a near miss---and that can be very destructive in combat. And so, measuring the human factor during these trials would allow us to capitalize on a very realistic training opportunity. We would therefore work on our ability to succesfully repair, to recover, and to fight the ship. Training to "reality" is an excellent way to avoid the principle of cascading casualties, wherein one material casualty leads in rapid succession to still others. Even before the shock trials, I had injected a measure of reality into our experience by shutting off the fuel valve to the main generator and observing the crew's reaction.

And finally, I intended to measure the tests not in terms of failure, but in terms of victory...and victory demanded the active approach, with all the extra effort and calculated risks that it implied.

An ancient Chinese proverb holds that "The more you sweat in peace, the less you bleed in war." In a very real sense, we need to apply that wisdom to our training. The digital world of the late Twentieth Century boasts intercontinental missiles capable of spanning the Atlantic in minutes. With strike time computed in ever decreasing increments, any major conflict will be a "come-as-you-are war." The time to prepare is before the crisis...arriving unprepared for the come-as-you-are war is tantamount to not showing up at all!

PREPARATIONS FOR THE SHOCK TRIALS

Our basic preparations began two years before the trials; the crew actually participated for fourteen months. We had to be ready just two months after YORKTOWN was commissioned. Three major considerations were site readiness, ship readiness, crew readiness. The site selected for the trials was about 65 miles East of Cape Canaveral, Florida, with an alternate test site 20 miles South of Key West. As it happened, Hurricane Diana intervened, so we did indeed move to the back-up site for the fourth and final shot.

Developing the Shock Team and getting them the support they needed was a primary concern. Integrated training was a cooperative effort among YORKTOWN, COMNAVSURFLANT Training Commands, and NAVSEA personnel. In all, over 700 people were involved from the beginning of in-port preparations up through the last detonation. They included people from NAVSEA, NAVELEX, ISEA, manufacturers, and contractors. About 140 of those rode the ship on shot days. These diverse groups developed into a great team and shared in all our objectives.

As for ship readiness and crew readiness, it's almost impossible to achieve one without the other. The human/engineering interface is extremely important in fighting the ship. We devised two systems to inspect all spaces: vertical and horizontal. Compartment check-off sheets were prepared prior to examination of every compartment to see if it could survive. There were times when my crew thought I was practicing overkill with these detailed preparations. But it was very instructive the day we tore down some of the equipment and discovered some things that would not have survived had we not adhered to our plans, which gave us the opportunity to take remedial action. For example, we found and corrected a cable arrangement that might well have resulted in a fire. Another concern was that the fire retardant doors throughout the ship weren't capable of passing a shock test. We were able to prove out a new hatch closure design that did remain operational throughout the trials.

We also had to decide what to keep aboard and what to offload. YORKTOWN carried more than two-thousand items of test equipment that were not shock hardened; the normal procedure is to remove all this gear before a shock trial. But in reality, we would need that test equipment during the course of the trials---just as we would need it during actual warfare. So we took a calculated risk: we kept it aboard; we designed special racks for it; and it survived with only one piece of equipment out of calibration. The rack design was actually so successful that it will probably save the Navy more money than was spent on the shock trials.

"CSOSS" became a major factor in our preparations. This is an idea borrowed from the engineering world and applied to the combat system. In essence, it's a Combat System Operational Sequencing System for initialization and casualty restoration of the combat system equipments. CSOSS ensured that all operators and technicians used precisely the same procedures when dealing with equipment.

All phases of our operations were monitored and reported to a single shock trials project manager, who communicated with the CO on all facets of the trials. And finally, we prepared for heavy weather---a challenge to both crew and ship, as any shiprider can tell you.

We spent a lot of time devising ways to fight the ship. One of my sailors made the mistake of saying that we could hardly expect to be as ready for the last shot as for the first. I immediately seized the opportunity to give an extemporaneous lecture on Victory. We were not, I thundered, going into this with negative expectations. Our goal was victory, and that meant No Cumulative Effects, No Cascading Casualties---always repair before the next shot.

As we moved closer to the date of the trials, there was total commitment on the part of the entire crew, as well as the shock test team. The crew was determined to fight this ship through the tests. We had all learned from our preparations, and that experience had become an inspirational one.

THE SHOCK TRIAL EXPERIENCE

YORKTOWN entered the trials fully capable in all warfare areas. Our goal was to maintain C-1 readiness in every mission area prior to every shot. The ideal was no material casualties---allowing the ship to continue tracking, linking, communicating, and simulating surface, air, and subsurface engagements. But in the event of a casualty, the first priority would be system restoration, followed by shock damage assessment in each mission area.

Basically, the trials consisted of four underwater explosions, each of increasing severity. In readiness for Shot One, YORKTOWN was at General Quarters, tracking air, surface, and subsurface targets. We were supported by:

--F-14 aircraft, as radar targets and data links

--EP-3A EMPASS aircraft, to evaluate RF radiation emitters

--Lear Jet aircraft, to evaluate close-in weapon system tracking performance and communication with SM-2 Missiles

--USS SCOTT (DDG-995), for LAMPS MK I helo support; and to act as target for surface search sensors; to monitor electronic emissions

--USS Charleston (LKA-113), explosive charge handling and helo support

--Navy EOD Team, rigging charges and making underwater hull inspections. (A first: underwater video monitoring, including video tape recording.)

--Coast Guard patrol craft, to divert other craft from area

--USNS MOHAWK (T-ATF 170), for area surveillance and to act as EOD operations platform

--Navy helo's and photographers for documentation

It was a very impressive operation, with many of the assets dedicated to the important task of gathering data.

The actual detonations signaled an experience without parallel. We experienced the shock waves...the scramble to get all systems up...and the pride of fighting the ship through conditions close to warfare. Although we did not accomplish all the goals we had set for ourselves, we did emerge battle-tested and battle-ready. We learned a lot about our ship---and a lot about ourselves.

On a larger scale, the trials validated the CG 47 class ship design and demonstrated the ability of complex on-board systems to withstand shock. YORKTOWN successfully restored fighting capability in all warfare modes in a relatively short time. This performance had never been matched by any ship subjected to an equivalent shock factor.

YORKTOWN proceeded then to Ingalls shipyard in Pascagoula for inspection; to undergo operational tests to define the shock effects; and for restoration to the pre-trial baseline. We sailed from Pascagoula only thirty-five days after Shot Four.

SUBSEQUENT EVENTS

Subsequent events have borne out the importance of YORKTOWN's shock trials. Certainly the rigorous training, the material preparations, and the reality of surviving near-miss detonations all contributed to ship and crew readiness. While

YORKTOWN was deployed in the Mediterranean, we participated in complex, two- and three-carrier battle force operations in the vicinity of Libya. YORKTOWN also provided air surveillance and command control information during the Achille Lauro terrorist intercept operation.

Many of the lessons learned during the YORKTOWN shock trials were directly applicable to another ship of the TICONDEROGA class, USS MOBILE BAY (CG 53), which was subjected to similar trials earlier this year. MOBILE BAY adopted similar methods of preliminary training, shock team organization, and use of CSOSS, as well as the goal of fighting the ship through the trials.

In my formal report on the YORKTOWN trials, I stated that every ship should experience a mild intensity explosion to evaluate its battle readiness...not only for material preparedness, but also to acquire operational training to combat the anticipated material casualties. I'm happy to say that the Navy is now requiring every shock-hardened new construction combatant ship to undergo a shock test.

On a personal level, my outlook on ship shock trials has come full circle. YORKTOWN demonstrated that the value of this experience goes beyond its basic purpose: it also pays off in material readiness, in training, and in battle readiness. It is cost effective. And it minimizes future risk and casualties.

I came away with a new appreciation for the many contributors: the people in the shipyards, fleet personnel, managers, contractors. I'm glad this team was on my side! And I have a new appreciation for those of you in this audience who are working every day to solve the new problems in dynamics. You are the folks who are going to give us tougher ships and combat systems.

I've carried these thoughts with me to my current assignment as Commander of the Naval Surface Warfare Center. Our mission is to support the Navy's Surface Forces as the principal research, development, test and evaluation center for surface ship weapons systems, ordnance, mines, and strategic systems support. NSWC plays a major role in AEGIS Combat System Development and life-cycle support. Part of our job was to support the USS MOBILE BAY (CG 53) shock trials last May and June. Our team included a Shipboard Power Group, an AEGIS Readiness Group, a Combat System Engineering Group, TOMAHAWK support team, and personnel to collect and disseminate combat system data.

Following these trials, the head of our AEGIS Program Office said: "Our NSWC AEGIS team ensured that the ship's combat system was treated as one system rather than a collection of piece parts." This is typical of the challenges imposed by the Navy's Revolution at Sea.

CONCLUSION

The program for this symposium is also a challenging one to me, both as a ship driver and as Commander of a Navy research and development center. There is no doubt that we are facing "New Horizons in Dynamics." Rear Admiral W. Norman Johnson, Commanding Officer of the Naval Base at Charleston, has expressed it well. Although his words have a distinct nautical flavor, the sentiment applies to other critical technology issues that you'll be considering here. Admiral Johnson described today's Navy as "atomic, electronic, and supersonic." He said, "We employ imperceptible heat, inaudible sound, and invisible light. Our various equipments and systems are not easy to maintain, nor easy to operate. Yet, the men and women on the Navy team continue to demonstrate that they can operate them proficiently."

In the final analysis, that's what it's all about. And that's why the Navy is demonstrating strong support for ship shock tests. In fact, we like that concept so much that we're going to let you have a shot at every new combatant ship that slides down the ways. We're going to be ready to fight our ships through these trials---and I know you're going to do everything in your power to give us tougher ships!

Thank you.

N88-18949

Overview of Multi-Input Frequency Domain Modal Testing Methods with an Emphasis on Sine Testing

Robert W. Rost
David L. Brown

This paper is concerned with an overview of the current state-of-the-art multiple-input, multiple-output modal testing technology. A very brief review of the current time domain methods will be given. A detailed review of frequency and spatial domain methods will be proesented with an emphasis on sine testing.

INTRODUCTION

In the mid sixties sine testing was the only method used for experimental modal analysis. It was used both for the forced normal-mode and the frequency-response methods. With the advent of Fourier Analysis testing methods, sine testing has been used primarily for normal mode testing, for making selected frequency response measurements to study non-linearities; or to gather data in high noise environments.

Sine testing had two major limitations: a) Due to its sweep time, it was considerably slower than the broadband Fourier methods and b) For nonlinear systems, the measurements were distorted. The distortion caused problems with the parameter estimation methods, however, it should be noted that the distortion is important for characterizing non-linearities. The practical advantage of sine testing included high signal-to-noise-ratio and controllable spectrum content.

Unfortunately this method was only competitive with random excitation when large numbers of transducers were permanently mounted to the test structure. In the past, considerable investment in transducer instrumentation limited sine testing to laboratories with significant resources.

As a result, in the early seventies single input random excitation became the method of choice for laboratory modal testing. In the late seventies, multiple-input random excitations methods were developed to generate a consistent database to work with the multiple-input parameter estimation algorithms under development at that time. These algorithms were primarily time domain algorithms which fit the measured multiple-input unit impulse or initial conditions responses. In order, to generate a consistent database, it is necessary to measure all of the response data simultaneous which again creates the situation which existed with sine testing. That is the requirement to monitor many transducer channels at once.

Recently, low cost instrumentation introduced by PCB Piezotronics[1-4], makes multiple-input/multiple-output frequency response function analysis affordable for the smaller testing laboratories with less resources. The continuing decrease in the per channel cost of measurement systems encourages multiple channel testing for experimental modal analysis. With this inexpensive multi-channel instrumentation, stepped sine excitation competes favorably with random excitation. That is, more test laboratories can now afford the many transducers required to make stepped sine test competitive.

As shown in Fig. 1, at higher numbers of channels sine testing is more efficient than broadband testing. This advantage is due to the fact that as the number of channels increases, the signal processing overhead increases more rapidly with random testing because sine testing is limited by sweep time instead of signal processing.

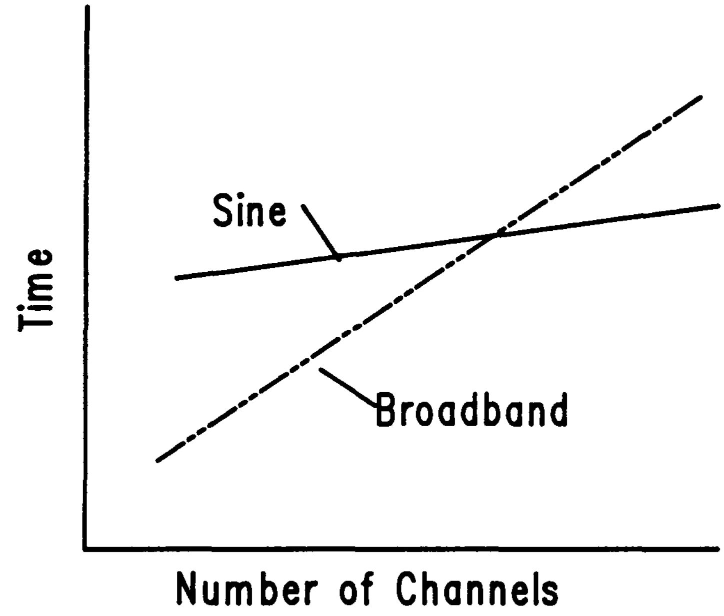

Figure 1. Comparison of sine vs. broadband testing

In fact for a test with six references and 750 response measurements, in the near future, a simple desktop computer will be able to perform the necessary signal processing. In contrast, for the same number of input and output points random testing would require a very powerful computer to perform real-time-signal processing.

To improve sine testing the new system being developed at UCSDRL implements a novel testing ideal called "spatial sine testing" (SST). Unlike the frequency response methods (FRF) which develops a data base of frequency response functions(temporal information) the new SST method develops a data base of forced modes of vibration(spatial information). This SST method also differs from the normal-mode method, which measures directly only the normal modes by a force appropriation technique.

The testing procedure in the SST method excites the structure with a forcing vector at preselected but arbitrary frequencies and measures the forced complex mode of vibration with an array of transducers. It stores this complex forced mode of vibration into the database along with the frequency and the measured forcing vector. The forcing vector and the frequency are chosen to generate a database of temporal and spatial information: not to tune a mode as in the normal-mode method. At a given frequency, the SST measures multiple forcing vectors and the resulting forced modes of vibration, and stores the results in the database.

Currently several advanced multiple reference parameter identification algorithms are capable of processing data from this kind of modal test. These methods process the data both in the frequency and the spatial domain.

SPATIAL DOMAIN

In the area of parameter identification, the spatial domain is a relatively new thought process . This concept describes the system frequency and/or impulse response function matrix in terms of the complex dot product of three fundamental characteristic functions; two complex spatial, and one complex temporal. The spatial characteristics are a function of geometry and the temporal characteristics a function of either time or frequency.

Thus, the measured frequency response function matrix can be described in this three dimensional complex space as functions of three sampled characteristic variables (p,q,ω_k). In other words, the frequency response functions occurred at discrete reference points q, response points p, and discrete frequencies ω_k.

This concept is difficult to visualize, since the matrix is represented by three dimensional complex characteristic space (Fig. 2). To more easily understand the process, view the variation along lines parallel to axes of the space. Lines parallel to the temporal axis correspond to individual frequency response functions (or unit impulse response functions in time domain). These frequency response functions consist of a summation of the temporal characteristics (unit amplitude SDOF frequency response functions), weighted by the two spatial characteristics, which define the other two axis of the characteristic space.

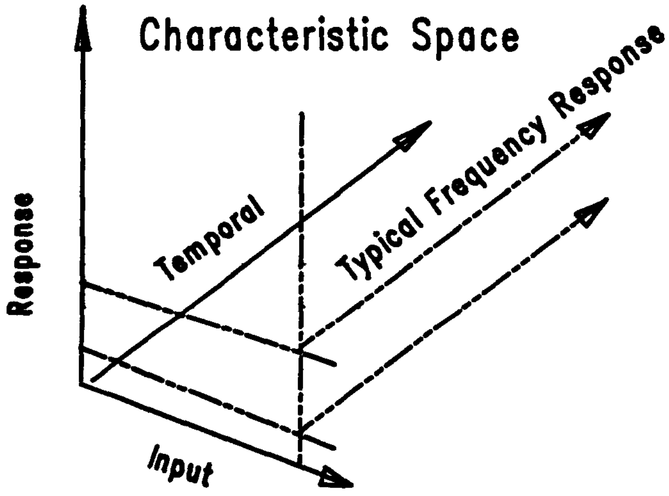

$$[h(t)] = [\psi][e^{\lambda t}][L]$$

Figure 2. Spatial domain

Lines parallel to the response axis correspond to forced modes of vibration. These forced modes consist of a summation of the system eigenvectors weighted by the input characteristic and the temporal characteristic.

Likewise, lines parallel to the input, or reference axis consist of a summation of the system eigenvectors weighted by the response characteristic and the temporal characteristic. The variation along these lines are referred to in the literature as the modal participation factors.

THEORY

In this section a brief summary of the algorithms that are currently being studied for use with the SST method will be given. These algorithms are the Polyreference Frequency Domain[5,6], the Multiple Reference Orthogonal Polynomial[7-9] and the Multi-MAC method[10-11]. Multi-MAC is a technique that seems well suited for the spatial domain sine test data. It is a spatial domain technique that temporally weights the forced modes of vibrations in determining the modal characteristics the test article.

POLYREFERENCE FREQUENCY DOMAIN

The displacement frequency response function for multiple input/output is given by:

$$[H_d(s)]_{N_0 \times N_i} = [\Psi][s \lceil I \rfloor - \lceil \Lambda \rfloor]^{-1}[L] \tag{1}$$

where:

- s Laplace variable
- $[H_d(s)]$ the transfer function matrix of size $N_0 \times N_i$, which is the Laplace transform of the impulse response matrix $[h(t)]$
- $[s \lceil I \rfloor - \lceil \Lambda \rfloor]^{-1}$ Laplace transform of $e^{\lceil \Lambda \rfloor t}$
- $\lceil I \rfloor$ identity matrix

The subscript d on the $[H]$ matrix indicates that the transfer function matrix is in terms of displacement over force. In order to obtain an expression for the transfer function in terms of velocity and acceleration in the frequency domain, the Laplace transformation properties can be applied immediately to Eq. (2). The resulting two equations, obtained for the transfer function matrix with respect to the velocity and the acceleration, are:

$$[H_v(s)]_{N_0 \times N_i} = s[H_d(s)] - [h(t)_{t=0}] \tag{2}$$

$$= s[H_d(s)] - [\Psi][L] \tag{3}$$

and

$$[H_a(s)]_{N_0 \times N_i} = s^2[H_d(s)] - s[h(t)_{t=0}] - [\dot{h}(t)_{t=0}] \tag{4}$$

$$= s^2[H_d(s)] - s[\Psi][L] - [\Psi]\lceil \Lambda \rfloor[L] \tag{5}$$

In order to compensate for the influence of the modes outside the frequency range of interest, an additional term can be added to the previous equations to compensate for these residuals effects. Adding the residual terms to Eq. (1), (3) and (5) and simplifying Eq. (3) and (5), by substituting the matrix $[T]$, the equations become :

$$[H_d(s)] = [\Psi]\,[T(s)] + [R_d] \tag{6}$$

$$[H_v(s)] = [\Psi]\lceil \Lambda \rfloor [T(s)] + [R_v] \tag{7}$$

$$[H_a(s)] = [\Psi]\lceil \Lambda \rfloor^2 [T(s)] + [R_a] \tag{8}$$

where

- $[T(s)] = [\, s \lceil I \rfloor - \lceil \Lambda \rfloor]^{-1}$ is a matrix of size $2N \times N_i$
- $[R_d]$ matrix for the residual effects of displacement, of size $N_0 \times N_i$
- $[R_v]$ matrix for the residual effects of velocity, of size $N_0 \times N_i$
- $[R_a]$ matrix for the residual effects of acceleration, of size $N_0 \times N_i$

Equations (6), (7) and (8) can be combined into one equation:

$$\begin{bmatrix} [H_d(s)] \\ [H_v(s)] \\ [H_a(s)] \end{bmatrix}_{3N_0 \times N_i} = \begin{bmatrix} [\Psi] \\ [\Psi]\lceil \Lambda \rfloor \\ [\Psi]\lceil \Lambda \rfloor^2 \end{bmatrix}_{3N_0 \times 2N} [T(s)] + \begin{bmatrix} [R_d] \\ [R_v] \\ [R_d] \end{bmatrix}_{3N_0 \times N_i} \tag{9}$$

It can be shown [13]that the characteristic equation, associated with Eq. (9) is of the form :

$$\Big[\, [A_0]^T \ \ [A_1]^T \ \ \lceil I \rfloor \,\Big]_{N_0 \times 3N_0} \begin{bmatrix} [\Psi] \\ [\Psi]\lceil \Lambda \rfloor \\ [\Psi]\lceil \Lambda \rfloor^2 \end{bmatrix}_{3N_0 \times 2N} = \big[0\big]_{N_0 \times 2N} \tag{10}$$

Equation (10) represents a matrix polynomial of order 2. Since the matrix coefficients have a dimension of N_0 this matrix polynomial has $2N_0$ poles. The 2N system poles represented by the matrix $\lceil \Lambda \rfloor$ are a subset of these $2N_0$ poles. The unknown matrix coefficients of the matrix polynomial, can be obtained from next equation [13]:

$$\Big[\, [A_0]^T \ \ [A_1]^T \ \ \lceil I \rfloor \,\Big] \times \begin{bmatrix} [H_d(s)] - [R_d] \\ s\,[H_d(s)] - [\Psi][L] - [R_v] \\ s^2 [H_d(s)] - s\,[\Psi][L] - [\Psi]\lceil \Lambda \rfloor [L] - [R_a] \end{bmatrix} = [0] \tag{11}$$

This equation means that the measured FRF's can be described by a linear frequency domain model with real matrix coefficients:

$$[A_0]^T\,[H_d(s)] + s\,[A_1]^T\,[H_d(s)] + s^2\,[H_d(s)] = s\,[R_1] + [R_0] \tag{12}$$

where:

- $[R_1] = [\Psi]\,[L]$ and is equal to the residue matrix.
- $[R_0] = \Big[[A_1]^T [\Psi] + [\Psi]\,[\Lambda]\Big] [L] + [A_0]^T [R_d] + [A_1]^T [R_v] + [R_a]$

The unknown matrices $[A_0]$, $[A_1]$, $[R_1]$ and $[R_0]$ are calculated by solving Eq. (12) in a least squares sense. The solution of the generalized eigenvalue problem, defined by Eq. (11), directly yields the complex system poles and the corresponding mode shapes for the structure.

MULTIPLE-REFERENCE ORTHOGONAL POLYNOMIAL METHOD

For a N degree-of-freedom linear system with viscous damping, the multiple-reference orthogonal polynomial method yields an auto-regressive moving average (ARMA) model of order (m,n) :

$$\sum_{k=0}^{m} [a_k]\, s^k \quad [H(s)] = \sum_{k=0}^{n} [b_k]\, s^k \tag{13}$$

where:

- $[H(s)]$ *transfer function matrix of size* $N_o \times N_i$.
- $[a_k]$ matrix polynomial coefficient of size $N_o \times N_o$.
- $[b_k]$ matrix polynomial coefficient of size $N_o \times N_i$.
- m order of matrix polynomial chosen in the Auto-Regressive part. $mN_o \geq 2N$.
- n order of matrix polynomial chosen in the Moving-Average part. $n \geq m+2$.
- N the degree-of-freedom of the system or the number of modes
- N_i number of excitation location.
- N_o number of response point.

In order to avoid the numerical ill-conditioning in Eq.(13), a set of complex orthogonal polynomials, with weighting function $q(s)$, is defined as:

$$\sum_{i=1}^{l} p_j(s_i)\, q(s_i)\, p_k(s_i)^* = \delta_{jk} \tag{14}$$

For the specific frequency range, these polynomials need be generated only once. The ARMA modal can then be expressed in this orthogonal basis, in which the numerical ill-conditioning can be avoided. The ARMA model is expressed as:

$$\sum_{k=0}^{m} [\alpha_k]\, p_k \quad [H(s)] = \sum_{k=0}^{n} [\beta_k]\, p_k \tag{15}$$

where:

- $[\alpha_k]$ matrix polynomial coefficient for orthogonal polynomials of size $N_o \times N_o$.
- $[\beta_k]$ matrix polynomial coefficient for orthogonal polynomials of size $N_o \times N_i$.
- p_k orthogonal polynomial of order k, which is a scalar function.

By choosing $[\alpha_m] = [I]$, Eq.(15) can be arranged and rewritten in matrix form for all spectral lines.

$$\begin{bmatrix} [H]^H[P_0]^H & \cdots & [H]^H[P_{m-1}]^H & -[P_0{}']^H & \cdots & -[P_n{}']^H \\ & & \vdots & & & \\ & & \vdots & & & \\ & \multicolumn{4}{c}{(\text{ for } s = j\omega_i\,,\ i=1,2,\ldots,l \text{ spectral line })} & \end{bmatrix} \times \begin{bmatrix} [\alpha_0]^T \\ [\alpha_1]^T \\ \vdots \\ [\alpha_{m-1}]^T \\ [\beta_0]^T \\ [\beta_1]^T \\ \vdots \\ [\beta_n]^T \end{bmatrix} = \begin{bmatrix} -[H]^H[P_m]^H \\ \cdot \\ \cdot \\ \cdot \\ \cdot \\ \cdot \\ \cdot \\ \cdot \end{bmatrix} \tag{16}$$

where:

- $[P_k]^H$ product of p_k^* and identity matrix $\lceil I \rfloor$ of size $N_o \times N_o$.
- $[P_k{}']^H$ product of p_k^* and identity matrix $\lceil I \rfloor$ of size $N_i \times N_i$.

The matrix coefficients in Eq.(16) can then be found by formulating the normal equation and solving the simultaneous equation. A transformation matrix is calculated in the polynomial generating procedure; thus, the power polynomial coefficients $[a_k]$ and $[b_k]$ can be calculated from orthogonal polynomial coefficients $[\alpha_k]$ and $[\beta_k]$ respectively. Once the $[a_k]$'s are found, the poles of the system, natural frequencies and damping characteristics, can be solved by setting the determinant of the characteristic equation equal to zero.

$$\det\Big(\sum_{k=0}^{m} [a_k]\, s^k \Big) = 0 \tag{17}$$

There are two ways of finding the residue matrices. One is to directly use the power polynomial coefficients $[a_k]$ and $[b_k]$

$$[A_r] = \lim_{s \to \lambda_r} (s-\lambda_r)\, [a(s)]^{-1}\, [b(s)] \tag{18}$$

where:

- $[a(s)] = \sum_{k=0}^{m} [a_k]\, s^k$
- $[b(s)] = \sum_{k=0}^{n} [b_k]\, s^k$

Since $[a(s)]$ is singular as $s \to \lambda_r$, the singular value decomposition is used for finding the generalized inverse of $[a(s)]$, then the residue matrices calculated. Another way of calculating residue matrices is in a second stage residue calculation. Base upon the pole information (frequency and damping) and the modal participation factors, obtained in solving the companion matrix of Eq.(17), a least square residue calculation for multiple reference FRF is applicable.

MULTI-MAC ENHANCED FRF METHOD

Multi-Mac is an extension of the concept of Modal Assurance Criterion (MAC). The concept of MAC is a calculation that is used to gain confidence in the estimates of modal vectors either by verifying that the estimates of different modal vectors are unique, that normal modes have been estimated, or that estimates from different rows or columns of the residue matrix for the same mode are identical. Multi-Mac is a spatial domain method of determining modal parameters based on multiple-reference frequency response functions. For linear systems with normal modes, the residue of any input/output combination is made up of three parts, the modal vector at the input location, the modal vector at the output location, and the scaling constant for that mode[10,11,19].

$$A_{pqr} = Q_r \psi_{pr} \psi_{qr} \tag{19}$$

Equation 19 can be expanded to form the complete residue matrix for any mode r.

$$[A_r] = Q_r \begin{bmatrix} \psi_{1r}\psi_{1r} & \psi_{1r}\psi_{2r} & \psi_{1r}\psi_{3r} & \cdots \\ \psi_{2r}\psi_{1r} & \psi_{2r}\psi_{2r} & \psi_{2r}\psi_{3r} & \cdots \\ & & & \\ \psi_{mr}\psi_{1r} & \psi_{mr}\psi_{2r} & \psi_{mr}\psi_{3r} & \cdots \end{bmatrix} \tag{20}$$

Where:

- A_{pqr} Residue for mode r at response point p and reference point q .
- $[A_r]$ residue matrix for mode r of size $N_o \times N_i$
- Q_r Scaling constant for mode r
- ψ_{pr} Modal vector for location p of mode r
- ψ_{qr} Modal vector for location q of mode r

From Eq.(20) it can be seen that there must be a linear relationship between any row or any column of the residue matrix for a particular mode. For example, if the structure was excited at points 1 and 2, then in column one every residue would have ψ_{1r} in common. Likewise, every residue in column two would have ψ_{2r} in common. The modal vectors at the output locations, ψ_{1r} through ψ_{mr}, must therefore be related since they define the same mode. If this linear relationship does not exist, either measurement errors have contaminated the data, the modes are closely coupled or, there is a repeated root at that pole location so that the residue is a linear combination based on input location. Also, from the basic theory of modal analysis, the modal vectors of two different modes must be orthogonal with each other and a weighting matrix such as the mass matrix. If estimates of the residues for the same mode but for different rows or columns is used, a principal component analysis can be used to determine the number of independent vectors that make up those residues. If one significant eigenvalue is found from the principal component analysis, then one mode is presented. If more than one significant eigenvalue is calculated, then there are more than one set of independent vectors that make up the residue matrix for that mode. Eq.(20) can be used to set up the principal component analysis. The size of the matrices is determined by the number of measurement locations and the number of modal vector estimates. The residue matrix can have more than one estimate of the modal vector for the same input/output locations. These estimates could be from different curve fitting algorithms.

$$[\overline{A_r}]^H \, [\overline{A_r}] = [W] \, [V] \, \lceil \Sigma \rfloor \, [V]^T \, [W]^T \tag{21}$$

Where:

- $[\overline{A}_r]$ estimated residue matrix of size $N_o \times N_k$, which is generated by putting N_k estimated modal vectors together side by side.
- $[W]$ diagonal weighting matrix of size $N_k \times N_k$
- $[V] = [v_1 \; v_2 \; \cdots \; v_{N_k}]$ is the matrix of eigenvectors
- $\lceil \Sigma \rfloor$ is the diagonal eigenvalue matrix

Eq.(21) will yield as many eigenvalues as the number of rows in the residue matrix. Some of these eigenvalues will be zero or of insignificant value. The number of significant eigenvalues will indicate the number of independent vectors that make up the residues at that frequency. Associated with each eigenvalue will be the eigenvectors for that eigenvalue which will number as many as the number of rows in the residue matrix. The weighting matrix that was used in Eq.(21) for this work was the identity matrix. A better weighting matrix would be to use the inverse of the square root of the mass matrix or an estimate of the inverse of the square root of the mass matrix from a finite element analysis. The matrix could also be an error matrix or a matrix that would allow different types of data in the residue matrix. For example, if both acceleration and displacement data was contained in the residue matrix, the multiplication of acceleration and displacement would not be dimensionally correct. But, the weighting matrix could be used to make the multiplication dimensionally correct[10]. Any estimate of the residue may be used in this procedure. Since, at resonance, the quadrature part of the frequency response function is proportional to the residue, the simplest method is to use the peak of the imaginary part of the frequency response estimate as an estimate of the residue. If leakage is present in the data, it is advantageous to use spectral lines that are adjacent to the highest peak in the imaginary part. These spectral lines will be less contaminated by leakage. In experimental procedures, the principal component analysis is applied for the quadrature part of FRF matrix, either one or several adjacent spectral lines are included in the analysis each time. This will yield a set of eigenvalues, which equals to the number of adjacent spectral lines by the number of references, for each analysis. The analysis can be exercised over the whole spectral range. All of these eigenvalues can then be plotted as a function of frequency, namely Complex Mode Indicator Function (CMIF)[5]. in which the significant eigenvalue peaks indicate normal modes nearby and the corresponding eigenvectors will be the independent vectors that make up the residue vectors at that frequency. Once the eigenvalues and eigenvectors have been calculated by the principal component analysis, the residues can be transformed to a new coordinate space which are mathematically guaranteed to be orthogonal with each other and the assumed weighting matrix. Therefore, if more than one eigenvalue of significant value is found, the orthogonal mode shapes that make up the estimate of the residue at that frequency can be computed. For example, if there are repeated roots, the residues that make up that repeated root will be calculated. If the modes are heavily coupled, unique modes will be estimated. But, the transformed modes will have the contamination of other modes removed and will be orthogonal with each other. Eq.(22) defines the transformation from the original residues to the new space for i'th significant eigenvalue. This transformation would be used for each eigenvalue of significant value. Therefore, if more than one eigenvalue of significant value is found, the transformation will yield orthogonal estimates of the residues. If more than one estimate of the residue is used for each row or column, these transformed estimates are summed together to reduce the variance. The matrix multiplication will therefore yield one residue for each measurement location. The variance of the modal vectors will be reduced in a least squares sense by $[1/n]^{1/2}$, where n is the number of average.

$$\{A_r\}_i' = [\overline{A}_r]\{v_i\} \tag{22}$$

The residue vectors can then be transformed by these eigenvectors. These transformed residues could be weighted by the mass matrix to yield mode shapes of the system. These new mode shapes are mathematically guaranteed to be orthogonal with each other. Using these transformed estimates of the residue vectors, an enhanced frequency response function can be computed which can be fit for estimates of the frequency and damping of that mode.

Note that the mode shapes found here were arbitrary scaled. The correct scaling can be made, after the frequency and damping values were found, by other residue calculation algorithms, ie. least square frequency residue calculation algorithm.

ANALYTICAL CASES

To compare the spatial domain characteristics of the Polyreference Frequency Domain (PFD), Multiple-Reference Orthogonal Polynomial (MROP) and the Multi-Mac Enhanced FRF (MMEFRF) algorithms, a theoretical data set of 9 references (3 point, 3 direction) and 270 responses (90 point, 3 direction) was generated. This data set was generated by synthesizing the modal parameters (frequency, damping and mode shape) of the "H-frame". The "H-frame" is a steel structure made for testing purposes at the University of Cincinnati Structural Dynamics Research Lab (UCSDRL). The geometry of the structure is shown in Figure1, with the reference point numbers circled. The modal model of the "H-frame" contains 19 modes. The modal frequencies and damping values are listed in Table 1, and the original mode shapes are shown in Figure 2. Since this data set is generated from the modal parameters of the actual structure, there is no significant physical loss. Since the exact modal parameters are known, the accuracy of these algorithms can be evaluated. The algorithms currently implemented at the UCSDRL are limited to six references. Therefore, the data was analyzed with six references taken from the set of nine. Two cases with different reference selections were studied.

The six references used in the first data set correspond to the three coordinate directions at points 72 and 75. As can be seen from Figure 1, any local mode of the cross beam will be poorly excited from these locations. For example, the mode at 312.6 Hz is a local mode of the cross-beam. Therefore, some difficulties might be expected with the estimation for this particular pole.

Figure 3 shows a typical driving point frequency response function for this data set. All three frequency domain algorithms were used to analyze this data set. For the PFD and the MROP, the analysis was done over several frequency bandwidth. This is normal since frequency domain algorithms are not suitable, in general, for large frequency ranges due to numerical problems. On the other hand, the MMEFRF was used over the complete frequency range. This method does not have the same numerical problems as the other two methods.

The complex mode indicator function (CMIF) is a plot of the eigenvalues of a principal component analysis with the redundent residue information as the input to the algorithm. If only one mode shape exists at a given frequency, the principal component analysis will have one eigenvalue of significant values with all other eigenvalues of insignificant value. The number of eigenvalues calculated depends on the size of the analysis. If a natural frequency is a repeated pole, the principal component analysis will have two significant eingenvalues for that frequency. Also, if the pole is a closely spaced root, the principal component analysis will yield as many eigenvalues as independent modes active at that frequency.

The MROP and MMEFRF both use the complex mode indicator function [5] (CMIF) to determine the number of modes in the frequency range of interest. The CMIF plot for the first data set is shown in Figure 4. The way to read a CMIF plot is as follows. The plot of the largest eigenvalue peaks wherever there is a pole. If a repeated pole exists, the plot of the second largest eigenvalue will peak at the same frequency as the plot of the largest eigenvalue. From Figure 4, it can be seen that the plot of the largest eigenvalue peaks at 18 different places, which means that the algorithm finds 18 poles in the whole frequency range. However, the data set was generated using 19 poles. Taking a closer look in the 312 Hz frequency range, the plot of the second largest eigenvalue peaks in this frequency range. Normally, the plot of the second largest eigenvalue peaks between poles. This means that the forced mode of vibration is a linear combination of two independent modes. While at a resonance frequency the plot of the second largest eigenvalue is very small, which means that only one mode is contributing to the forced mode of vibration. However, for this frequency the second pole is separated from the previous one to explain this peak. In this case, the CMIF plot indicates that there is a mode at this particular frequency. But this mode is not well excited from the references that were chosen. For this data set it was possible to find this pole by overdetermining the order of the polynomial in the case of MROP or by requiring the vector associated with the second largest eigenvalue at that frequency for the MMEFRF case. In the case of the PFD, the algorithm found this frequency but flagged it as a computational pole. So all three algorithms had some problems in detecting the particular mode that was poorly excited from the chosen references.

In the case of MMEFRF, the mode shapes are calculated in the first step. If the frequency and damping of the poles are required, an enhanced frequency response function is calculated for each pole. Then, this enhanced frequency response function is used to estimate the frequency and damping values using only the single reference algorithms. Since the enhanced FRF may be contaminated by other modes, it is necessary to use multiple modes algorithms for good frequency and damping estimations. For this example the single reference orthogonal polynomial method, which is a special case of MROP, is used for the frequency and damping estimation. If the frequency spacing of the enhanced FRF is evenly spaced, time domain algorithms such as Least Square Complex Exponential can also be used. The estimated frequency and damping values for each mode and each method can be found in Table 1. As can be seen from this Table, the MROP and MMEFRF are estimating the poles very well. The PFD gives a good estimate of the pole values but they are not as accurate at the ones obtained with the two other methods.

As a check on the accuracy of the estimated modes, a modal assurance criterion was calculated between the estimated modes for each of the algorithms, and the original mode shapes that were used to create the data set. The results can be found in Table 2. From these results, it can be concluded that all three methods found the correct mode shapes, except for the MMEFRF method, which had a poor estimate of 14th mode shape.

The modal parameters were estimated again on a second data set, using the MMEFRF method. This data set included the reference point 15 in the X direction, which replaced reference 75 in the Z direction. It was used to demonstate a set in which the 14th mode is well excited. If the interpretation of the CMIF plot, for the first data set, was correct, a CMIF plot should now be obtained in which the 14th mode shows up in the the plot of the largest eigenvalue. The second reason was to see if the MMEFRF could find a better estimate for the mode shape of the 14th pole, when this mode is well excited. The CMIF plot, that was obtained for this data set, is shown in Figure 5. As was expected, the 14th mode, which was better excited in this data set, shows up in the plot of the largest eigenvalue. The modal parameters that were found for this particular pole with MMEFRF improved and can be found in the last column of Tables 1 and 2.

As can be seen in Tables 1 and 2 all three methods gives good results on theoretical data as expected. With the PFD amd MROP methods it was necessary to break the frequency range into bands and estimate the number of modes in each band. The MMEFRF method could use the complete band and the number of modes and the modal coefficients were estimate directly from the CMIF. The MMEFRF method is simpler and faster to use but does not handle closely coupled modes as well as the other two methods at least for ideal data.

Some preliminary studies have been preformed with various types of noise added to the measurements. These results are sketchy and will be repeated in the future so that all the methods experience equivalent testing conditions. The test which have been performed indicates that all the methods handles random noise well but perform poorly with data which has frequency shifts. This was expected since it has been a consistent observation with all of the multi-input parameter estimation methods(time and frequency). It should be noted that it is the frequency shift problem with the multi-input algorithms which has led to testing procedures where all of the response data is measured simultaneous.

SYSTEM CONCEPT

As mentioned in the introduction the UCSDRL has been developing a spatial domain sine testing system (SST) with practicality, simplicity and low cost as goals. This system will help the experimentalist obtain a consistent, valid database. The system being developed attempts to minimize test setup time allowing more time for data acquisition and analysis. By instrumenting large numbers of data points (typically 64, 128, etc.), the lightweight motion sensors provide a more comprehensive data base while adding only a minimal, constant mass distribution. Accordingly, the resultant data base displays better spatial definition without the frequency shifts inherent in the method of "roving" accelerometers.

Modular mounting, wiring and calibration equipment eliminate many of the historic problems with setup, identification, calibration and management of large numbers of channels of data. Sensor signals are routed to patch panels which consolidate the individual cables into multiconductor ribbon cables carrying signals on to the signal conditioning equipment. Managing all channels in parallel, the signal conditioning automatically sets maximum gain and anti-aliasing filters the signals. Inexpensive digitizing and signal processing follow as the final steps in the data acquisition.

The force appropriation equipment consists of shakers, amplifiers and a low cost computer-controlled multiple channel digital to analog converter (DAC) system. The multiple channel DAC system currently under development would typically consist of 4, 8, or more channels (up to 32 channels) individually controlled from the system controller. The signal from each channel would be independently set for magnitude and phase. Several prototypes have been built and are currently being evaluated.

A personal computer controls the system, including the signal processing functions. Ideally, the personal computer should be able to acquire the data in real time. Although processing up to 512 channels of data seems like an insurmountable task for a personal computer, a four point discrete Fourier transform(DFT) considerably reduces the volume of data being processed. Since the signal conditioning contains anti-aliasing filters the sinusoidal signals do not need to be oversampled to gain the desired amplitude accuracy. Instead a simple four point DFT, involving only two additions, can be performed on the sinusoidal signals significantly reducing the amount of information processing overhead. In other words, for a 512 channel sine test only 2048 pieces of information need to be processed and stored in computer memory at one time and transformed into the frequency domain with 1024 additions. With an additional eight additions per channel, adaptive processing can be implemented to determine the signal-to-noise-ratio. As a result, the system could adaptively determine the number of averages needed to produce acceptable data at each frequency.

SUMMARY

The advent of current low cost per channel instrumentation creates a competitive forum for broadband modal testing. Now large data acquisition systems can be assembled less expensively than ever before. This economy stimulates renewed interest in sine testing, as the situation now exists where large scale sine testing systems can compete economically with broadband testing systems. Such a large scale spatial domain sine testing system is presently under development at UCSDRL.

Conceptually, the spatial domain sine testing system typically consists of up to 512 or more channels of STRUCTCEL motion sensors linked by the data acquisition system (DATA HARVESTER) with a personal or a small technical computer. The computer processes the data, archives the results and generates the excitation signal with a multiple channel DAC. A simple four point DFT significantly reduces the computational overhead of processing large channels of data. The spatial domain sine testing system essentially integrates available low cost instrumentation with sine excitation and advanced spatial and frequency domain parameter identification. The purpose of this research is to determine if spatial sine testing will become one of the next generations of modal testing methodologies.

ACKNOWLEDGEMENTS

The work described in this paper was partially supported by the U.S. Air Force under the contract "Experimental Modal Analysis and Dynamic Component Synthesis", Contract No. F-33615-83-C-3218.

The authors would also like to thank Tony Severyn, Filip Deblauwe, and C. Shih of the UCSDRL for their contribution to this paper.

REFERENCES

[1] Brown, D. L., "Keynote Speech - Modal Analysis - Past, Present and Future", Proceedings of the First International Modal Analysis Conference, Orlando Florida, November 1982.

[2] Lally, R. W., Poland, J. B., "A Low Cost Transducer System for Modal Analysis and Structural Testing", Sound and Vibration, January 1986.

[3] Poland, J. B., "An Evaluation of a Low Cost Accelerometer Array System, Advantages and Disadvantages", Master of Science Thesis, University of Cincinnati, Dept. of Mechanical and Industrial Engineering., 1986.

[4] Lally, M. J., Brown, D. L., "STRUCTCEL- A New Instrumentation System", Fourteenth Transducer Workshop, Colorado Springs Colorado, June 1987.

[5] Zhang, L., Kanda, H., Brown, D. L., Allemang, R. J., "A Polyreference Frequency Domain Method for Modal Parameter Identification", ASME Paper Number 85-DET-106, 1985.

[6] Lembregts, F., Snoeys, R. and Leuridan, J., "Multiple Input Modal Analysis of Frequency Response Functions Based on Direct Parameter Identification", Tenth International Seminar on Modal Analysis Part IV, University of Leuven Belgium, 1985.

[7] Shih, C. Y., Tsuei, Y. G., Allemang, R. J., Brown, D. L., "Extension of a Parameter Estimation Method to Multiple Reference Frequency Response Measurements", Eleventh International Seminar on Modal Analysis, University of Leuven Belgium, 1986.

[8] Vold, H., "Orthogonal Polynomials in the Polyreference Method", Eleventh International Seminar on Modal Analysis, University of Leuven Belgium, 1986.

[9] Van Der Auweraer, H., Leuridan, J. L., "Multiple Input Orthogonal Polynomial Parameter Estimation", Eleventh International Seminar on Modal Analysis, University of Leuven Belgium, 1986.

[10] Rost, R. W., "Investigation of Multiple Input Frequency Response Function Estimation Techniques for Modal Analysis", Doctor of Philosophy Dissertation, University of Cincinnati,1986.

[11] Allemang, R. J. "Investigation of Some Multiple Input/Output Frequency Response Function Experimental Modal Analysis Techniques" Doctor of Philosophy Dissertation University of Cincinnati Mechanical Engineering Department 1980, 358 pp.

[12] Allemang, R.J., Rost, R.W., Brown, D.L., "Multiple Input Estimation of Frequency Response Function: Excitation Considerations", ASME Paper Number 83-DET-73.

[13] Leuridan, J. "Some Direct Parameter Model Identification Methods Applicable for Multiple Input Modal Analysis" Doctoral Dissertation Department of Mechanical Engineering University of Cincinnati 1984, 384 pp.

[14] Vold, H., "Orthogonal Polynomials in the Polyreference Method", Proceedings, Eleventh International Seminar on Modal Analysis, Belgium, 1986.

[15] Van Der Auweraer, H., Leuridan, J.M., "Multiple Input Orthogonal Polynomial Parameter Estimation", Proceedings, Eleventh International Seminar on Modal Analysis, Belgium, 1986.

[16] Williams, R., Crowley, J., Vold, H., "The Multivariate Mode Indicator Function in Modal Analysis", 3rd IMAC, 1985.

[17] Brown, D.L., Zimmerman, R.D., Allemang, R.J., Mergeay, M., "Parameter Estimation Techniques for Modal Analysis", SAE Paper Number 790221, SAE Transactions, Volume 88, pp. 828-846, 1979.

[18] Allemang, R.J., Brown, D.L., Rost, R.R. "Multiple Input Estimation of Frequency Response Functions for Experimental Modal Analysis" U.S. Air Force Report Number AFATL-TR-84-15, 1984, 185 pp.

[19] Allemang, R.J., Brown, D.L., "A Correlation Coefficient for Modal Vector Analysis", Proceedings, International Modal Analysis Conference, pp.110-116, 1982.

[20] "Short Course Notes: Advanced Modal Analysis", University of Cincinnati, 1987.

[21] Van Der Auweraer, H., Snoeys, R., Leuridan, J.M., "A Global Frequency Domain Modal Parameter Estimation Technique for Mini-computers", to appear ASME, Journal of Vibration, Acoustics, Stress, and Reliability in Design.

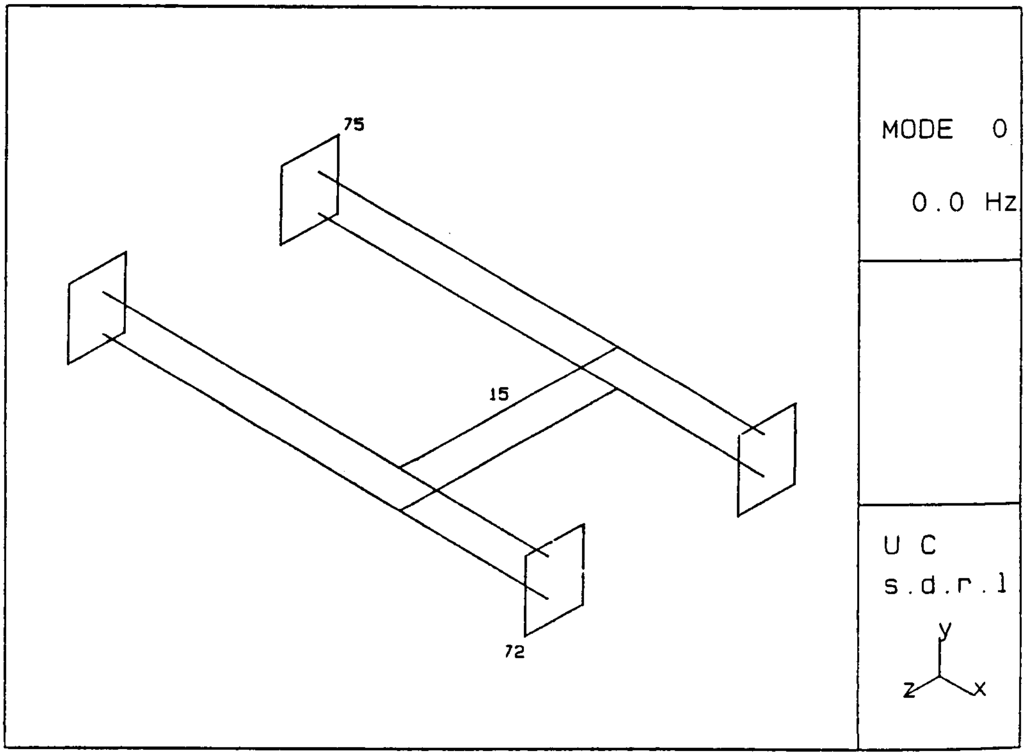

Figure 3. The H-frame structure with reference points shown

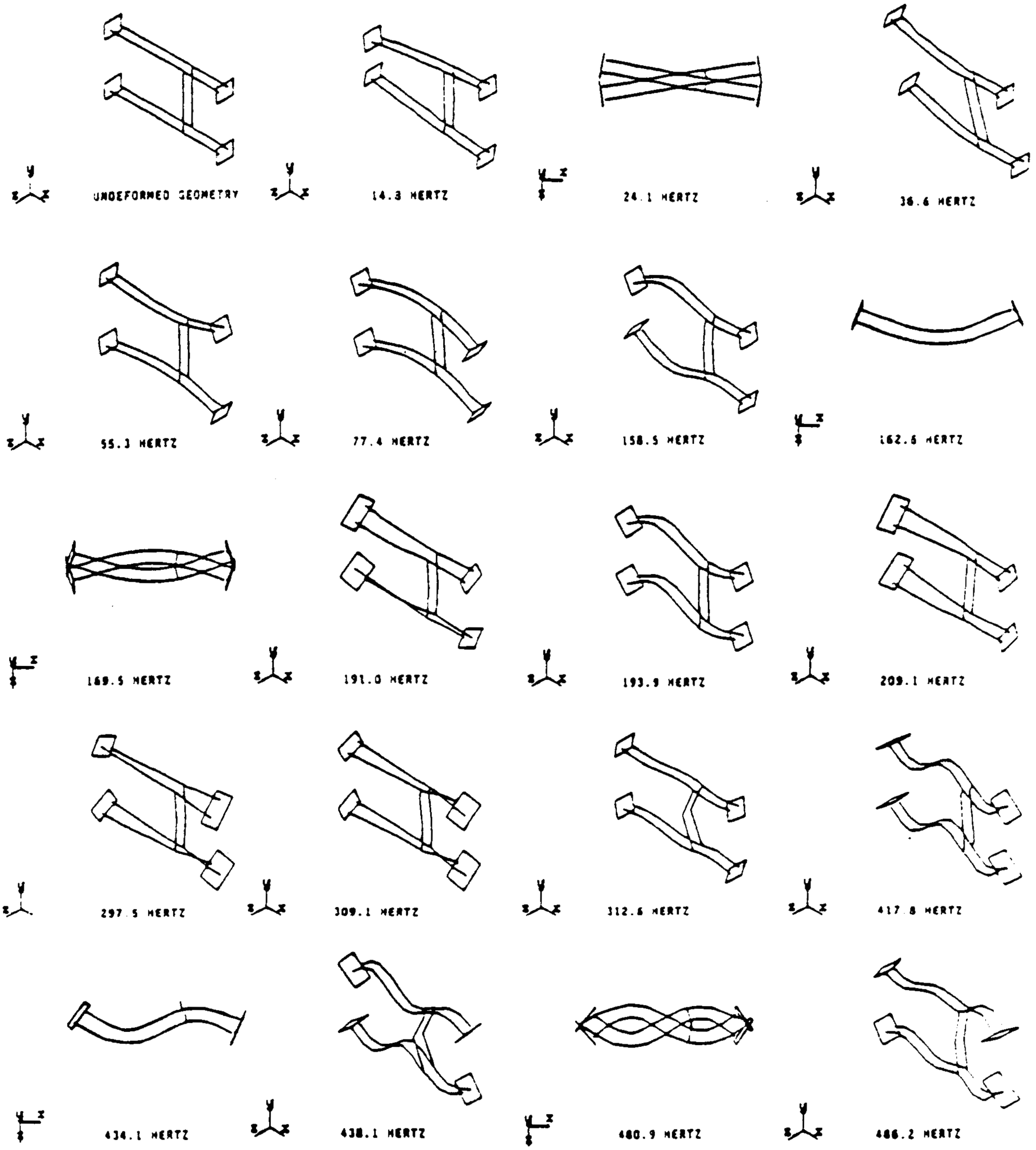

Figure 4. The original mode shapes of the H-frame structure

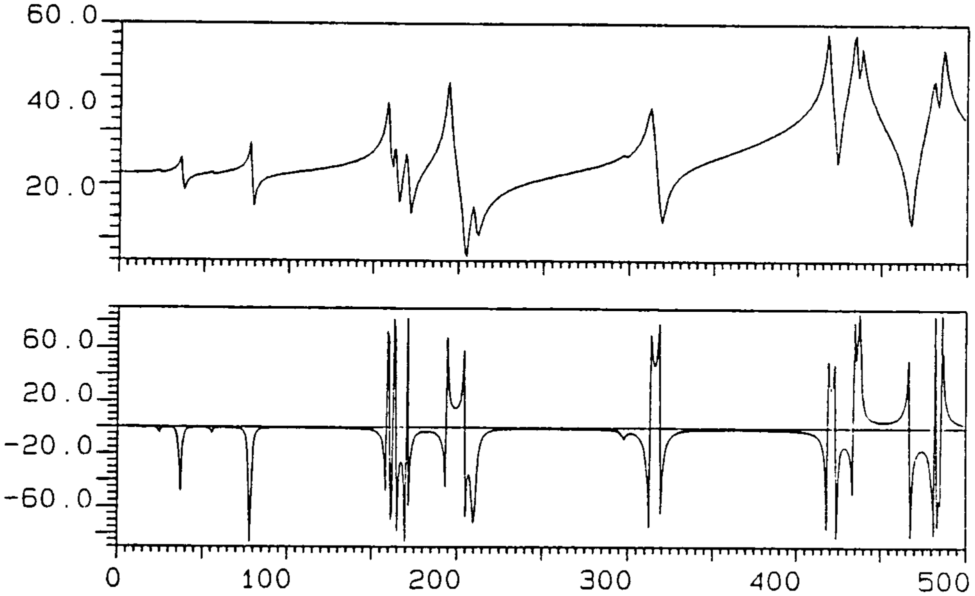

Figure 5. H-frame Driving Point Frequency Response Function

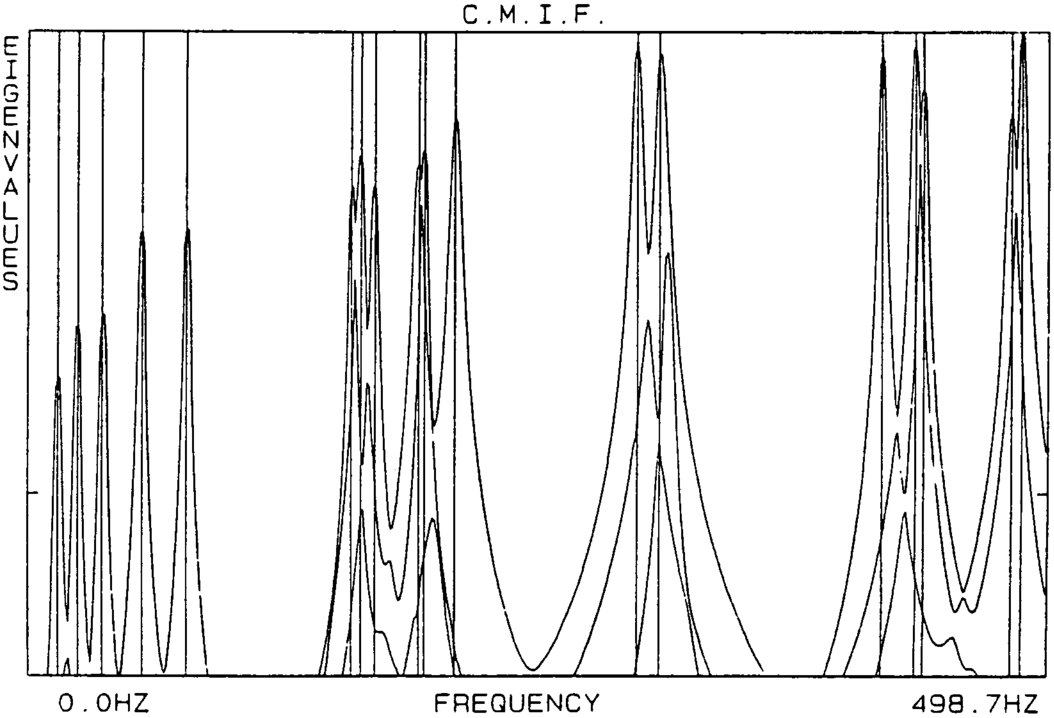

Figure 6. The CMIF plot of Case 1 data set, which showed mode 14 in second eigenvalue curve.

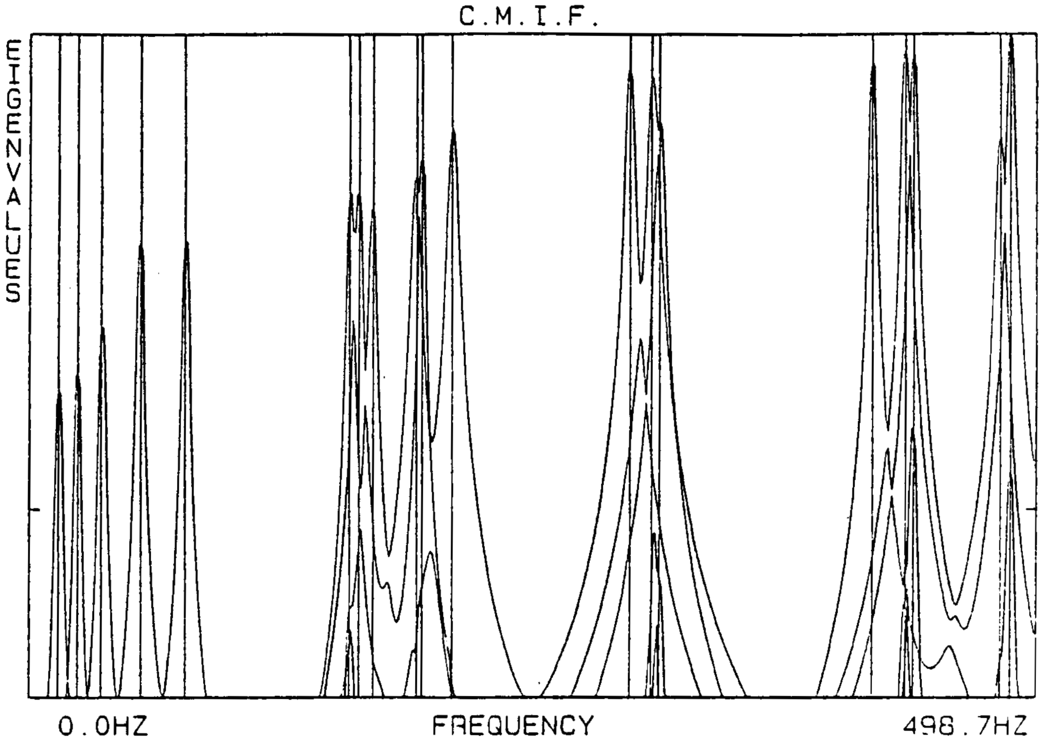

Figure 7. The CMIF plot of Case 2 data set, which showed 19 modes all exist in the largest eigenvalue curve.

Mode		Frequency/Damping Estimation Method				
		Data	PFD	MROP	MMEFRF	MMEFRF+
1	Freq. (Hz)	14.900	14.880	14.902	14.901	14.899
	Damp. (%)	5.148	5.149	5.149	5.147	5.152
2	Freq. (Hz)	24.087	24.094	24.086	24.087	24.087
	Damp. (%)	2.753	2.744	2.750	2.753	2.752
3	Freq. (Hz)	36.584	36.587	36.584	36.583	36.583
	Damp. (%)	1.984	1.965	1.981	1.984	1.984
4	Freq. (Hz)	55.294	55.291	55.294	55.293	55.293
	Damp. (%)	1.249	1.246	1.247	1.248	1.249
5	Freq. (Hz)	77.446	77.441	77.446	77.446	77.446
	Damp. (%)	0.901	0.992	0.900	0.901	0.901
6	Freq. (Hz)	158.539	158.527	158.541	158.540	158.541
	Damp. (%)	0.472	0.468	0.473	0.472	0.472
7	Freq. (Hz)	162.627	162.613	162.627	162.627	162.626
	Damp. (%)	0.611	0.611	0.611	0.612	0.612
8	Freq. (Hz)	169.477	169.492	169.477	169.477	169.477
	Damp. (%)	0.576	0.592	0.576	0.576	0.576
9	Freq. (Hz)	191.006	190.964	191.007	191.009	191.008
	Damp. (%)	0.793	0.755	0.793	0.795	0.795
10	Freq. (Hz)	193.900	193.896	193.900	193.901	193.896
	Damp. (%)	0.366	0.368	0.366	0.366	0.367
11	Freq. (Hz)	209.132	209.130	209.134	209.133	209.133
	Damp. (%)	0.759	0.743	0.759	0.761	0.761
12	Freq. (Hz)	297.551	297.523	297.551	297.550	297.549
	Damp. (%)	0.450	0.462	0.450	0.452	0.452
13	Freq. (Hz)	308.866	308.876	308.864	308.876	308.865
	Damp. (%)	0.539	0.561	0.539	0.542	0.538
14	Freq. (Hz)	312.401	312.529	312.402	312.106	312.402
	Damp. (%)	0.453	0.514	0.453	0.460	0.455
15	Freq. (Hz)	417.848	417.840	417.849	417.847	417.848
	Damp. (%)	0.198	0.205	0.198	0.198	0.198
16	Freq. (Hz)	434.071	434.044	434.071	434.066	434.076
	Damp. (%)	0.221	0.231	0.220	0.222	0.221
17	Freq. (Hz)	438.071	438.076	438.075	438.061	438.066
	Damp. (%)	0.211	0.212	0.212	0.213	0.213
18	Freq. (Hz)	480.966	480.961	480.968	480.971	480.977
	Damp. (%)	0.282	0.286	0.281	0.282	0.282
19	Freq. (Hz)	486.158	486.163	486.159	486.165	486.157
	Damp. (%)	0.209	0.213	0.209	0.212	0.212

Notes:		
	PFD	Polyreference Frequency Domain
	MROP	Multiple-Reference Orthogonal Polynomial
	MMEFRF	Multi-Mac Enhanced FRF
	MMEFRF+	Multi-Mac Enhanced FRF with Case 2 data set.

TABLE 1. Comparison of estimated frequency and damping

Modal Assurance Criterion				
Mode	Mode Shape Estimation Method			
	PFD	MROP	MMEFRF	MMEFRF+
1	0.999	0.999	1.000	0.999
2	1.000	1.000	1.000	1.000
3	1.000	1.000	1.000	1.000
4	1.000	1.000	1.000	1.000
5	1.000	1.000	1.000	1.000
6	1.000	0.996	1.000	1.000
7	1.000	1.000	1.000	1.000
8	0.999	1.000	0.999	1.000
9	0.947	0.997	0.997	0.997
10	0.999	0.999	0.998	0.998
11	0.999	1.000	0.999	0.999
12	1.000	1.000	1.000	1.000
13	1.000	1.000	1.000	1.000
14	0.991	1.000	0.637	0.999
15	1.000	1.000	1.000	1.000
16	1.000	1.000	0.998	0.999
17	1.000	1.000	0.993	0.998
18	1.000	1.000	0.991	0.985
19	1.000	1.000	0.999	0.999

Notes:	PFD	Polyreference Frequency Domain
	MROP	Multiple-Reference Orthogonal Polynomial
	MMEFRF	Multi-Mac Enhanced FRF
	MMEFRF+	Multi-Mac Enhanced FRF with Case 2 data set.

TABLE 2. Comparison of estimated mode shapes by MAC

DYNAMIC ANALYSIS

PRECEDING PAGE BLANK NOT FILMED

Dynamic Substructuring for Shock Spectrum Analysis Using Component Mode Synthesis

N88-18950

Barton W. McPheeters [1]
Avivi Lev [2]
Philip B. Bogert [3]
Rudolph J. Scavuzzo [4]

Component mode synthesis was used to analyze three different types of structures with MSC NASTRAN. The theory and technique of using Multipoint Constraint Equations (MPCs) to connect substructures to each other or to a common foundation is presented. Computation of the dynamic response of the system from shock spectrum inputs was automated using the DMAP programming language of the MSC NASTRAN finite element code.

INTRODUCTION

Computation time in dynamic analyses increases with either the square or cube of the number of degrees-of-freedom. As a result, there can be substantial savings in computer costs by using dynamic substructing methods in large dynamic problems. In some cases, finite element models become so large that only a few supercomputers can be used to solve the resulting dynamics problem. In these cases, dynamic substructing may be required.

Component mode synthesis methods, like those introduced in 1971 by MacNeal [1], are often used in dynamic substructuring. These techniques have been applied to superelement analyses in MSC NASTRAN. Most classes of problems can be solved with this procedure. However, response spectrum analysis problems using model synthesis methods have not been previously analyzed [2,3] with MSC NASTRAN. In this effort, both basic response spectrum methods and U.S. Navy DDAM shock analysis methods that require an evaluation of modal masses in the specification of the shock spectrum input are analyzed. In this paper, the theoretical background for the application of modal synthesis to shock spectrum problems and a numerical evaluation of the methods are presented.

THEORY

Three cases are considered in the theoretical development:

Case I: Single substructure attached to a residual structure (foundation).

---

(1) Engineer, NKF Engineering, Inc., Reston, Va
(2) Consultant, NKF Engineering, Inc., Reston, Va
(3) Director, Structural Dynamics Division, NKF Engineering, Inc., Reston, Va
(4) Consultant, NKF Engineering, Inc., Reston, Va, and Professor, Department of Mechanical Engineering, University of Akron, Akron, OH

Case II: A series of substructures attached to a residual structure (foundation).

Case III: Parallel substructures connected to each other and to a common residual structure (foundation).

Using these three cases, any linear structure can be divided into a number of substructures, analyzed, and combined using multipoint constraint (MPC) equations.

In all cases the eigenvalue analysis of the substructures to find mode shapes $\{\phi_i\}$ and frequencies $\{\omega_i\}$ is to be determined assuming a free-free substructure.

The equation of motion of a linear system can be written as:

$$[M]\{\ddot{U}\} + [K]\{U\} = \{f(t)\} \tag{1}$$

Expanding the displacement in terms of the free-free mode shapes:

$$\left\{ U \left[t \right] \right\} = \sum_{j} \left\{ \phi_j \right\} \xi_i \left[t \right] \tag{2}$$

Substituting into Equation (1):

$$\left[M \right] \sum_{j} \left\{ \phi_j \right\} \ddot{\xi}_j + [K] \sum_{j} \left\{ \phi_j \right\} \xi_j = \left\{ F \left[t \right] \right\} \tag{3}$$

Premultiply by $\{\phi_i\}^T$,

$$\left\{ \phi_i \right\}^T \left[M \right] \sum_{j} \left\{ \phi_j \right\} \ddot{\xi}_j + \left\{ \phi_i \right\}^T \left[K \right] \sum_{j} \left\{ \phi_j \right\} \xi_j = \left\{ \phi_i \right\}^T \left\{ F \left[t \right] \right\} \tag{4}$$

By virtue of the orthogonality property of vibration modes,

$$\begin{aligned} \left\{ \phi_i \right\}^T \left[M \right] \left\{ \phi_j \right\} &= m_i \delta_{ij} \\ \left\{ \phi_i \right\}^T \left[K \right] \left\{ \phi_j \right\} &= K_i \delta_{ij} \end{aligned} \tag{5}$$

and

$$f_i(t) = \{\phi_i\}^T \{F(t)\} \tag{6}$$

where:

m_i is the generalized mass of the ith mode

K_i is the generalized stiffness of the ith mode

f_i is the generalized force for the i^{th} mode

and

$$\delta_{ij} = \left\{ \begin{array}{ll} 1, & i = j \\ 0, & i \neq j \end{array} \right\} \tag{7}$$

Using these definitions, the equation of motion in generalized coordinates becomes:

$$m_i \ddot{\xi}_i + K_i \xi_i = f_i \tag{8}$$

for each mode, i.

Case I: Single Substructure

Assume that the connection points shown in Figure 1 represent four degrees-of-freedom designated 997, 998, 999, and 1000.

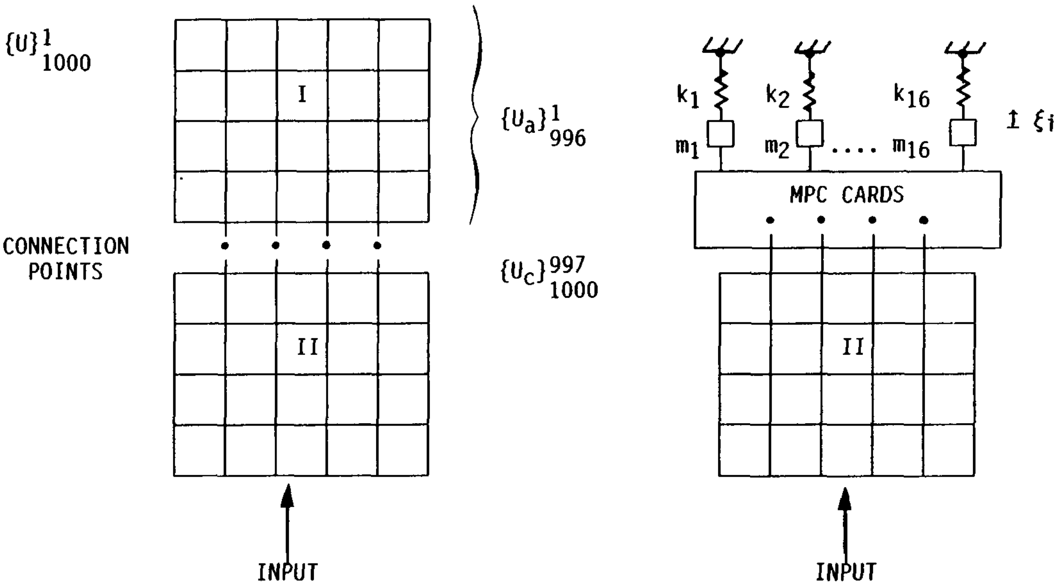

Figure 1. Case I: Substructure and Residual or Foundation Structure

Furthermore, it is assumed that 16 modes can be used to represent the substructure. Generalized stiffness, K_i, and generalized mass, m_i, are connected to each scalar mass point. The displacement of the scalar point is the modal displacement, ξ_i. The MPC cards which relate the connection degrees-of-freedom (997-1000) to the 16 modal displacements, ξ_i, can be written as:

$$\left.\begin{aligned}
U^{997} &= \phi_1^{997}\,\xi_1 + \phi_2^{997}\,\xi_2 + \cdots + \phi_{16}^{997}\,\xi_{16} \\
U^{998} &= \phi_1^{998}\,\xi_1 + \phi_2^{998}\,\xi_2 + \cdots + \phi_{16}^{998}\,\xi_{16} \\
U^{999} &= \phi_1^{999}\,\xi_1 + \phi_2^{999}\,\xi_2 + \cdots + \phi_{16}^{999}\,\xi_{16} \\
U^{1000} &= \phi_1^{1000}\,\xi_1 + \phi_2^{1000}\,\xi_2 + \cdots + \phi_{16}^{1000}\,\xi_{16}
\end{aligned}\right\} \qquad (9)$$

In defining the constraint equations above, it was discovered that fewer modes were required for an accurate solution if only translational degrees are included in the constraint equations at the connection points. After a response spectrum analysis has been run on the reduced structure connected to the residual structure by multipoint constraint, Equation (9), it is simple to recover the internal component substructures' displacement. For substructure I shown schematically in Figure 1 with 1000 displacement degrees-of-freedom, the internal displacements for the jth mode of the reduced dynamic model are given in terms of the 16 scalar point (generalized) displacements.

$$\left\{ U_j \right\}_{1000}^{1} = \sum_{i=1}^{16} \left\{ \phi_i \right\}_{1000}^{1} \bullet \xi_{ij} = {}_{1000}^{1.}\!\left[\Phi \right]^{16} \left\{ \xi_j \right\}_{16}^{1} \qquad (10)$$

Once the displacements are known, stress, forces, etc., are easily determined in NASTRAN using the element stiffnesses matrices. All that remains is to sum the desired quantities over the modes with either the NRL sum (Navy DDAM) or SRSS sum (Earthquake Spectrum Analysis). Thus, the steps needed to use the component mode synthesis method are as follows:

(1) Determine the free-free mode shapes, ϕ_i, generalized mass, m_i, and generalized stiffness, K_i, for the substructure.

(2) Choose a sufficient number of modes of the substructure to cover the frequency range of interest.

(3) Model the residual structure (foundation) and scalar points for each mode using grounded generalized masses and stiffnesses.

(4) Connect the component mode representation of the substructure to the residual structure with multipoint constraint equations (MPCs) as defined in Equation (9).

(5) Determine the modal mass of the combined structure to ensure that a sufficient percentage of the total mass is included in the model. If the total mass is less than required, the number of modes in the substructure must be increased.

(6) If the modal mass requirement is satisfied, determine the dynamic stresses on the residual structure and

recover the stresses in the component substructures with Equation (10).

Case II: Series of Substructures

For this case the method is almost identical with Case I. The free-free modes of vibration must be determined for each substructure. The residual structure is then modeled; each substructure is modeled with scalar points, generalized stiffnesses, and generalized masses for the modes to be considered. MPC cards, as defined previously in Equation (9), relate the connection points of the residual structure to the first substructure. Each substructure is related to the next substructure through a different set of MPC cards based on compatibility of the deflections of the physical connection points between the substructures. This will be shown in detail below. In defining these new MPCs that connect substructures, the dependent degree of freedom relating substructure, S_i, to substructure, S_{i+1}, must be selected from S_{i+1} (see Figure 2). Otherwise, a mode is lost in the resulting combined structure.

As an example of this method, assume that each substructure, S_i, in Figure 2 can be represented by four modes. Mode shapes for the first substructure, S_1, are designated $\{\phi_i\}$ and for the second substructure, S_2, the modes are designated $\{\bar{\phi}_i\}$, etc.

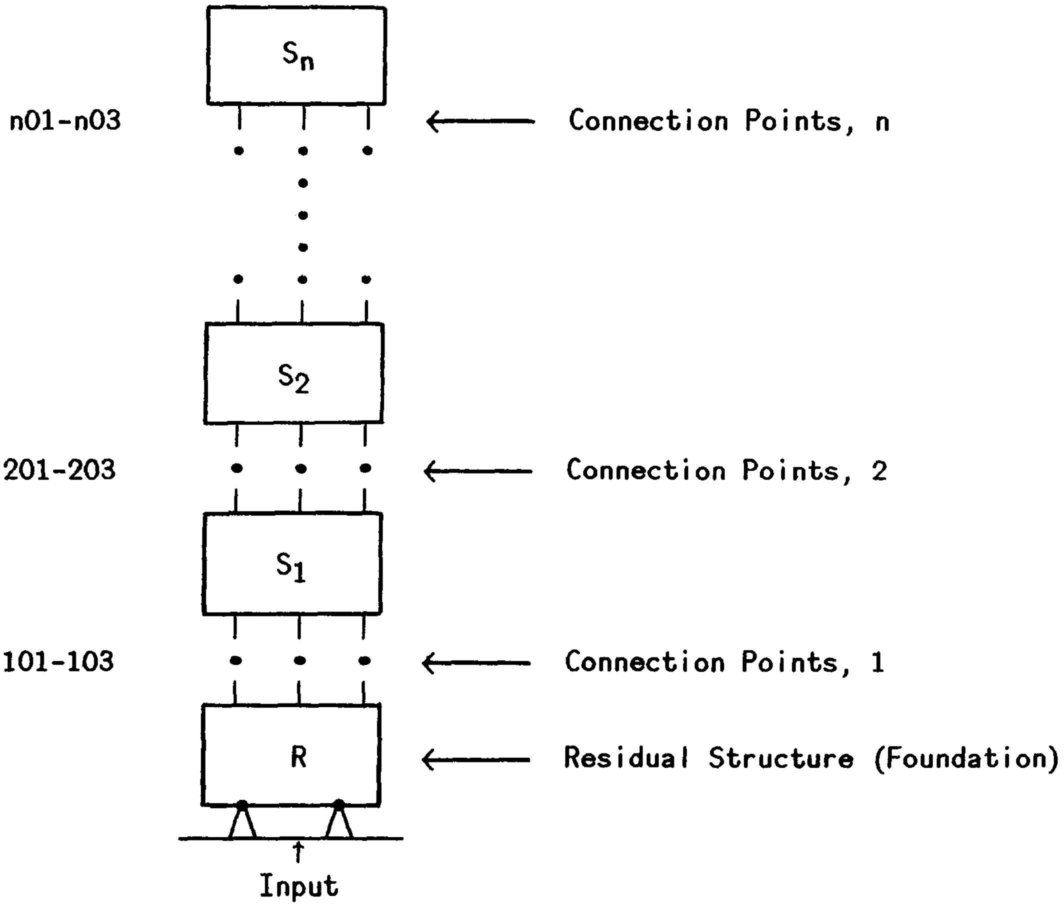

Figure 2. Case II: Series of Substructure S_1 to S_n

Thus, the MPCs connecting S_1 to R are similar to Equation (9):

$$\left.\begin{array}{l} U^{101} = \phi_1^{101}\xi_1 + \phi_2^{101}\xi_2 + \cdots + \phi_4^{104}\xi_4 \\ \vdots \\ U^{103} = \phi_1^{103}\xi_1 + \phi_2^{103}\xi_2 + \cdots + \phi_4^{104}\xi_4 \end{array}\right\} \qquad (11)$$

The equations that relate substructure, S_1, to substructure S_2, are developed as follows in the absence of physical points, U, in the reduced dynamics model.

Recovery of internal displacements, U, in substructure S_1 is given by Equation (10). Writing explicitly for the connection points 201-203 only for any mode:

$$\begin{array}{l} U^{201} = \phi_1^{201}\xi_1 + \cdots \phi_4^{201}\xi_4 \\ \vdots \\ U^{203} = \phi_1^{203}\xi_1 + \cdots \phi_4^{203}\xi_4 \end{array} \qquad (12)$$

But, displacements for 201-204 can also be recovered from the mode shapes and generalized displacements for substructure S_2, $\bar{\phi}_i$, and $\bar{\xi}_i$, respectively. Equations similar to (12) can be written for U_{201} through U_{203} in terms of substructure S_2, that is in terms of ϕ_i and ξ_i. Compatibility of displacement gives us the required MPC equation. That is:

$$\begin{array}{l} U^{201} = \bar{U}^{201} \\ \vdots \\ U^{203} = \bar{U}^{203} \end{array} \qquad (13)$$

or in terms of the mode shapes and generalized displacements:

$$\left.\begin{array}{l} \phi_1^{201}\xi_1 + \cdots + \phi_4^{201}\xi_4 = \bar{\phi}_1^{201}\bar{\xi}_1 + \cdots + \bar{\phi}_4^{201}\bar{\xi}_4 \\ \vdots \\ \phi_1^{203}\xi_1 + \cdots + \phi_4^{203}\xi_4 = \bar{\phi}_1^{203}\bar{\xi}_1 + \cdots + \bar{\phi}_4^{203}\bar{\xi}_4 \end{array}\right\} \qquad (14)$$

Note again, in order to obtain all modes the dependent MPC point should be one of the eigenvector components of the second substructure's mode shapes, $\bar{\phi}$.

Case III: Substructures Connected in Parallel and to Each Other

This case is illustrated in Figure 3. Substructure S_1 could be connected to substructure S_2 by a shaft or some type of spring element for example. Assume that the free-free mode shapes of S_1 broken at point 21 are $\{\phi\}$ and those of S_2 are $\{\bar{\phi}\}$. If an MPC card like that defined in Equation (14) is written to tie the two substructures together at point 21, one point must be dependent. Using this procedure, a mode is lost in the eigenvalue analysis of the combined structure. In order to avoid this deficiency, an extra scalar point can be used that has a displacement of 0. Practically, the point must be held to ground with a spring at least two orders of magnitude larger than other portions of the structure (to ensure a '0' deflection value). MPC equations can be written with respect to this extra point. This scalar point is the dependent point.

$$U_A + \phi_1^{21}\xi_1 + \dots + \phi_n^{21}\xi_n - \bar{\phi}_1^{21}\bar{\xi}_1 \dots - \bar{\phi}_n^{21}\bar{\xi}_n = 0 \qquad (15)$$

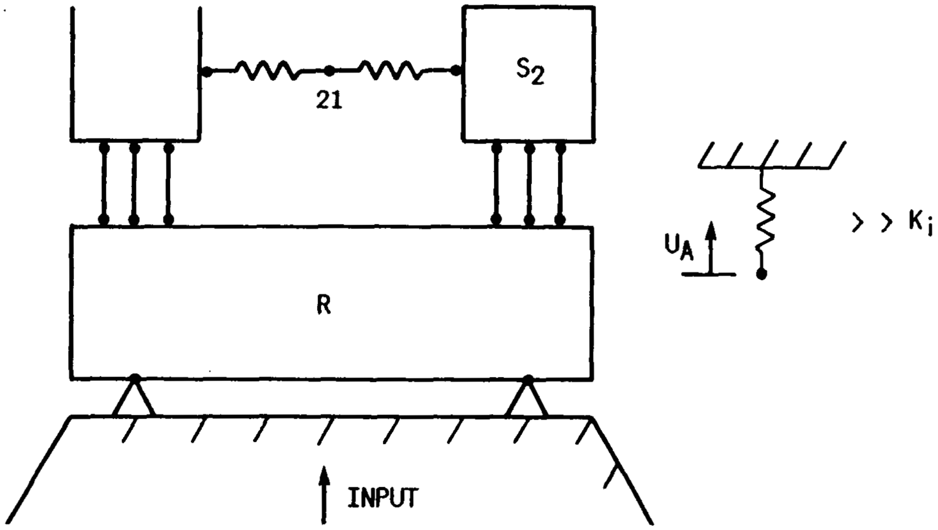

Figure 3. Case III: Substructures Connect to Each Other and to a Residual Structure, R

Since the stiffness of the extra scalar point A is high, $U_A \simeq 0$, and

$$\sum \phi_i^{21}\xi_i \simeq \sum \bar{\phi}_i^{21}\bar{\xi}_i \qquad (16)$$

Thus, this approach results in approximately the correct MPC relationship defined in Equation (14) and retains all modes designated in the substructure.

DISCUSSION OF RESULTS

In order to test the theory developed for Cases I, II, and III, a series of test problems has been developed. In this section the models and results are described.

Case I: Single Substructure Attached to a Foundation

The basic theory was tested on the model described below and shown in Figure 4.

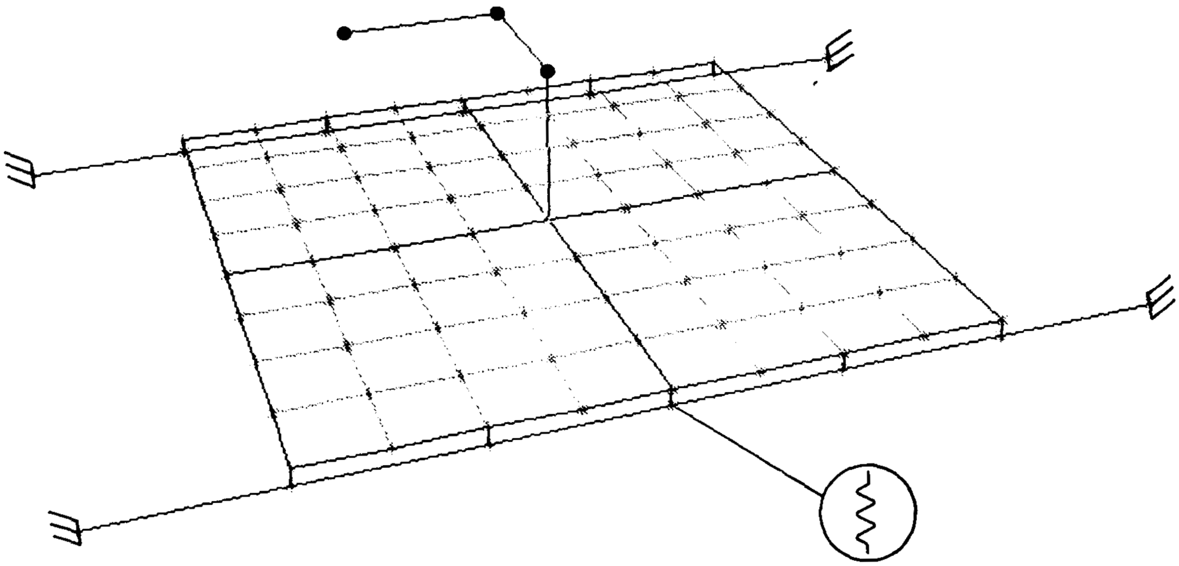

Figure 4. Case I: Basic Model of Single Substructure Attached to a Foundation

A beam stiffened flat plate and three directional cantilevered beam with a concentrated mass at the end were supported on three directional translational springs supported at each of 10 locations. The support locations are on the girders which are fixed at both ends. First, a response spectrum analysis was run on the complete problem with an arbitrary shock response spectrum providing a uniform base motion. Next, the structure was divided. The stiffened flat plate and cantilevered beam became the substructure while the springs and girders became the residual structure. An eigenvalue analysis was then performed on the unsupported substructure. Free-free modes, generalized masses, and stiffnesses were determined for 50 plate modes out of a possible 400 in one case and 25 plate modes out of a possible 400 in a second case. These, in turn, were used to represent the component substructure. The appropriate scalar points (generalized coordinates), generalized masses (concentrated mass cards), and generalized stiffnesses (spring cards) were built into the NASTRAN model of the residual structure. The connection to the residual structure which consisted of multipoint constraint equations were incorporated into the NASTRAN model via MPC cards. Programs have been written to automate the inclusion of the component modes representation of the substructure into the residual structure.

Next, an eigenvalue analysis of the reduced structure (see Figure 5) was performed.

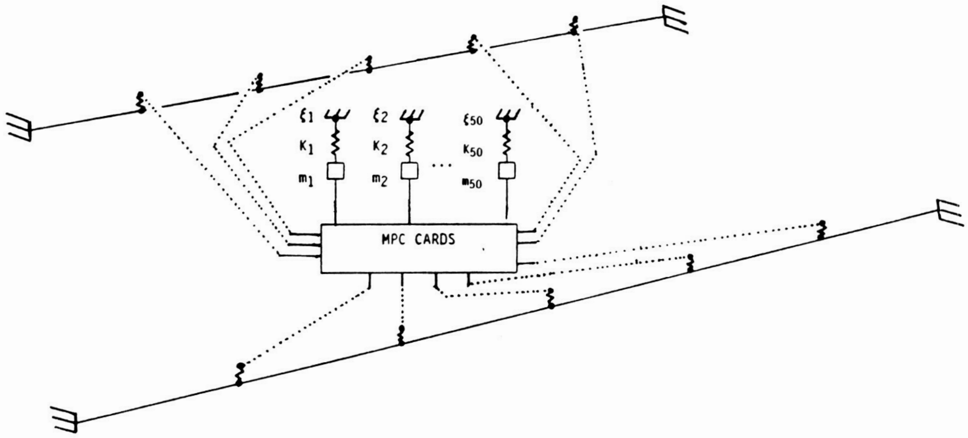

Figure 5. **Case I: Reduced Dynamics Model of Single Substructure/Foundation**

The eigenvalue quantities for the complete model and the reduced component mode representations are shown in Tables 1, 2, and 3, respectively.

The final step is to recover the displacements, forces, and stresses internal to the substructure. This calculation has not been possible to date in MSC NASTRAN for response spectrum analysis and was accomplished by using Equation 10. In response spectrum analysis, inputs are specified on a mode-by-mode basis. For U.S. Navy DDAM analysis, the total stress is determined from the NRL sum of the modal stresses. NRL contour plots for maximum principle stress due to vertical uniform base acceleration for the plate substructure for both the complete model and CMS models are shown in Figure 6.

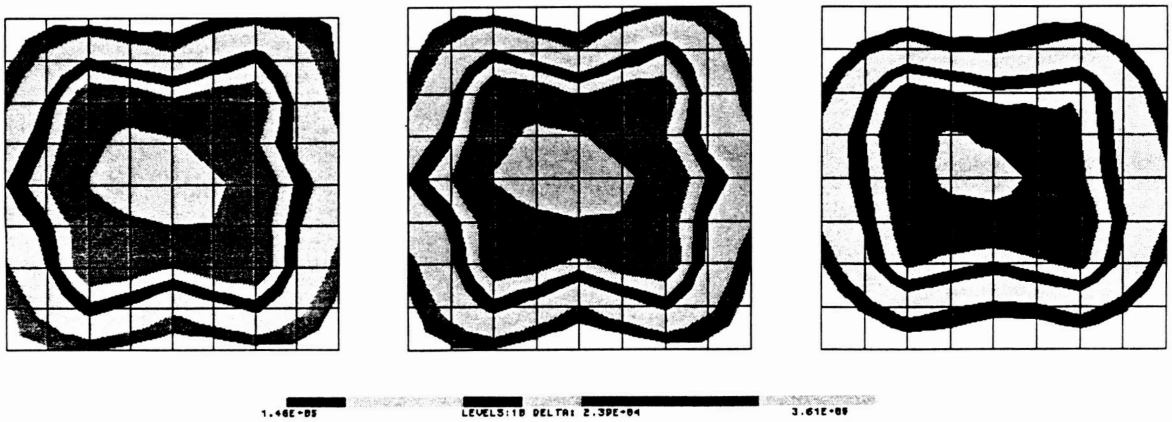

Figure 6. **Case I: NRL Contours of Maximum Principal Stress for Complete Model, CMS Model (50 Modes) and CMS Model (25 Modes)**

Table 1. Case I: Complete Model Eigenvalue Analysis Results

MODAL EFFECTIVE MASS TABLE

		MODAL WEIGHT		CUMULATIVE WEIGHT		
MODE	FREQ(HZ)	POUNDS	%	POUNDS	%	PARTIC.
1	0.832	50402.78	38.79	50402.78	38.79	1.14E+01
2	1.115	2629.47	2.02	53032.25	40.81	2.61E+00
3	1.464	31946.30	24.59	84978.55	65.40	-9.09E+00
4	2.358	470.23	0.36	85448.78	65.76	-1.10E+00
5	3.370	1038.63	0.80	86487.41	66.56	-1.64E+00
6	5.804	106.24	0.08	86593.65	66.64	5.24E-01
7	6.955	0.14	0.00	86593.78	66.64	-1.88E-02
8	9.022	0.36	0.00	86594.14	66.64	-3.06E-02
9	9.853	2681.81	2.06	89275.95	68.71	-2.63E+00
10	13.837	0.00	0.00	89275.95	68.71	5.01E-13
11	14.035	0.00	0.00	89275.95	68.71	-3.36E-04
12	17.952	18062.16	13.90	107338.12	82.61	6.84E+00

Table 2. Case I: CMS Model Eigenvalue Analysis Results (50 Modes)

MODAL EFFECTIVE MASS TABLE

		MODAL WEIGHT		CUMULATIVE WEIGHT		
MODE	FREQ(HZ)	POUNDS	%	POUNDS	%	PARTIC.
1	0.833	50179.50	38.62	50179.50	38.62	1.14E+01
2	1.116	2666.01	2.05	52845.51	40.67	2.63E+00
3	1.469	32074.36	24.68	84919.88	65.35	-9.11E+00
4	2.360	484.04	0.37	85403.91	65.73	-1.12E+00
5	3.376	1048.68	0.81	86452.59	66.53	1.65E+00
6	5.813	106.81	0.08	86559.41	66.62	5.26E-01
7	6.960	0.13	0.00	86559.53	66.62	-1.82E-02
8	9.061	0.35	0.00	86559.88	66.62	-3.01E-02
9	9.922	2731.86	2.10	89291.74	68.72	-2.66E+00
10	13.859	0.00	0.00	89291.74	68.72	-9.06E-09
11	14.051	0.00	0.00	89291.74	68.72	-1.00E-05
12	18.035	18966.68	14.60	108258.42	83.32	7.01E+00

Table 3. Case I: CMS Model Eigenvalue Analysis Results (25 Modes)

MODAL EFFECTIVE MASS TABLE

		MODAL WEIGHT		CUMULATIVE WEIGHT		
MODE	FREQ(HZ)	POUNDS	%	POUNDS	%	PARTIC.
1	0.839	50573.37	38.92	50573.37	38.92	-1.14E+01
2	1.128	2334.33	1.80	52907.70	40.72	2.46E+00
3	1.478	31913.13	24.56	84820.83	65.28	-9.09E+00
4	2.365	486.54	0.37	85307.37	65.65	-1.12E+00
5	3.382	1051.63	0.81	86358.99	66.46	-1.65E+00
6	5.823	103.41	0.08	86462.40	66.54	-5.17E-01
7	7.005	0.06	0.00	86462.45	66.54	1.19E-02
8	9.531	0.25	0.00	86462.70	66.54	-2.54E-02
9	10.352	2831.56	2.18	89294.27	68.72	-2.71E+00
10	14.269	0.00	0.00	89294.27	68.72	-2.83E-03
11	14.386	0.00	0.00	89294.27	68.72	-1.91E-08
12	18.481	24091.79	18.54	113386.06	87.26	-7.90E+00

The stresses and stress distribution show excellent agreement when 50 plate modes (up to 90 Hz) are used. Some accuracy is lost when only 25 modes (up to 30 Hz) are chosen, but the pattern is still similar, and peaks are in the same locations. It is, therefore, necessary to choose enough modes to ensure inclusion of the important ones.

Case II: A Series of Substructures Attached to a Residual Structure (Foundation)

Case I covered the methodology involved in connecting a substructure (generalized coordinates) to the residual (physical coordinates). Case II demonstrates the situation where two substructures are connected directly to each other. The technique, in the absence of physical points, is described in the section on theoretical development. The test problem for this case consists of a simple beam with one degree of freedom per grid point in the lateral direction (see Figure 7).

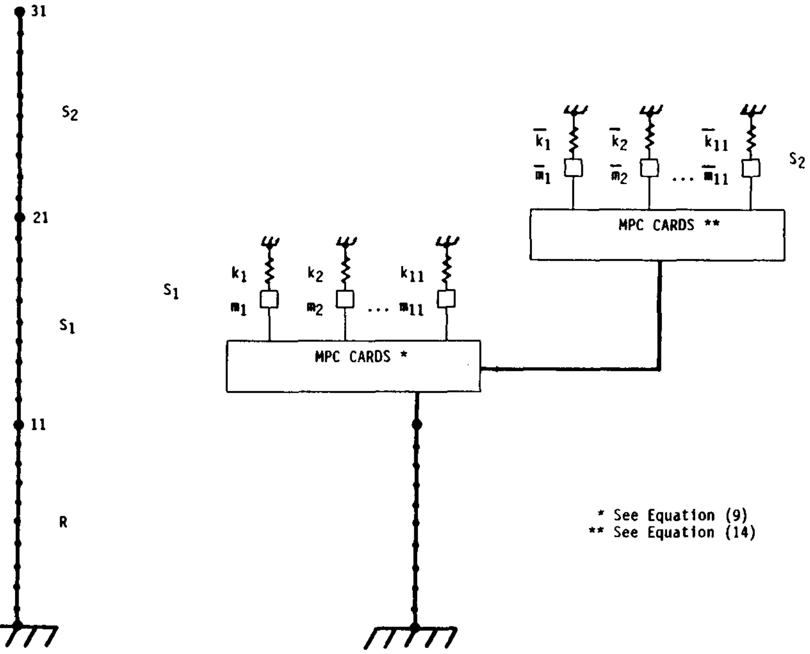

Figure 7. **Case II: Basic Model of a Series of Substructures Connected to Each Other and to a Residual Structure**

In this case, all 30 modes were considered in the complete model and all 11 modes in each substructure were retained in their component modes' representation. All output results, both in the eigenvalue analysis and internal displacements recovered in the substructures, agreed to nine significant figures.

Case III: Parallel Substructures Connected to Each Other and to a Common Residual Structure

The sample problem for this case is similar to that considered in Case I except that two identical spring supported plate structures are connected to each other with very stiff springs and supported on extended common girders. A plot of the model is shown in Figure 8.

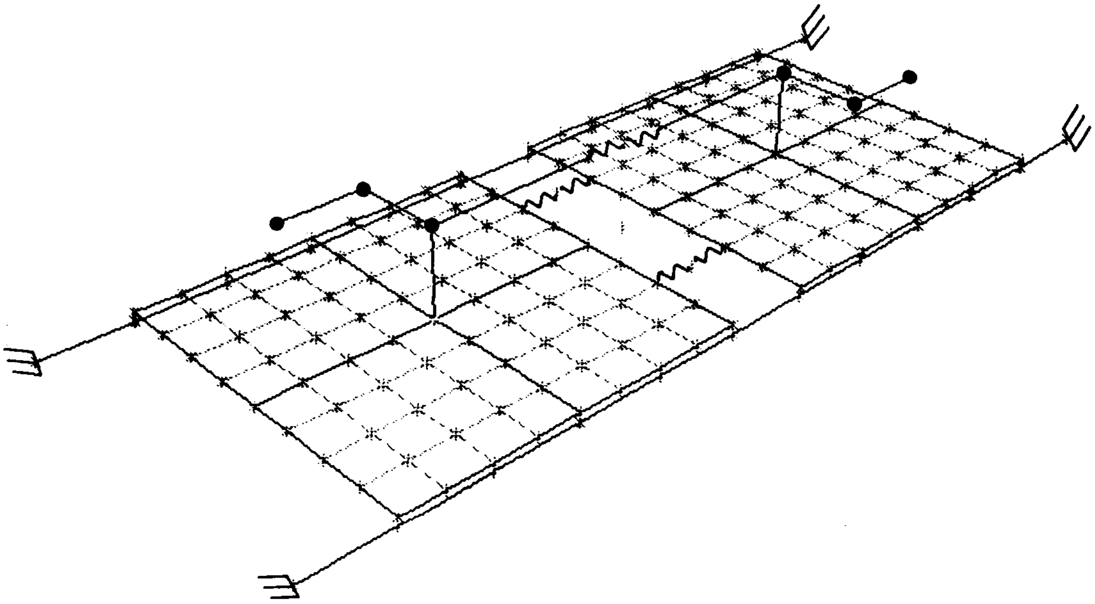

Figure 8. **Case II: Model of Parallel Substructures Connected to Each Other and to a Common Foundation**

The shock response spectrum analysis was again run for the complete model and free-free component modes were determined for the two substructures. The CMS analysis is similar to that of Case I with the extra constraint equation between substructures as in Case II, with the additional modeling technique described in the theoretical development of Case III. A new scalar point was defined and connected to a very stiff spring and used as the dependent degree of freedom in the constraint equations relating the two substructures. This allowed all other terms in the constraint equation to be independent which, for unknown reasons, was required in MSC NASTRAN for good agreement with the complete model (exact case). Eigenvalue results for both cases are shown in Tables 4 and 5. Stress contours are shown in Figure 9. Fifty modes were considered of a possible 400 in each plate. The agreement, again, is excellent.

Table 4. Case III: Complete Model Eigenvalue Analysis Results

MODAL EFFECTIVE MASS TABLE

		MODAL WEIGHT		CUMULATIVE WEIGHT		
MODE	FREQ(HZ)	POUNDS	%	POUNDS	%	PARTIC.
1	0.842	6528.56	2.57	6528.56	2.57	-4.11E+00
2	0.902	0.00	0.00	6528.56	2.57	3.75E-08
3	1.275	44744.48	17.65	51273.04	20.22	1.08E+01
4	1.409	0.00	0.00	51273.04	20.22	2.78E-08
5	1.985	50777.22	20.03	102050.27	40.25	1.15E+01
6	1.985	0.00	0.00	102050.27	40.25	4.94E-06
7	2.603	42138.27	16.62	144188.53	56.86	1.04E+01
8	3.176	0.00	0.00	144188.53	56.86	-1.74E-09
9	3.566	2623.81	1.03	146812.34	57.90	2.61E+00
10	3.593	0.00	0.00	146812.34	57.90	-1.11E-08
11	5.728	0.00	0.00	146812.34	57.90	2.07E-09
12	5.815	4647.64	1.83	151459.98	59.73	3.47E+00
13	6.221	478.06	0.19	151938.05	59.92	1.11E+00
14	6.223	0.00	0.00	151938.05	59.92	5.47E-09
15	7.075	2392.79	0.94	154330.84	60.86	2.49E+00
16	7.683	0.00	0.00	154330.84	60.86	2.85E-10
17	9.271	0.00	0.00	154330.84	60.86	-5.53E-10
18	9.391	2050.21	0.81	156381.05	61.67	2.30E+00
19	10.232	0.00	0.00	156381.05	61.67	2.34E-12
20	12.625	0.30	0.00	156381.36	61.67	2.81E-02
21	13.756	0.00	0.00	156381.36	61.67	-1.02E-11
22	13.856	0.00	0.00	156381.36	61.67	1.15E-03
23	14.176	0.00	0.00	156381.36	61.67	3.48E-12
24	14.690	197.13	0.08	156578.50	61.75	-7.14E-01
25	14.828	3.84	0.00	156582.34	61.75	9.97E-02

Table 5. Case III: CMS Model Eigenvalue Analysis Results

MODAL EFFECTIVE MASS TABLE

		MODAL WEIGHT		CUMULATIVE WEIGHT		
MODE	FREQ(HZ)	POUNDS	%	POUNDS	%	PARTIC.
1	0.844	6692.56	2.64	6692.56	2.64	4.16E+00
2	0.909	1.06	0.00	6693.62	2.64	5.25E-02
3	1.279	43532.91	17.17	50226.53	19.81	-1.06E+01
4	1.424	0.02	0.00	50226.55	19.81	7.57E-03
5	2.030	44787.91	17.66	95014.47	37.47	1.08E+01
6	2.161	18.66	0.01	95033.13	37.48	2.20E-01
7	2.650	49267.34	19.43	144300.47	56.91	1.13E+01
8	3.378	24.65	0.01	144325.13	56.92	-2.53E-01
9	3.611	1694.85	0.67	146019.98	57.59	2.09E+00
10	5.234	3.33	0.00	146023.31	57.59	-9.28E-02
11	5.830	3100.32	1.22	149123.64	58.81	-2.83E+00
12	5.836	1483.05	0.58	150606.69	59.40	1.96E+00
13	6.230	549.92	0.22	151156.61	59.61	-1.19E+00
14	6.242	17.05	0.01	151173.66	59.62	-2.10E-01
15	7.100	2620.00	1.03	153793.66	60.65	-2.60E+00
16	8.974	0.98	0.00	153794.64	60.65	-5.03E-02
17	9.465	2012.26	0.79	155806.89	61.45	-2.28E+00
18	10.303	3.59	0.00	155810.48	61.45	-9.63E-02
19	13.785	0.00	0.00	155810.48	61.45	2.53E-03
20	13.849	0.00	0.00	155810.48	61.45	-5.91E-04
21	14.355	0.01	0.00	155810.48	61.45	-3.72E-03
22	14.533	0.07	0.00	155810.56	61.45	1.38E-02
23	15.096	15.09	0.01	155825.66	61.45	-1.98E-01
24	15.148	85.75	0.03	155911.41	61.49	4.71E-01
25	16.808	41.10	0.02	155952.50	61.50	3.26E-01

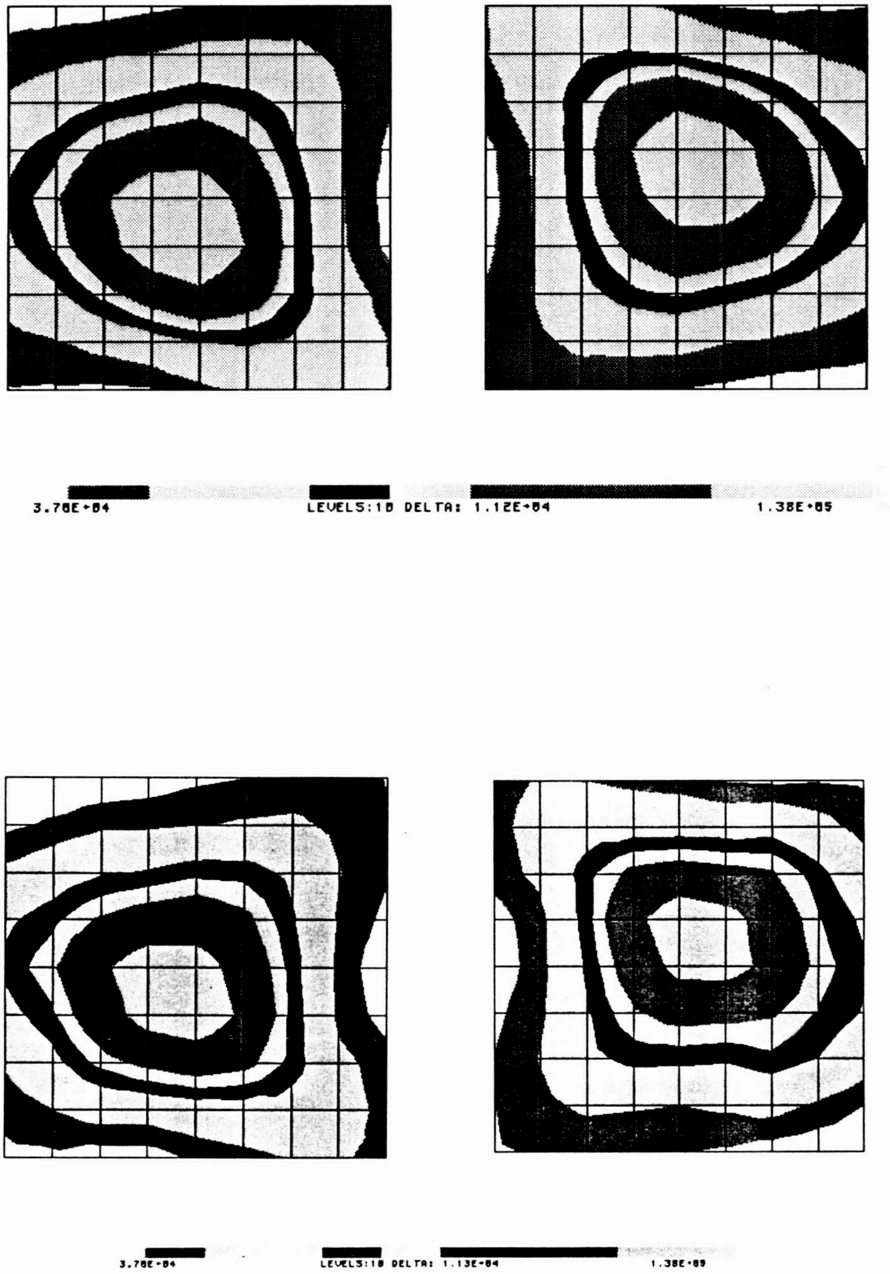

Figure 9. Case III: Contour of Maximum Principal Stress for Complete and CMS Models

OTHER APPLICATIONS

The sample problems discussed in the previous section are very basic, but illustrate the effectiveness and accuracy of Component Mode Synthesis. In addition to the response spectrum analyses discussed, the methodology was also applied to transient analysis. The theory is the same. Recovery of displacements, forces, and stresses in the component substructure is done per timestep rather than per mode. Implementation in MSC NASTRAN required a different set of DMAP instructions consistent with the transient rigid formats. Preliminary results for Case I were excellent, within 2 percent of the complete case for component substructure principal stresses for all timesteps checked. Work in this area is ongoing.

Additionally, the technique is very useful in problems where reanalysis of large models would be prohibitive. One example is a system in the design phase where model changes are being made with each new analysis, particularly if one component of a system is changing frequently and the component mode representation of the other components remains unchanged. Eigenvalue analysis need only be performed for the changing component and the resulting system dynamic model is very small compared to a complete physical model of the system. For large problems, CMS can help analysts realize a significant savings in time and cost.

Another example where an even greater economy can be realized is that of a large nonlinear problem where only a portion of the system is nonlinear. This would be the case for resiliently mounted shipboard propulsion or generator equipment where the mounts exhibit nonlinear characteristics. The residual structure would contain the nonlinear part of the system. In the transient analysis where frequent stiffness matrix updates may be required, the matrix sizes are small because of the Component Mode Synthesis. Recovery of data for the component structures is still linear and based on the connection point displacement time histories from the nonlinear analysis.

CONCLUSIONS

Dynamic substructuring by component mode synthesis is an effective and accurate way to simulate the dynamic characteristics of large systems. If enough modes are considered, there is relatively little loss in accuracy, unlike simple dynamic reduction methods (i.e., static condensation, Guyan reduction). Work is ongoing to determine a concept (analogous to the modal mass for fixed base structures) to evaluate relative importance of modes for free/free structures. The reduction of model size afforded by CMS makes possible on moderate sized mainframes (such as a VAX 11/780) analyses that otherwise might require a supercomputer.

REFERENCES

1. Richard H. MacNeal, *"A Hybrid Method of Component Mode Synthesis,"* Computers and Structures, Vol. 1, 1971, pp. 591-601.

2. E. Dean Bellinger, *"Component Mode Synthesis for External Superelements,"* The MacNeal-Schwendler Corporation, 1986.

3. *"MSC/NASTRAN User's Manual,"* The MacNeal-Schwendler Corporation, 1985.

N88-18951

NASDA's New Test Facilities for Satellites and Rockets

Mitsuhiro Tsuchiya

Recently, the space development activities for the practical purposes are progressing in the world. For the development of large satellite, rocket, space station and spaceplane, new technology at the field of space simulation has been required. Based on the results of our basic study and investigation on the technology, National Space Development Agency of Japan (NASDA) has decided to construct the integrated environmental and structural test facilities for the future large satellites. Presently , these facilities are under construction . This paper presents the outline of NASDA's new test facilities and some technical considerations , especially for the unique vibration test facility .

1. Introduction

Recently, we are developing H-2 rocket, 2 ton class large geostationary earth orbit (GEO) satellite Engineering Test Satellite Ⅵ, (ETS-Ⅵ) Free- Flyer and Japanese Experimental Module (JEM) of the space station under the co-operation with NASA and ESA , for the 1990's space applications . These future spacecraft become larger in dimensions and heavier in weight . With the development of advanced spacecraft, more severe test specifications are required for the environmental and space simulation test facilities .

The environmental and space simulation tests for our satellites and rocket components are performed at Tsukuba- Space- Center (TKSC) of NASDA . Our current facilities were constructed for the satellites which are launched by N and H-1 rockets . And the requirements for the future large spacecraft are beyond the capacities of these facilities .

From this situation ,we have studied environmental technologies for the future large satellites for several years. In 1983, we started to make the preliminary investigation on the future test facilities . In 1985,we got test engineer's opinion from the space industries in our country.

Based on the groval evaluation of the results of our studies, we made a construction plan of new environmental test facilities ,in 1986 .

Presently,our new facilities are under construction at TKSC . And it will be initially used for the development tests of ETS-Ⅵ in 1989.

In this paper , our philosophy for new test facilities, the outline of each facility and in paticular, some of the technical uniqueness of vibration test facility are discussed.

2. Philosophy of New test Facilities

Fig. 1 shows total system of our new test facilities. Our philosophy is to perform all tests of a spacecraft in one building, which we call " integrated test building " .

ESA/ESTEC and IABG have a plan to improve test capabilities by adding some equipments and facilities for next generation satellites. And CNES/INTESPACE , The Institute of Space and Astronautical Science of Japan (ISAS) have also attractive concentrated test facilities.

However, our new test systems and facilities will be one of the most advanced ones in the world . Next generation environment facilities will have this tendency.

Here, we discribe the requirements for our facilities.

(1) High capacities for large spacecraft in the 1990's.
(2) Ability to perform 4 spacecraft tests at once .
(3) High efficiency of test operation.
(4) Low cost of test operation.
(5) Applicability to future space business.
(6) Environment test levels specified from H-2 Rocket.

Based on the above requirements,we designed and made the building layout as shown in Fig . 2 .

Due to above requirements , the performance of our facilities are summarized as shown in Table 1.

Table 2 shows the full schedule about test facilities total plan.

Fig .1 Total System of New Test Facility

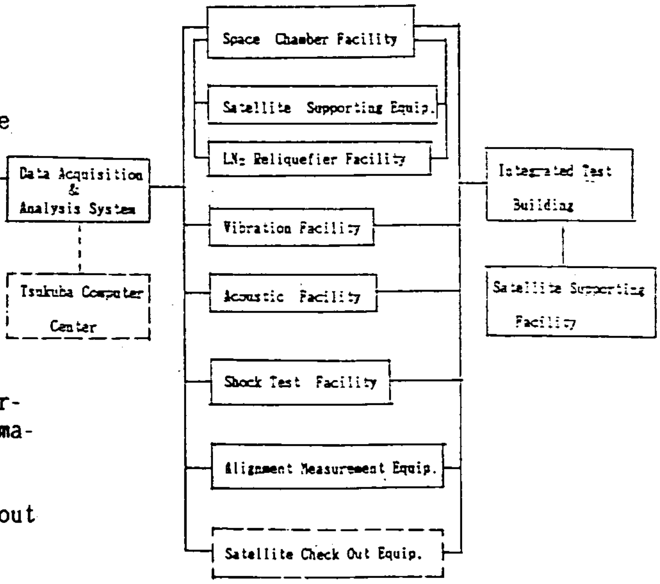

Table .1 Features of New Test Facilities

1 . Target -----2 Ton class satellites (at GEO)
2 . High Efficiency
3 . Can Test Many Satellites at a Time
4 . Low Cost
5 . Open to Many World's Users

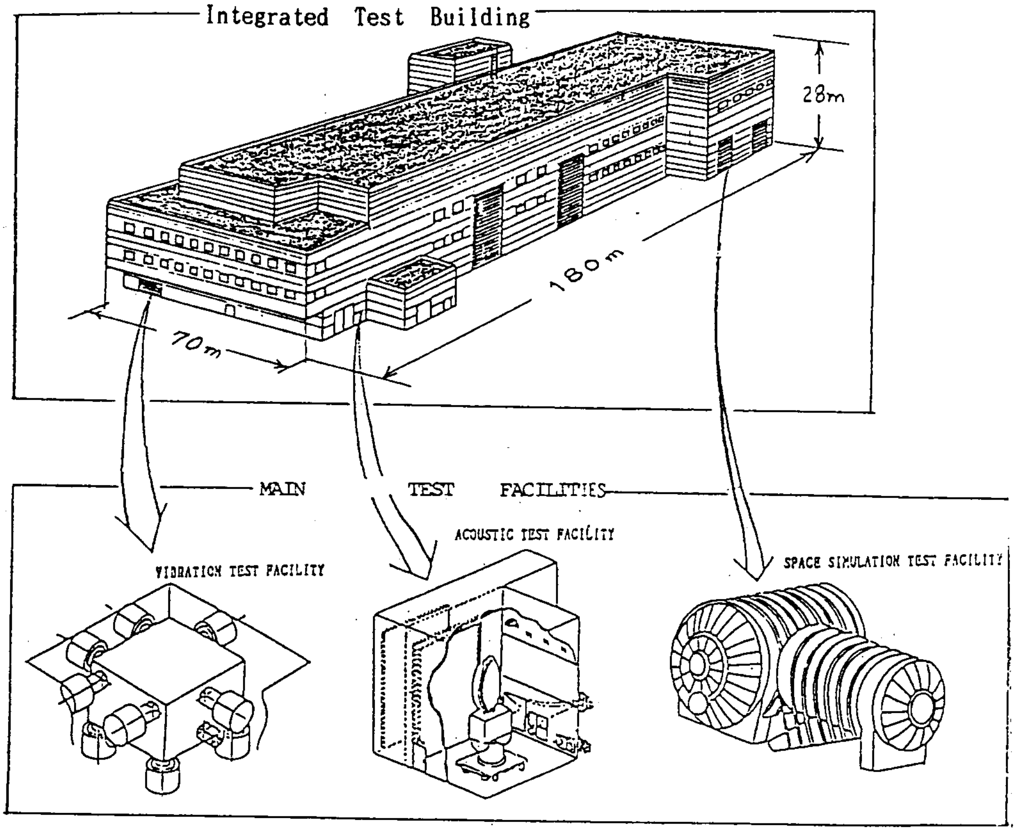

Fig .2 New Test Facilities and Integrated Test Building

Table .2 Project Plan of Integrated Test Facility

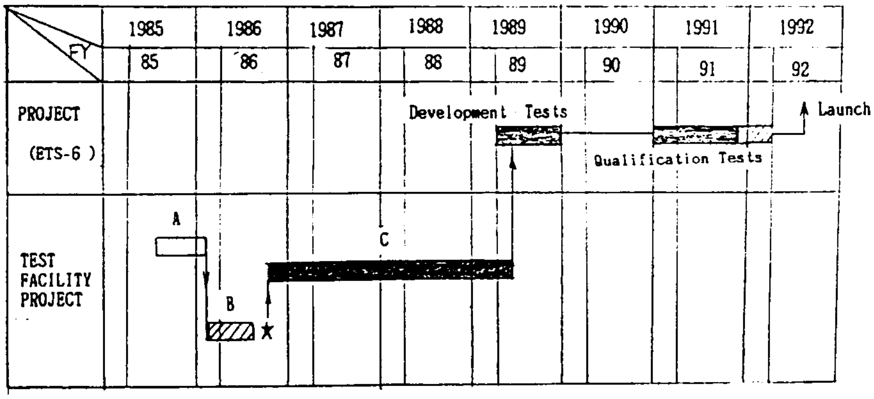

Total Span ---- 4 Years (7 Years including basic studies)

PHASE

A : Preriminary Studies and Test System Plan

B : 1 NASDA's detail investigation including industries' opinion

2 Project Planning

3 Decision of contractors

C : Construction of facilities .

3. Vibration Test Facility

Fig. shows the bird's-eye view of the vibration test facility, which is a three dimensional vibration system . We can perform the vibration tests of three directions separately without removing the test specimen from the table.

Therefore , we can complite the test for a spacecraft shorter period than that of conventional test facility ,which results in high operational efficiency .

The new vibration system consists of 4 vertical and 3 horizontal shakers for each axis , totally 10 shakers .
From the results of our trade-off studies, we decided to adopt electrodynamic shaker rather than hydrodynamic one,from the operational and control point of view .
The test table has 3mX3m size , which is made of aluminum alloy and supported through 12 hydrostatic joints . We designed the joint to move in 5 degrees of freedom . Using the table support system composed of these joints the control system becomes less complicated .

The specification of the vibration facility is shown in Table 3 .

Here , we explain some technical features of the system .

(1) Principle of the Supporting System

Fig .4 shows a free body diagram of the rigid supporting table movement .
To move the rigid table in one direction , two surfaces of the table in parallel with the direction of the motion have to be supported at two points in one surface and at three points in another surface.
Our supporting system adopts this principle .

However , for the horizontal slidings in X and Y direction , one more points is added to the above three points for resisting the rolling moment forces due to the test specimen .

Fig .5 shows the location of the spherical pad bearings which are used at each point due to the above principle .

(2) Mechanism of Spherical Pad Bearing

The hydrostatic joint designed for our system , which we call " spherical pad bearing " , restricts only one degree of freedom of the motion .

Fig .6 shows a cross section of the spherical pad bearing .
As shown in Fig .7, the spherical pad bearing has five degree of freedom of the motion . In this joint , one degree of freedom of the motion , which is the motion along the connecting line between the joint base and the supporting table, is restricted .

One of the technical key points in our system is to develop the hydrostatic joint, especially to increase the rigidity of the joint . Presently , the rigidity in the axial direction of the joint is designed to be approximately 8×10^7kg/mm .

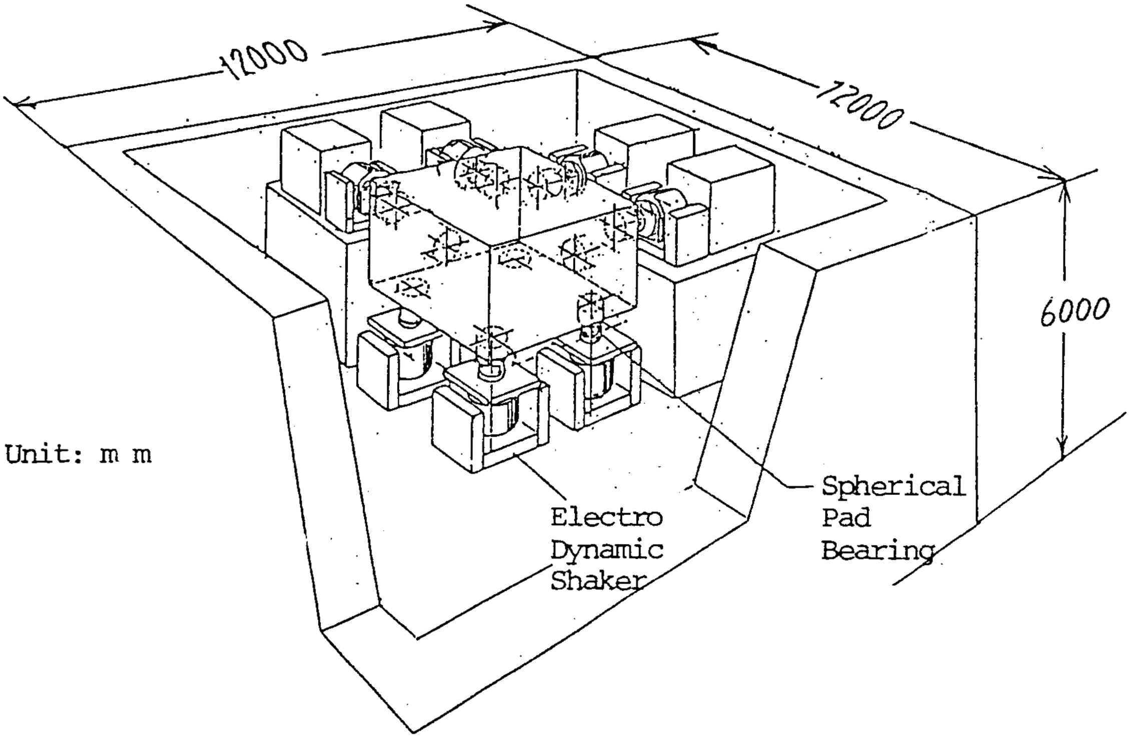

Fig. 3 Vibration Facility (Shaker and Table Assembly)

Table. 3 Vibration Test Facility Specification

TOTAL PERFOMANCE	3 *DIRECTIONAL* SHAKER SYSTEM WEIGHT CAPABILITY : 4.5 tons (9,900 *lbs.*) FREQUECY RANGE : SINE 5 - 100 Hz RANDOM 5 - 200 Hz (Low Level) TRANSIENT OVERTURNING MOMENT CAPABILITY : 6 0 ton-m (434,000 *ft.–lbs.*)
SHAKER	LDS ELECTRODYNAMIC SHAKER VERTICAL ; 9.5 tonF X 4 shakers HORIZONTAL ; 9.5 tonF X 3 shakers X 2 directions (21,000 *lbs.*)
TEST TABLE	DIMENSION : 3 m × 3 m : (9.8 X 9.8 *ft.*) Aluminum alloy
CONTROL	Genrad, digital for amplitude control LDS, analog for current-phase control

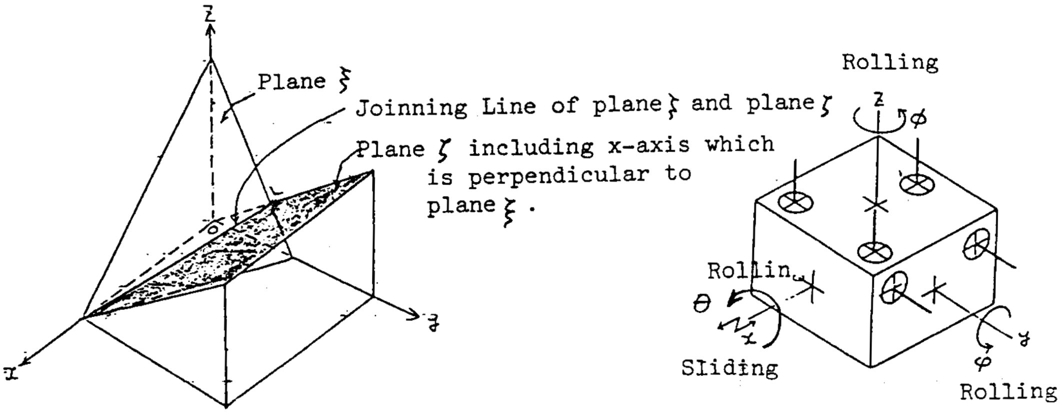

Fig. 4 Principle of Supporting in the Free Space

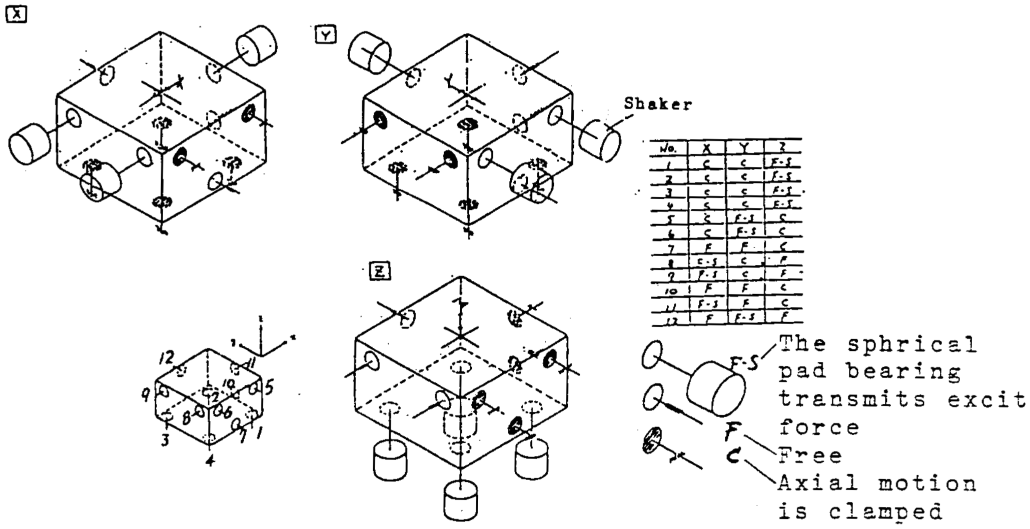

No.	X	Y	Z
1	C	C	F-S
2	C	C	F-S
3	C	C	F-S
4	C	C	F-S
5	C	F-S	C
6	C	F-S	C
7	F	F	C
8	C-S	C	F
9	F-S	C	F
10	F	F	C
11	F-S	F	C
12	F	F-S	F

Fig. 5 Distribution of the Spherical Pad Bearings and their Function for Each Excitation Axis

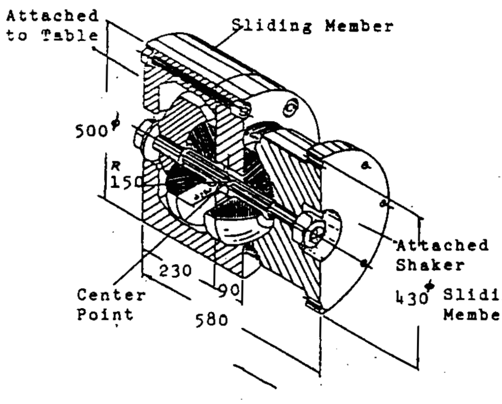

Axial Stiffness : 8×10^{7} Kg/mm

Fig .6 Spherical Pad Bearing

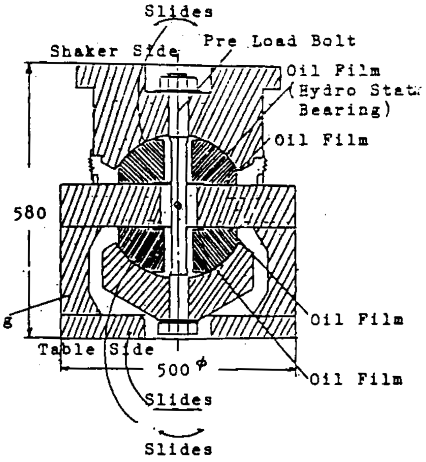

Fig. Cross Section of Spherical Pad Bearing

4 . Space Simulation Test Facility

Fig.8 shows the space simulation test facility , which enables us to perform solar simulation test , IR simulation test , and vacuum thermal cycle test .

The vacuum chamber is a horizontal hammer type one with a full- open-door . This type of door enables us to use the chamber volume efficiently , because it is allowed to set a large specimen up to the chamber diameter .
The efficient chamber volume , $13^{\phi}\mathrm{m} \times 16^{L}\mathrm{m}$, was determined from the requirements of spacecraft and precision of solar simulator design .
The efficient beam diameter of the solar simulator is 6 m .

One of the most advanced technologies adopted in this facility is the collimation mirror composed of glass coated CFRP segments . This mirror is light weight . Therefore , it requires a simple mechanism for the tempereture control as shown in Fig .9 .

And to operate the chamber system at low cost , we reuse the vaparized N_2 through the LN_2-Reliquefier facility .

The specification of the space simulation test facility is shown in table 4 .

5 . Acoustic Test Facility

Fig .10 shows the acoustic test facility . In this facility , we adopted a compressed air type system which is the same type as the current facility and is superior to the GN_2 blow - down type system in operational test efficiency .

The maximum overall sound pressure level (SPL) is 151dB, and one-third octave band spectrum shaping is performed with the degital controller ,which consists of a redundant system .

The volume of the new reverberation chamber is approximately 1600 m^3 (10.5m×9.0m ×$17.0^{H}\mathrm{m}$) . And also this facility is provided with a supporting cart for large spacecraft .

The specification of the acoustic test facility is shown in Table 5 .

6 . Data Acquisition and Analysis System

Fig . 11 shows the data acquisition and analysis system . This system is a kind of data processing center with the LAN , which consists of data analysis and management computers and terminals at each test area .

We can use this system not only to process the data acquired at each test and to establish the data base of spacecraft design and tests, but also to storage ourselves technical potential.

The new facility has high speed data processing , and the data memory of 40 GB .laser disk .

Table 6 shows the characteristics of the data acquisition and analysis system .

ORIGINAL PAGE IS
OF POOR QUALITY

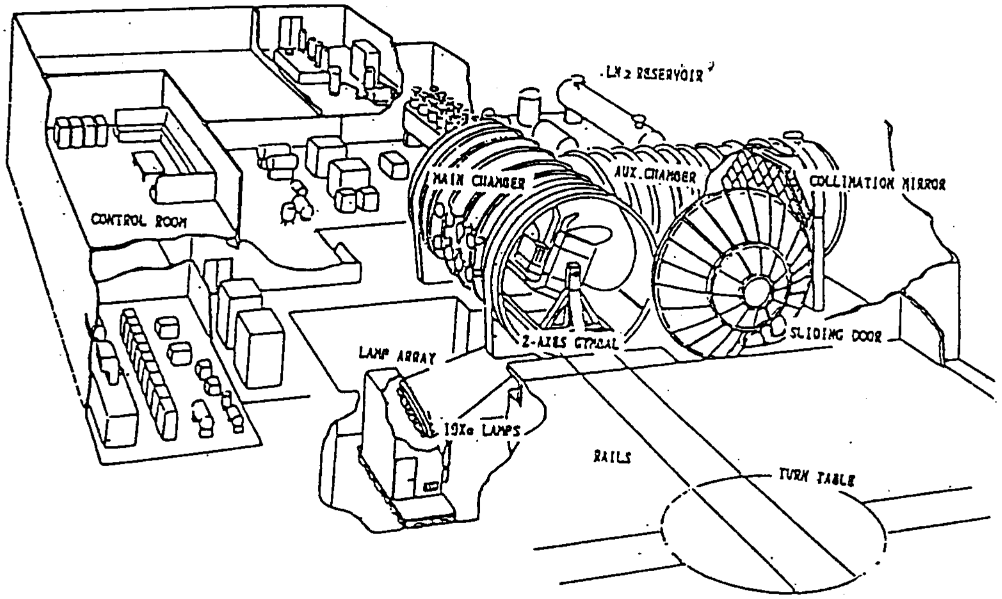

Fig. 8 Space Simulation Test Facility

Table. 4 Space Simulation Test Facility Specification

VACUUM VESSEL	HORIZONTAL HAMMER SHAPE USABLE VOLUME : 13 m diam. X 16 m long
VACUUM SYSTEM	ULTIMATE PRESSURE : 1 X 10^{-7} torr within 16 hours (empty) ROUGHING SYSTEM : 4 Oil Rotary Pumps and Mechanical Booster Pumps HIGH VACUUM SYSTEM : 3 Turbomolecular Pumps (4.900 l/s ea.) 4 He Cryosorption Pumps (28.000 l/s ea.) 2 He Cryo Pumps (1.700.000 l/s ea.)
SHROUD SYSTEM	100 K (LN_2) -100 to 60°C (GN_2)
SOLAR SIMULATOR	BEAM DIAMETER : 6 m INTENSITY : 1.3 solar constant (Max.) UNIFORMITY : ± 6% at Reference Plane SOURCE : 30 kW Xe lamp x 19 COLLIMATION MIRROR : Glass coated CFRP segmental mirror (Al deposited)
MOTION SIMULATOR	WEIGHT CAPABILITY : 5 tons SPIN RATE : 0 - 10 RPM (continuous and step) ATTITUDE RANGE : Horizontal ± 90 deg.

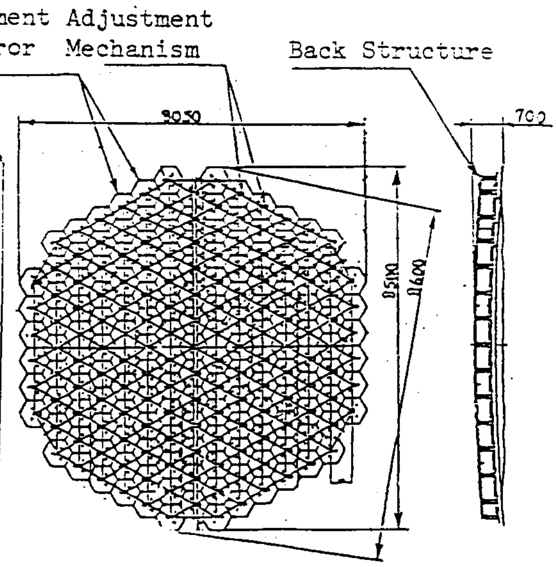

Shape	Spherical (163 Hexagonal Segments)
Material	Glass coated CFRP + Al honeycomb
Reflecting Surface	Aluminium with SiOx Coating

Fig. 9 Collimation Mirror

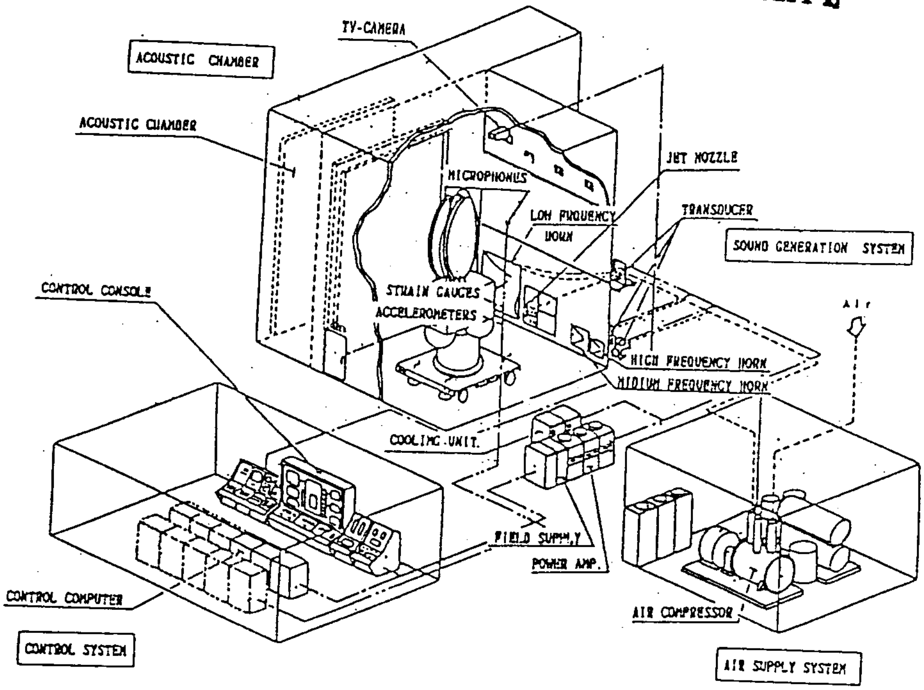

Fig. 10 Acoustic Test Facility

Table 5 Acoustic Test Facility Specification

TOTAL PERFRMANCE	COMPRESSED AIR · SYSTEM SOUND PRESSURE LEVEL : 151 dB (O.A.) SPECTRUM RANGE : 25 Hz - 10 kHz (1/3 oct.band width)
AIR COMPRESSOR	AIR FLOW RATE : 245 Nm³/min. MOTOR : 1440 kW
SOUND GENERATOR	TRANSDUCER : EPT-200 (10kW) X 3 EPT-1094 (10kW) X 4 JET NOZZLE (0.2kW) X 1 HORN : 25 Hz X 1 100 Hz X 1 200 Hz X 1
CONTROL	1/3 oct.band DIGITAL CONTROL
ACOUSTIC CHAMBER	DIMENSION : 10.5 W X 9.0 D X 17.0 H (m) ACCESS DOOR : 7.0 W X 13.0 H (m) approx. VOLUME : 1,600 m³ (56,500 ft³)

ORIGINAL PAGE IS
OF POOR QUALITY

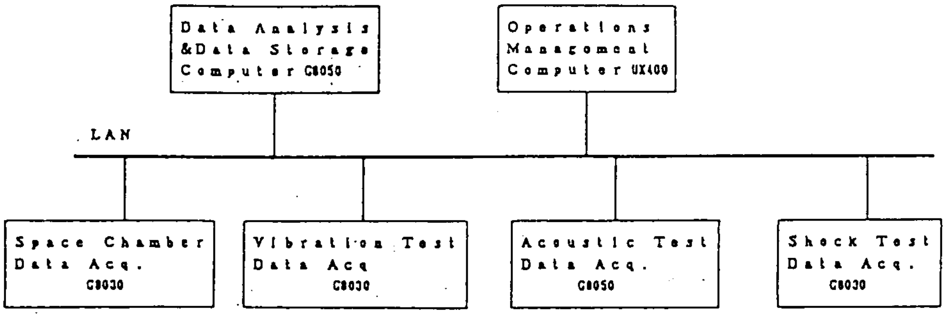

※Feature
- Using the LAN System
- Compatible with each other
- High Speed Data Processing
- Large Digital Data Memory (Laser Disk 40GB)

Fig. 11 Data Acquisition and Handling System

Table. 6 Data handling System Characteristics

1. VIBRATION	3. ACOUSTIC
Data Acquisition Channel--------ACC. 300ch. Strain 50ch. Frequency Range--5~100Hz (Sin.) 5~200Hz (Ran) Sampling Rate ---800 sam/ sec Data Analysis FFT , PSD , Trancefer Func. Ana. Wave Form Analysis Notch Level Analysis Analysis and Print Out Time-- 44 min. 350 cH (FFT.PSD.f-g)	Data Acquisition Channel---ACC. 200 cH. Strain 30cH. Microphone-12cH. Frequency Range ACC. 5~2kHz Sampling Rate ACC.&STR. 8k/sec Microphone 40 k / sec Data Analysis 1/1. 1/3 Oct Analysis PSD, AL-SPL Transfer Func. Analysis Analysis and Print Out Time---25 min. 200cH (PSD,1/1 ,AL-SPL)
2. SPACE CHAMBER	4. SHOCK
Data Acquisition Channel-------Temp. 800 cH . Calorimeter 300cH. Analog Sig. 50 cH . Digital Sig. RS232Cx2 Scanning Speed--10 msec. 100m sec/cH Measurement Interval -- 2 min. Data Processing Scan Print, Senser vs. Time Print and Prot Average Print ,ΔT/t Print and Plot Equilibrium Search Print , Limit Check Min. Max. of Sensor Defind Calolimeters Process. Equilibrium Frequency Bar Graph. Prediction of Equilibrium ,	Data Acquisition Channel---ACC. 200cH Frequency Range 20~10kHz Sampling Rate 50 kHz Sam./sec Data Analysis FFT , SRS , Wave Form Analysis Analysis and Print Out Time--25 min. 200 cH. (FFT , SRS ,)

7 . Integrated Test Building

Fig . 12 shows the integrated test building .
The total-area of this building is about 1800 m^2 and the layout is shown in Fig. 13 .

There are two test area . One is the static test area and another is the dynamic test area .
The spacecraft test rooms have the cleanness of class 100,000 .
To keep the high cleanness of the building , two types of air lock loading room are adopted for the entrance of satellites and its supporting equipments .
Especially, in this building , a large preparation area is provided to satisfy a variety of user's requirements .

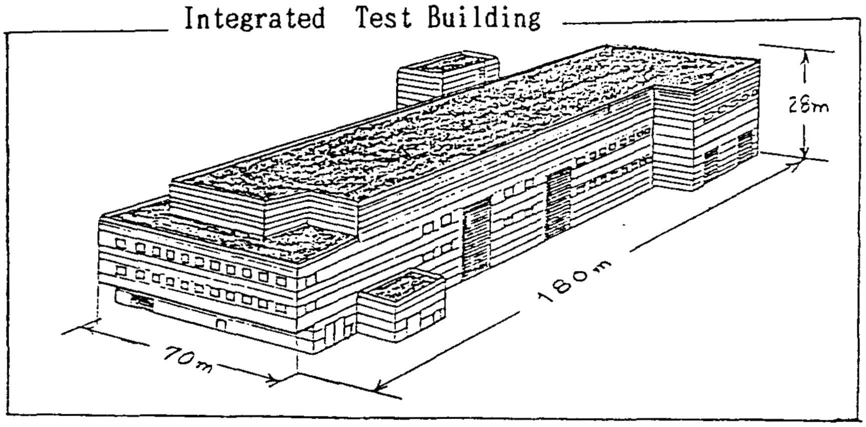

Fig . 12 Integrated Test Building

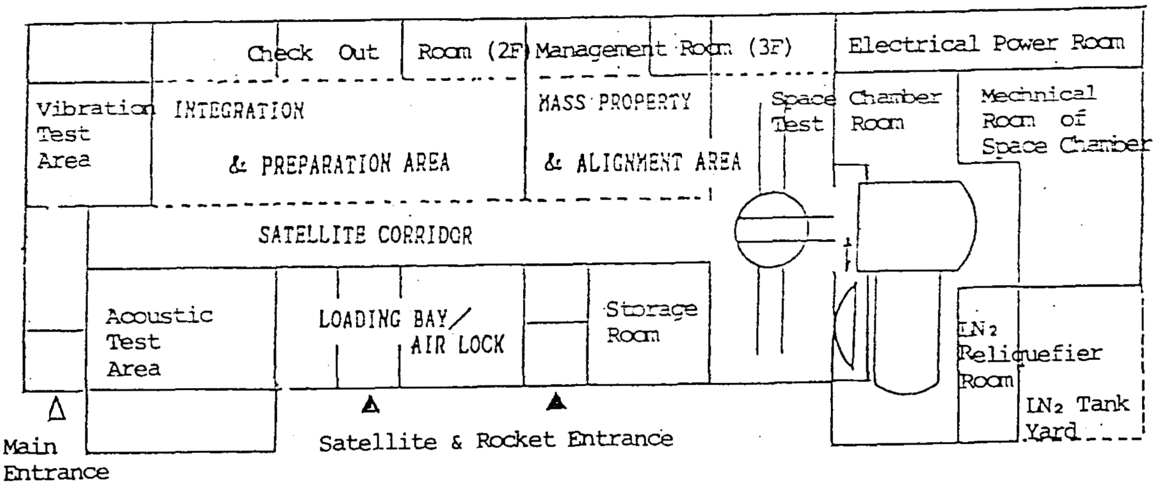

Fig .13 Layout of Integrated Test Building

8. Conclusions

We presented the outline of NASDA's new test facilities, our philosophy of NASDA's future spacecraft development and some technical key points of our vibration test system.

Our new facilities' "easy and low cost operationability" will answer to the requirements of many users in the world and open a door to the tests of their future large spacecraft.

We will be able to present some detail performances of the facilities at the next chance.

DYNAMIC TESTING

N88-18952

Design and Dynamic Testing of an Instrumented Spacecraft Component

Thomas J. Dwyer

This paper presents details relating to the design and subsequent vibration and shock tests of a spacecraft component for a severe vibration and shock environment. The design process and analysis method involves the use of finite element analysis coupled with the Modal Strain Energy method with Risk Graphs to determine and adequacy of the design. The vibration levels experienced by box parts are reduced by the application of passive constrained layer viscoelastic damping treatments that significantly improve component reliability. All significant internal components were fully instrumented in both the random vibration and shock tests, the latter being done on a Mechanical Impact Pyro Simulator now in use at General Electric. In addition information is presented detailing successful testing of another component with the General Electric shock facility and resultant responses are compared with another shock-generating assembly that critically damaged the unit. Correlation between analysis and test data is good, validating the modeling and analysis techniques.

INTRODUCTION

This paper presents details relating to the design and subsequent vibration and shock tests of a spacecraft component for a severe vibration and shock environment. The design process and analysis method involves the use of finite element analysis coupled with the Modal Strain Energy method with Risk Graphs to determine the adequacy of the design. The vibration levels experienced by box parts are reduced by the application of passive constrained layer viscoelastic damping treatments that significantly improve component reliability. All significant internal components were fully instrumented in both the random vibration and shock tests, the latter being done on a Mechanical Impact Pyro Simulator now in use at General Electric. In addition information is presented detailing successful testing of another component with the General Electric shock facility and resultant responses are compared with another shock-generating assembly that critically damaged the unit. Correlation between analysis and test data is good, validating the modeling and analysis techniques.

DISCUSSION

The black box discussed (thought to be a typical black for Aerospace applications) consists of multiple mechanical and electrical components coupled with numerous Printed Wire Boards (PWBs) supported within a rigid container. The PWBs generally contain the most vibration sensitive parts (such as relays) and hence are candidates for vibration attenuation efforts. The PWBs are structurally tied to the box by guide rails, multi-pin electrical connectors and support brackets. PWB weights are generally under 2 pounds, and board surface areas are under 80 square inches.

A significant number of spacecraft and component anomalies have been attributed to the launch vibration environment (Figure 1). In addition vibration is a major cause of failures occurring during ground environmental testing of spacecraft, components, and subsystems. This trend is coupled with increasingly severe vibration and acoustic environments as shown by Figures 2 and 3 and corresponding increases in failures with higher vibro-acoustic levels.

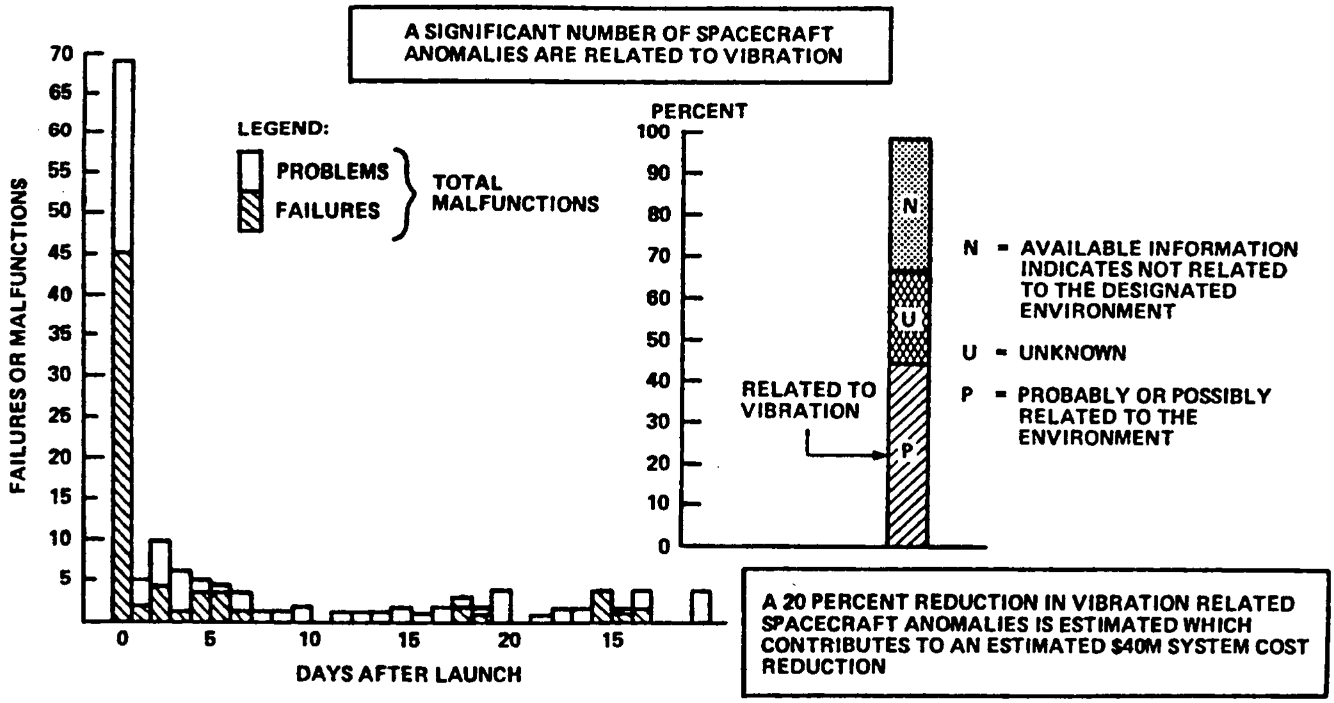

A SIGNIFICANT NUMBER OF SPACECRAFT ANOMALIES ARE RELATED TO VIBRATION

A 20 PERCENT REDUCTION IN VIBRATION RELATED SPACECRAFT ANOMALIES IS ESTIMATED WHICH CONTRIBUTES TO AN ESTIMATED $40M SYSTEM COST REDUCTION

Figure 1 Summary of Early Satellite Anomalies

Integration of passive viscoelastic damping treatments into the design of spacecraft component mounting structures (including PWBs) significantly improves spacecraft reliability and effectively reduces the trend of increased vibration severity. An additional benefit is increased damping in orbit which reduces response to onboard disturbances. Constrained Layer Damping Assemblies (CLDAs) are typically applied in strips running lengthwise across the board with a Viscoelastic Material (VEM) sandwiched between a stiff constraining layer and the

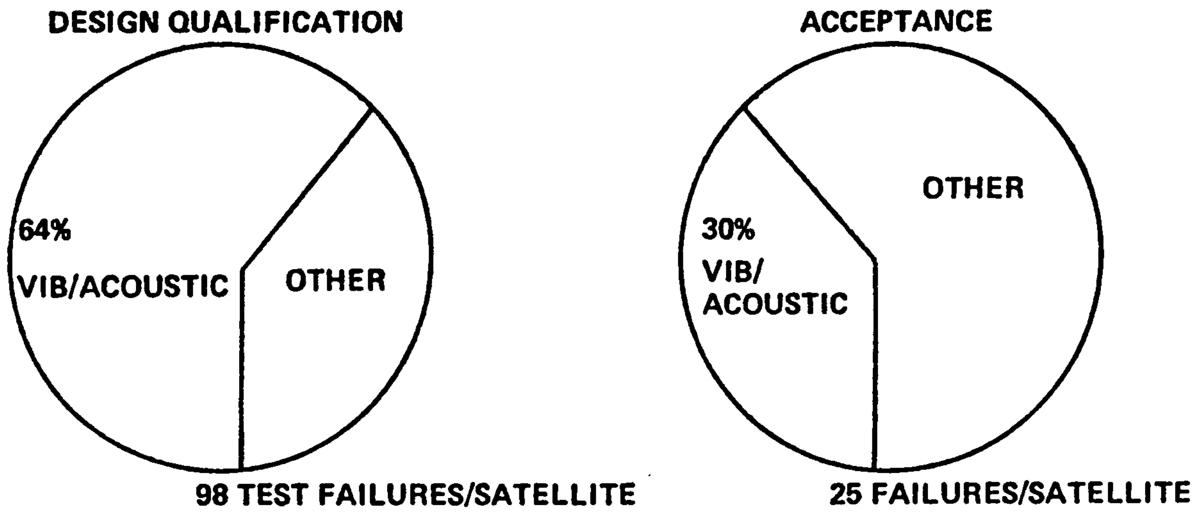

REF: OCT 82 AEROSPACE TESTING SEMINAR

A 50% REDUCTION IN VIB/ACOUSTIC GROUND TEST FAILURES IS ESTIMATED

Figure 2 Summary of Vibroacoustic Test Failures

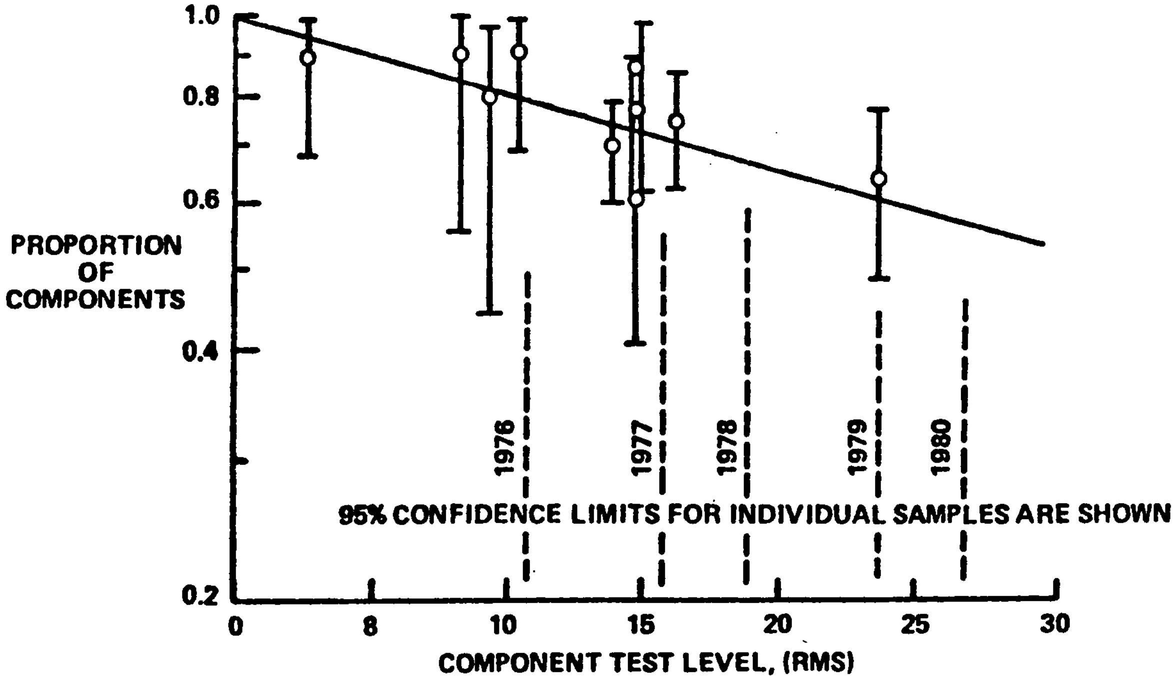

ABOUT 40% OF COMPONENT DESIGNS REQUIRE CHANGES

Figure 3 Components Passing Vibration Tests board surface. The CLDA is placed to maximize the strain energy in the VEM, although this is not always possible due to PWB component mounting. All PWBs within the box have CLDAs, as well as several other critical box surfaces. A typical PWB with CLDA is shown in Figure 4.

To determine the dynamic adequacy of the PWB designs, Finite Element Models (FEMs) of the integrally damped PWBs are constructed (see Figure 5) in which the viscoelastic material is represented by finite element solid elements and the base and upper constraining layer with shell elements with offsets. A standard modal extraction run is executed and the Modal Strain Energy Method used to determine the modal and damping characteristics of the boards. This method is based on the principle that the ratio of composite structural loss factor to viscoelastic material loss factor for a given mode of vibration can be estimated as the ratio of elastic strain energy in the viscoelastic material to the total elastic strain energy in the entire structure when it deforms into the particular undamped mode shape. This ratio multiplied by the viscoelastic material loss factor yields the modal loss factor.

The analysis results are used to determine the dynamic adequacy and effectiveness using a Risk Graph (Figure 6), a system that produces a design classification as a function of fundamental frequency, damping, board characteristics, and the random vibration environment. Basically, for a given random vibration environment, regions of variable amounts of design risks are generated that are based on both experience and analysis considering maximum deflection lines. Approximate response of a single degree of freedom oscillator to an acceleration Power Spectral Density (PSD) which is constant at all frequencies is calculated and used as a basis upon which to classify the design effectiveness. A second criteria used in a Risk Graph is the acceleration, since the Grms response is an indication of the overall severity of the environment that the piece-parts (diodes, crystals, resistors, relays) must endure. A 30 Grms response is recommended as a design goal for all boards although 50 Grms designs have been employed in cases where the boards do not have vibration-sensitive items (such as relays) in the most severe vibration axis and where spacing and other parameters limit damper applications. The final boundary is based on the amount of structural damping predicted by an analysis method, currently the MSE approach. This method has been employed effectively and successfully in numerous General Electric spacecraft and development programs.

The box successfully passed a fully instrumented vibration test with no vibration-related anomalies. The random vibration testing employed standard electrodynamic shakers and the shock testing was done on a Mechanical Impulse Pyro Simulator (MIPS) in limited use throughout the industry. Figure 7 illustrates the MIPS test setup used for component shock testing at General Electric.

The box was tested to random vibration levels of 18 Grms in one axis and approximately 13 Grms in the remaining two axes with no vibration-related anomalies related to the vibration testing validating both the passive damping treatment and the analysis method. All boards within the box as well as various other critical locations both in and on the container were instrumented with microminiature accelerometers during the test, and data from these accelerometers are summarized in Table 1. The accelerometers were located in the area of the maximum response. Measured Composite Loss Factors were obtained using circle fits to the high level random response data and are on the order of 0.25 for all boards except one. The fundamental board resonances are in the 130 to 250 Hz range and did not couple with the container resonance which is above 400 Hz. It is clear that the passive damping treatment, which is introduced with a minimum weight impact to the component, provides an effective method of reducing the board response to the vibro-acoustic energy and hence greatly reduces the chances of vibro-acoustic related failures. In addition because of the excellent correlation

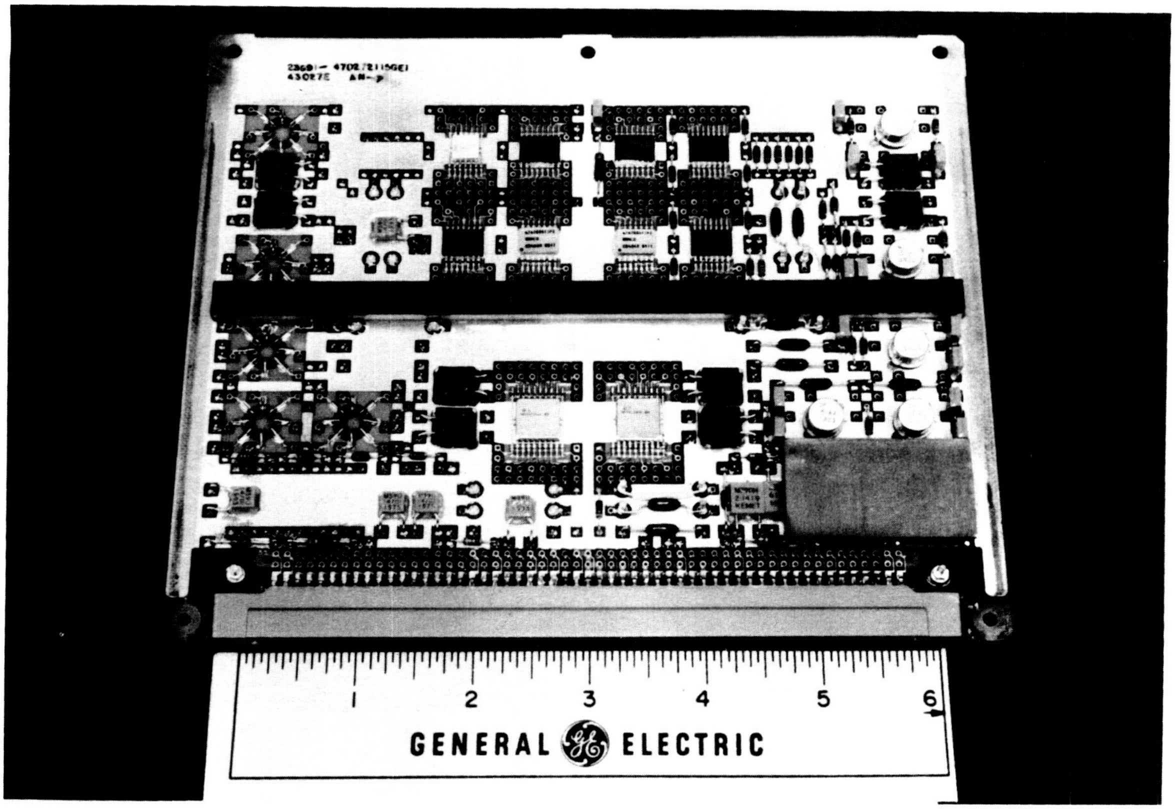

Figure 4 Typical Damped PWB with Damper shown on Board Center

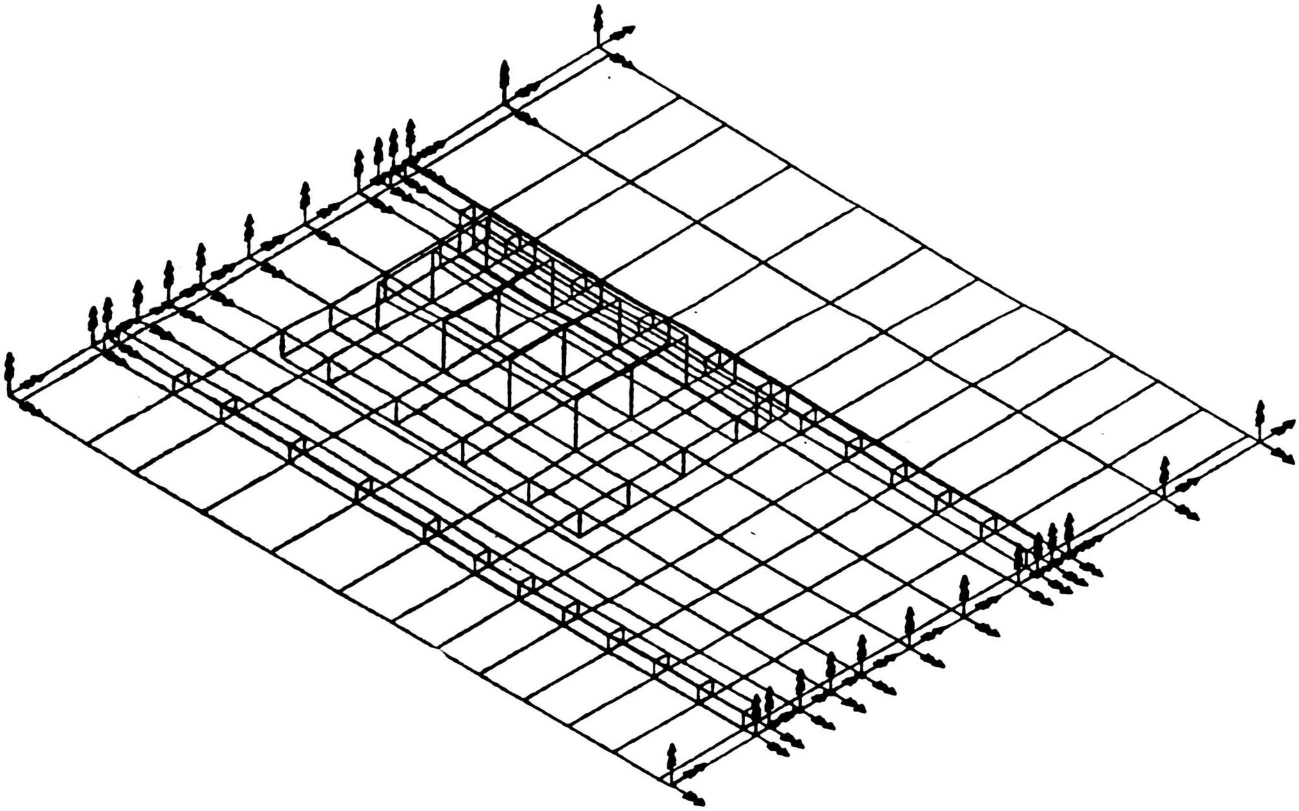

Figure 5 Typical PWB FEM with Tantelum Shield Representation

ORIGINAL PAGE IS
OF POOR QUALITY

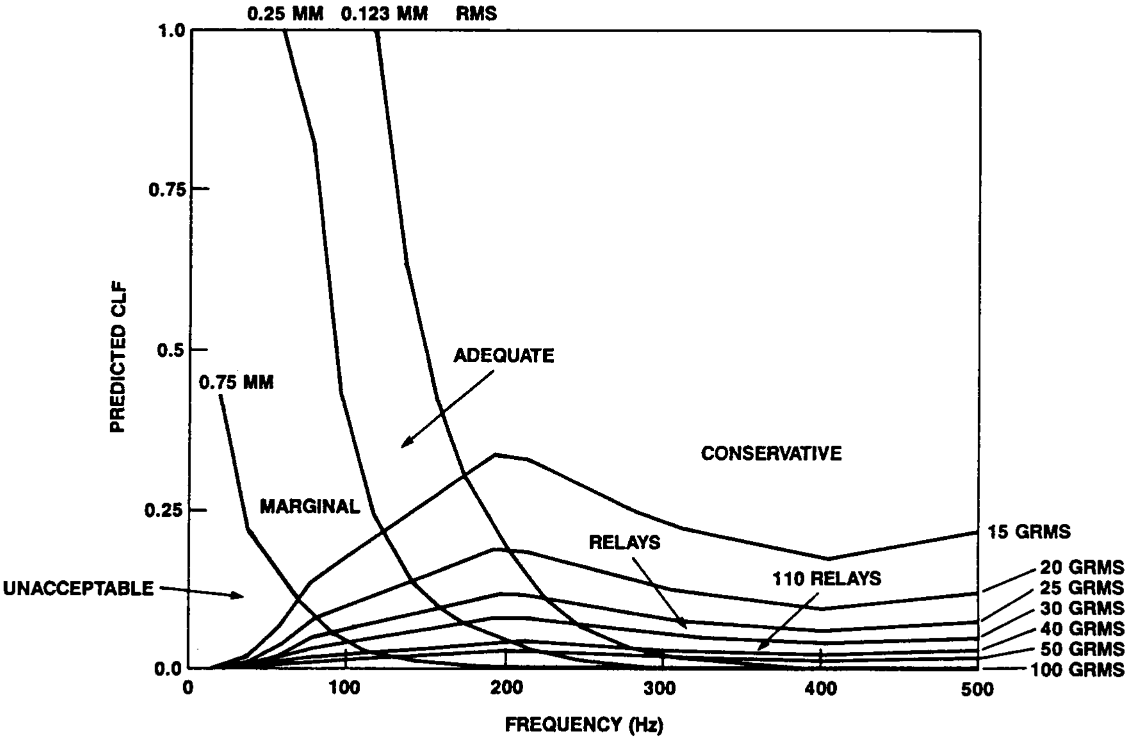

Figure 6 Risk Graph used to Classify Design Adequacy

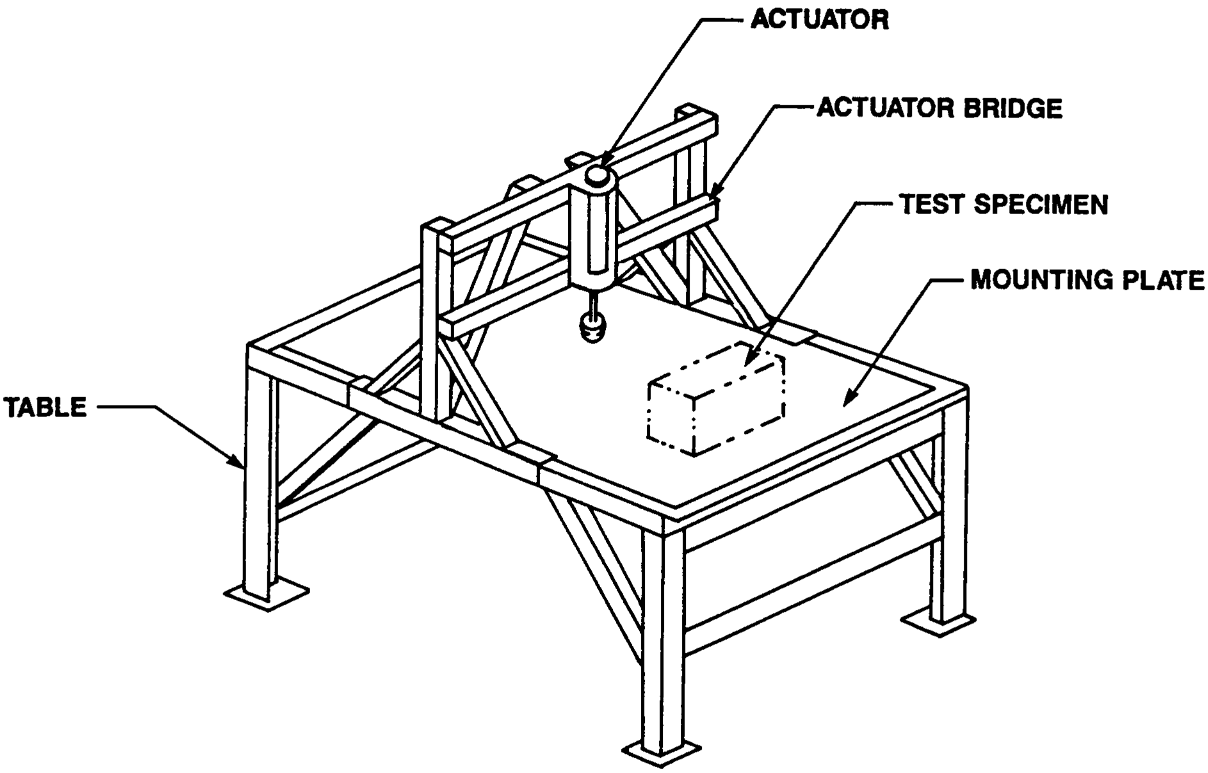

Figure 7 GE MIPS Facility

Table 1 Comparison between Vibration Test and Analysis Results

PWB	TEST F_1	TEST η_1	TEST GRMS	ANALYSIS F_1	ANALYSIS η_1	F_1 $\frac{\text{ANALYSIS}}{\text{TEST}}$	η_1 $\frac{\text{ANALYSIS}}{\text{TEST}}$	RISK GRAPH CLASSIFICATION	
								TEST	ANALYSIS
5	189	.37	31.4	156	.31	.83	.84	CONSERVATIVE	ADEQUATE
6	178	.31	33.5	187	.32	1.05	1.03	CONSERVATIVE	CONSERVATIVE
7	202	.22	33.6	147	.22	.73	1.00	CONSERVATIVE	ADEQUATE
8	144	.25	28.6	153	.34	1.06	1.36	ADEQUATE	ADEQUATE
9	226	.23	35.6	229	.20	1.01	.87	CONSERVATIVE	CONSERVATIVE
10	243	.24	37.1	290	.19	1.19	.79	CONSERVATIVE	CONSERVATIVE
12	173	.13	27.4	147	.20	.85	1.54	ADEQUATE	ADEQUATE
13	127	.26	20.2	123	.21	.97	.81	ADEQUATE	ADEQUATE

between test results and analysis predictions, the MSE approach is a reliable method of predicting PWB performance in what is thought to be a typical vibration environment. Responses in this box are thought to be typical for similar applications throughout the industry and can be scaled for other random environments by analysts wanting to determine PWB response characteristics for their application.

The peak Shock Response Spectrum (SRS) that the box was exposed to was approximately 12000 g and represents the input at the interface with the table mounting surface. The data summarized in Table 2 provides a definition of the environment within the box resulting from the MIPS simulation of the pyrotechnic environment. It indicates relatively high SRS levels for parts mounted directly to the PWBs - on the order of 1000 to 2000 g. The PWBs do provide a significant attenuation of the MIPS plate environment (2000 g or less for the 12000 g input) and the component structural environment as measured by wall response (3000 to 7000 g). This attenuation is expected in view of the relatively low resonant frequencies of the PWBs. The PWB having the lowest resonant frequency is PWB 13 while PWB 10 has the highest resonant frequency. As one would expect, the PWB 13 SRS is significantly less than PWB 10 SRS. Again responses in this box are thought to be typical for similar applications throughout the industry and can be scaled for other shock environments by analysts wanting to determine PWB response characteristics for their application.

Another example of a MIPS component illustrated in Figure 8 which sustained catastrophic internal damage and mounting feet deformation during prior pyro shock testing of the unit at another facility. That facility (Figure 9) is quite different that the MIPS facility thus affecting the path taken by the shock wave from the impact point to the unit. In addition in the previous test the flight unit itself was used during system calibration with some 67 hits made during the calibration resulting in probable unit over-testing. To resolve the question of whether the component failures resulted from being over-tested/over-exposed or whether the design was susceptible to normal-axis shock, another unit was tested at the General Electric MIPS facility.

The unit was exposed to an approximate SRS peak input of 5000 g in both tests. However, upon examination of the test data presented in Table 3, it is clear that the component responses were grossly different between the two test methods. For an approximate normal axis input of 3300 g, responses at the top of

Table 2 Summary of Shock Response Spectra Maximum Values and Frequency

PWB	DESCRIPTION	RUN 16 (Y-X)		RUN 17 (Y-X)		RUN 20 (Y-Z)		RUN 22 (Y-Z)	
		PEAK SRS (G)	FREQ (Hz)	PEAK SRS (G)	FREQ (Hz)	PEAK SRS (G)	FREQ (Hz)	PEAK SRS (G)	FREQ (Hz)
	INPUT-X	12930	5079	12623	5079	1706	8063	1808	9050
	INPUT-Y	6083*	8063	6131*	8063	6314*	2850	6280*	3200
	INPUT-Z	1694	4525	1902	8063	10629	5701	10560	5701
	PLATE CORNER (X)	3406	5701	3363	5701	4728	5701	4623	5701
	PLATE CORNER (Y)	5921	5079	5761	4525	5522	6400	5524	5701
	PLATE CORNER (Z)	4341	3200	4179	6400	3147	5701	3289	5701
5	PWB	873	1131	928	1131	393	5079	458	5079
6	PWB	3771*	4031					557	5701
7	PWB					763	897	650	4031
8	PWB	1086	1131	1280	1131	1207*	3591	1371	3591
9	PWB	1514	1600	1654	1269	938	3200	1043	6400
10	PWB	980	1795	1248	800	1771	10159	1869	10159
11	PWB								
12	PWB	1174	5701	856	2539	1918	4031	2007	5079
13	PWB	427	448	650	503	532	2015	1096	1600

*REFERENCE SHIFT IN SIGNAL

the component for the MIPS test were on the order of 2500 g, whereas responses with the Impact Facility illustrated by Figure 9 were some 12000 g. It is obvious that the unit as tested on the MIPS assembly experienced grossly lower response levels than experienced on the other test apparatus. The primary differences are due to the path the energy takes before reaching the component and a 2000 Hz component resonance that was magnified by a system resonance with the Impact Facility in the same frequency band. It is concluded that the MIPS set-up is a better representation of the actual environment that the unit will experience in flight application and imposes far less structural risk due to the test assembly than the Impact Facility.

CONCLUSIONS

Details have been presented relating to the design and subsequent vibration and shock tests of a spacecraft black box for a severe vibration and shock environment. The design process and analysis method involves the use of FEM coupled with the MSE method with Risk Graphs to determine the adequacy of the design. The vibration levels experienced by box components are reduced by the application of CLDAs which significantly improve component reliability. All significant internal components were fully instrumented in both the random and shock vibration tests, the latter being done on a MIPS now in use at General Electric. In addition information is presented detailing successful testing of another component with the General Electric shock facility and resultant responses are compared with another shock-generating assembly that critically damage the

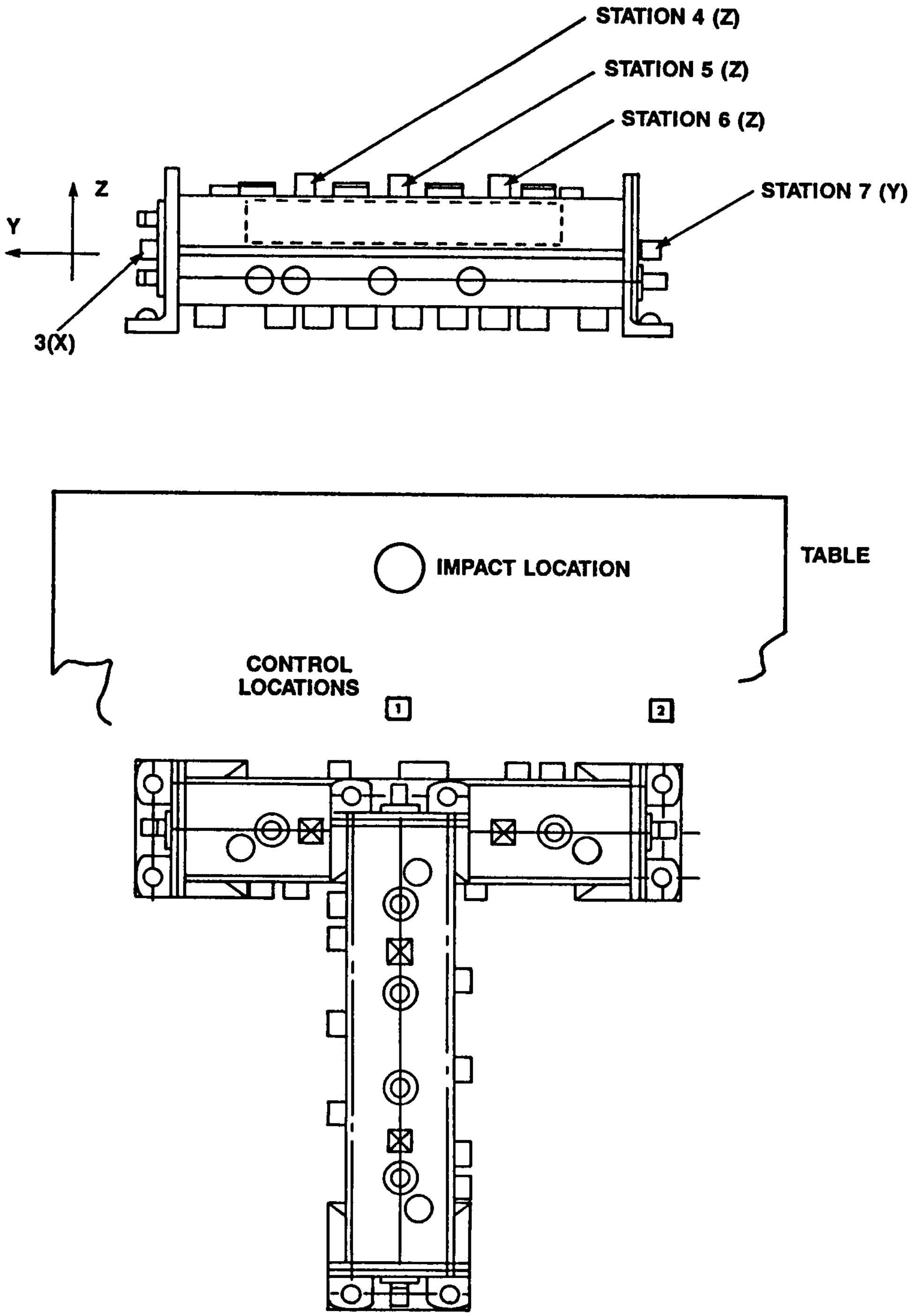

Figure 8 Component Tested on General Electric MIPS Facility

unit. It is sufficient to say that for approximately the same input to the unit, any component response and damage potential is significantly reduced with a MIPS shock test assembly. Responses documented for this vibration environment are thought to be typical for similar applications throughout the industry and can be scaled for other vibration environments by analysts wanting to determine PWB characteristics for their application.

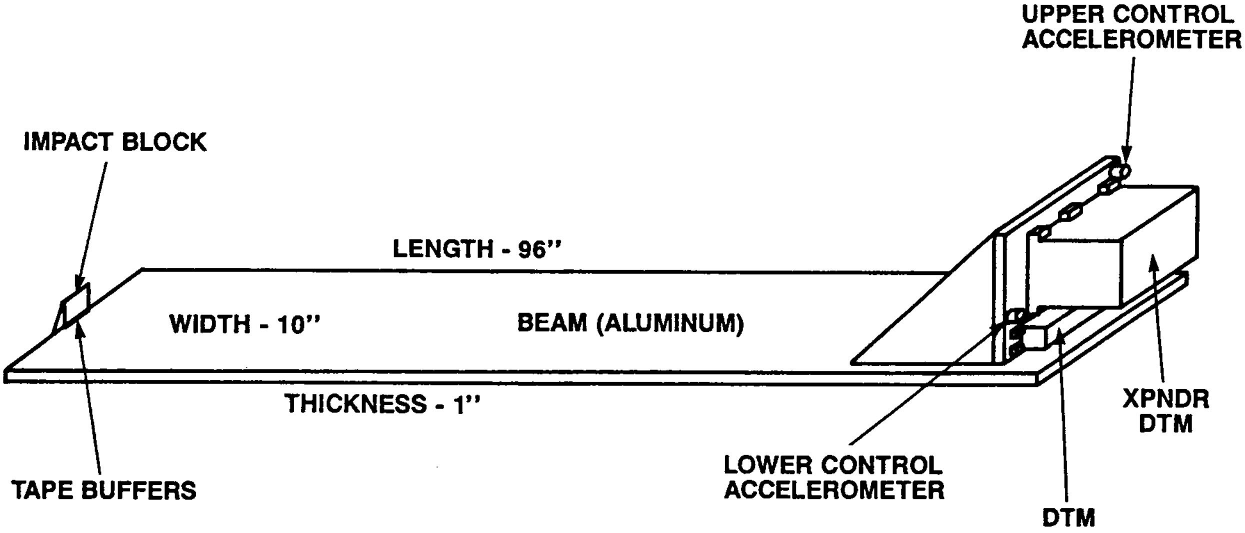

Figure 9 Test Assembly that Damaged Component

Table 3 Time History Summary

RUN #6 YZ

DESCRIPTION	STATION	MIPS TIME HISTORY PEAK G'S O-P	IMPACT TIME HISTORY PEAK G'S O-P
CONTROL	1X	800	--
CONTROL	1Y	4900	--
CONTROL	1Z	3400	3363
CONTROL	2Z	1900	--
SIDE NEAR J1/J2	3X	500	--
TOP END	4Z	3400	(5443)*
TOP CENTER	5Z	3300	11954
TOP END	6Z	2900	(5443)*
SIDE NEAR J3	7Y	1800	--

RUN #7 XZ

DESCRIPTION	STATION	MIPS TIME HISTORY PEAK G'S O-P	IMPACT TIME HISTORY PEAK G'S O-P
CONTROL	1X	3400	--
CONTROL	1Y	800	--
CONTROL	1Z	3200	3363
CONTROL	2Z	1700	--
SIDE NEAR J1/J2	3X	1100	--
TOP END	4Z	2900	(5443)*
TOP CENTER	5Z	2500	11954
TOP END	6Z	2300	(5443)*
SIDE NEAR J3	7Y	850	--

*MEASURED IN Z DIRECTION ON THE SIDE OF UNIT

Vibration Testing of Aft Deckhouse Structure of USNS OBSERVATION ISLAND (T-AGM-23)

Jeffrey M. Komrower
Douglas S. Wright
M. Pakstys

Abstract

This paper deals with vibration measurements on a large ship deckhouse structure. The structure had been modified to be able to accommodate the added mass of a large radar dish. The test was performed in order to investigate a possible resonant condition during dish operation after excessive vibration levels were reported by the ship's crew. The modal test revealed the lowest structural mode of the deckhouse to be well above the maximum blade rate frequency. It was also determined that forced vibrations of the deckhouse did occur during radar dish rotation, but no evidence of a resonance condition was apparent. Excessive vibrations felt by the ship's crew were a result of a nonstandard mode of dish operation that occurred when the dish was allowed to hit the stops at the end of its rotation.

Introduction

This paper summarizes the results of a modal test and analysis that was performed on the aft deckhouse structure of a naval ship. The vessel was initially built as a "Mariner" class merchant ship and was later converted for naval use. The ship (Figure 1) is 564 feet long and displaces approximately 19,000 tons. Modifications to the aft deckhouse structure were performed to enable the structure to support a large radar dish (not shown). The deckhouse is shown in Figure 2. During radar dish operation, ship's personnel noticed excessive vibration levels in the deckhouse. This caused concern regarding the effect of the large added mass of the radar system on the deckhouse structure during underway conditions as well as vibration of the deckhouse caused by dish rotation.

The dynamic characteristics of the deckhouse were determined by modal testing to investigate the possible excitation of a deckhouse natural mode of vibration during radar dish operation. Vibration data was also taken while the ship was underway to determine if a natural vibrational mode of the deckhouse/radar dish structure could possibly be excited during normal ship operating conditions.

The aft deckhouse is a large structure that is approximately 54 feet wide by 55 feet deep and extends five levels above the ship's deck. The structure is tied into the hull by large I-beams and has also been reinforced by additional I-beams in the vertical and athwartship direction. The radar dish is also a very large structure with a dish diameter of 30 feet. The total weight of the dish and supporting base structure is approximately 100 tons and its height is the equivalent of about four deck levels. A review of the deckhouse modification plans revealed that the structure was not as heavily reinforced in

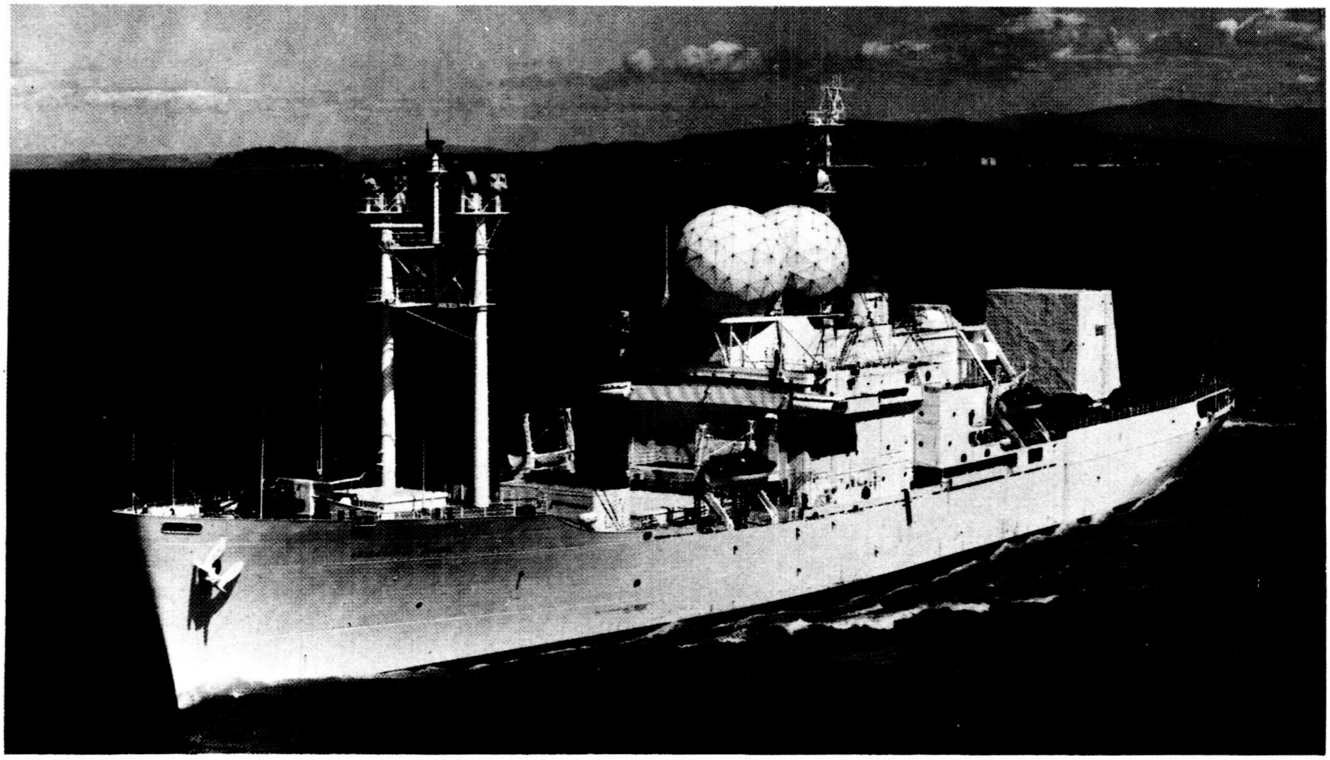

Figure 1. USNS OBSERVATION ISLAND (T-AGM-23)

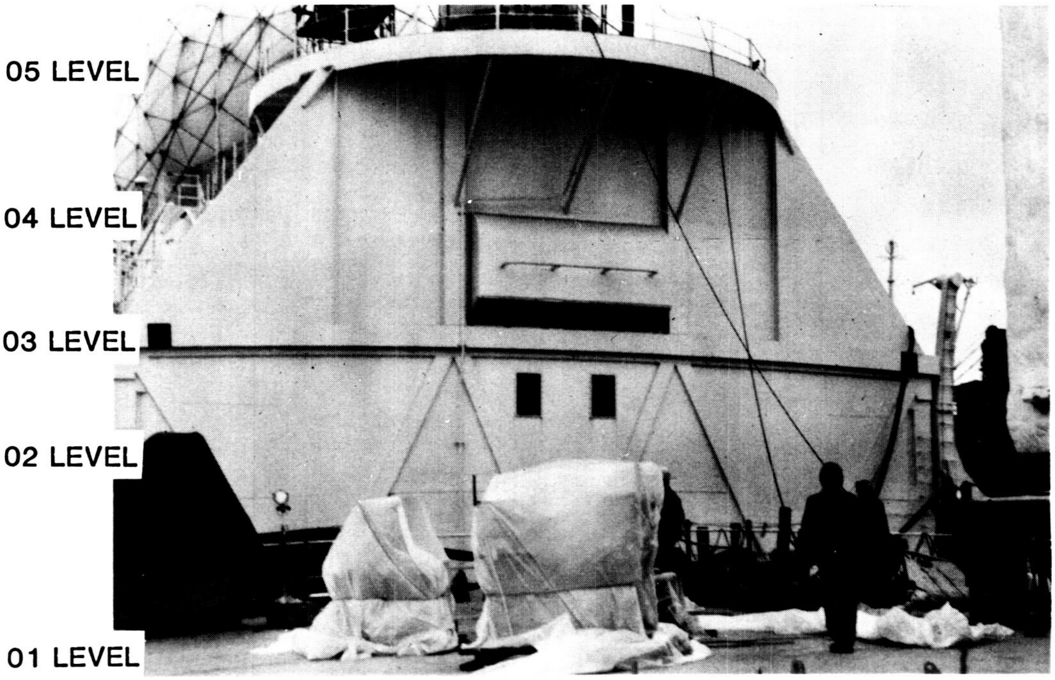

Figure 2. Deckhouse of Ship (looking forward)

the fore/aft direction as in the other two directions. During radar dish rotation, it was believed that the large rotary inertia generated by dish rotation was causing a torsional motion of the deckhouse.

Testing Approach and Procedures

Testing of the aft deckhouse structure was performed in two stages. First a modal survey was performed while the ship was at dockside and then vibration data was taken during transit from Seattle to Honolulu, Hawaii. Once the ship reached port in Honolulu, some additional vibration data was taken during rotation of the radar dish.

A stationary force and roving accelerometer technique was used to acquire modal test data. Prior to the full modal survey of the deckhouse structure, a preliminary survey was performed using an instrumented hammer. The response from this survey provided general information on the dynamic characteristics of the structure. This information, along with logistical considerations, was used to determine suitable locations for the attachment of the inertial mass exciter head (shaker) to assure data quality and adequate excitation in the subsequent full modal survey. The hammer used was a PCB 12-pound sledge. A load cell in the hammer tip and a magnetically applied triaxial accelerometer were connected to constant current power supplies. The signals from the power supplies were then wired into a Zonic Structural Analysis system which processed the data through anti-aliasing filters, analogue-to-digital (A/D) converters and a Fast Fourier Transform (FFT) analyzer.

Burst random excitation was used to acquire data for the full modal survey. Excitation was applied to the structure using a Zonic X-CITE hydraulic exciter system. The test setup is shown schematically in Figure 3. The exciter head was bolted to an adapter plate that was welded to the deckhouse structure.

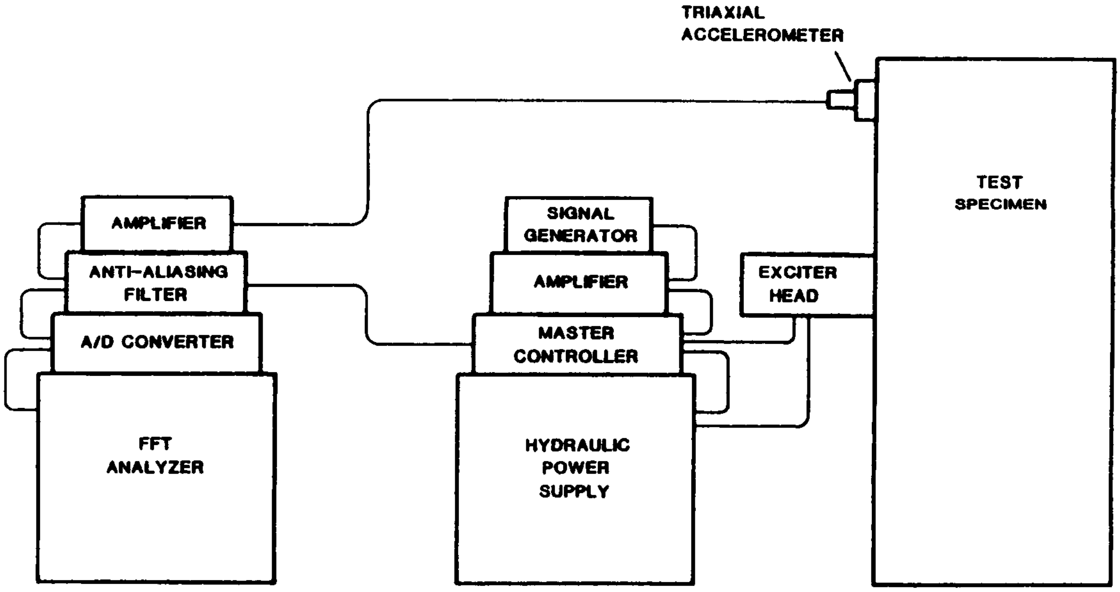

Figure 3. Test Setup for Shaker Excitation

The shaker attachment point is shown in Figure 4. A load cell in the exciter head was connected to the X-CITE system master controller whose output was input to the structural analyzer. A feedback control loop in the master controller allows accurate control of the input force levels and assures that constant force levels can be maintained throughout the data acquisition. The exciter head is hydraulically driven and is capable of inputting forces of up to 1,000 pounds up to 250 Hz. Burst random excitation was used in which a pulse of random noise in a specified frequency range was applied to the structure. The response to the excitation, as in the preliminary survey, was measured using a high sensitivity triaxial accelerometer on a magnetically mounted block. For each measurement point the responses from 20 shaker bursts were averaged.

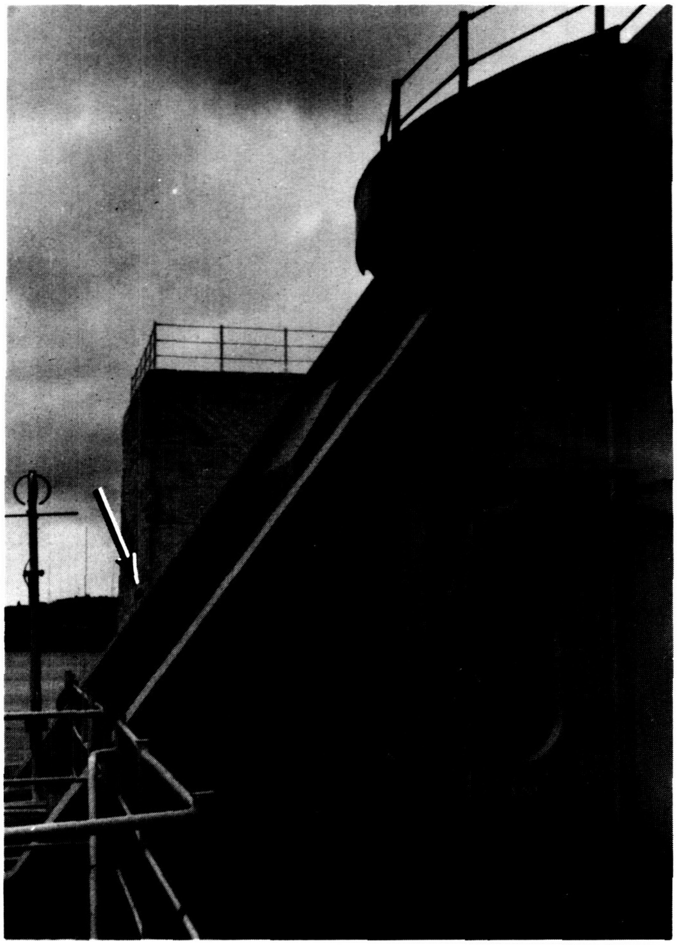

Figure 4. Shaker Attachment Point on 03 Level (looking aft)

To ensure that all modes of interest were excited, two surveys were performed: one using fore/aft excitation and the other using excitation in the vertical direction. A total of 98 measurement locations were taken for each survey.

ORIGINAL PAGE IS
OF POOR QUALITY

Modal Test Results

A total of five modes of vibration were extracted up to 50 Hz. Mode 1 at 21.6 Hz was primarily a vertical mode with all decks of the deckhouse in phase. There was a slight athwartship motion with all decks in phase and the radar dish ring out of phase. This mode shape is shown in Figure 5.

Mode 2 had a frequency of 28.3 Hz and was the first torsional mode about the Z-direction with a slightly coupled vertical motion. This mode shape is shown in Figure 6.

Mode 3 at 30.3 Hz was primarily a vertical motion of the 03 and 04 deck levels and the radar dish ring coupled with slight athwartship motion.

Mode 4 had a frequency of 39.5 Hz and was a torsional mode of the deckhouse with second order bending of the aft bulkhead of the deckhouse. There was very little motion of the forward end of the deckhouse structure.

Mode 5 with a frequency of 47.4 Hz was a vertical mode of the 03 through 06 levels that was coupled with a slight torsional motion.

Conclusions

The results of the modal test revealed natural frequencies that were higher than expected. The lowest natural mode of vibration at 21.6 Hz showed that the deckhouse was a fairly stiff structure. Measurements taken during rotation of the radar dish as well as during underway conditions showed no evidence of a resonance problem. The lowest deckhouse frequency was well above the first blade passing frequency as well as its first harmonic. Since this was the maximum ship speed, no resonance problems at lower ship speeds would be expected. Upon further investigation and first-hand observation of the vibration levels present during radar dish rotation, it was determined that significant forced vibrations did result during dish rotation, but that a resonance condition was not evident. The excessive vibration levels that were experienced by the ship's crew occurred during a mode of operation when the rotation of the dish was stopped suddenly by hitting the stops at the extreme range of its rotation. This is not a normal mode of operation, and it was determined that there was no cause for concern if normal rotation procedures were followed.

Initial plans called for a complete finite element analysis of the deckhouse structure and correlations with test data. Correlations were first to be made on the modal level. A transient analysis was then to be performed that made use of data measured at the base of the deckhouse during ship underway conditions as input. Correlations with measured responses at various places around the deckhouse were then to be performed. However, analysis of test results revealed that a resonance problem was not evident and hence the customer made a decision to terminate the analysis effort.

Acknowledgements

The authors would like to thank Mr. Art Fields of Advanced Marine Enterprises and Mr. Lou Lemos of the Military Sealift Command for their on-site support during the test.

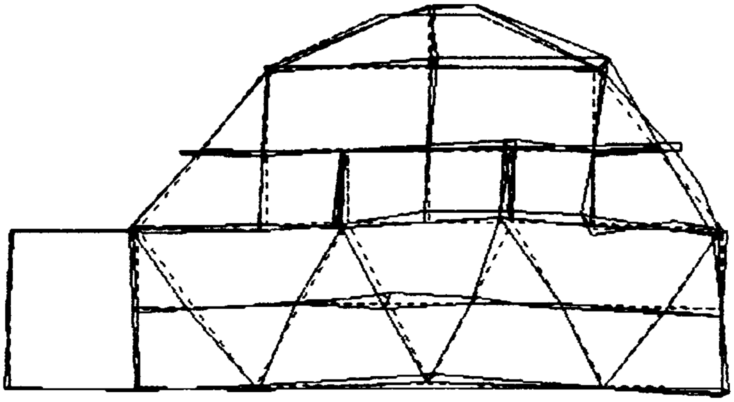

Figure 5. Mode Shape of First Mode and Vibration

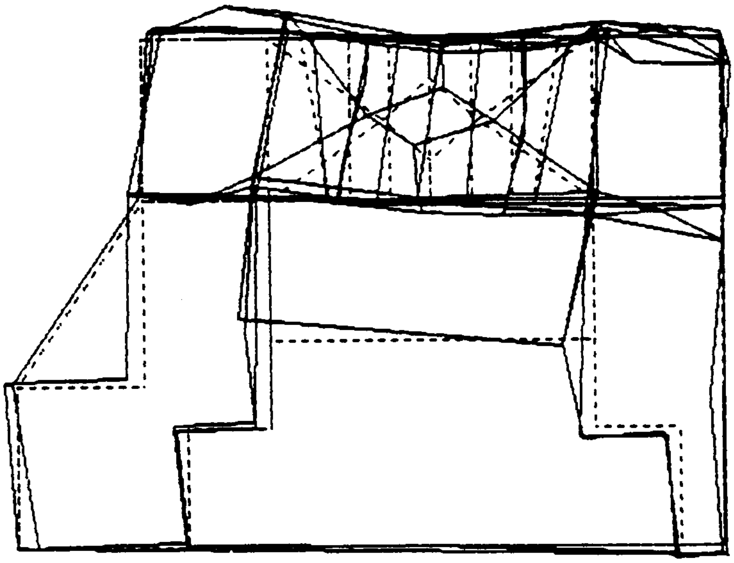

Figure 6. Mode Shape of Second Mode of Vibration

References

1. Ewins, D.J., Modal Testing: Theory and Practice, Research Studies Press Ltd., 1984.

N88-18953

Random Vibration (Stress Screening) of Printed Wiring Assemblies

Gilbert J. Bastien

This paper summarizes the results of a Random Vibration Stress Screening (RVSS) study on the determination of upper and lower vibration limits on Printed Wiring Assemblies (PWA). It is intended to serve as a guideline for engineers and designers who make decisions on PWA features to withstand the stresses of dynamic testing and screening. The maximum allowable PWA deflection, "G" levels, and PSD levels are compared to the expected or actual levels to determine if deleterious effects will occur.

INTRODUCTION

Analytical methods are developed to determine the maximum random vibration levels which will cause fatigue failure in the PWA components or in the bare board itself. The reversing stresses on the component leads is given special emphasis in the analysis. In the case of RVSS, the designer must attempt to determine the maximum vibration levels which can be exerted on the PWA in order to suface the maximum number of quality and workmanship defects without causing deleterious effects to the components or the board. Often RVSS levels are chosen as a default from a DOD guideline and the subsequent screen is either benign or overstressful. Thus it is useful to have design or test guidance on the upper vibration limits for the PWA. The lower limit for RVSS is needed to determine if there will be sufficient force in the RVSS to surface a sufficient number of available workmanship or quality defects in the PWA.

Random vibration is basically a gaussian distribution of reversing force vectors and as such, it is necessary to make some simplifying assumptions in the development of the algorythms presented here. The simplifications are reasonable first estimates; however, they should be considered estimates and subject to test verification. Only classical cases were analyzed since there is an extremely large number of possible configurations and variations of PWA's and component mix. The components which were analyzed are dual-in-line micro electronic devices (IC's), capacitors, resistors, and leadless chip carriers (LCC's).

TYPICAL RVSS PLAN

The plans shown in Figures 1(a) - 1(c) indicate the basic process steps and the relative reliability ($\bar{R}$) of the process. The indicated reliability is only used to illustrate the relative degree of improvement and not a measured value. Plan 1(a) shows only a one pass RVSS and a test with a repair process. A repaired PWA is not re-screened. Process 1(b) allows for re-screening to filter out any defective component or workmanship flaws. Process 1(c) basically is the same as 1b except that a small PWA test is added during RVSS to detect any intermittents which may occur with vibration.

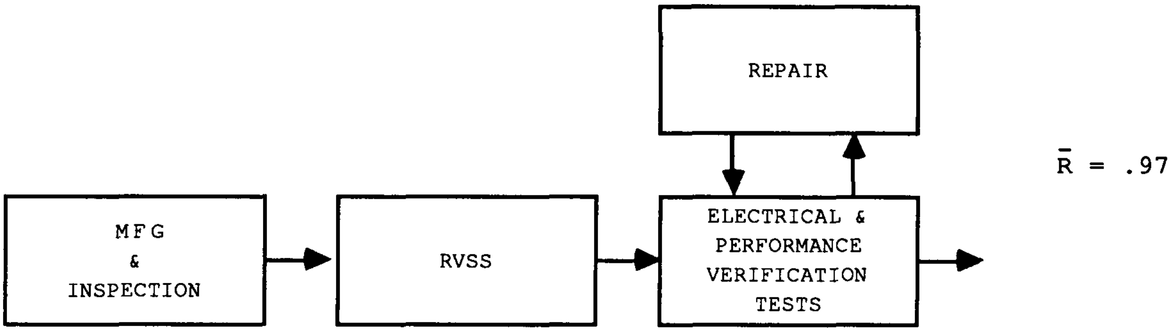

FIGURE 1(a). BASIC RVSS PLAN, STANDARD QUALITY LEVEL

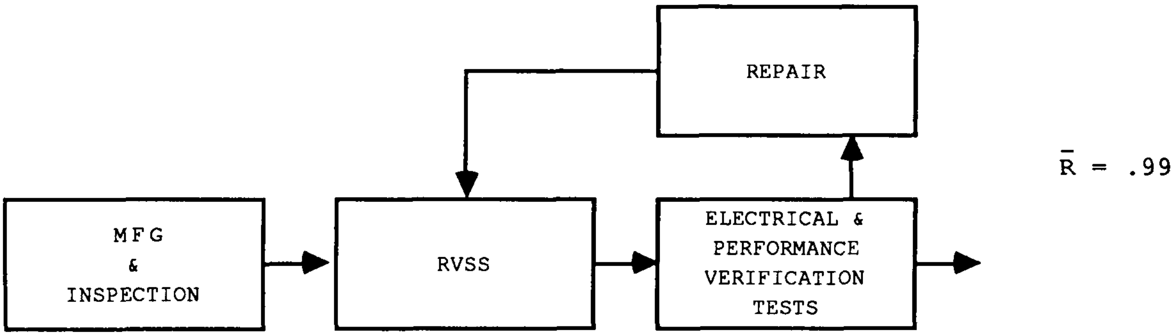

FIGURE 1(b). BASIC RVSS PLAN, HIGH QUALITY LEVEL

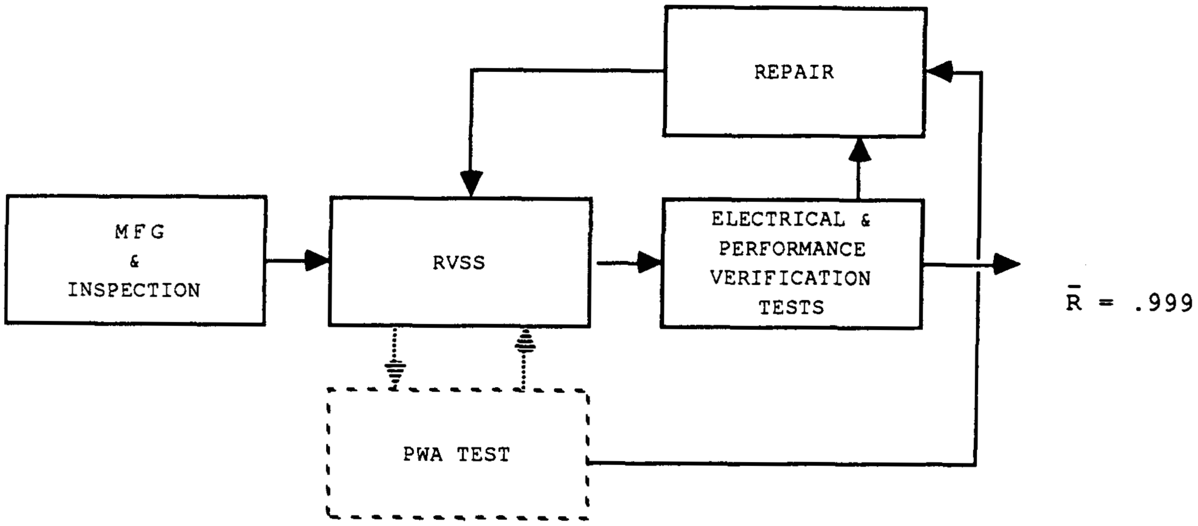

USED WITH POWER-ON TESTS
AND FOR DIAGNOSTICS

FIGURE 1(c). BASIC RVSS PLAN, VERY HIGH QUALITY LEVEL.

RELATIVE VALUE OF PWA STRESS SCREENING WITH PRE- AND POST-TESTS

Stress screening in general may be categorized in its effectiveness by the illustration in Figure 2. Although the actual numbers may vary from vendor to vendor, there is sufficient data in the field to roughly quantify the relative effectiveness of screening and testing operations. However, the values vary from contractor to contractor. Figure 2 shows that a good pre-screen visual and functional test may surface even more defects than any of the screens. Without the random vibration stress screen, approximately 16% of the defects on a PWA may pass the factory undetected. These ratios vary with each contractor.

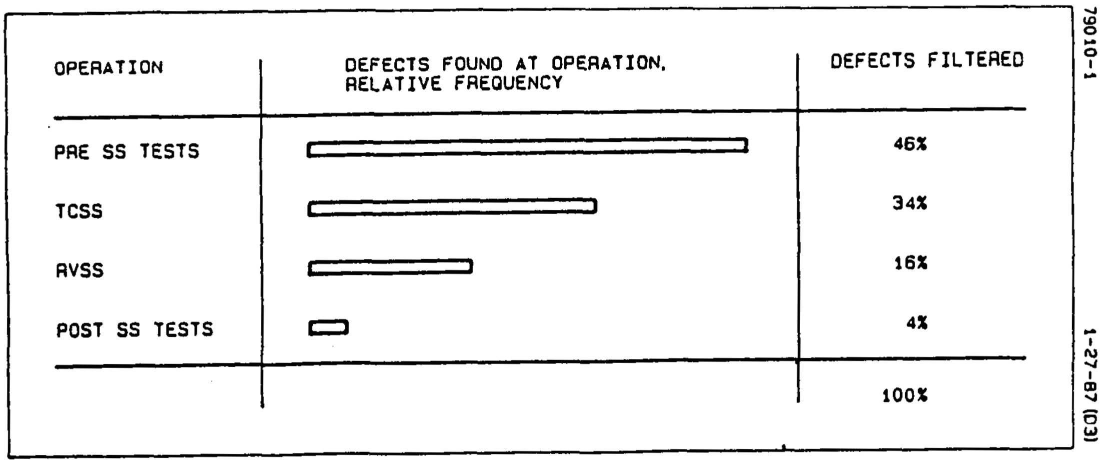

OPERATION	DEFECTS FOUND AT OPERATION, RELATIVE FREQUENCY	DEFECTS FILTERED
PRE SS TESTS		46%
TCSS		34%
RVSS		16%
POST SS TESTS		4%
		100%

FIGURE 2. RELATIVE EFFECTIVENESS OF PWA STRESS SCREEN AND TEST OPERATIONS

RVSS WINDOW AND EXPECTED FALLOUT

The operating stress screen range or window is shown in Figure 3. The objective of a RVSS development program is to determine the upper and lower threshold and produce the optimum level within the window. The upper level may be determined by trial and error or by a combination of analysis and testing. The later approach is preferred since it gives insight to the physical constraints of the PWB, components, and materials involved. The RVSS levels may be obtained by trial and error i.e., determination of the level which produces minimal fallout and the level which causes deleterious effects. The question will inevitably arise, however, "How much higher can we go without over stressing?"

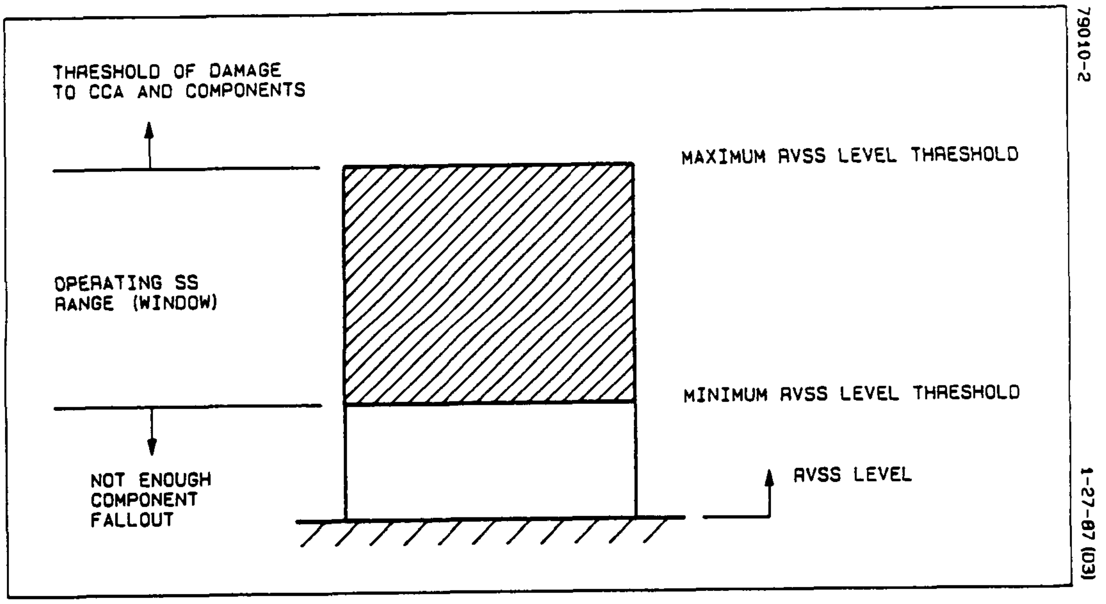

Figure 3 RVSS WINDOW

PWA RVSS INPUT PROFILES AND DYNAMIC CHARACTERISTICS

The input profile of a RVSS is extremely important to the response of the PWA. The response R(f) is proportioned to the transfer function H(f) of the structure multiplied by the input function I(f), as seen in Equation 1.

$$R(f) = |H(f)| \, I(f) \quad (1)$$

The transfer function H(f) includes all structures between the forcing function (the shaker table) and the unit under test (UUT). This may include a vibration fixture and PWA holder box. Thus, the response on the PWA may include its own dynamic properties plus all the other supporting structure properties. The nature of the random vibration is that it will produce all frequencies in the spectrum range simultaneously, which will stimulate all parts into resonance which have resonances in the input spectrum range. The input level (amplitude) will only further amplify the motion. A high input level at low frequency resonances may cause excessive bending damage to certain parts, such as the PWB or particular microelectronic devices.

Figure 4(a) shows the NAVMAT profile, which rolls off at the low and high end of a 2000 Hz spectrum. The roll off at the low end helps to diminish the bending stresses on the PWA. The roll off at the high end reduces the high response of small high natural frequency components. The center area between 80 and 350 Hz is the main area of excitation. Most PWA's have natural frequencies in this range. Certain PWA defects, however, may be surfaced with more stimulation at the low frequencies. A profile such as that shown in Figure 4(b) may be used if it does not cause damage to the PWA. If the overall level of .04 is too high and some design damage results, then the overall level may be dropped. There is some evidence that this profile may be a more effective screen at a lower Grms level than the NAVMAT profile.

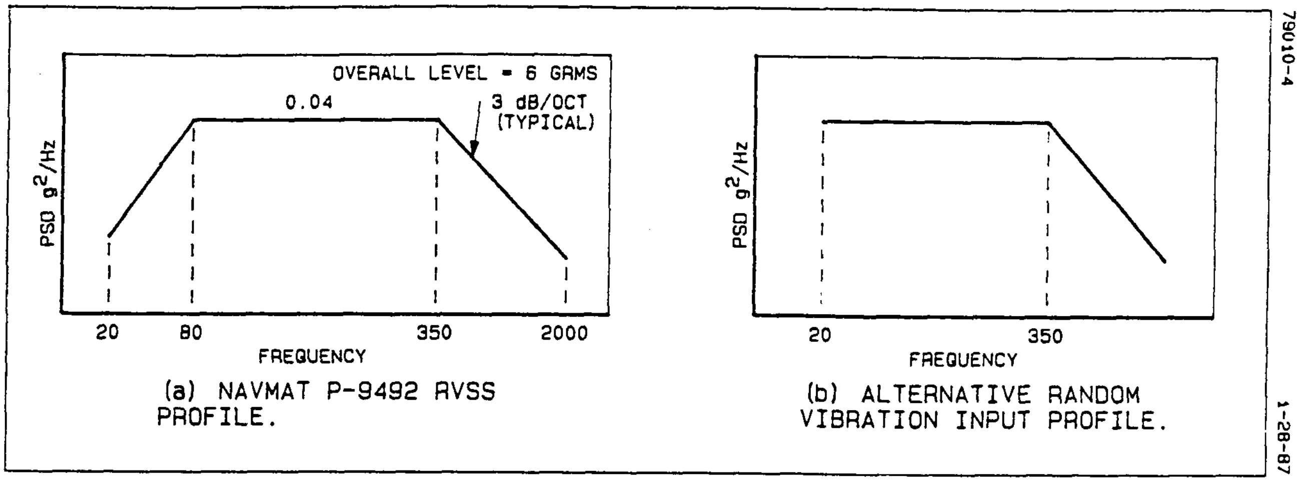

(a) NAVMAT P-9492 AVSS PROFILE.

(b) ALTERNATIVE RANDOM VIBRATION INPUT PROFILE.

FIGURE 4. INPUT PROFILES

Figure 5 shows a graph of a time history response of a PWA. The time history curve has limited application. However, it does show that there is a good signal voltage and there are no visible signal anomalies. Figure 6(a) is a wide band random vibration process typical of an input profile to the shaker table. Figure 6(b) is a narrow band random vibration process typical of a PWA response to an input from Figure 6(a).The frequency spectrum in Figure 6(b) might be a response to a time history of Figure 5.

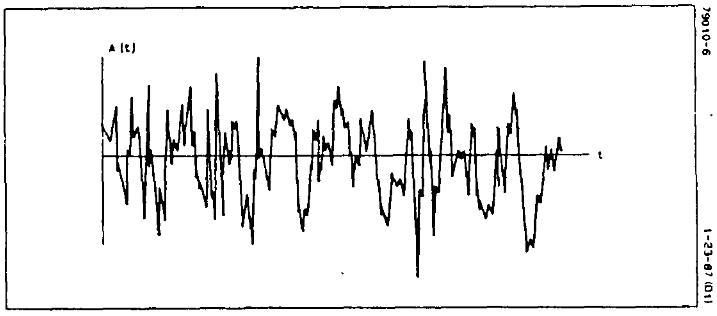

FIGURE 5. RANDOM VIBRATION TIME HISTORY

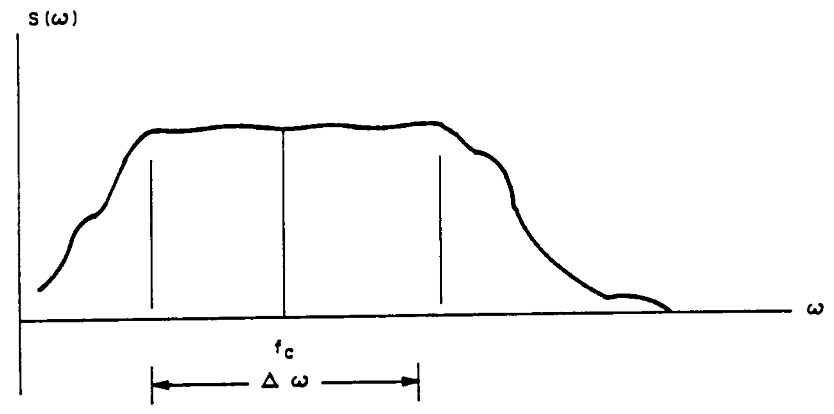

MEAN SQUARE SPECTRAL DENSITY S (ω) SAME ORDER OF MAGNITUDE ACROSS Δ ω AS f_c

(a) WIDE BAND RANDOM PROCESS

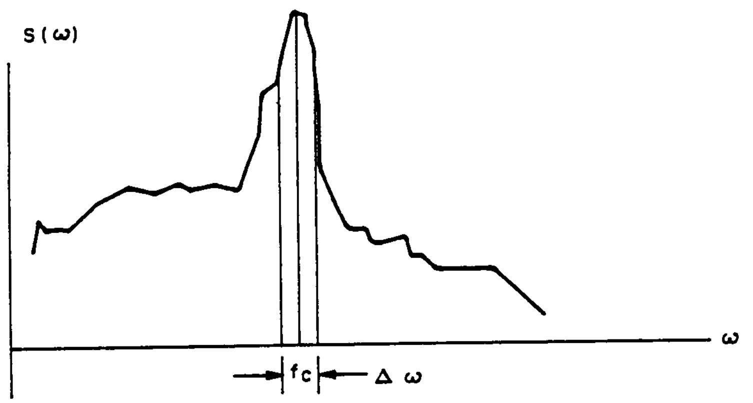

THE NARROW BAND PROCESS IS TYPICALLY ENCOUNTERED AS A RESPONSE TO A STRONGLY RESONANT VIBRATORY SYSTEM WHEN THE EXCITATION IS WIDE BAND.

(b) NARROW BAND RANDOM PROCESS

FIGURE 6. RANDOM VIBRATION CURVES

RESPONSE PROFILES TO RANDOM VIBRATION

The RVSS response curve for a given input can be shown as:

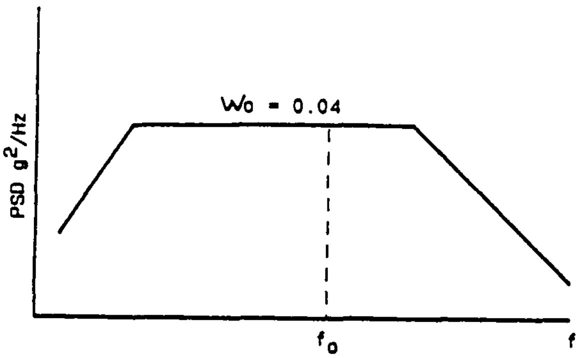

RVSS INPUT

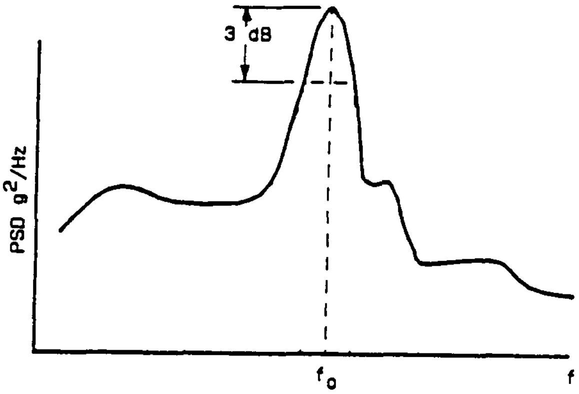

RVSS RESPONSE

From Crandall[1]

$$G_r = \sqrt{\frac{\pi f_n Q \omega_o}{2}} \tag{2A}$$

where Q = Magnification of Motion at resonance.

Since $Q \approx \sqrt{f_n}$, at the PWA resonance frequency

$$G_r = \sqrt{\frac{\pi f_n^{1.5} \omega_o}{2}} \tag{2B}$$

EQUIVALENT SINE ACCELERATION TO PRODUCE SAME FATIGUE AS RANDOM VIBRATION

From Harris and Crede[2] and from $Q \approx \sqrt{f_n}$,

$$G_{RMS} = 1.5 \left(\frac{\pi\ f_n\ \omega_o}{2\ Q}\right)^{1/2} \tag{3}$$

For peak acceleration,:

$$G_{peak} = 2.7 \left(\frac{f_n\ \omega_o}{Q}\right)^{1/2} \tag{4}$$

Equations (3) and (4) show the G_{RMS} and G_{PEAK} equivalents for sine acceleration equivalence to random vibration. The sine equivalent G level produces somewhat questionable test results. A sine equivalent did not produce the same results as the RVSS. However, it may be preferred by some companies. Possibly the

---

[1] S.H. Crandall, "Random Vibration in Mechanical Systems", Academic Press, N.Y., 1963

[2] C.M. Harris and C.E. Crede, "Shock and Vibration Handbook", McGraw Hill, N.Y., 1976

determination of the proper sweep rate plus an appropriate G level would produce the same results.

MAGNIFICATION FACTORS AT RESONANCE, Q

The displacement magnification factor Q is the magnification at resonance; for example, at

$$f/f_n = 1.$$

By definition, the Q depends on the damping ratio,

$$\zeta = C/C_{crit}$$

Figure 7 shows a magnification factor curve for a single degree of freedom system.

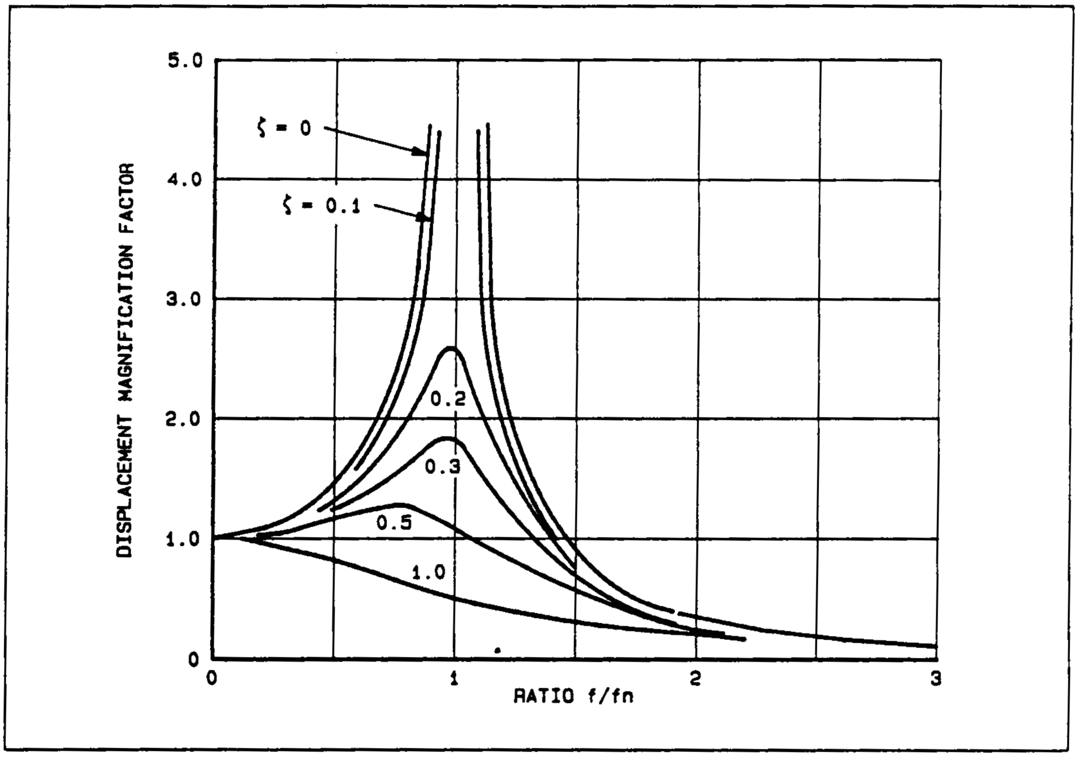

79010-10

1-30-87

FIGURE 7. MAGNIFICATION FACTOR VERSUS FREQUENCY RATIO

For PWAs, the " ζ " varies with the natural frequency and other factors. However, Q may be estimated as shown in equation (5) if test data is not available.

$$Q = K\sqrt{f_n} \tag{5}$$

Where K is an approximate empirical correction factor for a wide variety of PWAs. A graph of frequency vs.K is shown in Figure 8.

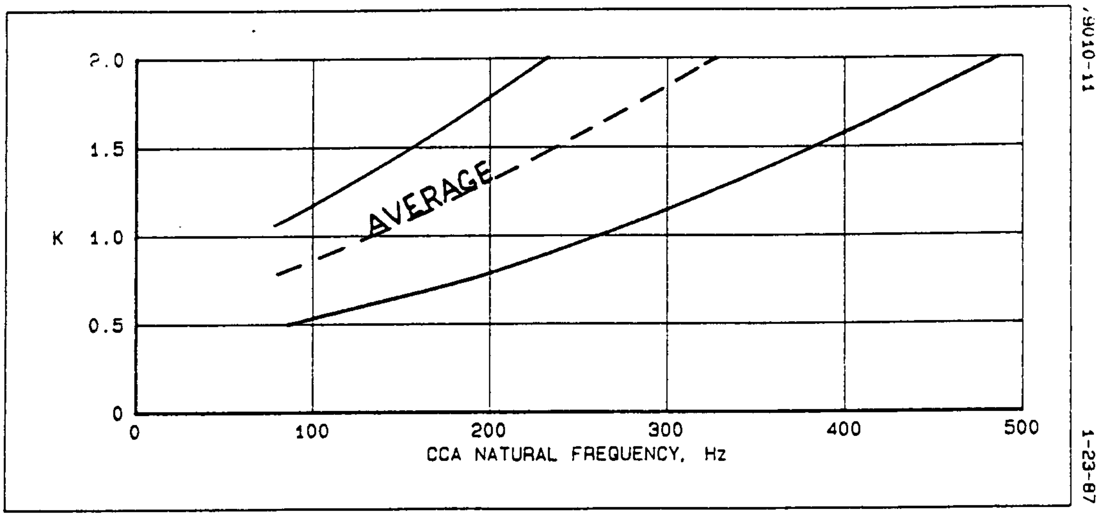

FIGURE 8. CORRECTION MULTIPLICATION FACTOR FOR Q (MAGNIFICATION AT RESONANCE) FOR PWAs

From the standard formula (Equation 6) for determination of the natural frequency for any simple single degree of freedom system,

$$f_n = \frac{3.13}{\sqrt{\delta_o}} \tag{6}$$

or :

$$\delta_o = \left(\frac{3.13}{f_n}\right)^2 \quad \text{(for 1 G)}$$

For an applied vibration input:

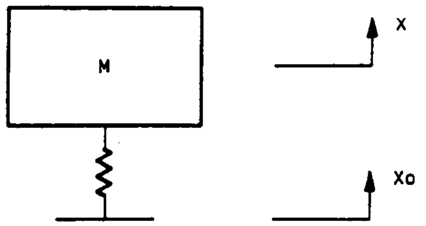

SINGLE DEGREE OF FREEDOM

and $X = X_o Q$ for magnification at resonance. Therefore, for a general PWA Equation(7) may be used as an estimate for determination of displacement.

$$\delta = \delta_o Q = \left(\frac{3.13}{f_n}\right)^2 K\sqrt{f_n} = 9.8\ f_n^{-1.5}\ K \tag{7}$$

For example, estimation of PWA displacement at resonance, given $f_n = 120$ Hz, from Figure 8, $K = 0.9$;

$\delta = 9.8\ (120)^{-1.5}\ 0.9 = \underline{.0067"}$

OTHER METHODS OF DETERMINING Q (GIVEN TEST DATA)

Calculating Q by the "3 dB Down" Method ..This is a quick estimate method but is not quite as accurate as the next two methods.

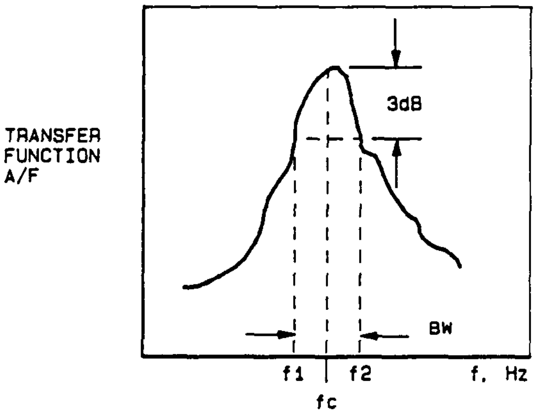

NOTE:
THE BAND WIDTH MAY BE ESTIMATED IN DESIGN AS $BW = 2\zeta fc$

$$\zeta = \frac{BW}{2\ f_n};\ Q = \frac{1}{2\zeta};\ BW = f_2 - f_1 \tag{8}$$

For our example, $f_n = 160$ and BW = 18 Hz, then Q = 8.9

Calculating Q by the Band Width High and Low Frequency Measurement. This is perhaps the most accurate method but requires a Fast Fourier Transform (FFT) analyzer:

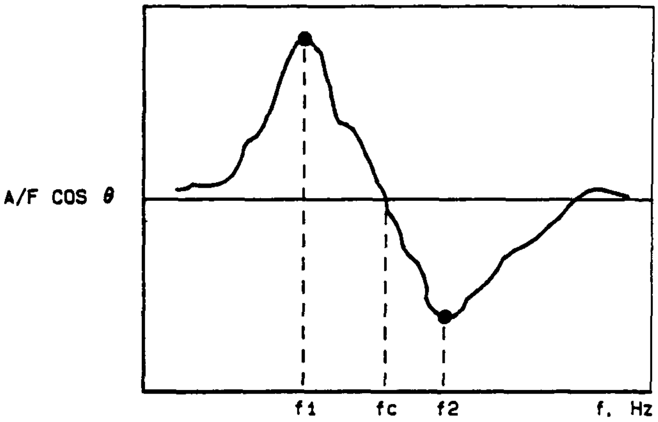

$$Q = \frac{1}{2\zeta} = \frac{\left(f_2/f_1\right)^2 + 1}{\left(f_2/f_1\right)^2 - 1} \qquad (9)$$

e.g., $f_n = 160$, $f_2 = 168$, $f_1 = 150$, so $Q = 8.9$.

Calculating Q by the Input/Output Wave-Ratio. This is probably the most popular method of computing Q; from the figure below,

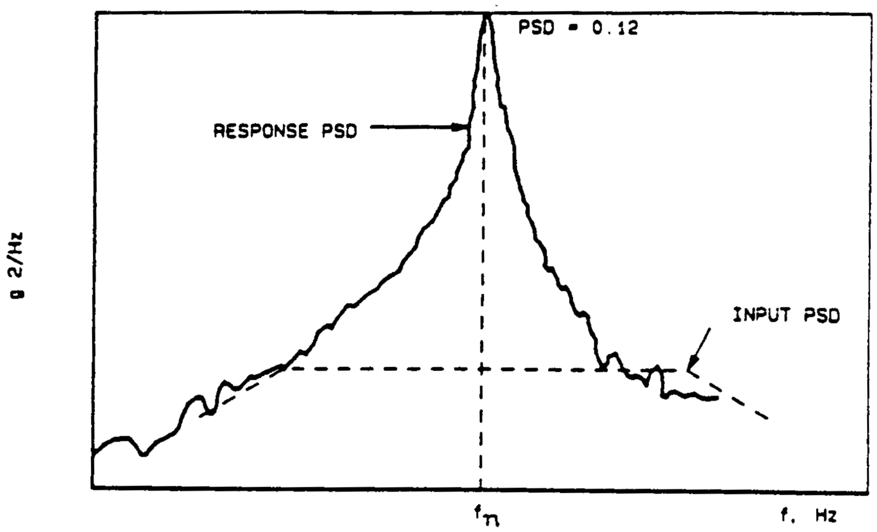

Input PSD = .0015 g^2/Hz at f_n
Response PSD = .012 g^2/Hz at f_n
$Q = \sqrt{0.12/.0015} = 8.9$

Calculating Q Directly by FFT, Response/Input Ratio. The magnification ratio factor Q ma;y be determined directly by testing the PWA for response to input ratio across the entire spectrum by use of a direct transmissibility (TR) analysis by an FFT analyzer. Some FFT analyzers, however, do not have this capability. The figure below is a direct TR analysis which for very low values of ζ is almost equal to Q, the magnification factor.

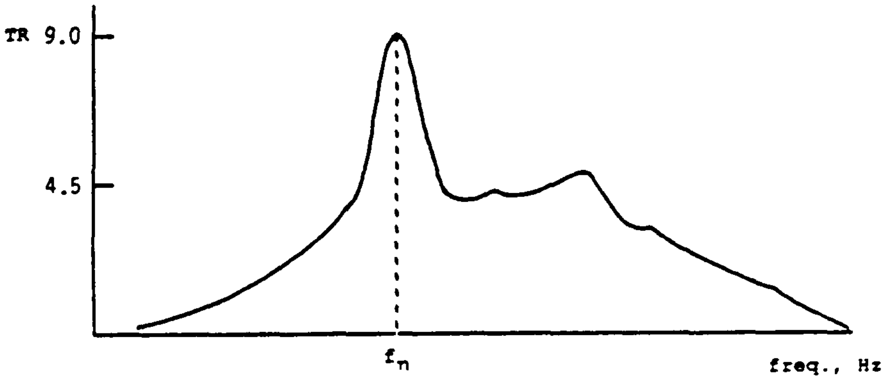

In the above figure, the TR = 8.9; Q ≈ 8.9

GENERAL MODE SHAPES FOR PWAS

Two PWAs are analyzed using ANSYS finite elements to determine the mode shapes. Actual modal analysis results confirm the mode shapes mainly at the lower frequencies. The PWAs sometimes do not behave as analyzed at higher frequencies, due to the non-linearity of the boundary condition (or edge restraints) and non-linearity of the PWB/component. The mode shapes shown in Figures 8 and 9 are provided for reference and to show that the first mode is usually curved, as assumed in this report. Of course, the amount of distortion is greatly exaggerated for viewing purposes. The actual amount of deflection and distortion diminishes greatly at higher frequencies. Thus the distortion is much smaller at f = 635 Hz than at f = 164 Hz.

FIGURE 9. MODE SHAPES FOR 7 X 9 PWA

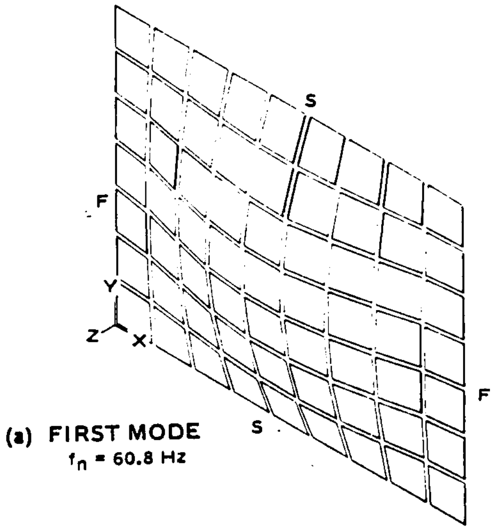

(a) FIRST MODE
$f_n = 60.8$ Hz

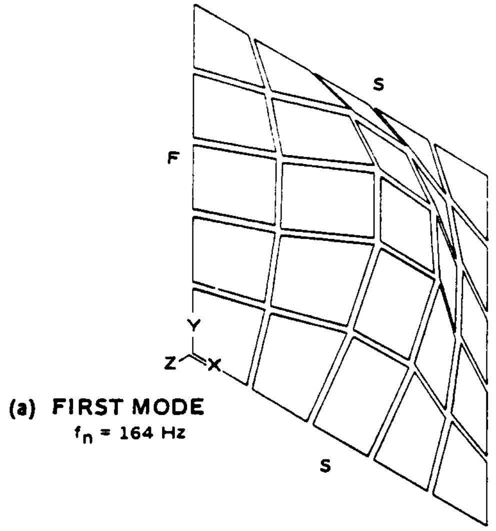

(a) FIRST MODE
$f_n = 164$ Hz

FIGURE 8. MODE SHAPE FOR 5" X 5" PWA

RVSS RESPONSE OVERVIEW

Ideally, the response of a PWA for a random vibration input is dependent on its own structural transfer function. In the real world, the response takes into account the transfer function of all the supporting structures and the shaker itself, as was discussed previously. Thus, the resultant response curve is a conglomeration of PWA dynamic characteristics plus all the support system.

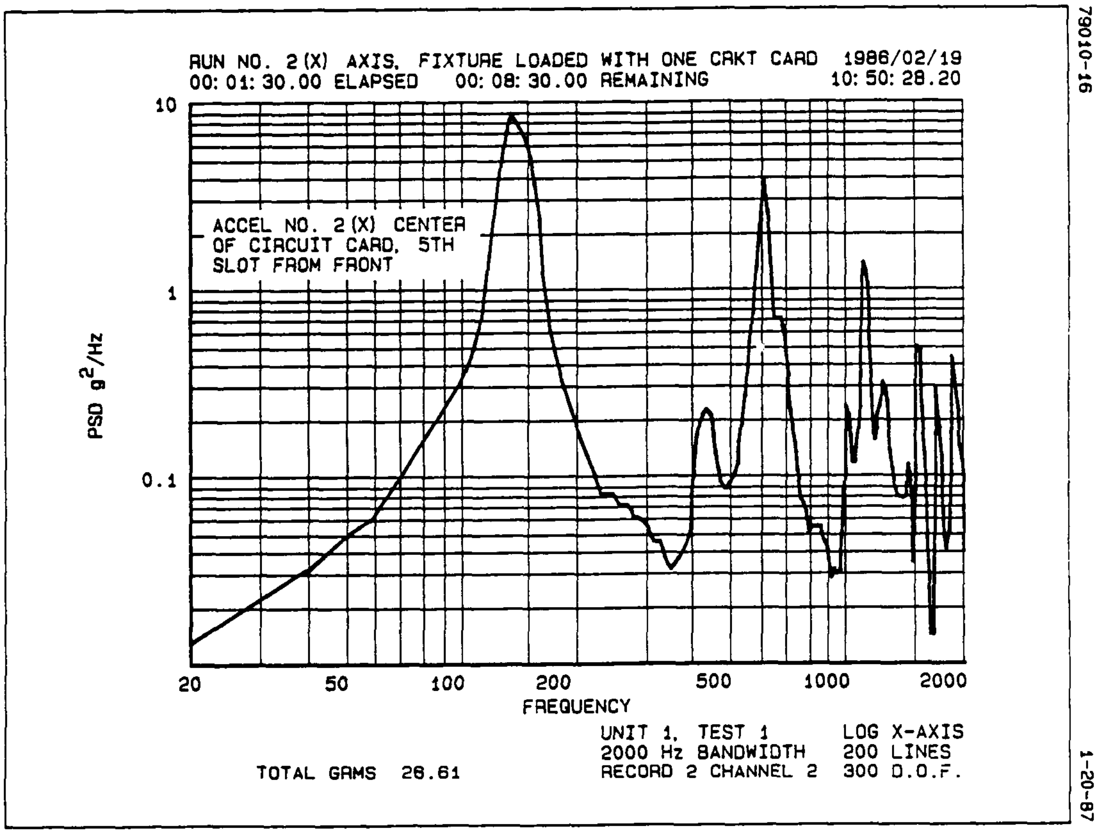

FIGURE 10. RESPONSE OF A TYPICAL PWA

Figure 11 shows a typical PWA signature analysis and response measurement setup. Note that a PWA must have a very light weight accelerometer for measurement at its center, and the input accelerometer may be any weight since it is attached to a rigid fixture.

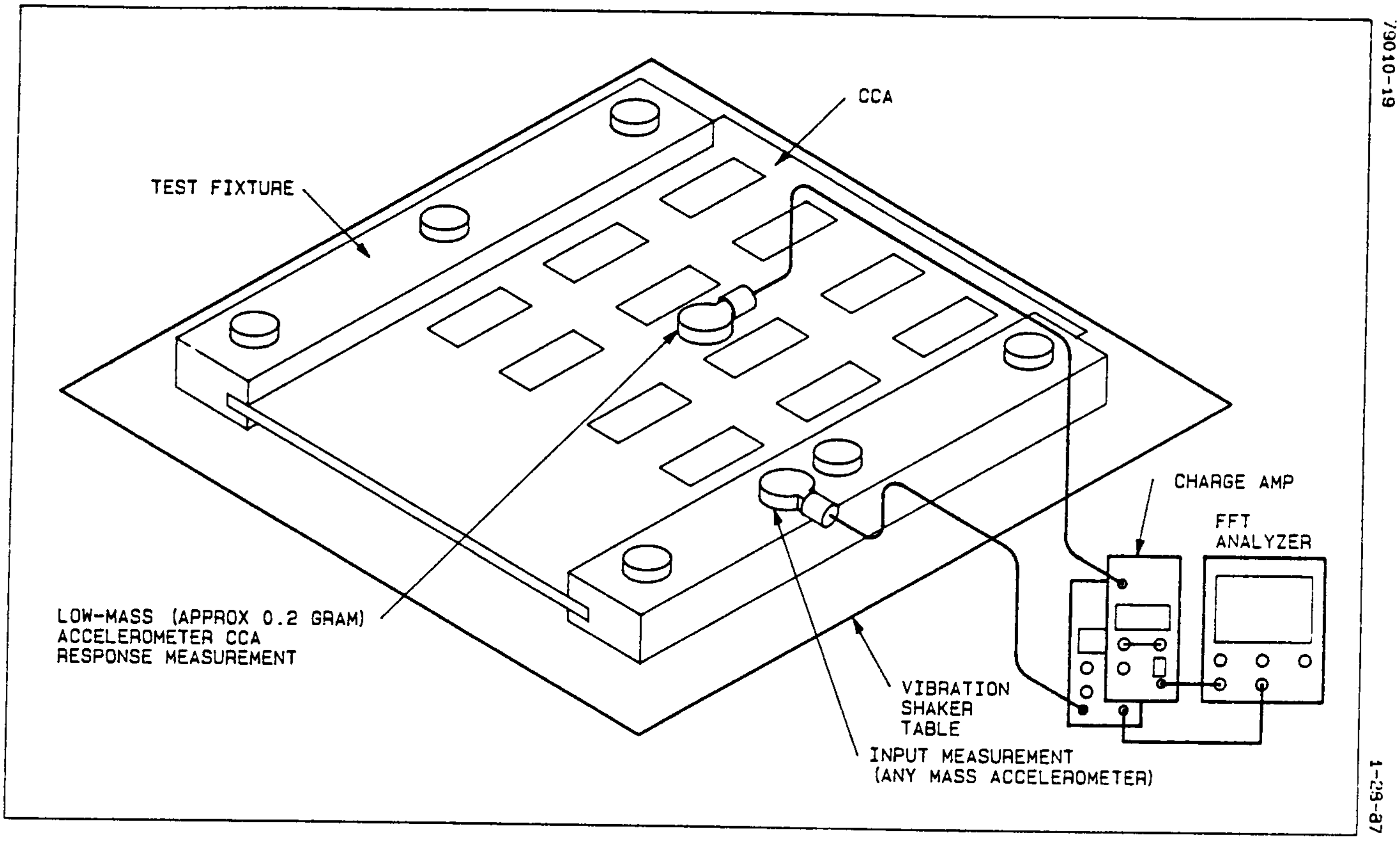

FIGURE 11. PWA TEST SETUP FOR INPUT AND RESPONSE MEASUREMENT

RANDOM VIBRATION RESPONSE ANALYSIS

Refer to the random vibration response shown in Figure 10. In random vibration, the Power Spectral Density (PSD) in G^2/Hz is obtained on a spectrum analyzer by converting real-time data (G's vs.time) into the frequency domain data by a fast fourier transform (FFT). The data may be analyzed more usefully in the frequency domain. Essentially, the spectrum data is divided into constant value filtered bandwidths (BW). The bandwidth, for a specific FFT analyzer (sometimes called the bin width), is obtained by dividing the frequency spectrum range by the number of lines of resolution:

$$BW = \frac{\text{SPECTRUM RANGE}}{\text{NO. OF VERTICAL LINES OF RESOLUTION}} \tag{10}$$

$$\text{e.g., } BW = \frac{2000 - 20}{200} = 9.9 \text{ Hz}$$

The bandwidth is increased by about 50% if the Hanning function is turned on (which is normal). Thus, BW = 9.9 x 1.5 = 14.85 Hz

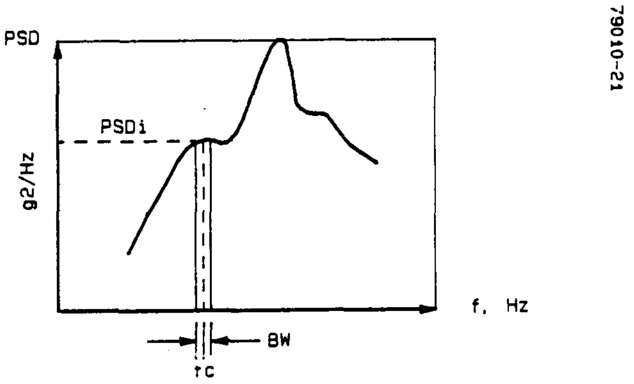

FIGURE 12. DETERMINATION OF G VS. F

The bandwidth varies for each type of analyzer and spectrum range selected. The G acceleration value is computed for each BW, squared, and divided by the constant BW, thus PSD (G^2/Hz) See Figure 12. Although the actual curve is constantly changing with time, a profile is obtained by averaging 64 to 128 times. The G levels of the PSD curve may thus be calculated in reverse by taking a value of PSD corresponding to BW and performing the following calculation:

$$G_{RMS} = \sqrt{PSD_i \times BW} \tag{11}$$

Each "G" is plotted for each center frequency (f_c). The overall effective G_{RMS} is obtained by integrating the entire curve. This is automatically furnished by most analyzers. The overall Grms is essentially the square root of the sum of powers at each frequency. If the G computation is not available on the analyzer, it may be computed manually. It can be seen that the peaks represent a significant part in the overall Grms level. The log-log scale can often be deceiving for judging the bandwidths at each peak.. The results are shown in Figure 13.

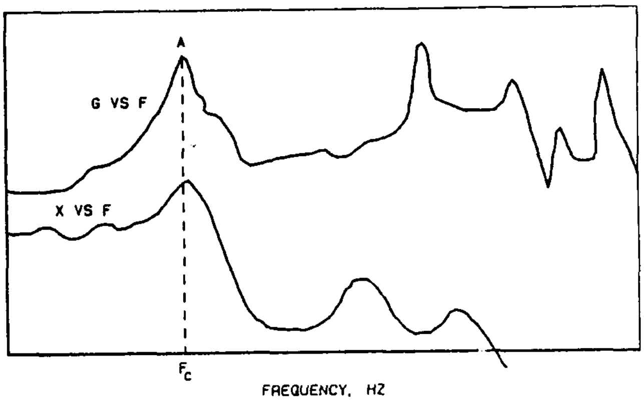

FIGURE 13. PSD CURVE CONVERTED TO G_{RMS} AND X_{RMS} VS FREQUENCY

The waveform is now somewhat more subdued due to the square root effect, but the peaks remain evident. Note that the majority of the deflection energy (X_{RMS}) occurs between the lowest frequency and the first mode. The balance of the energy is mostly all velocity energy. If we make an assumption here that the PWA acts like a single degree of freedom (SDOF) system which tests show is nearly the case, the dynamic behavior is much like one spring and one mass at its first natural frequency.

$$\text{from:} \quad a = x\omega^2 \text{ or } G = \frac{x\omega^2}{386}, \text{ where } x = \text{inches} \tag{12}$$

$$\text{Since } \omega = 2\,\pi\, f, \text{ then } x = \frac{386\ G}{(2\ \pi\ f)^2} = \frac{9.8\ G}{f^2}$$

For PWA's, $x = \delta$.

DETERMINATION OF PWA RELATIVE DEFLECTION FROM TEST DATA

The determination of the response of the PWA relative to its edge (the input) is the goal of the response analysis. The absolute PSD, G, and displacement of the PWA was obtained. The displacement is shown in Figure 14. Subtracting the maximum displacement of the PWA at the critical frequency from the input displacement at the same frequency provides a fair evaluation of the displacement.

$$\delta_{PWA\ (relative)_{f_1}} = \delta_{ABS_{f_1}} - \delta_{EDGE_{f_1}} \tag{13}$$

Thus in the case shown, the lowest natural frequency of the PWA (first mode) also is the worst case for PWA displacement. As stated before. The analysis requires test data for an actual PWA. However, the first mode response can also be estimated by analytical techniques. The $PWA_{(relative)}$, or δ_{REL} for short, is then compared to the maximum allowable δ_{REL} for PWAs discussed in detail in the following sections of this report. One important aspect of relative motion is that for discrete components (such as axial lead types), the component has no differential motion with the PWA at frequencies lower than the discrete component resonance frequency. At resonance of the discrete component, the component moves out of phase with the PWA and this is where the component wires are stressed. At frequencies above the component natural frequency, the component hardly moves at all, thus nearly no stress. The bending of the PWA, however, can cause lead wire stress.

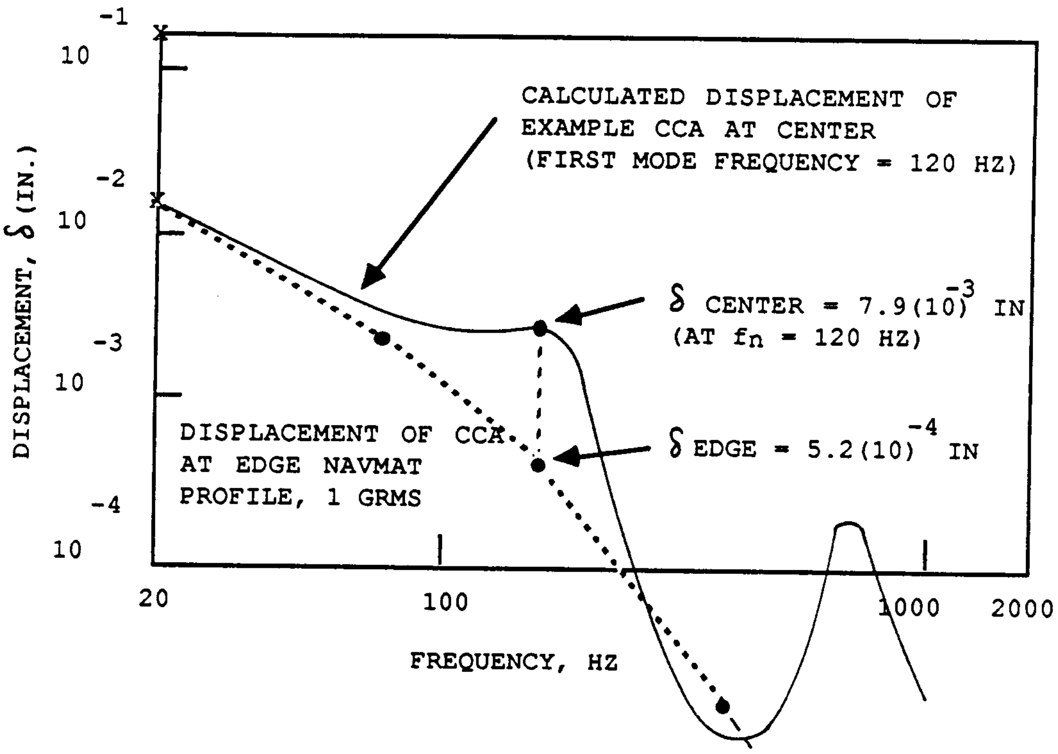

FIGURE 14. DISPLACEMENT OF PWA AT CENTER AND EDGE (BASED ON EXAMPLE)

From Figure 14,

$$\delta_{REL} = 7.9 \times 10^{-3} - 5.2 \times 10^{-4} = 7.38 \times 10^{-3} \text{ in.}$$

Another method to estimate relative displacement is to apply the Crandall theory, Eqn. (2a):

$$G = \sqrt{\frac{\pi}{2} f_n \, Q \, \omega_o}$$

also since,

$$x = \frac{9.8 \, G}{f_n^2} \quad \text{and} \quad Q \approx \sqrt{f_n}, \text{ with } K \approx 1$$

then

$$\delta = x = \frac{9.8}{f_n^2}\left(\frac{\pi}{2} f_n \, f_n^{1/2} \omega_o\right)^{1/2} = 12.3 \left(\frac{\omega_o}{f_n^{5/2}}\right)^{1/2} \qquad (14)$$

As an example, from figures 11 and 13;

$$\delta = 12.3 \left(\frac{.04}{120^{5/2}}\right)^{1/2} = 6.19 \times 10^{-3} \text{ in.}$$

$$\delta_{REL} = 6.19 \times 10^{-3} - 5.2 \times 10^{-4} = =5.67 \times 10^{-3} \text{in.}$$

Thus both methods are reasonably close; however, the first method is the more accurate since the second method is for broadband input, and the NAVMAT curve is not a full broadband across the spectrum. The later method, however, is used in design since the actual curves are usually not available until long after the design stage.

DETERMINATION OF MAXIMUM ALLOWABLE PWA "G" LEVEL FROM TEST DATA

An alternative method to determine whether or not the maximum allowable displacement will be exceeded is to calculate the response G profile, as was done in Figure 15, and to superimpose a line on the curve which represents the maximum permissible G level vs. frequency given a value for maximum relative PWA deflection (δ) at the center.

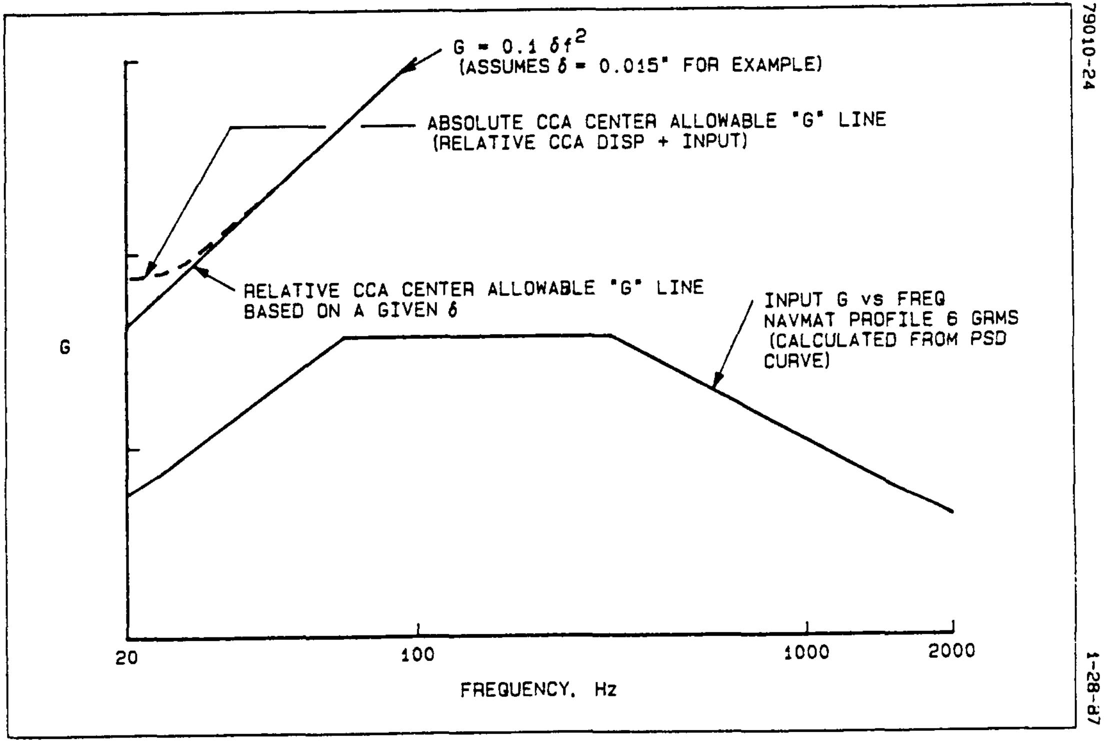

FIGURE 15. RELATIVE AND ABSOLUTE PWA CENTER ALLOWABLE DISPLACEMENT LINE (BASED ON EXAMPLE PWA)

From Figure 15, the absolute and relative PWA center allowable displacement line is determined. The relative displacement is a plot of the equation $G = 0.1 \delta f^2$. The absolute is the addition of this equation plus the input. The

NAVMAT profile (six G_{RMS} input) was used in this example. Note the contribution of the input to the absolute PWA curve. The absolute G line is needed to compare to the absolute G response line in order to compare apples to apples.

The absolute PWA center allowable displacement is plotted on the G vs. frequency response curve in Figure 16.

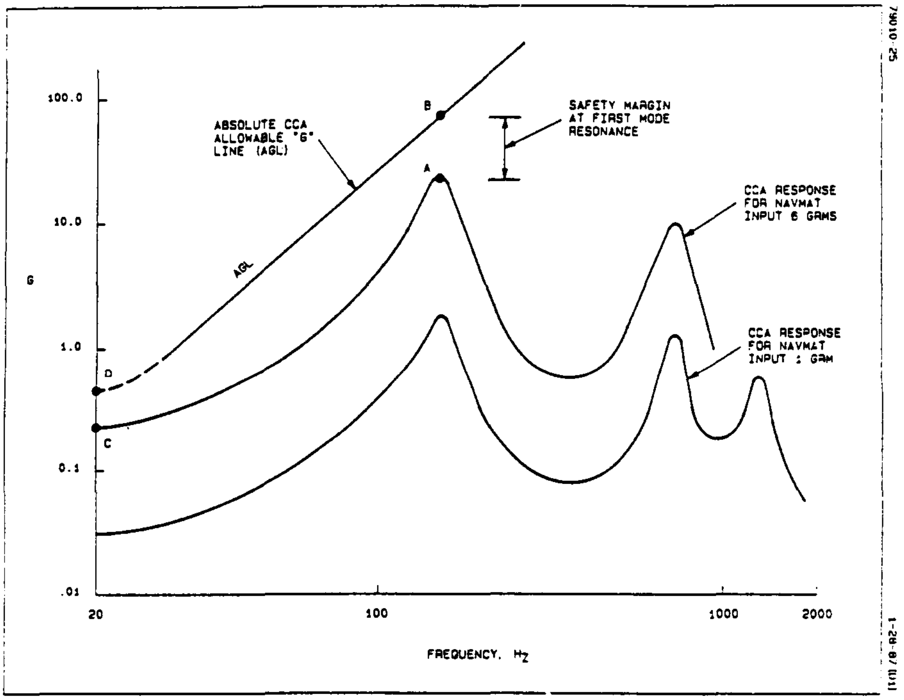

FIGURE 16. MAXIMUM ALLOWABLE PWA "G" INPUT LEVEL

As described above, the absolute allowable G line is obtained by adding the input to the relative allowable G line i.e.,

G ABS. (PWA) = INPUT G + G REL. (PWA) each frequency.

Note from Figure 16, the PWA allowable G line (AGL) is established based on a selected maximum allowable deflection (δ) of the PWA at its center. The manually calculated (or analyzer computed display) G vs. frequency response curve is superimposed on the AGL curve and the safety margin obtained. Note that there are two critical areas. The points A & B indicate the safety margin for the first mode resonance, which may be the most critical for causing deleterious effects to the component leads. Points C & D indicate the safety margin at the lowest imposed frequency. Points A & B may be the most critical and thus both areas should be considered for determining the maximum G response. The higher frequencies do not appear to impose a threat to the PWB or its components since the safety margin is very high. The saftey margin should be approximately a factor of 3 to allow for the 3σ statistical variation which could triple the the stress 3% of the time. Recall, however, that the AGL shown above was for establishing the maximum deflection or bending of the PWA and does not address lateral or transverse vibration.

The AGL is an approximate method of establishing a limit for the PWA response, but it is not as accurate as the comparison of the PWA actual deflection to the maximum permitted deflection. The response is based on at least 64 to 128 data averages on a spectrum analyzer (which takes only a few seconds). In addition, the bandwidth of the first mode peak contributes to the accuracy. However, as an approximation, tests show it is a reasonably good guideline for most applications.

DETERMINATION OF MAXIMUM ALLOWABLE PSD LEVEL FROM TEST DATA

A maximum allowable PSD level may be obtained by a method similar to the AGL method discussed previously. The premise is as before, namely that a deflection (δ) of the PWA in bending is established from one of the criteria in the following sections. From equation (12),

$$G = 0.1\ \delta\ f^2 \tag{15}$$

This operation establishes the limit of G for a given δ at a given frequency. By squaring the equation and dividing by the filtered bandwidth of Equation (16), we may obtain an allowable PSD limit line (APL) similar to the AGL line.

$$\begin{aligned} G^2/BW &= \left(0.1\ \delta\ f^2\right)^2 \qquad (16) \\ &= 0.01\ \delta^2\ f^4/BW \quad g^2/Hz \end{aligned}$$

Equation (16) is the relative APL. The absolute APL is obtained in a similar fashion to the absolute AGL, namely by adding the input PSD curve to the relative APL, i.e,

$$\overline{APL} = 0.01\ \delta^2\ f^4/BW + \omega_o \tag{17}$$

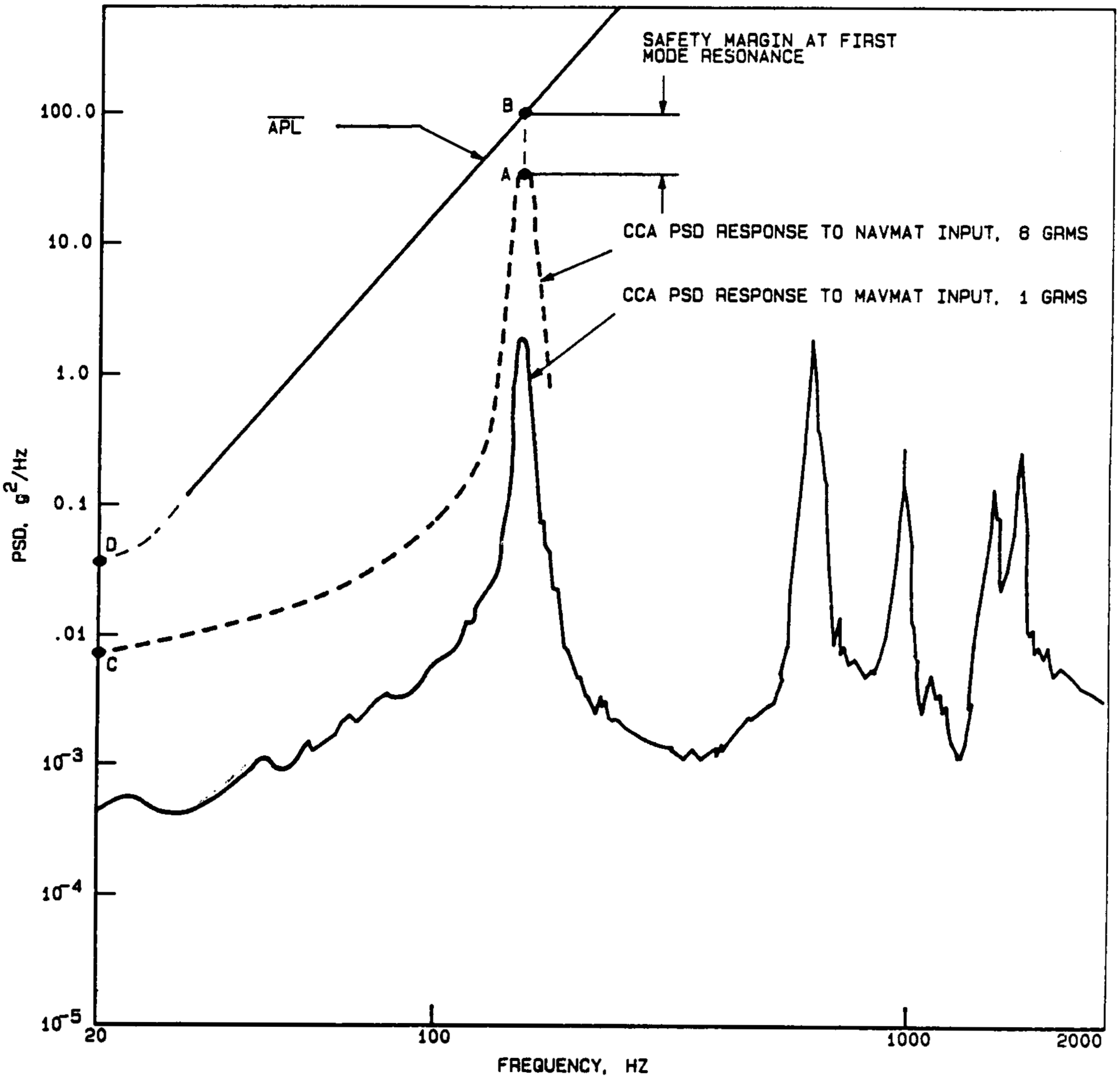

FIGURE 17. MAXIMUM ALLOWABLE PSD INPUT LEVEL

Figure 17 shows the PWA response at two different NAVMAT levels and the allowable PSD limit line. The safety margins are shown similar to the ones in figure 16.

Once again, this method is only approximate and is not preferred to the direct displacement comparison method. The accuracy of this method depends on the same factors mentioned previously. The advantage of this method is that it offers a quick way to check for problems.

PWB BENDING PARAMETERS

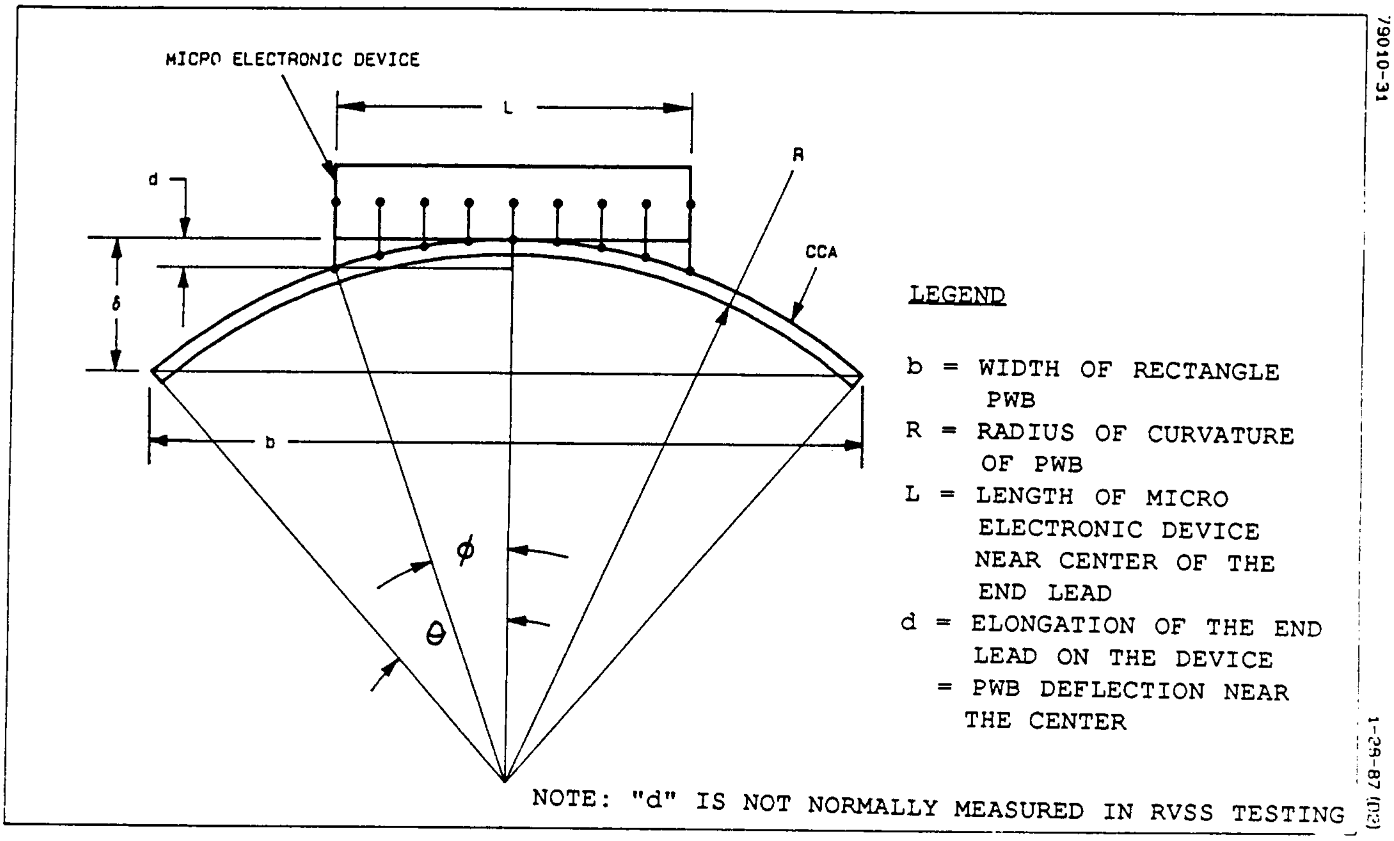

NOTE: "d" IS NOT NORMALLY MEASURED IN RVSS TESTING

FIGURE 18. PWB DEFLECTION PARAMETERS

From Figure 18,

$$d = \frac{L^2}{8R} \quad \text{or} \quad R = \frac{L^2}{8d} \qquad (18)$$

$$\delta = R\left(1 - \cos\theta\right) = \frac{R\,\theta^2}{2} \qquad \text{and} \qquad \delta = \frac{8\,b^2\,d}{8\,L^2} = \left(\frac{b}{L}\right)^2 d \qquad (19)$$

or rearranging

$$d = \delta\left(\frac{L}{b}\right)^2 \qquad (20)$$

IC LEADS IN BENDING

The integrated circuit (IC) undergoes stress as result of PWB bending (see Figure 19). The following analysis provides a simple method to determine the stress in the IC leads and the maximum allowable PWA deflection.

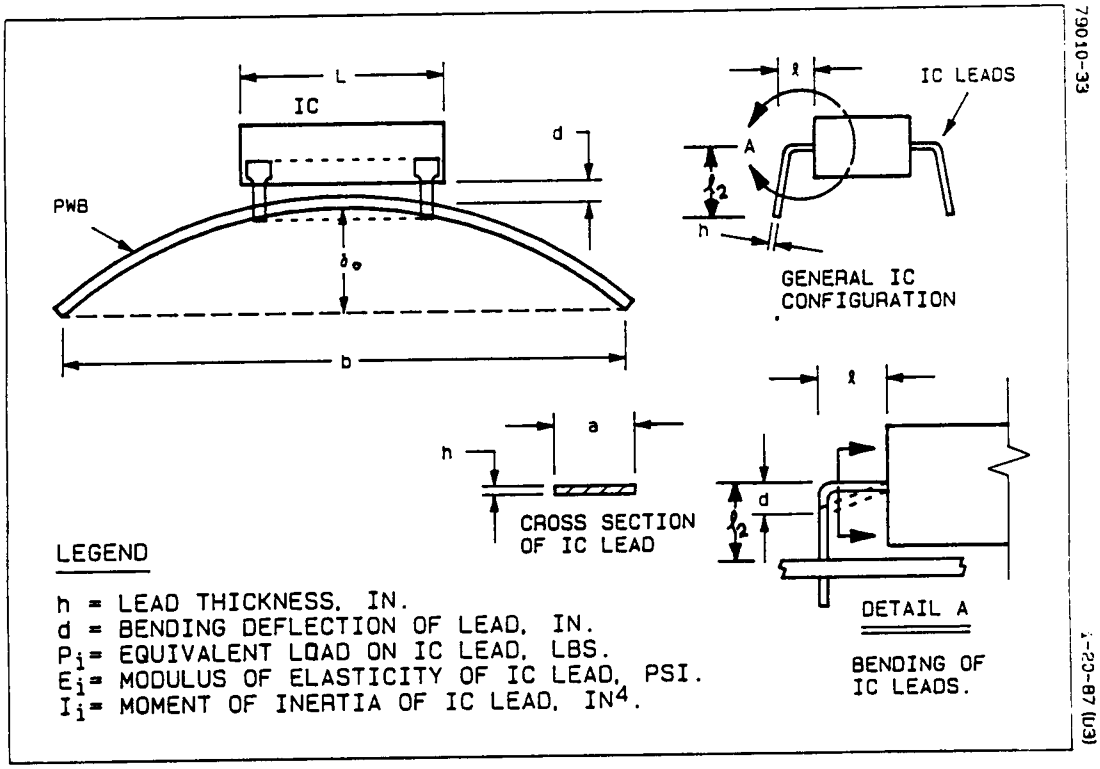

FIGURE 19. GENERAL DIP/IC ATTACHMENT TO PWA

It is desired to determine the stress on the end leads of the DIP for a given PWA displacement.

From the frame structure:

The DIP end leads are deflected a distance "d" (See Figure 23)

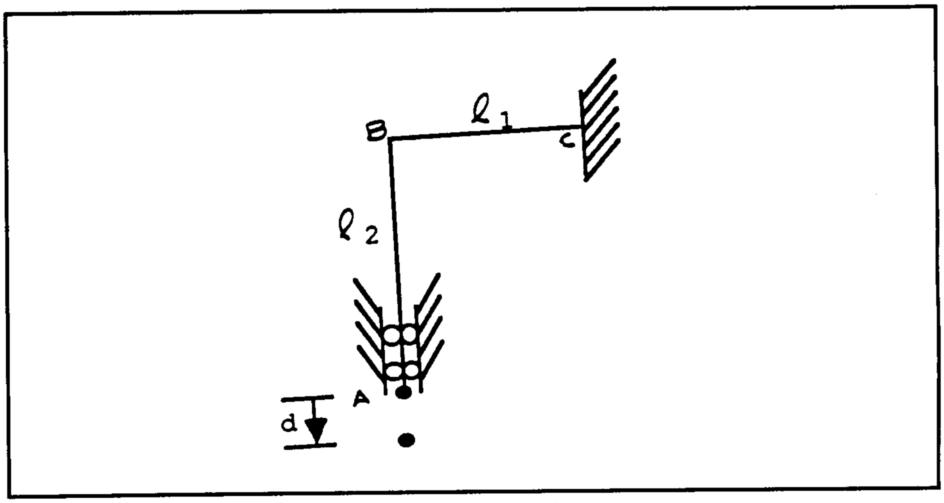

FRAME ANALOGY
FROM THE THEOREM OF CASTIGLIANO

$$d_{TOTAL} \approx \frac{P}{E\ I}\left[\frac{l_1^3}{3} + l_1^2\ l_2 - \frac{l_1^3\left(l_1 + 2l_2\right)}{2\left(l_1 + l_2\right)} - \frac{l_1^2\ l_2\left(l_1 + 2l_2\right)}{l_1 + l_2}\right]$$

For most DIPs, $l_2 \approx 4\ l_1$

$$d_{TOTAL} \approx \frac{113}{30} \times \frac{P\ l_1^3}{E\ I}$$

The stress on the end lead is:

$$\sigma = \frac{M\ C}{I} \quad \text{and} \quad M = 9/5\ P\ l_1 \quad \text{and} \quad d = \frac{\delta}{(b/L)^2}$$

$$\sigma = \frac{9 \quad 30 \quad E \quad h}{2 \quad 113 \quad 5 \quad l_1^2}\ \frac{\delta}{(b/L)^2} = \frac{.239\ E\ W}{l_1^2}\ \frac{\delta}{(b/L)^2}$$

or, solving for the PWA deflection in terms of the DIP lead stress,

$$\delta_{MAX} = \left[\frac{4.18\ \sigma_{MAX}\ l_1^2}{E\ h}\right]\left(\frac{b}{L}\right)^2 \qquad (21)$$

The DIP leads may be Kovar or alloy 42. See Table 1 for properties. The stress level is selected on the basis of fatigue normally. The "l_1" value is .030" for many DIP designs. The "h" value is approx. .010".

TABLE 1. MATERIAL DATA FOR KOVAR AND ALLOY 42

Properties	Kovar	Alloy 42
Ultimate Strength	77,500 psi	70,000 psi
Yield Strength	40 - 59,500 psi	35 - 50,000 psi
E, Modulus of Elasticity	20,000 psi	21,000 psi
Se, Endurance Limit (Fatigue Strength, Estimate Only)	38,750 psi	35,000 psi

A corrective curve (Figure 20) is shown below for modification of equation (21) to allow for the stiffening effect of the component on the PWA. The correction factor is based on some testing of ordinary PWA's and comparison to ANSYS analysis.

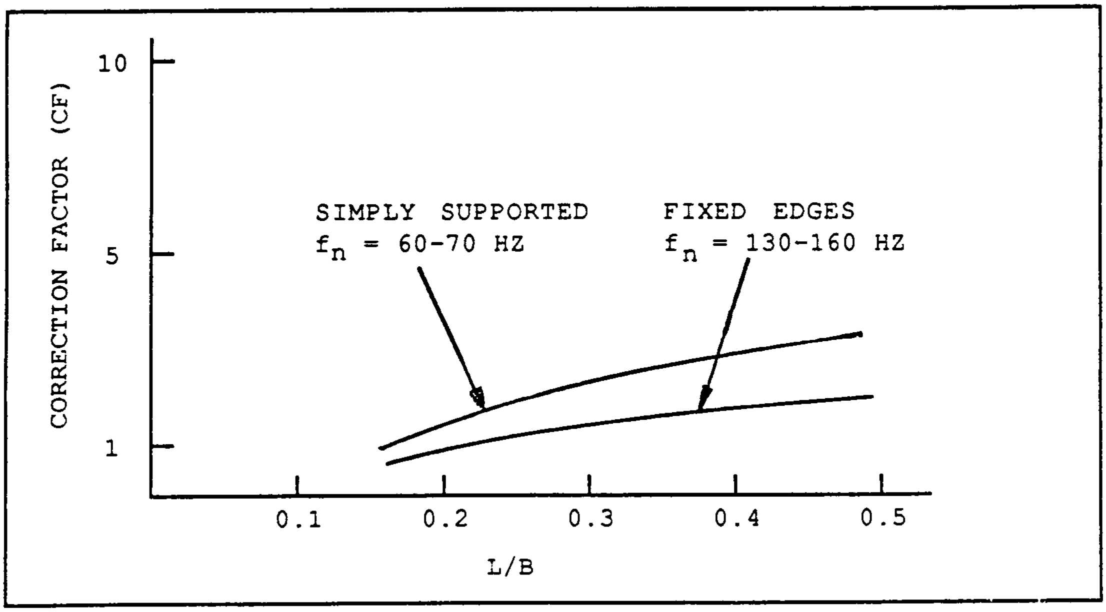

FIGURE 24. CORRECTION FACTOR FOR δ_{MAX} FROM EQUATION (22)

PWB IN BENDING

<u>PWA with Simple Support Edge Restraints</u> A retangular flat plate may be approximated by a beam whose length is equal to the width of the short side. The higher the ratio of a/b, the more accurate the assumption. The formulas for an ordinary beam with the appropriate boundary conditions may be used. The simplicity of this method lends itself to simple use standard beam equations. The method is illustrated below and is sometimes referred to as the 10% slice method. In this method, the MC/I formulas apply.

The equation for the deflection of a simple supported beam is found in almost all strength of materials text books and structural analysis manuals. The beam length is "b" and the width is assumed to be 10% of the "a" dimension.

As a quick estimate approach, the PWB may be analyzed as a beam with the length of the beam equal to the PWA side "b", and the width equal to 10% of length "a." Thus, the configuration shown below is assumed.

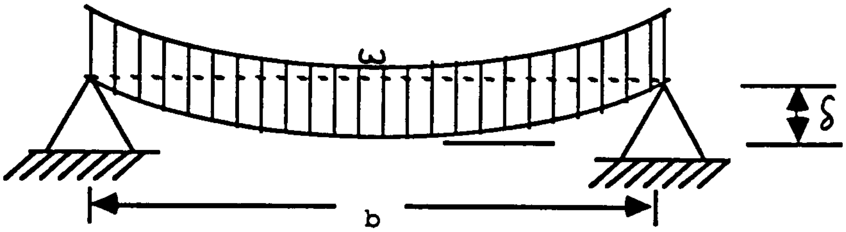

SIMPLY SUPPORTED BEAM

The equation for the deflection of a beam uniformly loaded across the span and simply supported is:

$$\delta = \frac{5\ w\ b^4}{384\ E\ I} \quad \text{where } w = \frac{W}{b}$$

LEGEND

δ = Deflection, in
b = Short side span of PWA, in
w = Distributed load, lb/in
W = Total load, lb
M = Moment, in-lb
E = Modulus of Elasticity, lb/in^2
I = Moment of Inertia, in^4

The moment at the center is:

$$M = \frac{w\ b^2}{8} = \frac{W}{b}\,\frac{b^2}{8} = \frac{W\ b}{8}$$

$$\delta = \frac{5\ w\ b^4}{384\ b\ E\ I} = \frac{5}{384}\,\frac{W\ b^3}{E\ I} \tag{22}$$

and

$$\delta = \frac{5\ M\ b^2}{48\ E\ I} \tag{23}$$

The bending stress at the center of the PWb is:

$$\sigma = \frac{M\ C}{I} = \frac{48\ E\ I\ \delta}{5\ b^2}\,\frac{t}{2\ I} = \frac{4.8\ E\ \delta\ t}{b^2} \tag{24}$$

"I" and "C" may have to be calculated for PWAs with cooling ducts and/or thermal mounting plates; however for a flat plate:

$$\delta_{MAX} = \left[\frac{0.208\ \sigma_{MAX}}{E}\right]\frac{b^2}{t} \tag{25}$$

TABLE 2. PROPERTIES OF PWB MATERIALS

Material	E, psi	Fatigue Strength, n = 10^7 cycles
G-10	2.00×10^6	20,000
Polyimide	2.75×10^6	18,000
Aluminum Oxide	45.0×10^6	12,500

PWA with Fixed Edge Restraints - PWAs are not always restrained as a simple support. A more tyical restraint is a fixed end type which is shown in Figure 21.

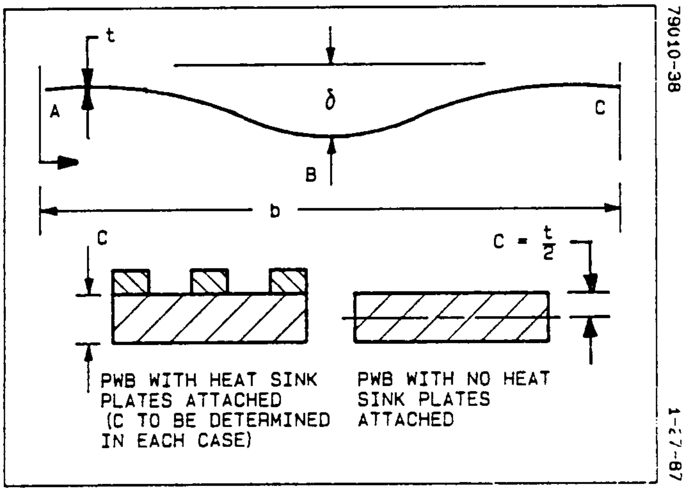

FIGURE 21. FIXED EDGE PWB

In this case, the equation for deflection of a fixed edge beam is:

$$\delta = \frac{W\,b^3}{384\,E\,I} \qquad \text{and} \qquad M = \frac{W}{12\,b}\left(6bx - 6x^2 - b^2\right)$$

$$M_A = .083\ Wb \qquad M_B = .04\ Wb$$

Therefore,

$$\delta = \frac{M_A}{.083b} \cdot \frac{b^3}{384\,EI} = .031\,\frac{M_A b^2}{EI}$$

The stress at "A" is:

$$\sigma = \frac{MC}{I} = \frac{\delta\,EI}{.031\,b^2} \cdot \frac{t/2}{I} = 16.1\,E\,\delta\,\frac{t}{b^2}$$

or

$$\delta_{MAX} = \left(\frac{.062\,\sigma_{MAX}}{E}\right) \cdot \left(\frac{b^2}{t}\right) \tag{26}$$

ANOTHER APPROACH TO PWB BENDING

A "Simple Support" approach can be analyzed as follows:

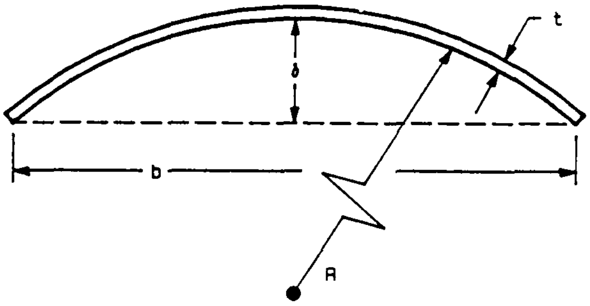

BASIC BEAM IN BENDING

For a structure in bending, the moment and radius of curvature is related by:

$$\frac{1}{R} = \frac{M}{E\,I}$$

$$\frac{8\,\delta}{b^2} = \frac{M}{E\,I} \quad \text{where } M = \frac{I\,\sigma}{t/2}$$

$$\frac{8\,\delta}{b^2} = \frac{2\,\sigma\,I}{t\,E\,I} = \frac{2\,\sigma}{t\,E}$$

$$\delta = \frac{2\,\sigma}{t\,E}\,\frac{b^2}{t} = \left(\frac{.25\,\sigma_{MAX}}{E}\right)\frac{b^2}{t} \qquad (27)$$

This compares to Equation (25)

LEADLESS CHIP CARRIERS (LCCs) AND PWB IN BENDING

Leadless chip carriers (LCC's) such as that shown in Figure 22 present a somewhat different problem for determination of the maximum bending and deflection of the PWA in vibration. LCC's may be used on ceramic PWB's which has a material stiffness 16-20 times higher than ordinary G-10 fiber glass epoxy. In the LCC, there are no leads to be stressed. However, the solder tabs at the interconnection act like small springs with different applied forces on them depending on the compliance and curvature of the PWB. The end solder tabs on the LCC are the highest stressed much the same as the DIPs. The soldering quality and workmanship may be particularly important in this type of interconnection since a weak solder joint, cold solder joints, solder voids, etc., directly affect the failure mode. The development of the maximum bending and deflection criteria leads to:

For example,

$$\delta = \left(\frac{\sigma_s l_s}{E_s}\right) \left(\frac{b}{L}\right)^2 \qquad (28)$$

where σ_s = Stress level in the solder joint, psi
l_s = Effective length of the solder joint, in
E_s = Modulus of Elasticity of Solder, psi

A typical length (l_s) at the solder joint may range from .001" to .003". (See Table 3 for solder strength and other parameters.)

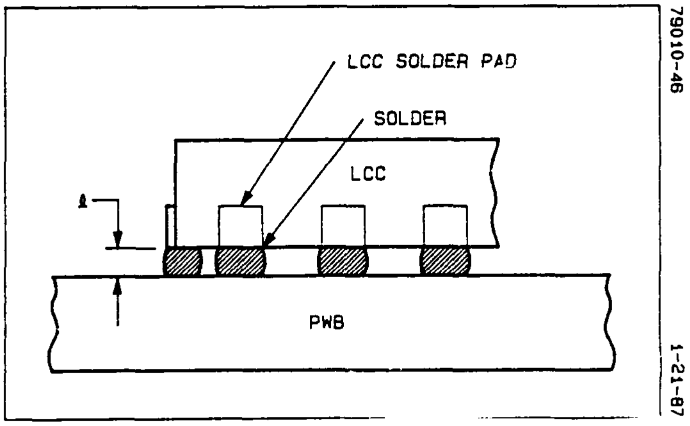

FIGURE 22. LCC SOLDER INTERCONNECTION

TABLE 3. SOLDER STRENGTH VALUES

Sn/Pb/In	U.S. psi	S.S psi	F.S. (estimate) psi	E (estimate) psi x (10)6
63/37/--	7700	5400	3100	4.6
50/--/50	1720	1630	690	3.4
50/50/--	6200	6200	2500	18.0
--/50/50	4670	2680	1870	2.0

Sn = % tin
Pb = % lead
In = % indium

LEGEND U.S. = Ultimate Strength, psi
S.S. = Shear Strength, psi
F.S. = Fatigue Strength, psi
E = Modulus of Elasticity, psi

From Figure 23, a LCC loaded PWA with power on or in a high temperature environment (or both) may affect the overall fatigue strength of the solder due to local hot spots. Thus temperature, quality and soldering workmanship all directly affect the strength of the LCC/PWA. A combined thermal and vibration stress screen would cause 50% reduction in fatigue strength during a 55°C hot cycle (using 63/37 solder). Thus, the RVSS would have to be reduced in a combined environment.

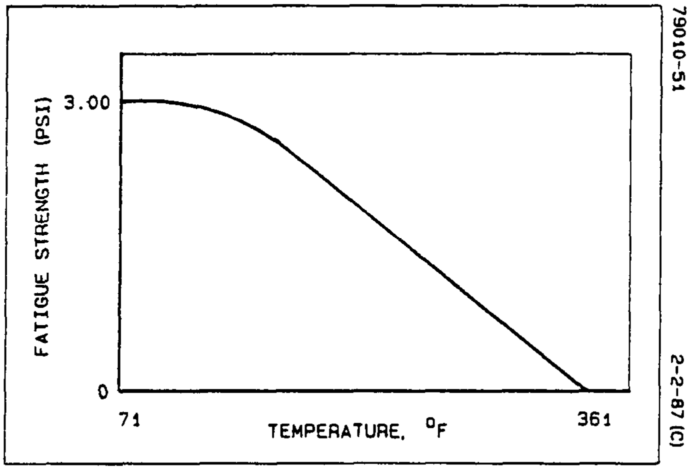

FIGURE 23. FATIGUE STRENGTH VS TEMPERATURE FOR 63/37/0 SOLDER ESTIMATED VALUES

DETERMINATION OF PWA NATURAL FREQUENCY BY PLATE METHOD

The general equation below is used to solve the general deflection of a PWA with given boundary conditions. The general deflection formula may then be used to determine the natural frequency of the PWA.

$$\delta = \iint A \sin\left(\frac{m \pi x}{a}\right) \sin\left(\frac{n \pi y}{b}\right)$$

Note: δ is in the perpendicular direction to the PWA surface.

The result is of the form,

$$\delta = \delta_0 \sin\left(\frac{\pi x}{a}\right) \sin\left(\frac{\pi y}{b}\right)$$

The solution for natural frequency is derived for any geometry and various boundary condition. The solutions were plotted for a given weight density ($w/ab = .017$ lb/in^2), Modulus of Elasticity ($E = 2 \times 10^6$ psi), Poisson's ratio ($\mu = .12$), and PWB thickness ($t = .062"$). The values of natural frequency may thus be obtained directly from the plots. If values other than the above are used, correction factors may be used and are shown at the end of this section. The basic stiffness factor used in all cases to determine the natural frequency is as follows.

From Meirovitch[1], the stiffness factor of a plate in general is given by "D",

$$D = \frac{E\ t^3}{12\ (1 - \mu^2)} \tag{29}$$

LEGEND
E = Modulus of Elasticity, psi
t = PWA thickness, in
μ = Poisson's ratio, dimensionless
ρ = $W/abg = \gamma L/g$ mass density, lb sec^2/in^3
W = Total weight of the PWA, lb
γ = Density, lb/in^3
a = Long length of the PWA, in
b = Short length of the PWA, in
g = Acceleration of gravity, 386.4 in/sec^2

Two simple cases are calculated for example purposes.

Case 1[2]

For a PWA with all edges simply supported, the natural frequency is given by:

$$f_n = \frac{\pi}{2}\sqrt{\frac{D}{\rho}}\left(\frac{1}{a^2} + \frac{1}{b^2}\right)$$

for epoxy-glass G-10 $\mu = .12$ and $E = 2 \times 10^6$ psi

$$D = 1.69 \times 10^5\ t^3\ \frac{\text{lb in}^3}{\text{in}^2} \quad \& \quad \rho = \frac{W}{abg} \quad \& \quad g = 386\ \text{in/sec}^2$$

$$f_n = 1.27 \times 10^4\ t^3\ a\ b\left(\frac{1}{a^2} + \frac{1}{b^2}\right)$$

Example a x b = 5" x 5.5", t = .062" PWA and where W = 1.0 lb:

$$f_n = 1.27 \times 10^4\ (.062)^3 (5)(5.5)\left(\frac{1}{5.0^2} + \frac{1}{5.5^2}\right) = 71\ \text{Hz}$$

---

[1] L. Meirovitch, "Elements of Vibration," McGraw Hill, N.Y., 1975

[2] D.S. Steinberg, "Vibration Analysis for Electronic Equipment", J. Wiley & Sons, 1973

Case 2[1]

Example plots of natural frequencies for given rectangular plate geometries are provide for various boundary conditions (see Figures 24,25). The weight density, modulus of elasticity, PWB thickness, and Poisson's ratio are assumed for simplicication purposes and the assumed values are as stated at the beginning of this section. Other plots for other boundary conditions available on request to the author

To determine natural frequency, find the closest boundary condition case and obtain the natural frequency, f_n.

<u>PLOT CORRECTION FACTORS.</u>

1. <u>WEIGHT DENSITY CHANGE.</u> Calculate F = W/ab.
   If $W/ab \neq .017\ \text{lb/in}^2$, then multiply the natural frequency f_n by $\sqrt{.017/F}$
   e.g., if $F = .025\ \text{lb/in}^2$ and $f_n = 100$ Hz
   $$f_n\ (\text{corrected}) = \sqrt{\frac{.017}{.025}}\ 100 = 82.5\ \text{Hz}$$

2. <u>MODULUS OF ELASTICITY CHANGE.</u> Determine E.
   If $E \neq 2.00 \times 10^6\ \text{lb/in}^2$, then multiply natural frequency f_n by
   $$\sqrt{\frac{E}{2.00 \times 10^6}}$$
   e.g., if $E = 2.75 \times 10^6$ and $f_n = 100$ Hz
   $$f_n\ (\text{corrected}) = \sqrt{\frac{2.75 \times 10^6}{2.00 \times 10^6}}\ 100 = 117\ \text{Hz}$$

3. <u>POISSON'S RATIO CHANGE.</u> Any $\mu < .03$ does not significantly change the result and does not require a correction factor.

4. <u>PWB THICKNESS CHANGE.</u> Determine t.
   If $t \neq .062"$, then multiply natural frequency f_n by
   $(t/.062)^{3/2}$
   e.g., if $t = .10"$ and $f_n = 100$ Hz
   $$f_n\ (\text{corrected}) = \left(\frac{.10}{.063}\right)^{3/2}\ 100 = 200\ \text{Hz}$$

---

[1] Ibid

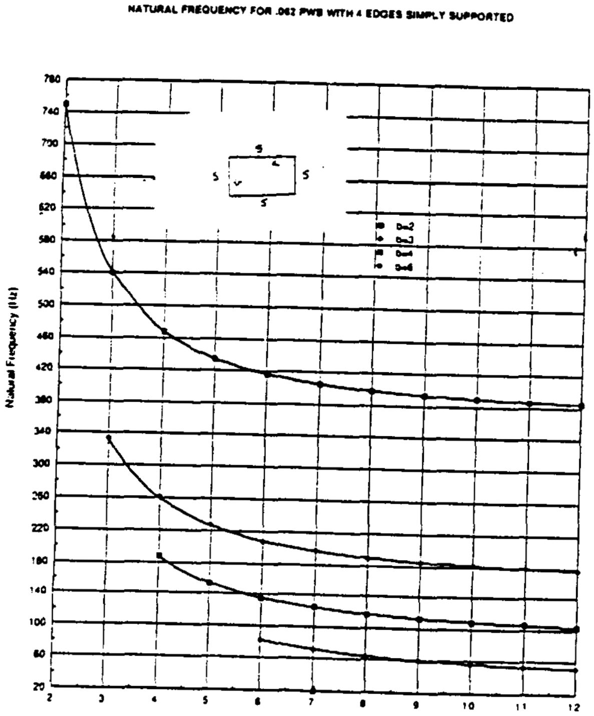

FIGURE 24.

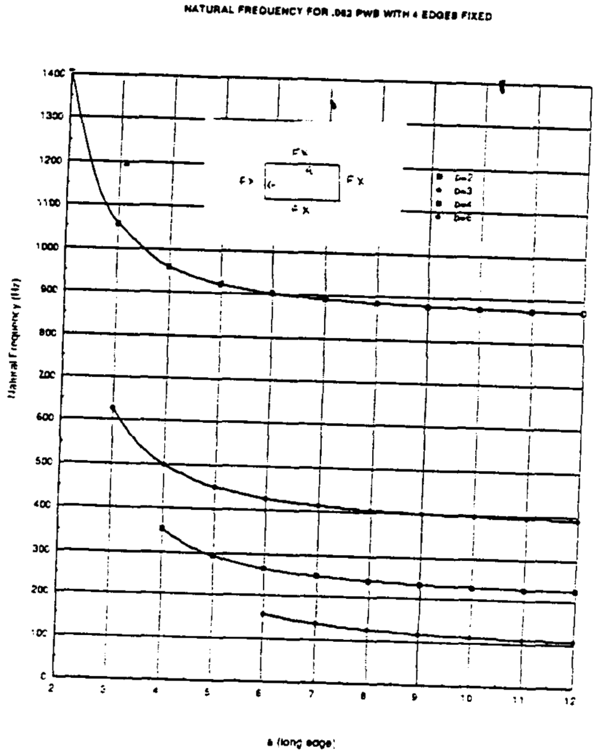

FIGURE 25.

AXIAL LEAD COMPONENTS AND PWB IN BENDING

An axial lead component, such as that shown in Figure 26, is subjected to stress in the leads when a PWA deforms as shown. Equation (31) shows that the stress increases directly as the d/l ratio increases and is also proportional to the span of attachment L. Thus, the components with the highest values for these two parameters are more likely to be damaged in vibration. Equations (32) and (34) provide a guide for the maximum deflection (δ) of the PWA. The values for lead allowable stress and Modulus of Elasticity (E) are obtained from Table 4. It can be seen that steel and nickel wires are very similar structurally. The weight of the component is not a major consideration in this case, but it is important in lateral and transverse vibration. Bonding agents will hold the component down and decrease some of the stress in the lead wires due to vertical motion. There will always be stress in the wires due to PWA bending however.

TABLE 4. LEAD MATERIAL DATA

Lead Material	E 10^6 psi	U.S. psi	S.S. psi	F.S. psi
Steel	30	60,000	30,000	33,000
Nickel	31	52,000	26,000	28,000
Copper (H)	17	48,000	24,000	17,000
Copper (S)	17	33,000	16,500	11,000

LEGEND: E = Modulus of Elasticity
U.S. = Ultimate Strength, psi
S.S. = Shear Strength, psi
F.S. = Fatigue Strength, psi

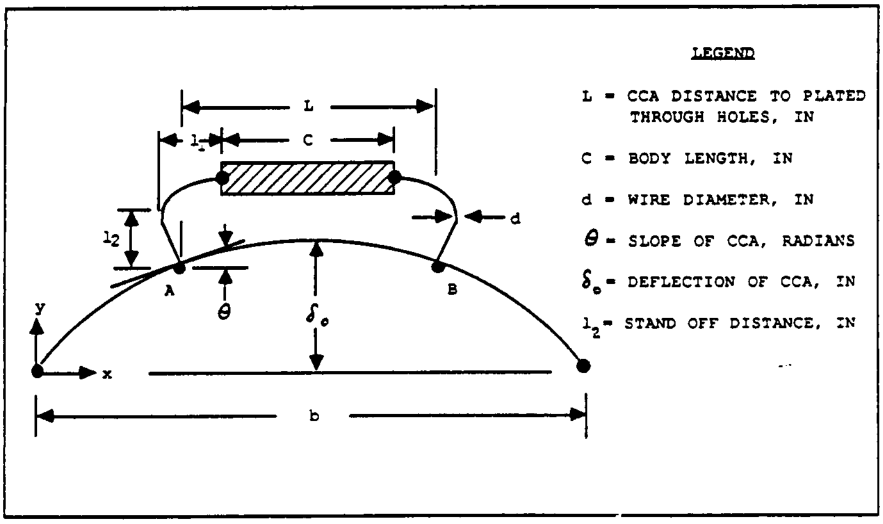

FIGURE 26. DISCRETE AXIAL LEAD COMPONENT IN BENDING

Axial Lead Components and PWB, Simple Support. A typical axial lead component is mounted on a PWA with simple supported edges. The stresses and maximum permitted PWA deflection is analyzed.

From Figure 34:

$$y = \delta_0 \sin\frac{\pi x}{b}$$ (General Sine Shape for PWA in Bending

$$\theta = \frac{dy}{dx} = \delta_0 \frac{\pi}{b} \cos\frac{\pi x}{b} \quad \text{and} \quad x = \frac{b - L}{2}$$

$$\theta = \delta_0 \frac{\pi}{b} \cos\frac{\pi (b - L)}{2b} = \frac{\delta_0 \pi}{b}\left(\cos\frac{\pi}{2} - \frac{\pi l}{2b}\right)$$

$$\theta = \frac{\delta_o \pi}{b} \sin\frac{\pi l}{2b} = \frac{\delta_o \pi}{b}\frac{\pi l}{2b}, \text{ since for } \theta \ll 1, \sin\theta = \theta$$

$$\theta = \frac{\delta_o \pi^2 L}{2b^2} \text{ radians} \qquad (30)$$

Determination of Stress on Leads. The leads of the component shown in Figure 34 are stressed when a PWA is deflected. The leads are pulled down a distance "d" and twisted through an angle θ as shown below:

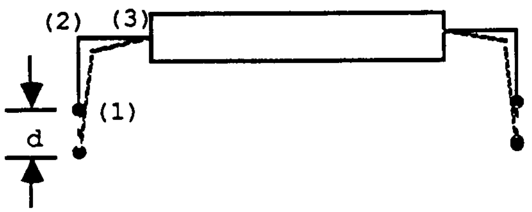

(A) LEAD PULL DOWN

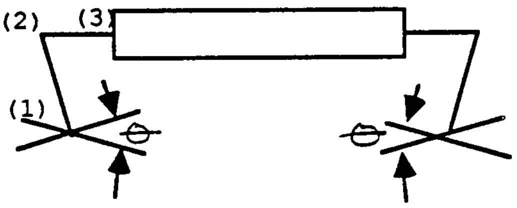

(B) LEAD TWIST

The stress in the leads is therefore composed of two parts (bending and twisting - the twisting actually amounts to another form of bending). The stress analysis is therefore performed in two parts, (A) and (B).

Part A

From a derivation similar to equation (21),

where h = d and d = diameter of lead.

And

$$\delta_{MAX} = (\mathbf{F})\left(\frac{\sigma_{MAX}\ l_1^2}{E\ d}\right)(b/L)^2 \qquad (31)$$

Where $\mathbf{F} \approx 1.048\ (l_2/l_1)$ and $0.1 < (l_2/l_1) < 4.0$

Part B

Given the figure shown,

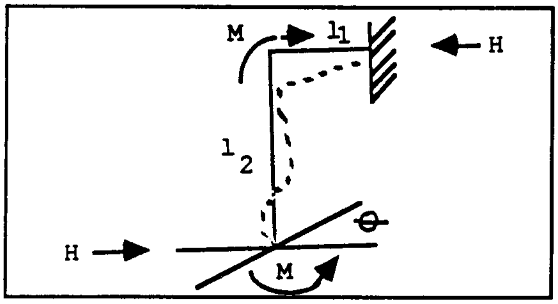

θ = angle of twist of PWA

M = movment induced in lead

$$\sigma_B = \frac{MC}{I} = \left(\frac{\delta_o \pi^2 L E I}{4 b^2 (l_1 + l_2)}\right)\frac{d/2}{I} = \left(\frac{\pi^2 E d}{8 (l_1 + l_2)}\right)\left(\frac{L}{b^2}\right)\delta_o \tag{32}$$

and

$$\delta_{MAX} = \left(\frac{8 \sigma_{MAX} (l_1 + l_2)}{\pi^2 E d}\right)(b^2/L) \tag{33}$$

NOTE: More information on this subject including axial lead components and methods to determine maximum RVSS input levels may be obtained by contacting the author.

SPACE SHUTTLE MAIN ENGINE VIBRATION

N88-18954

Rocketdyne Automated Dynamics Data Analysis and Management System *

Robert B. Tarn

An automated dynamics data analysis and management system implemented on a DEC VAX minicomputer cluster is described. Multichannel acquisition, FFT analysis, and an online database have significantly improved the analysis of wideband transducer responses from Space Shuttle Main Engine testing. Leakage error correction to recover sinusoid amplitudes and correct for frequency slewing is described. The phase errors caused by FM recorder/playback head misalignment are automaticallly measured and used by analysis applications to correct the data. Data compression methods are described and compared. The system hardware is described. Applications using the database are introduced, including software for power spectral density, instantaneous time history, amplitude histogram, fatigue analysis, and rotordynamics expert system analysis.

ADDAM SYSTEM DEVELOPMENT

Historically, the analysis of wideband data from Space Shuttle Main Engine (SSME) hot-fire tests has involved a time-consuming manual analysis of power spectral density (PSD) plots, isoplots, root mean square (RMS) time history plots, tracking filter plots, and the like. Manual annotation, comparison, and trend analysis to determine the dynamic characteristics of the hardware under test, assess engine health, and detect anomalous behavior required many hours. More detailed analysis of test responses, such as precise phase correlation, amplitude distribution analysis, and use of instantaneous time histories, was often prohibitively time consuming; these special applications were usually reserved for major anomally or engine failure investigation.

The requirements of SSME hot-fire test data analysis have expanded since the early test program (1977-1978). Increased test frequency, test duration, number of transducers, and analysis bandwidth have imposed a combined 15-fold increase in processing demand. The extensive tape handling needed to complete the data processing for a typical SSME test resulted in unacceptable delays in test turnaround. The possibility of overlooking early warnings of component failure increased due to the volume of data and limited resource of skilled personnel to evaluate it. A quantum jump in the systems and methods of wideband data processing and analysis was needed.

---

*Portions of the work reported herein were sponsored by NASA/Marshall Space Flight Center under Contract NAS8-27980.

Significant advancement has been made at Rocketdyne with the Automated Dynamics Data Analysis and Management (ADDAM) system. ADDAM is an integrated acquisition, digitization, mass storage, and analysis system implemented on a DEC VAX minicomputer cluster. Two multichannel acquisition subsystems, one 16-channel and one 28-channel, can acquire and Fourier transform all data from a single FM tape at wideband data rates up to 256,000 samples per second. All analyses needed to evaluate the behavior of the engine and to diagnose the engine health can be drawn from the digitized data, thus avoiding the multiple handling of the FM tapes. Figure 1 illustrates the simplified processing scheme for a typical SSME test. The typical data processing times before, during, and after phase-in of the ADDAM system, since it went online in November 1985, are shown in Fig. 2. This system is now being used to reduce all wideband measurements for entire test durations at a sampling rate of over 10 kHz in real time, an aggregate of over 2 gigabytes (GB) of data for a typical 520-second test. The data storage requirement has been met using state-of-the-art optical disk media. From this raw data base, all standard analyses are drawn, and automation of the manual analysis is underway.

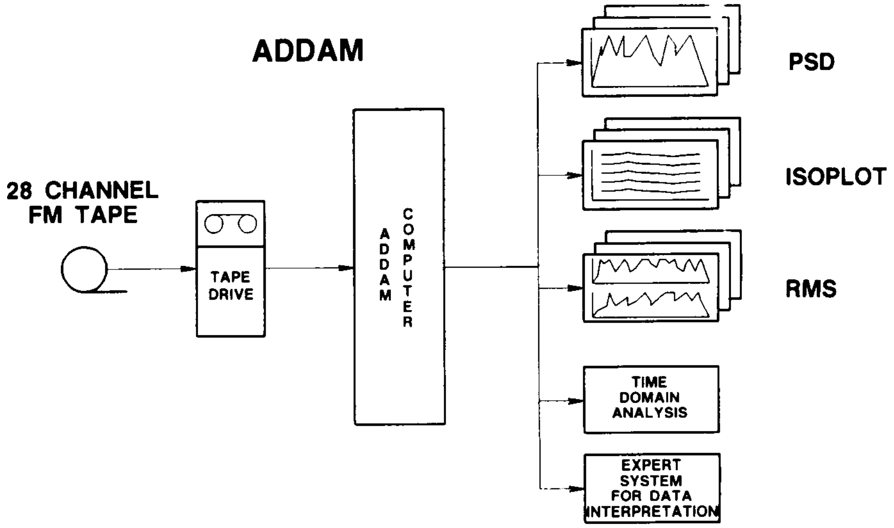

- 14/28 CHANNELS AT A TIME
- 800/1600 SECONDS MAXIMUM
- AUTOMATED TAPE CONTROL
- AUTOMATED SETUP AND CALIBRATION
- MULTI-BAND ANALYSIS FROM SINGLE ACQUISITION
- DIGITAL STORAGE OF RESULTS
- PREVIOUS TEST DATA IN DISK LIBRARY FOR IMMEDIATE RECALL

Fig. 1. Multiple Analyses from Single FM Tape Playback

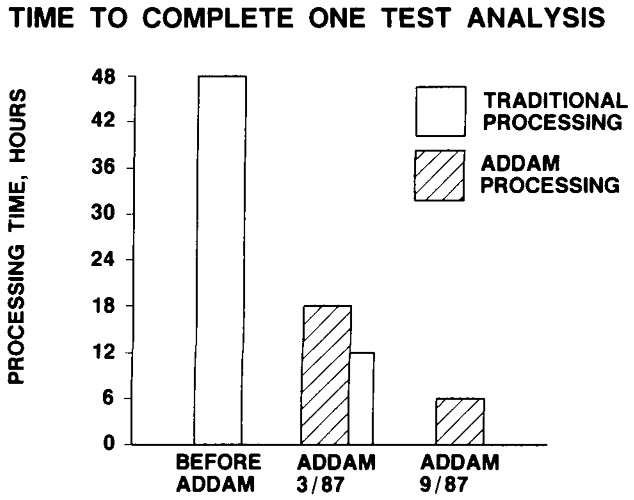

Fig. 2. Reduced Data Processing Using ADDAM

DIGITIZATION CAPABILITIES

To provide a comprehensive and quality database needed for diverse analytical disciplines, the ADDAM system made a number of technical advances. The following describes a few of these.

High Analysis Bandwidth

Many real-time data analysis systems rely on the use of a guard band to minimize alias error. The relatively low rolloff rates of the anti-alias filters of many systems require such caution. The filters employed on the ADDAM system have such sharp rolloff (130 db/octave) that the transition region can be neglected in most cases. As a result, the data of the ADDAM system are often alias free up to the Nyquist frequency. While alias error can occur for a small transition band, the offsetting benefit is increased analysis bandwidth.

Leakage Error Correction

Rectangular windowing is used to permit inverse transformation of the database FFT records. Windowing which ensures that the data sequence is zero at the ends of the sample frame prevents recovery when the FFT is inverse transformed. Leakage occurs when the frequency of a sinusoid does not fall exactly on a multiple of the analysis bandwidth, and is often described as a loss of energy from a primary spectral band into adjacent bands. However, another effect of leakage error is a slewing of the estimate of the frequency, since the FFT analysis can only resolve to within the analysis bandwidth.

Leakage error in the power spectral density is reduced by ADDAM routines using side band integration to estimate the total magnitude of sinusoids, and an amplitude weighted centroid method to more precisely determine their frequencies (Fig. 3):

$$a_c = \sqrt{a_{i-2}^2 + a_{i-1}^2 + a_i^2 + a_{i+1}^2 + a_{i+2}^2} \tag{1}$$

$$f_c = f_i + \Delta f^*(a_{i+1} - a_{i-1})/(a_{i+1} + a_i + a_{i-1}) \tag{2}$$

Table 1 demonstrates the relative error between a leakage-free analysis, a typical case for a sinewave not aligned on an analysis band, and the result of ADDAM leakage error correction. Application of this technique has resulted in elimination of the "chatter" in tracking filter analysis when the actual frequency is between analysis bands.

Phase Correction

Variation in the alignment of the FM tape recorder and playback heads produces large phase errors due to time delays between channels on the FM tape (Fig. 4). These errors have been found to be as large as 120 degrees at 200 Hz. An algorithm was developed [1] to routinely determine these phase errors using analysis of a high-frequency, squarewave calibration signal sumultaneously recorded on all channels of a tape. The multiple superharmonics of the squarewave provide the means to determine the channel-to-channel phase errors.

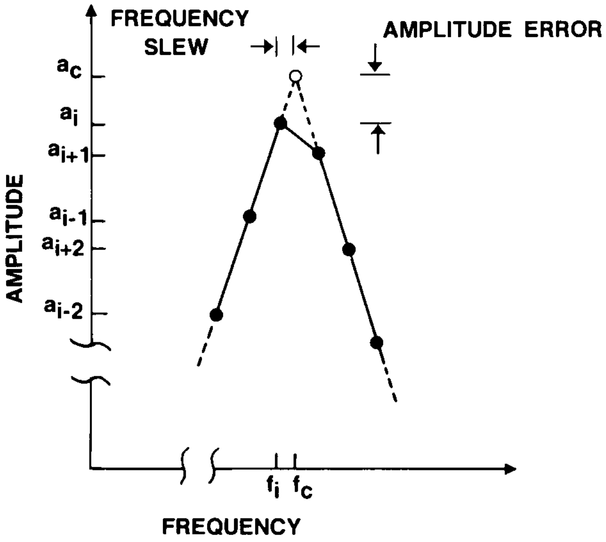

Fig. 3. Leakage Error Correction

Table 1. Leakage Error Correction Data

	NO LEAKAGE	WITH LEAKAGE	LEAKAGE CORRECTION
AMPLITUDE	1.	0.858 (14%)	0.973 (3%)
FREQUENCY, Hz	100.	99.7	99.8

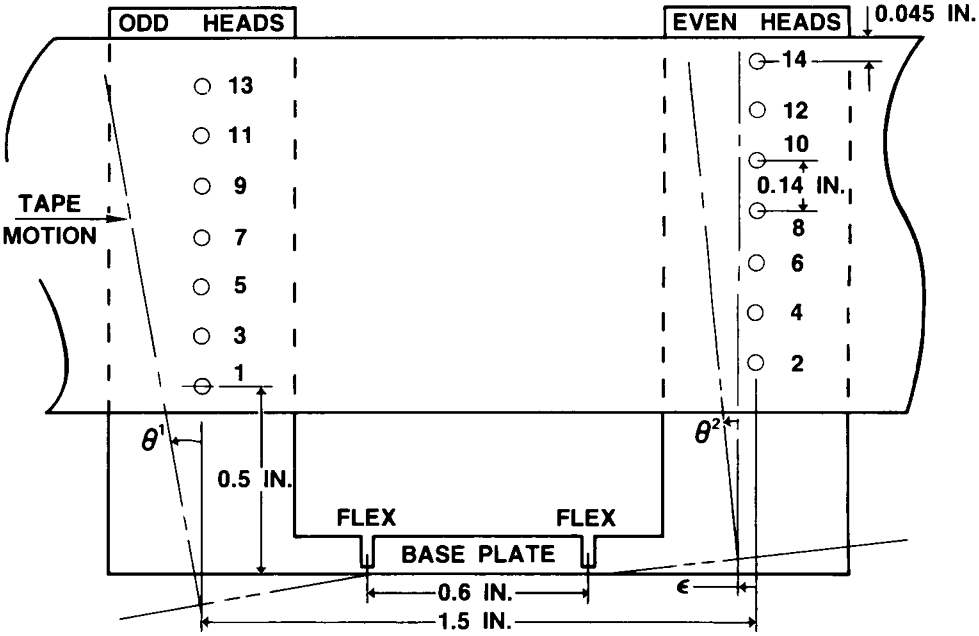

Fig. 4. FM Tape/Head Geometry

The transfer function phase (Fig. 5) at the fundamental and superharmonics of the squarewave is used to obtain an estimate of the phase slope (deg/Hz) of each transfer function. The transfer functions are scanned for points of high coherence using the transfer function phase confidence interval (Fig. 6) defined as [2]:

$$\Delta\phi_{ij} = \text{arc sin}[2/(n-2) * F_{2,n-2;\beta} * (1-\hat{\gamma}_{ij}^{2})]^{1/2} \qquad (3)$$

where

n = sampling degrees of freedom

β = desired statistical level of confidence

$F_{2,n-2;\beta}$ = 100 β percentage point of an F-distribution for degrees of freedom 2 and n-2

$\hat{\gamma}_{ij}^{2}$ = square of the coherence between the ith and jth channels

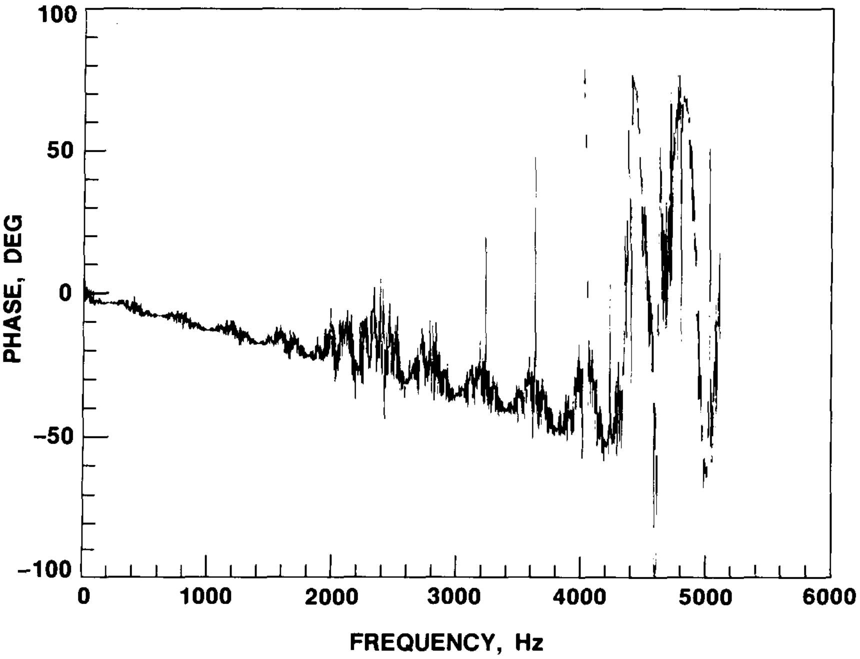

Fig. 5. Phase Calibration Signal Transfer Function Phase

The phase data that pass a tolerance test on $\Delta\phi$ (e.g., 2 degrees) are unwrapped into approximate colinearity and linear regression is then used to determine the phase slope, α, for each transfer function. The transfer function phase can be assumed to have a zero intercept, therefore the linear regression equation becomes

$$\alpha = \Sigma f_i \, \phi_i / \Sigma f_i^{2}, \; i=1,m \qquad (4)$$

where

m = number of transfer function points used in the linear regression

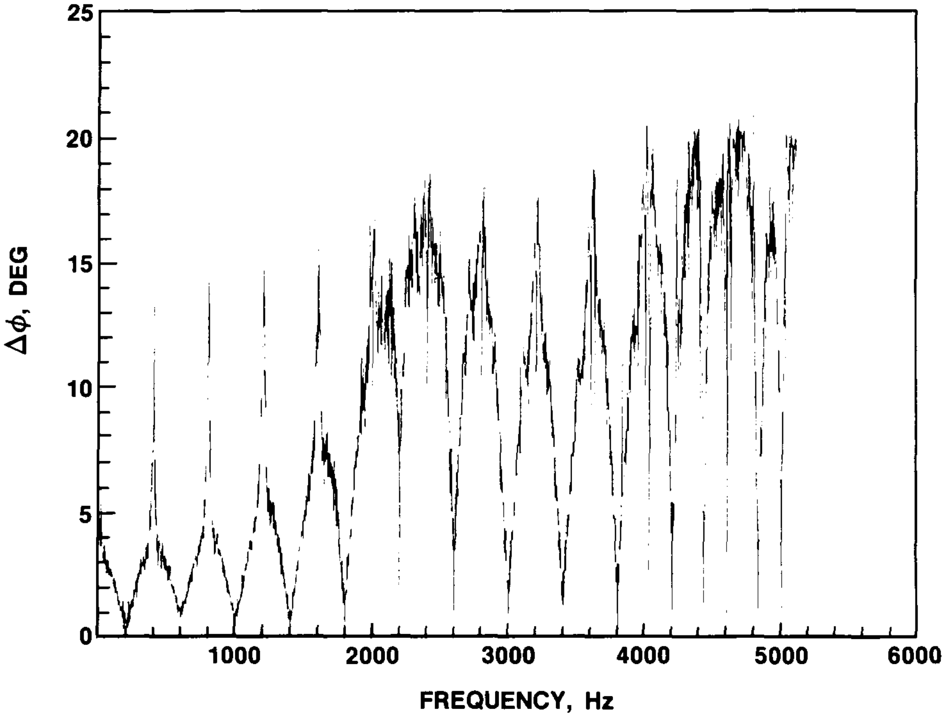

Fig. 6. Transfer Function Phase Confidence Interval

The standard error of regression can be computed using

$$\sigma = [(\Sigma\phi_i^2 - \alpha\Sigma f_i\ \phi_i + \alpha^2\ \Sigma f_i^2)/(m-1)]^{1/2} \tag{5}$$

The phase slope estimates are then improved using the method of least squares to fit them to the model of the tapehead geometry (Fig. 4) given by

$$\begin{aligned}\alpha_{ij}(\theta_1, \theta_2, \epsilon) = \ & [i * \mathrm{MOD}(i,2) - j * \mathrm{MOD}(j,2)] * \theta_1 \\ & + [i * \mathrm{MOD}\ (i-1,2) - j * \mathrm{MOD}(j-1,2)] * \theta_2 \\ & + [\mathrm{MOD}(i-1,2) - \mathrm{MOD}(j-1,2)] * \epsilon\end{aligned} \tag{6}$$

where

α_{ij} = phase slope of channel i relative to channel j

Although many combinations of transfer functions may be used in the least-square fit, the best results are obtained by using only the extreme upper and lower channels on the heads. This phase correction method has been tested using data generated with known phase errors, demonstrating that the phase errors are determined to within 0.3 degree at 200 Hz.

The kth element of an FFT vector, R_k, can be corrected to eliminate phase error by complex rotation to R_k' using

$$\phi_k = (1-k) * \alpha \tag{7}$$

$$R_k' = R_k * \exp(\sqrt{-1} * \phi_k) \quad (8)$$

Time history data can be corrected by offsetting the temporal arrays according to the time delay given by

$$\tau = \alpha/(\Delta f * 360) \quad (9)$$

where

Δf = analysis bandwidth

Data Storage Reduction

Data compression methods have been developed and tested. These consist of 16-bit and 12-bit floating point formats and a 16-bit normalized integer format that limit real number precision and dynamic range but substantially reduce storage requirements.

The alternative floating point formats developed for the ADDAM system employ various allotments of bits between the mantissa and the characteristic to achieve reduced storage. Table 2 shows the construction of four floating point formats that have been tested. Type 32 is the VAX 32-bit format (uncompressed). Since floating point numbers can be normalized such that the most significant mantissa bit is set (binary fraction is always greater than or equal to 0.5), this bit is implied in all of these formats.

Table 2. Compressed Floating Point Formats

FORMAT TYPE	CHARACTERISTIC BITS	MANTISSA BITTS	MAXIMUM ERROR, %	DYNAMIC RANGE, dB
32	8	23	0.000012	1500
16	8	7	0.78	1500
16-1	5	10	0.098	190
12	5	6	1.5	190

As shown in Table 2, the dynamic range and precision of the resulting compressed number is adequate for most analysis purposes. Type 16-1, with a maximum truncation error of less than 0.1%, is a good combination of reduced storage, adequate dynamic range, and acceptable precision.

For the 16-bit normalized integer format, each component of a block of data is normalized by the block maximum (block scale), then multiplied by 32,767 and converted to integer type. Normalized integer formats are much faster to compress and uncompress, but the relative precision results are very different than with the floating point formats.

The normalized integer format precision is determined by the block scale and the number of "counts" in a signed 16-bit integer (32,767). The amount of relative error varies with the magnitude of the number; near the full-scale value, the relative error is only 0.003 percent, but for data at 2 percent of full scale the truncation error is 0.15 percent. Dynamic range, however, is not limited since the block scale determines the dynamic range and is stored in full 32-bit floating point format.

HARDWARE DESCRIPTION

A cluster of VAX 11/750 and MicroVAX computers has been created to facilitate control of the simultaneous digitization, database maintenance, analysis, and data transmission tasks required by the integrated ADDAM system (Fig. 7). Functional redundancy of all critical processes is also provided, including CPUs, disk drive capacity, drive controllers, and high-rate data acquisition subsystems.

Automated analysis of test data requires a high efficiency of the front-end process that digitizes signals reproduced from FM tapes, transforms the digitized time histories into Fourier coefficients, and stores the data for use in analysis tasks. The system is flexible with regard to the data acquisition specifications (AC/DC coupling, anti-alias filter frequency, sampling rate, FFT block size, and acquisition start/stop times), and the system completely controls these parameters along with the FM tape operation via digital interface with the host computer.

The anti-alias filter settings are selectable from 10 to 100,000 Hz., and filter rolloff is 130 db/octave. Sampling rates for each channel are selectable from 20 to 500,000 Hz.. Bipolar analog-to-digital converter precision of 15 bits and fixed input sensitivity of 5 volts provides high resolution and overrange free data. FFT processors transform digitized time history points into Fourier coefficients, with a minimum block size of 128 points and maximum block size of 16,384. The FFT processor speed is 0.007 second for a 4096-point block.

The acquisition subsystems include sufficient mass storage to allow them to operate independently of the VAX I/O processors during data acquisition, and are capable of storing digitized time histories for up to 800 seconds of data from 28 channels at a sampling rate of 20,480 Hz. (0.9 gigabytes). Real-time acquisition and FFT transformation are typically performed with a sampling rate of 10,240 Hz and block size of 4096 samples. At higher sampling rates or larger block sizes, the system digitizes the data in real time, and post-processes to perform the FFT calculations.

The acquisition subsystems are also functional as general purpose array processors to perform a wide variety of mathematical functions using data downloaded from the host computers, including inverse FFT transformation, thus greatly increasing the speed and analytical capability of the system.

To interface with the data systems at the Marshall Space Flight Center, the ADDAM system will include communications hardware to transmit over the NASA Program Support Communications Network (PSCN). This link will eliminate the delay of FM tape transmittal between the various test and analysis centers (Fig. 8), thus greatly decreasing the test turnaround time.

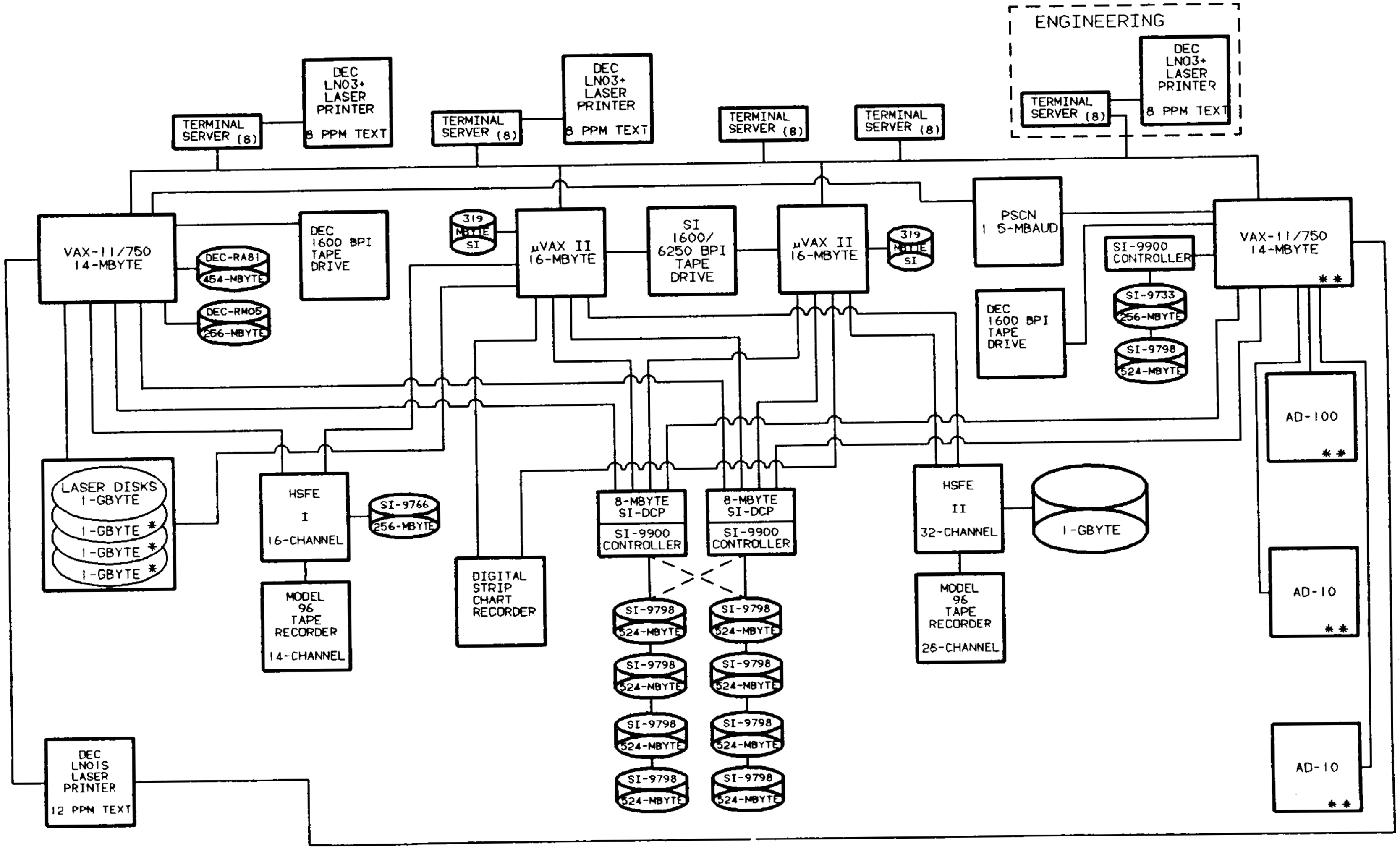

NOTE ALL DISK DRIVES ARE SHOWN WITH FORMATTED CAPACITY
** ROCKETDYNE HYBRID SIMULATION EQUIPMENT

Fig. 7. ADDAM System Schematic

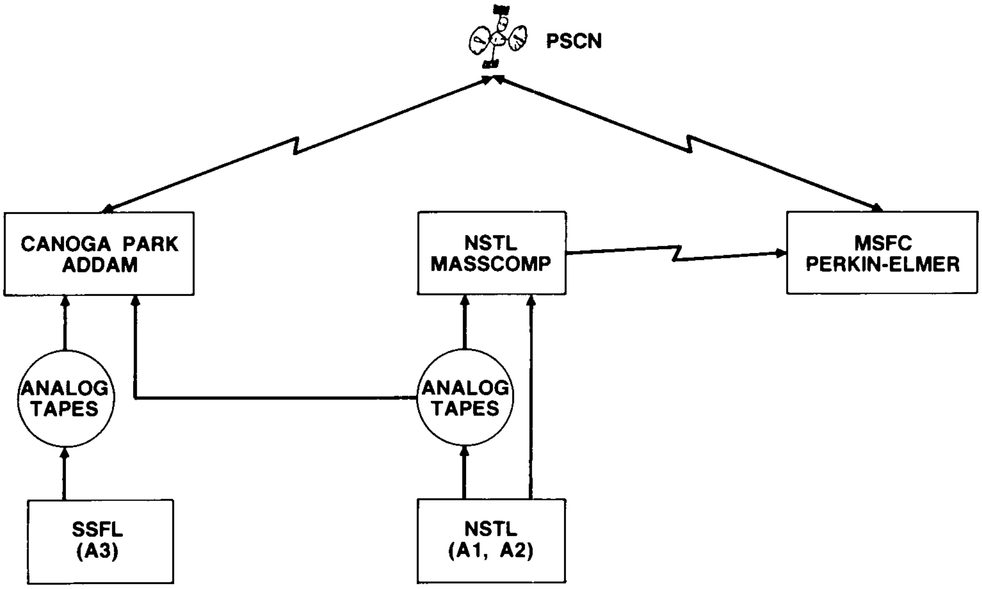

Fig. 8. PSCN Communication Network

QUICKLOOK - ADDAM DATABASE "WORKHORSE"

The standard analyses needed for quick test turnaround are provided by the ADDAM QUICKLOOK program. PSD, RMS time history, isoplot (waterfall plot), amplitude histogram, and instantaneous time history analyses are all available through this program in batch mode or interactively. Examples of these analyses are shown in Fig. 9 and 10.

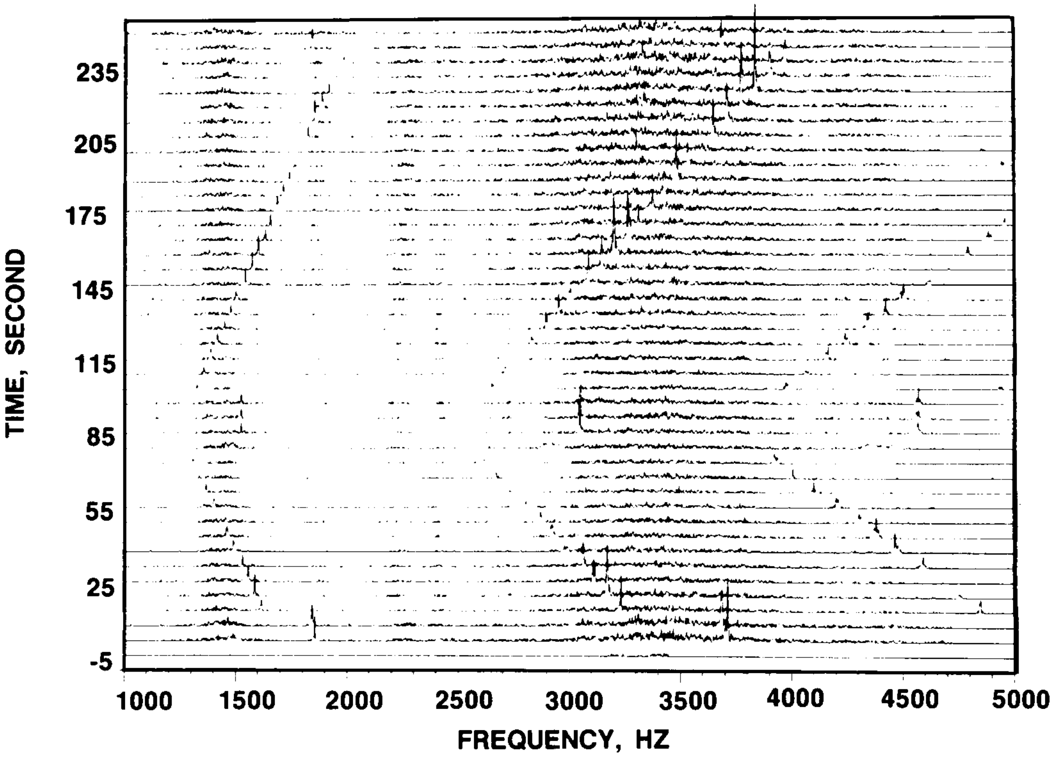

Fig. 9. QUICKLOOK Isoplot Analysis

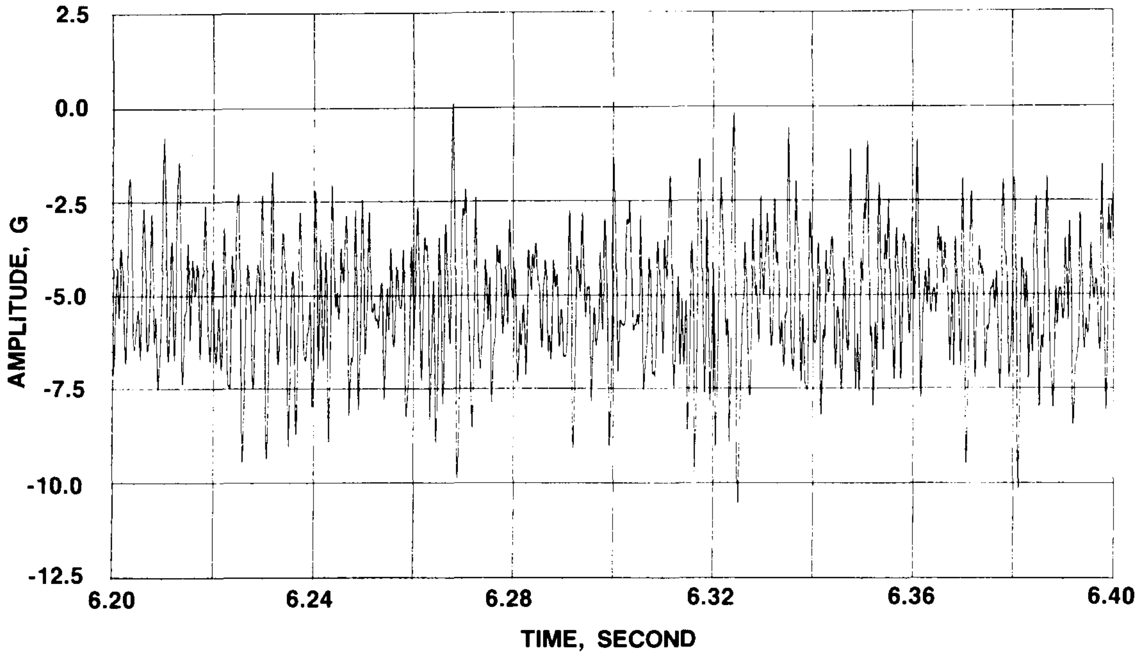

Fig. 10. QUICKLOOK Instantaneous Time-History Analysis

Automation of the system is progressing toward that illustrated in Fig. 11. Batch processing may be requested using an interactive program called REQUEST. The REQUEST program organizes all of the data requirements and envokes the data acquisition and analysis systems to perform the necessary functions. If data are needed, the ADDAM system issues an operator request to mount the appropriate FM tape. For requests that can be satisfied using data previously digitized and stored, the appropriate archive disk is mounted and the analysis proceeds. Once verified by the expert system and reviewed by an ADDAM database manager, results are delivered back to the requestor.

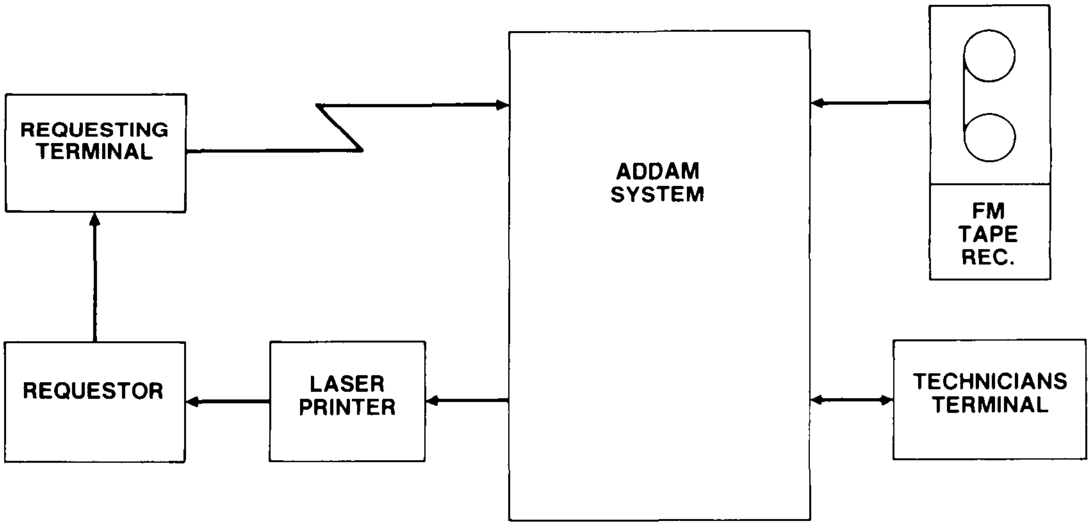

Fig. 11. Data Request Automation

For selected measurements, responses are being statisticized over many tests. The principal independent parameters governing the dynamic responses have been identified as engine power level, oxidizer and fuel tank pressures, hardware configuration, and preburner mixture ratio. Sample records are currently grouped according to power level for ensemble analysis. The maximum, minimum, mean, and standard deviation of a transducer's ensemble responses are being databased, and will be used in automated data verification and anomally detection routines. Ensemble maximum (envelope) and mean responses are overlayed with PSDs computed over records of comparable independent parameter conditions (Fig. 12).

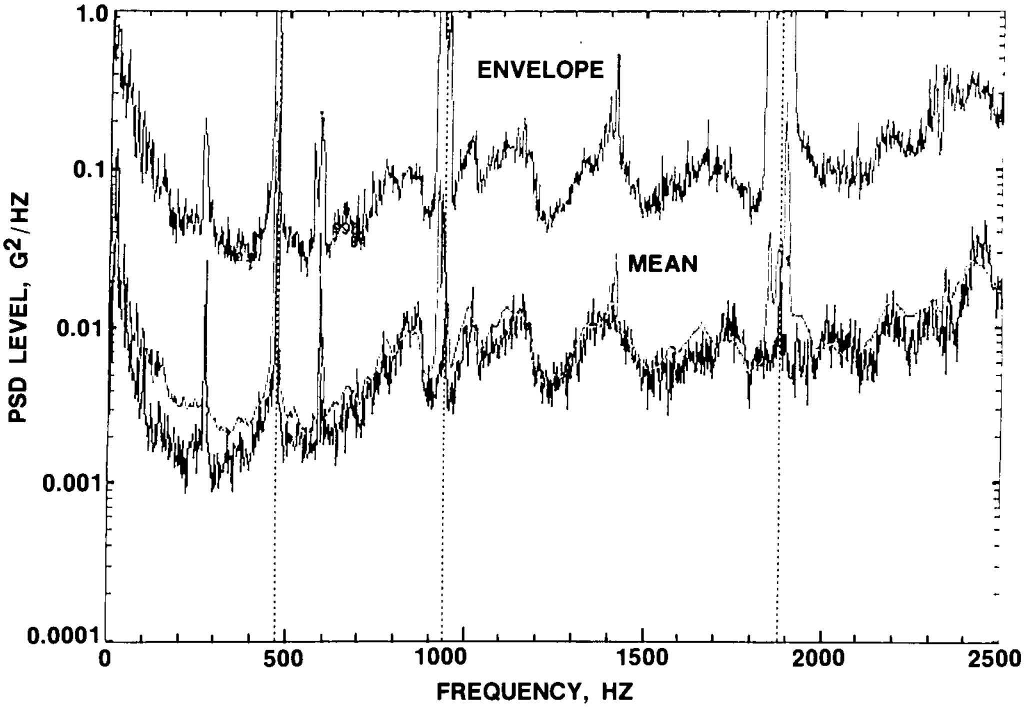

Fig. 12. Envelope Overlay with QUICKLOOK PSD Analysis

INTEGRATED DATA ANALYSIS APPLICATIONS

The ADDAM system has contributed toward significant enhancement of the analytical capabilities of structural and dynamic analysis disciplines at Rocketdyne by providing a reliable source of comprehensive test data. The following are a sampling of analysis applications developed on and made part of the system.

Fatigue Analysis

Rocketdyne's RIDLE and FDAS fatigue life evaluation codes perform analysis in the frequency and time domain, respectively. Using these codes on the ADDAM system, component life can be more realistically and accurately predicted. Fatigue damage analysis, for instance, is now computed using actual time-history responses for entire test durations. This improvement has resulted in life extention for many critical SSME components. Distribution fitting (Fig. 13) is increasing the accuracy of frequency domain methods.

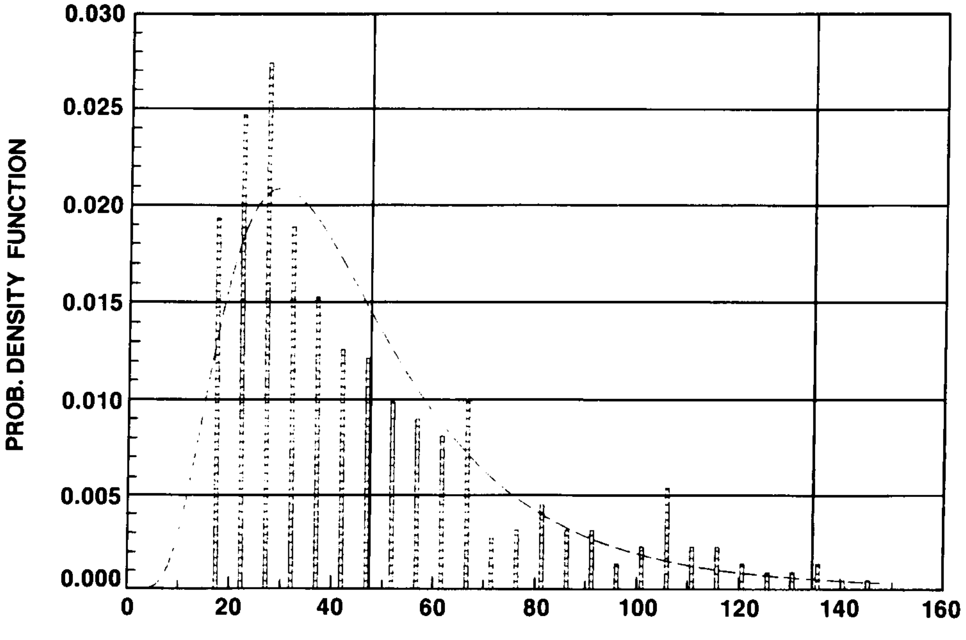

Fig. 13. Probability Density Function and Curve Fit

High-G Impeller Analysis

Hotfire testing of the SSME high pressure oxidizer turbopump (HPOTP) has identified impellers with high synchronous dynamic loads. Using the ADDAM system, analysis is underway to identify the cause of these high dynamic loads. Precise phase correction (±2 degrees of shaft rotation) is needed to compute bearing load magnitude and phase angle time history from strain gages located on the bearing support structure.

Rotordynamic Expert System

Definition of principal independent variables for the SSME dynamic environment and correlation analysis using multifunctional regression has been used to define the relationships between these independent variables and the engine dynamic environments. A team of experts reviews data from the ADDAM system and identifies "expected events" (indicating the nominal operation of the turbopumps), and "unexpected events" (indicating data of unknown origin, or anomalies). Hypotheses of the source of anomalies are made and tested by various methods. For example, correlation with the statis- ticized ensemble responses, previous test and trends, component test data, computer simulations, and expert experience are used to test the expert system hypotheses.

A prototype expert system (ADDAMX), developed using a rule induction expert system tool called EX-TRAN 7, analyzes rotordynamic data from the low and high pressure fuel and oxidizer turbopumps on the SSME. It is capable of identifying the synchronous vibrations of the rotating machinery, the feed throughs from one turbopump to another, and some critical bearing frequencies. Figure 14 illustrates a PSD analysis processed by the ADDAMX expert system. The plot notation includes frequency, PSD level, and source identification for the sinusoidal components of the signal. The final product is a report on the operation of the turbopumps.

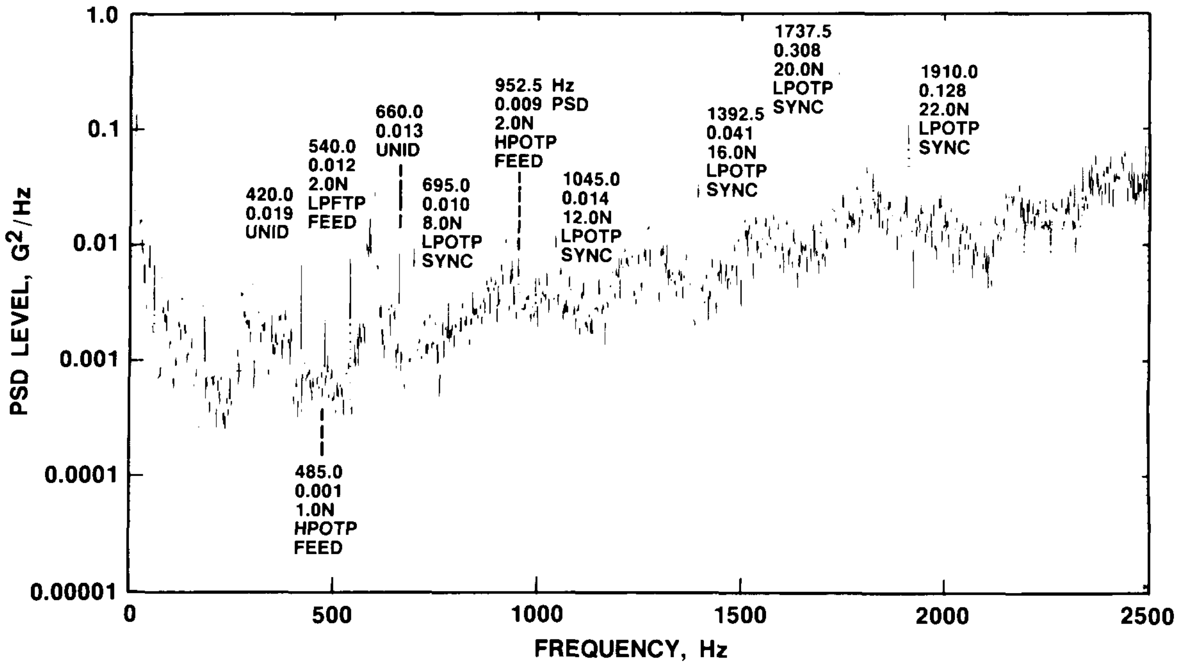

Fig. 14. Rotordynamic Expert System PSD Analysis

CONCLUSION

The ADDAM system has significantly advanced the art of data analysis at Rocketdyne. Since going online in November 1985, the system has dramatically reduced test turnaround time. The database is now comprised of data for the most recent 100 tests, with an aggregate duration of 43,265 seconds. There are 5856 individual measurements, requiring over 55 gigabytes of mass storage, distributed on the system's online magnetic media and archive optical disk media. For any of these data, the expected retrieval time is only a few minutes.

The system's digitization and analysis capability has improved the quality of the data by providing high analysis bandwidth, leakage error correction, and phase error correction. Data storage reduction methods have increased the system storage capacity.

The cluster of VAX computers and peripheral equipment provides an analytical muscle that is supporting improvements in analytical tools used in diverse engineering disciplines. The future development of the expert systems integrated with the database will affect improvements in quality and efficiency at Rocketdyne for years to come.

REFERENCES

1. Rocketdyne internal letter from J. R. Fenwick to J. E. Cusack on 11 April 1986 - Subject: FM Tape Recorded Data Phase Errors and Recommended Calibration Procedures.

2. R. K. Otnes and L. Enochson, Applied Time Series Analysis, Vol. 1, John Wiley and Sons, 1978.

ISOLATION AND DAMPING

N88-18955

Spacecraft Redesign to Reduce Microphonic Response of a VCO Component

J. C. Strain
S. Mittal

ABSTRACT

Reaction wheel vibration was found to induce out-of-specification sidebands on the carrier frequencies of some spacecraft components containing mechanical Voltage Control Oscillators (VCOs). Concurrent investigations were performed to redesign the VCOs to reduce their response to the wheel vibration, and to design a reaction wheel isolation system to reduce the vibration input to the affected components. Component level tests have indicated that both efforts produced viable solutions. The redesigned VCO will be incorporated into future spacecraft of the series, while affected spacecraft already in production will be retrofitted with the reaction wheel isolation system.

INTRODUCTION

This paper describes redesign efforts made to resolve a problem with a vibration sensitive Voltage Control Oscillator (VCO) assembly on the Defense Satellite Communications System III (DSCS III) Spacecraft. The mission of the DSCS III Satellite is to provide an enhanced military communications capability through the 1980s and 1990s. At anytime, four DSCS III satellites, each with a ten year mission life, operate in geosynchronous orbit to provide worldwide protected services to ground, sea, and airborne forces.

The DSCS III satellite is designed to be placed into a low inclination geosynchronous orbit on either the Titan 34D/IUS, Titan 34D/Transtage or Shuttle/IUS launch systems. The satellite can be configured for a dual launch with either a DSCS III satellite or another DSCS III in a tandem launch mode, as shown in Figure 1. Also shown in this figure is the satellite in its orbital configuration. On orbit stabilization is about all three axes with four Attitude Control System reaction wheels.

The DSCS spacecraft has several components which contain microphonic VCOs. During the production cycle of the program, it was found that in some vehicles the VCOs in two components on the North Equipment Panel may be sensitive to the vibration induced by the reaction wheels. Out of specification sidebands were noted on the carrier of affected components at multiples of the 400 Hz pulse which runs the wheels. Sidebands were greatest and out of specification at 1600 Hz. Significant sidebands were also noted at 3200 Hz.

The problem was to redesign the spacecraft to reduce the amplitude of sidebands caused by reaction wheel excitation with minimal impact on the cost and the production schedule. A two pronged approach was used for the solution. Structural changes were sought to reduce sensitivity to the 1600 Hz and 3200 Hz excitation by VCO component evaluations. Simultaneously, investigation was begun to reduce the excitation through reaction wheel isolation. This paper discusses the two solution approaches, results of the investigations and recommended solutions along with test results. The next section discusses VCO component evaluations and is followed by a section on the design for vibration isolation.

VCO COMPONENT EVALUATION

The VCO assembly is shown in Figure 2. The outer box consists of machined aluminum sides and a separator wall running through the middle of the box. The box has an aluminum top cover attached by means of five screws. The figure shows the box with the top cover partially removed to reveal details. The resonator rod is located in the lower right cavity. It is a hollow rod supported on two L-shaped rexolite brackets. The left bracket is glued to the bottom of the box whereas the middle bracket is attached to the outer side with two screws. The right end of the rod is screwed to the outer wall. The left end of the rod is attached to a strap spring. A probe extends from the middle wall in between the two brackets.

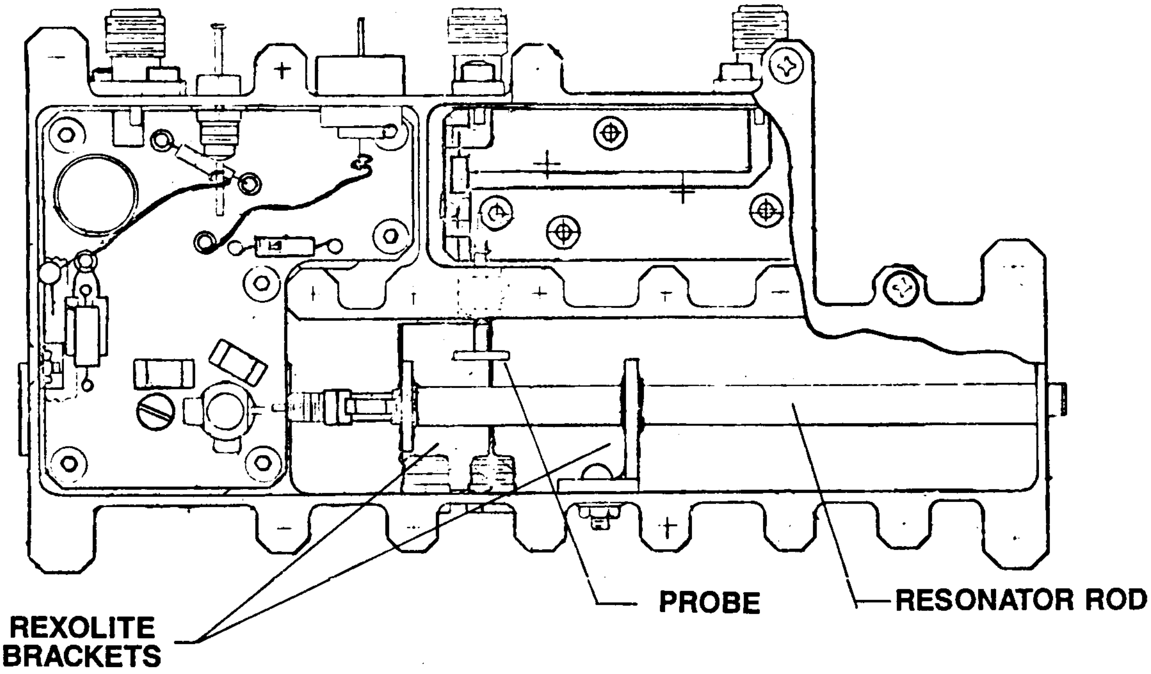

Figure 2. VCO Assembly (Top View)

The component evaluation was performed in three phases. In Phase I, dynamic analysis was performed on the VCO assembly and components to determine vibrational characteristics and recommend any solutions. The Phase II consisted of performing impedance hammer tap tests on the component hardware to validate the analytical model. Shaker tests of the component were conducted in Phase III of the evaluation process. This involved verification of analytical predictions and recommended design changes.

Dynamic Analysis of VCO Components

A detailed NASTRAN finite element model of the VCO assembly was made with the SUPERTAB/IDEAS system. The analysis was performed on the IBM 3090 system with the MSC/NASTRAN finite element program. The model is shown in Figure 3. Special care was taken to model the resonator rod stiffness and inertia distribution and its attachment to the VCO outer box. Rexolite brackets were modelled in detail to provide for variable fixity, to and offsets from the box center lines. The model consisted of 254 structural elements, 153 nodes and 175 dynamic degrees-of-freedom. A number of simpler component models were analyzed to trace the source of the 1600 Hz amplification. These included the probe model, the strap spring model, plate models to represent VCO outer box sides, and the resonator rod on its bracket model extracted from the overall assembly model. Of these component models, only the resonator rod model provided a clue to the sideband problem. It revealed that the rod resonant frequencies are very sensitive to the bracket fixity. The natural frequency varied from 1458 Hz to 2291 Hz for the first bending mode in the lateral plane and from 2036 Hz to 3289 Hz for the first bending mode in the vertical plane depending on the bracket attachment conditions. The rexolite brackets themselves, as originally designed, appeared to be very flexible.

The eigenvalue analysis performed on the VCO assembly showed that there are no natural frequencies below 1500 Hz. The first two modes calculated are shown in Figures 4 and 5, where the dotted lines represent the deflected shape superimposed on the undeformed configuration shown by the solid lines. The natural frequencies were found to be 1949 Hz and 2618 Hz for the two beam bending modes. This analysis was based on the assumption that the left bracket is glued

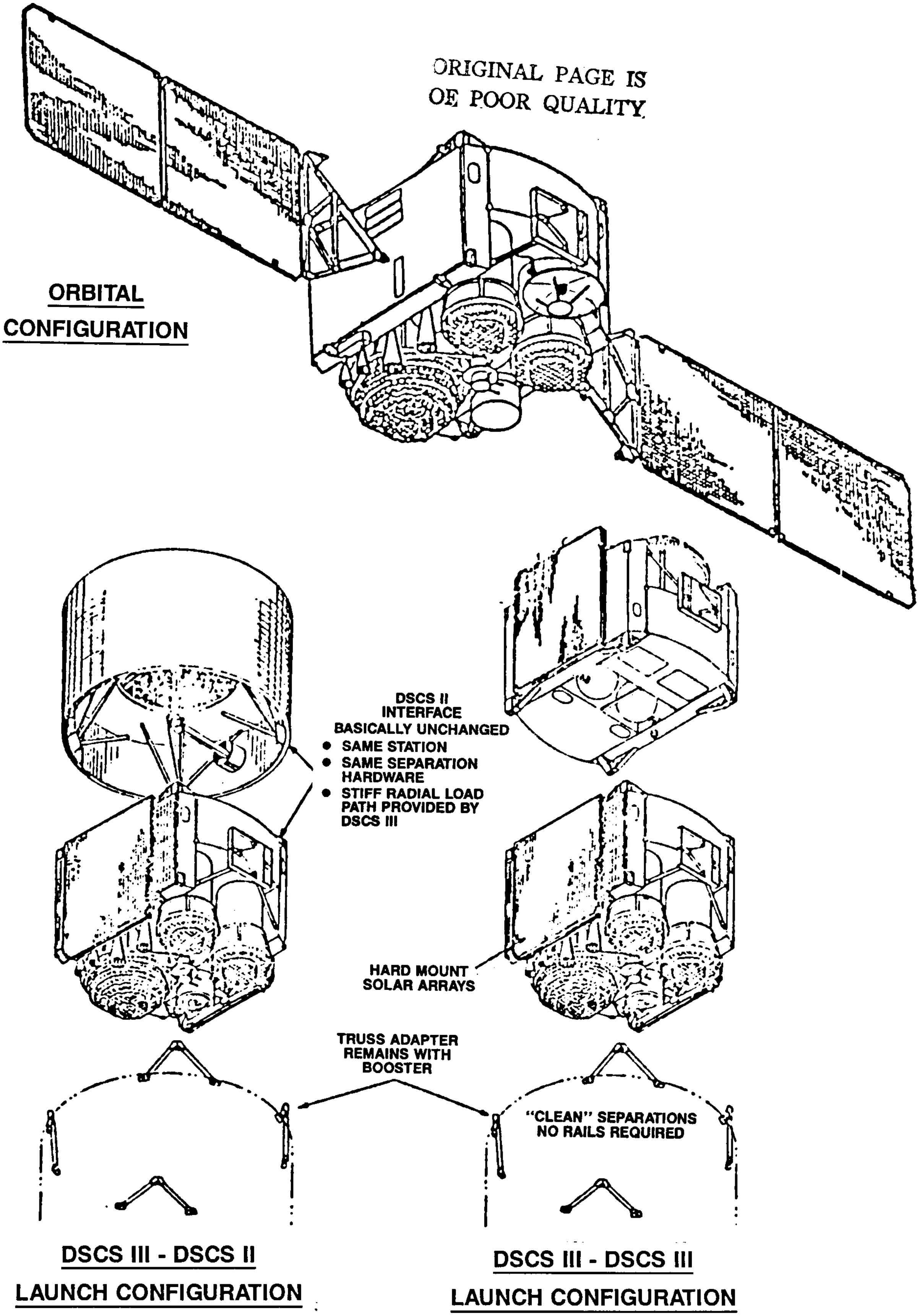

Figure 1. DSCS III Spacecraft Configurations

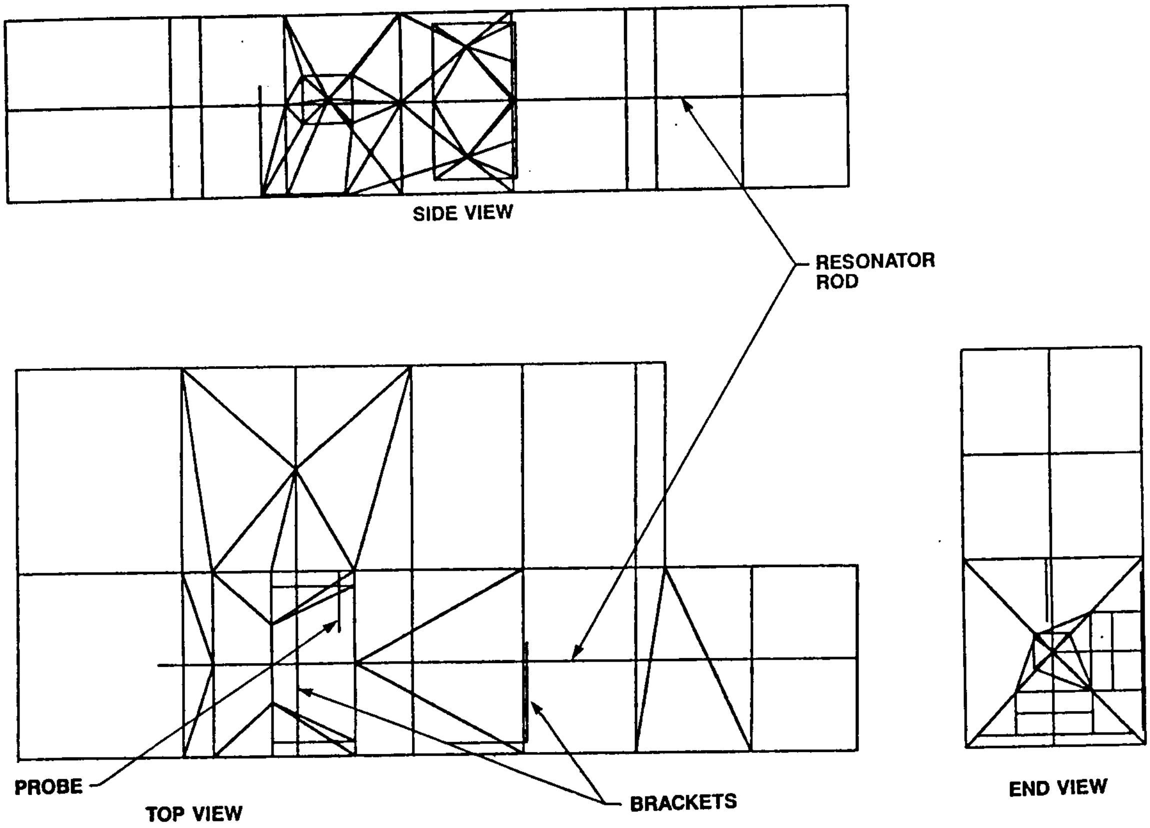

Figure 3. VCO Assembly Finite Element Model

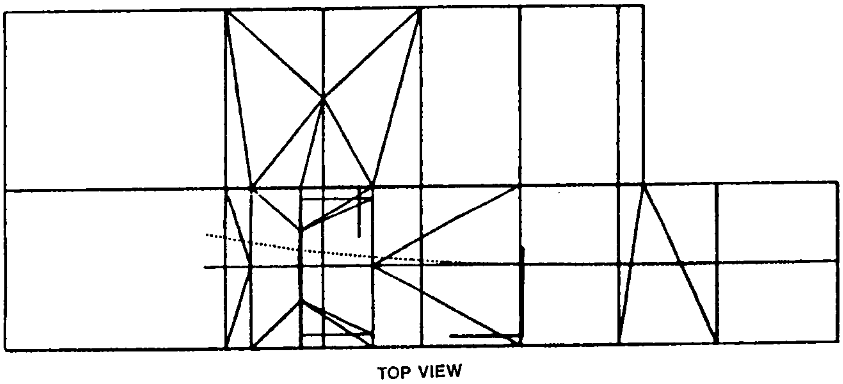

Figure 4. VCO First Mode (Beam-Lateral at 1949 Hz)

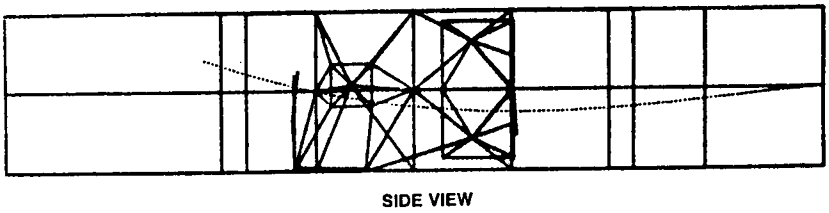

Figure 5. VCO Second Mode (Beam - Vertical at 2618 Hz)

to the bottom of the box. Inspection of the VCO hardware that had shown the sideband problem revealed that the bracket fixity was less than the perfectly glued condition. This fact coupled with the results of rod model analysis led to a redesign of the brackets shown in Figure 6. The reanalysis on the new configuration confirmed that the resonator rod modes in the frequency range of 1600 Hz and 3200 Hz have been eliminated. Figures 7 and 8 show the two lowest frequency modes for the redesigned configuration. These represent overall box modes which are not expected to cause any sideband problem.

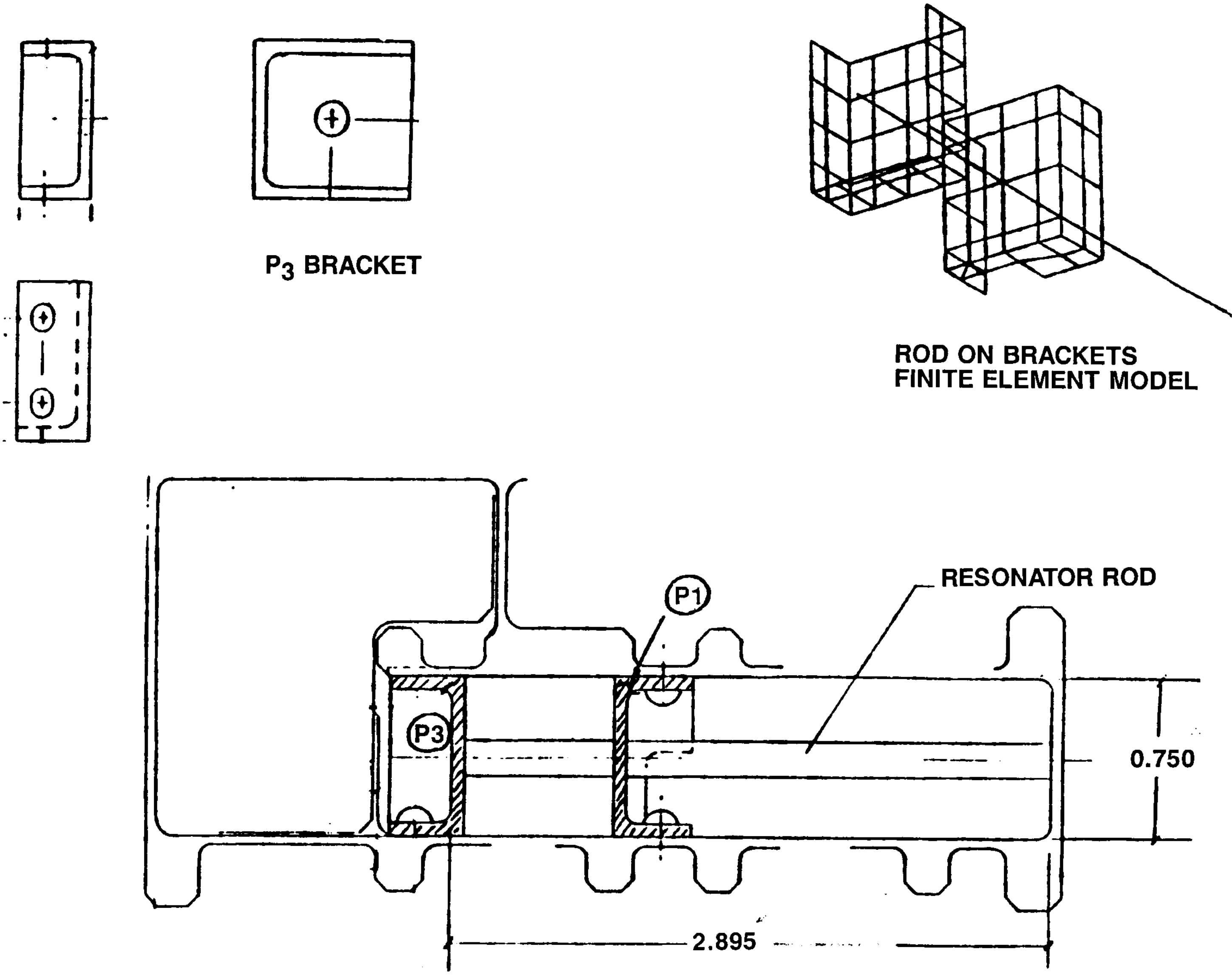

Figure 6. Redesigned VCO with New Brackets

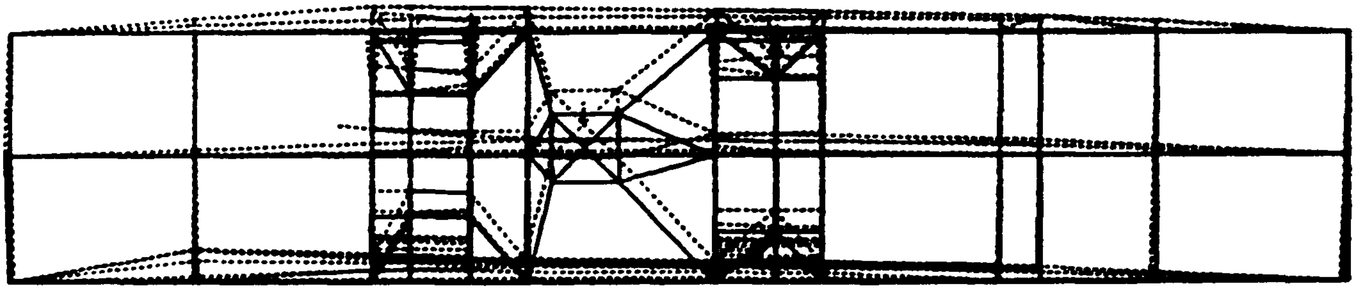

Figure 7. First Mode at 2606 Hz of Redesigned VCO

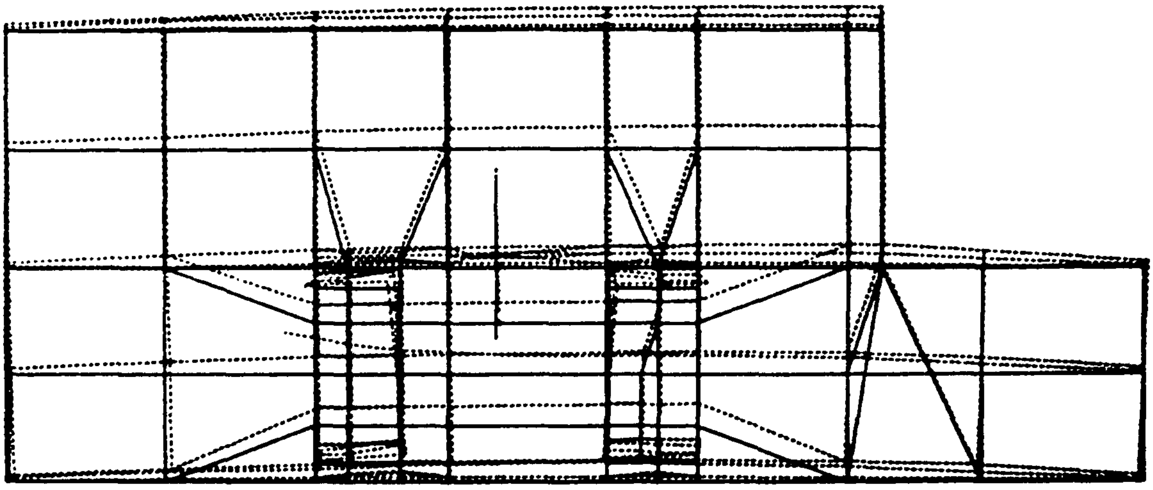

Figure 8. Second Mode at 3039 Hz of Redesigned VCO

VCO Tap Test Results and Correlation with Analysis

A series of tap tests were conducted on an engineering model unit of the VCO assembly to determine natural frequencies and to validate the analytical model. Two accelerometers were used on the resonator rod. Initial tests were conducted with the cover-off conditions to facilitate the accelerometer relocation and for ease of measurements. The analytical model was modified to match the test conditions and the accelerometer weights were included. The VCO assembly was suspended by means of three cords attached at screw mount locations to simulate free-free boundary conditions. The results of the tap tests are summarized in Table 1. Corresponding analytical results are shown in Table 2. Tests conducted with the cover-off conditions consistently showed natural frequencies at around 850 Hz and 1450 Hz which correspond well with the analytical results. Tests with the cover-on condition have measurement related problems and no conclusive data was recorded. However, good correlation with the analytical results for the first series of tap tests was deemed sufficient to validate the analytical model.

Table 1. Summary of Tap Test Results

Run #	Top Cover On/Off	Accelerometer Locations	Tap Location	Natural Frequency (Hz)
1	Off	A and B	rod	f1 = 850 f2 = 1475 f3 = 2300
2	Off	A and B	outside	f1 = 850 f2 = 1450 f3 = 2300
3	Off	A'and C	outside	f1 = 840 f2 = 1410 f3 = 2200
4	On	A and B	outside	f1 = 2650 f2 = 2850 f3 = N/A
5	On	A'and B	outside	f1 = 1950 f2 = 2500 f3 = 3000

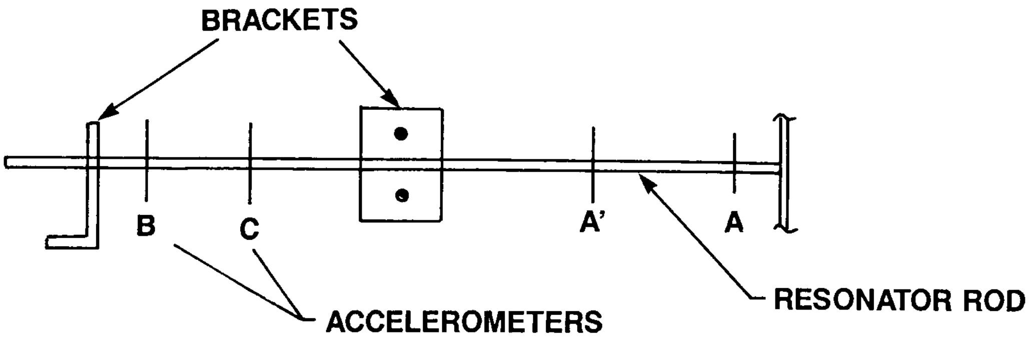

Table 2. Summary of Analytical Results

Run #	Top Cover On/Off	Bracket Design	Bracket Flexibility	Natural Frequency (Hz)	Mode Shape Description
1	Off	Original	Screws/ Screws	f1 = 866 f2 = 1422 f3 = 1760	Box Twisting Beam Lateral Box Side
2	On	Original	Screws/ Screws	f1 = 1412 f2 = 1964 f3 = 2852	Beam Lateral Beam Vertical Probe Bending
3	On	Original	Glue/ Screws	f1 = 1950 f2 = 2618 f3 = 2946	Beam Lateral Beam Vertical Probe Bending
4	On	New with Complete Bulkhead	Glue/ Screws	f1 = 2606 f2 = 3039 f3 = 3470	Box/Probe Box Twisting Box Bending

VCO Shaker Test Results and Analysis Verification

The VCO assembly was subjected to low level sine vibration tests to measure the sideband response. Tests were first performed with the original rexolite bracket configuration and then repeated with the resonator rod supported on the recommended brackets. Figures 9, 10 and 11 show the sideband amplitude to the carrier in the three axes as a function of frequency. The responses show significant reduction in sidebands when the recommended design change was implemented for the resonator rod support brackets. For example, in the Y-axis there was a 32 dB reduction at 1600 Hz and a 30 dB reduction at 3200 Hz. Similarly, reductions of 16 dB at 1600 Hz and 24 dB at 3200 Hz were measured in the Z-axis. Accounting for the variation in the fixity conditions between the analysis and the implemented hardware, this test provided a valuable verification of the analytical predictions and confirmed the validity of the recommended configuration.

ISOLATION EVALUATIONS

Tests were performed on a flight vehicle to determine which of the four reaction wheels were contributing significantly to the sideband response of the affected components. Each wheel was run separately and all four simultaneously while the sidebands were measured. One of the four wheels was found to be the major contributor. Exchanging this wheel with another determined that the wheel itself did not produce excessive vibration. Any wheel in this location would transmit enough excitation to the VCO to produce the out of specification sidebands. An isolation system was therefore designed to reduce the transmittance from this location at frequencies which could simulate a vibration response of the VCO resonator rod.

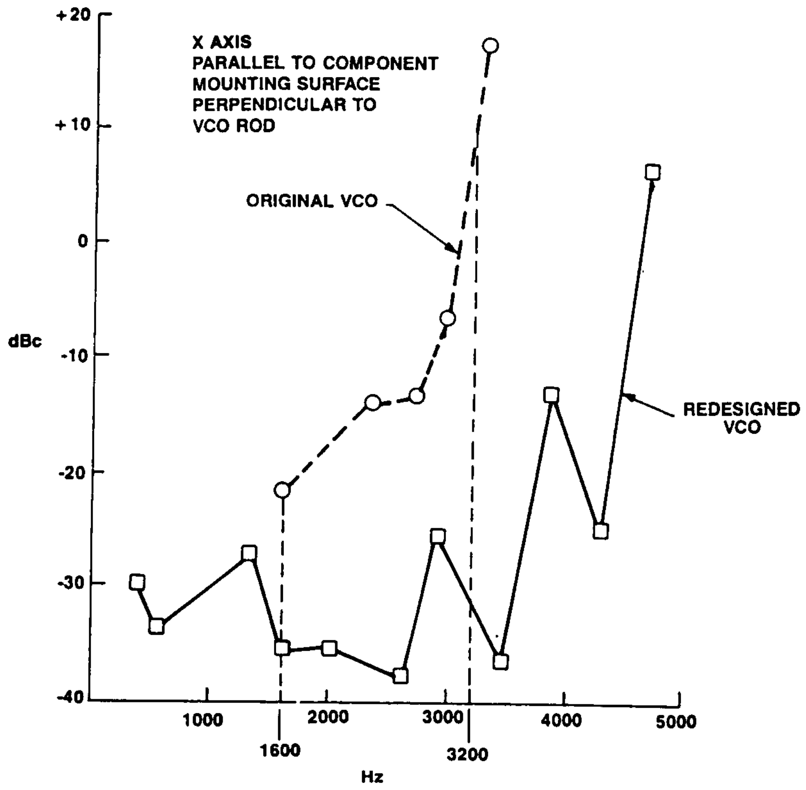

Figure 9. Component Vibration Response (Sideband to Carrier Ratio)

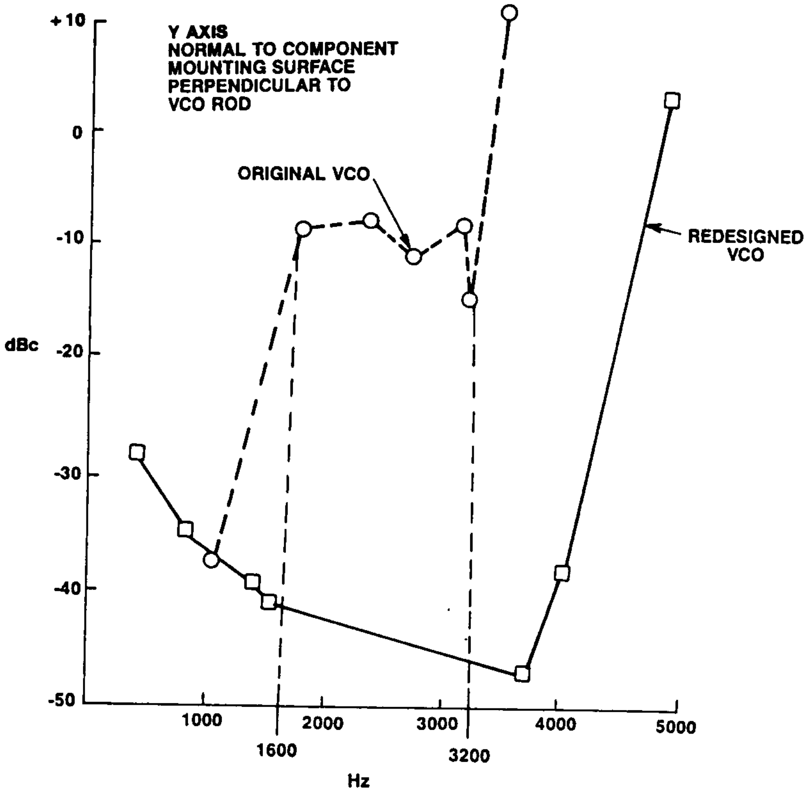

Figure 10. Component Vibration Response (Sideband to Carrier Ratio)

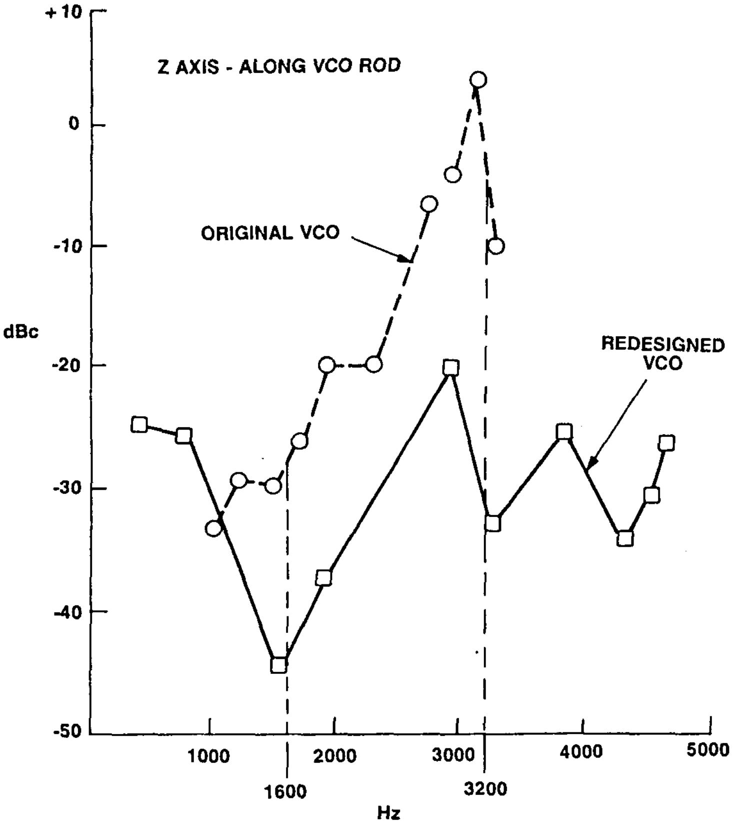

Figure 11. Component Vibration Response (Sideband to Carrier Ratio)

Isolation System Design

Isolation concepts were evaluated based on used of four isolators supporting a wheel to provide six degrees of freedom wheel isolation. Due to space limitations, no suitable commercial isolator could be found which could be put on the reaction wheel without some vehicle modification. It was therefore decided to design a damped stainless steel spring isolator which would fit into the available space, picking up existing bolt holes and requiring no modification to either the mounting surface or the reaction wheel harnessing. To use a commercial silicone isolator, it was determined to be necessary to invert the wheel, to change its direction of rotation, to reroute harness, and to use an interface adaptor plate. The steel spring mounts were preferred since they would cause a smaller impact to the interface and be lighter weight. Use of the silicone mounts which have an elastometer load path also required investigation to ensure adequate material properties for the space environment.

The preliminary requirement from spacecraft control system considerations was for an isolator frequency of approximately 100 Hz so as to provide no appreciable magnification below 1 Hz. The final design of a steel spring isolator meeting this requirement is shown in Figure 12. The flexible portion of the spring is .055 inch thick stainless, .5 inches wide. The fatigue requirement of design for four lifetimes is also met by this design. The damping treatment inside the spring was .25 inch thick GE SMRD 100F90B with a .030 inch thick stainless steel

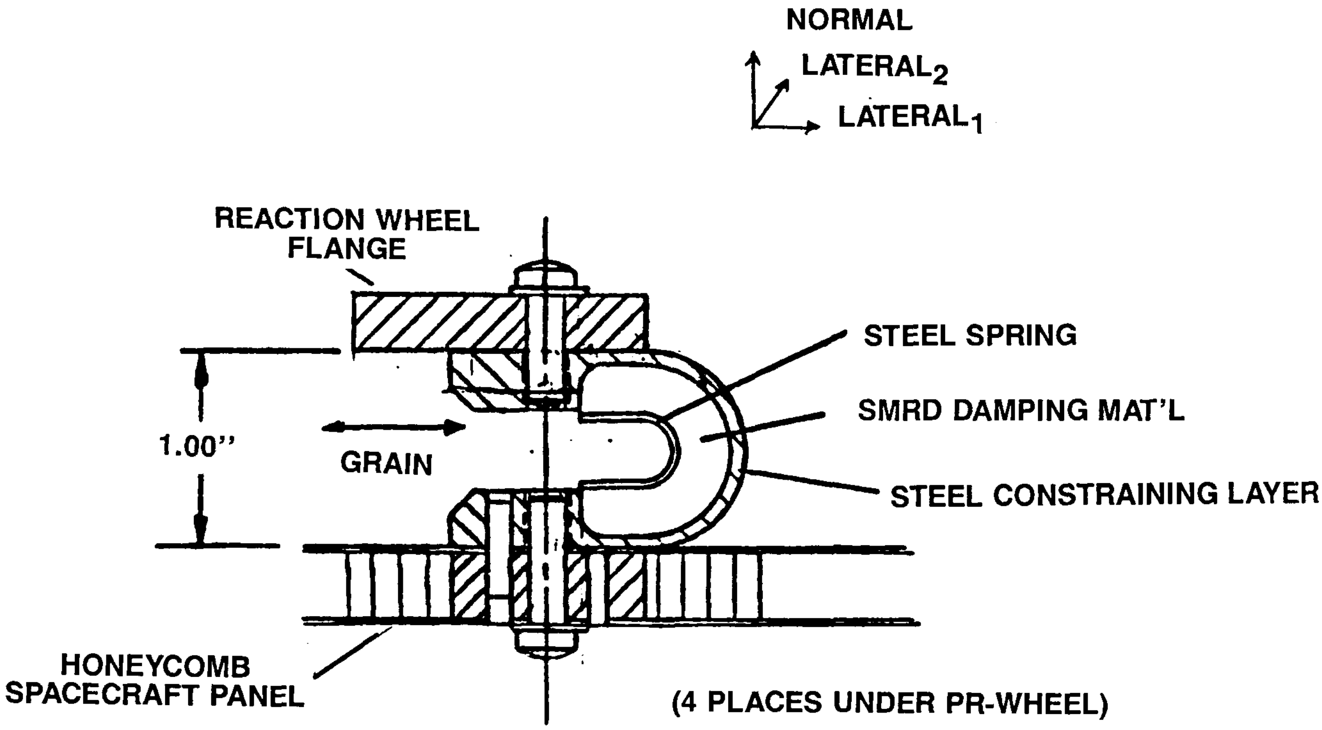

Figure 12. Isolation Mount Assembly Detail

constraining layer, providing a loss factor of approximately .3 ($\zeta = .15$). This high damping will minimize dynamic loads at the isolator resonance while still providing good high frequency isolation. A base shake test performed on these isolators with an Engineering Model reaction wheel showed their fundamental frequencies to be 120 Hz laterally and 130 Hz axially with a measured Q of approximately 3 in both directions.

The chosen commercial silicone mounts have two attachment holes each. To avoid modification of the honeycomb structure to which the reaction wheels attach, a milled aluminum adaptor ring (Figure 13) was designed to provide an interface which would pick up the four existing mounting holes. A base shake test on these mounts showed the fundamental frequencies to be 105 Hz and 115 Hz in the lateral and axial directions respectively. Damping at resonance was adequate providing a Q of about 7.

Test Results

Both the steel spring isolators and the commercial mounts were tested mounted to a simple plate fixture which was readily available (Figure 14). With an Engineering Model Reaction Wheel providing the excitation, vibration was measured on the fixture and on the wheel mounting flange. These tests showed that the steel spring isolators did not work well on excitation normal to the plate at both 1600 Hz and 3200 Hz. Isolation was very good in the lateral directions. The silicone isolators were found to work well on 3200 Hz vibration in all three directions, but they did not provide good isolation of the 1600 Hz excitation.

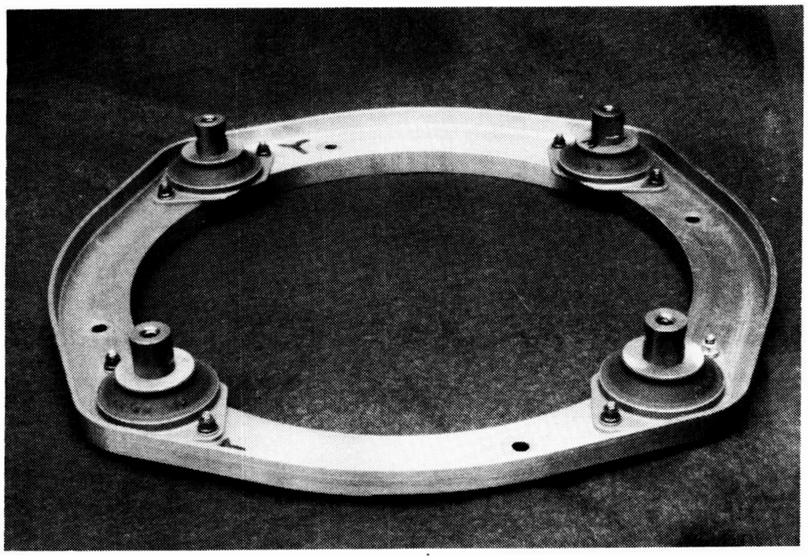

Figure 13. Silicone Isolators and Adaptor Ring

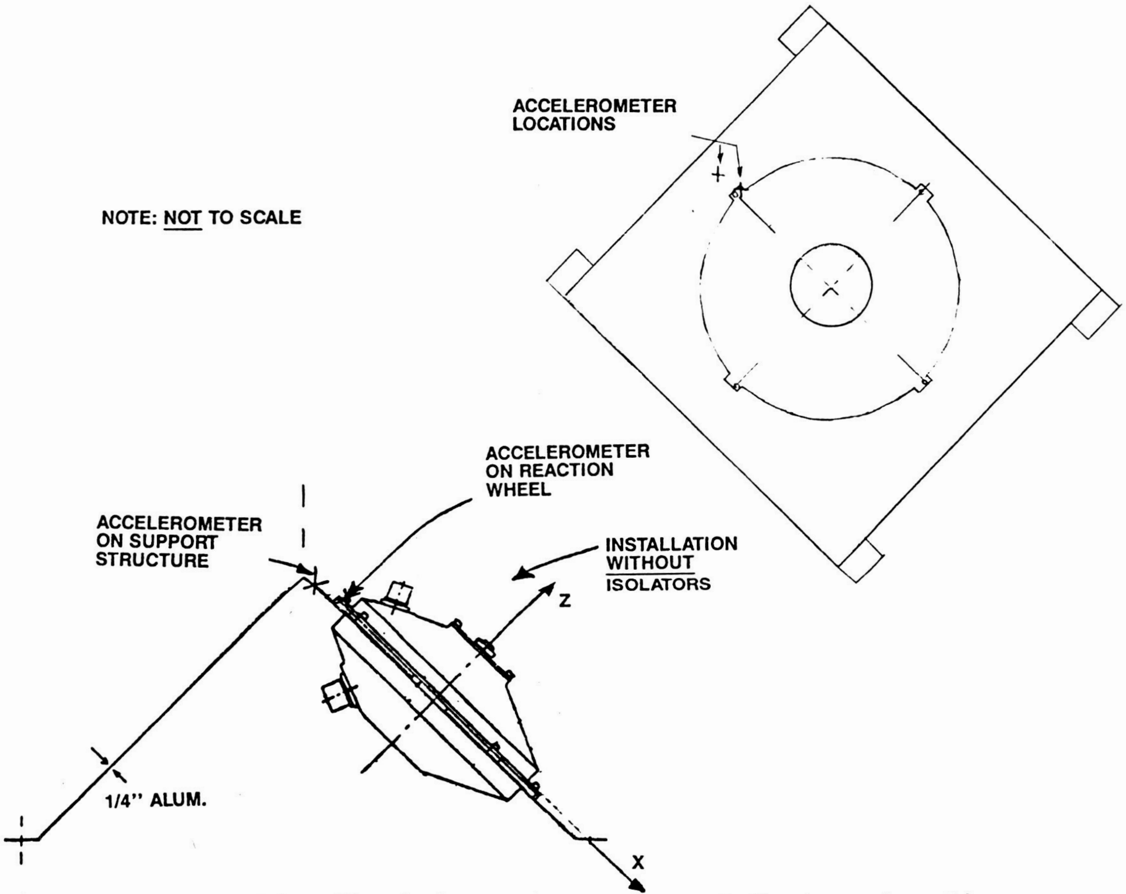

Figure 14. Reaction Wheel in Attitude Control Engineering Fixture

Since neither set of mounts was shown to be clearly superior to the other, and the extent to which the mounting structure of the spacecraft would change the results was unknown, further tests were performed on a prime spacecraft structure. A prime centerbody structure, without North or South panels attached, was made available for the further evaluations. Figure 15 shows this centerbody structure. To reduce the possibility of damage to this structure when the North and South equipment panels are not attached, honeycomb panels are attached in

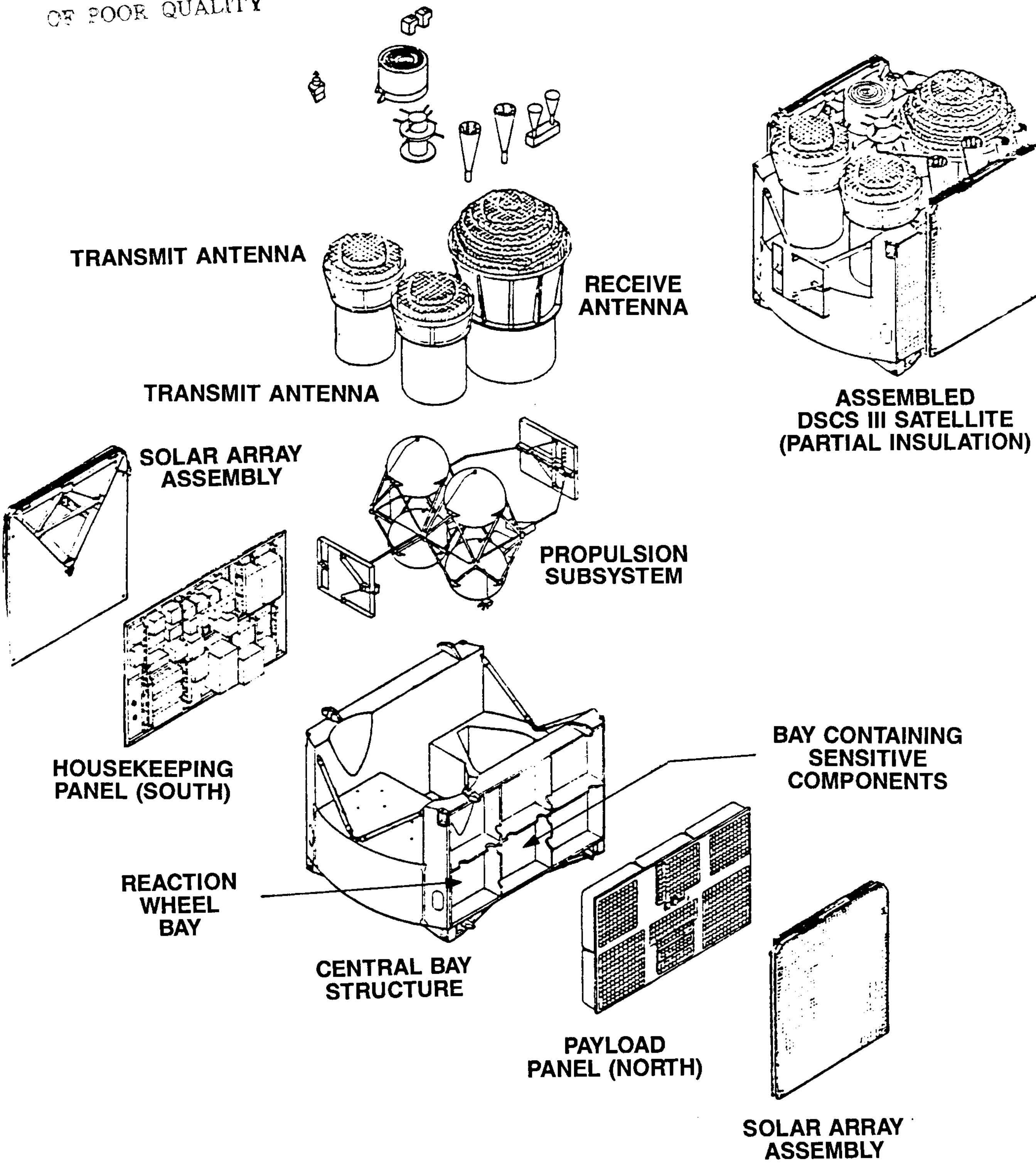

Figure 15. DSCS III Spacecraft Major Assemblies

their place to add stiffness to the structure and were in place during these tests. Four tests were run on the centerbody with an engineering reaction wheel providing the excitation in the location which showed the highest transmissibility to the components with sidebands. The three other wheel locations were also filled with engineering wheels to have their weight in place, but these other wheels were not run. The response was measured on a bulkhead adjacent to the mounting bolt for the running wheel. This was done for the running reaction wheel hard mounted to the spacecraft and for this wheel mounted through three sets of isolators: the steep spring mounts, the previously tested commercial silicone mounts, and a set of softer silicone mounts as it was determined from the control system analysis that these isolators, at about a 55 Hz frequency would be acceptable.

A sample from these tests is shown in Figure 16 which shows Z axis accelerometer response due to reaction wheel excitation for all four mounting conditions. Figure 17 summarizes the results of these tests in a bar graph for all three axes. The steel isolators are seen to have worked as well as the silicon mounts in two axes (X and Z) at 1600 Hz. For the Y axis the silicone mounts were clearly superior. Rather than spend additional time in cut and try to improve the Y axis performance of the steel mounts it was decided to proceed using the soft silicone isolators.

The silicon mounts were tested on a shaker to qualification levels in random vibration and inspected for damage. They passed the qualification test and questions as to their suitability for use in space were resolved satisfactorily.

CONCLUSIONS

The resonator rod supported on the existing brackets was found to be a potential cause for the sideband problem observed on some of the spacecraft assemblies. The two pronged approach of modifying the VCO rod to reduce its response to wheel excitation and isolation of the reaction wheel to reduced the level of the disturbance proved to be very successful.

The beam resonant frequencies were found to be very sensitive to the bracket stiffness and fixity. A timely solution was recommended with a revised bracket design to eliminate the resonance problem from mechanical vibration.

The reaction wheel isolation design was found to be practical from both structural dynamic and control system analyses. Retrofit of this design change onto already built spacecraft with out-of-specification sidebands has been planned. The implementation will be via an adaptor plate between the isolators and the spacecraft so that no rework will be required on the spacecraft except for a harness modification.

Both solutions must still be tested on a fully assembled spacecraft (the real North and South panels may change the degree of isolation) and measurements must be performed on the affected components to determine the extent to which the sidebands have been reduced. Sideband reduction on a fully assembled spacecraft will be the true indication of the success of this investigation.

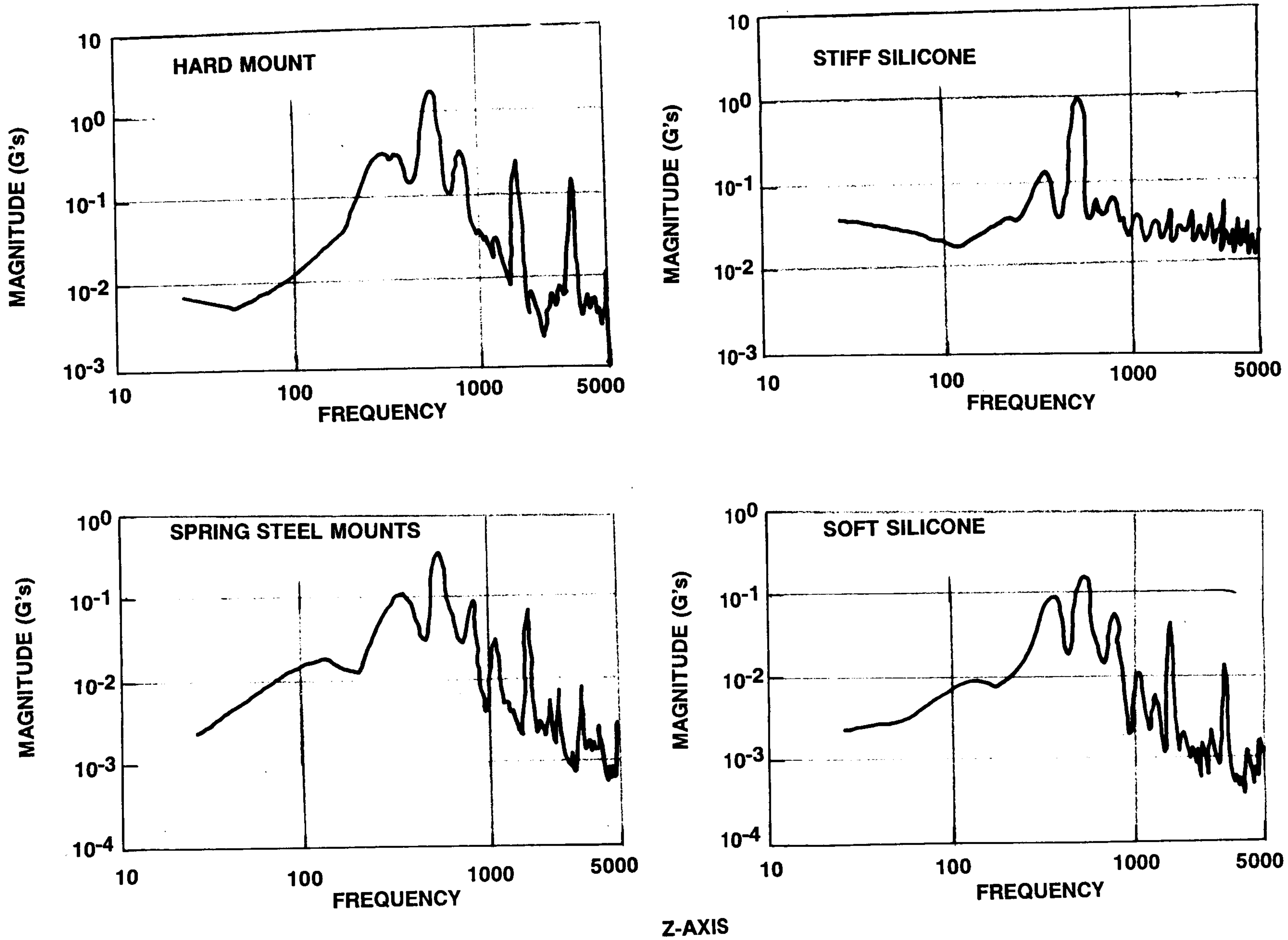

Figure 16. Centerbody Panel Response to PR - Wheel Spacecraft Axes (Fig. 3-6)

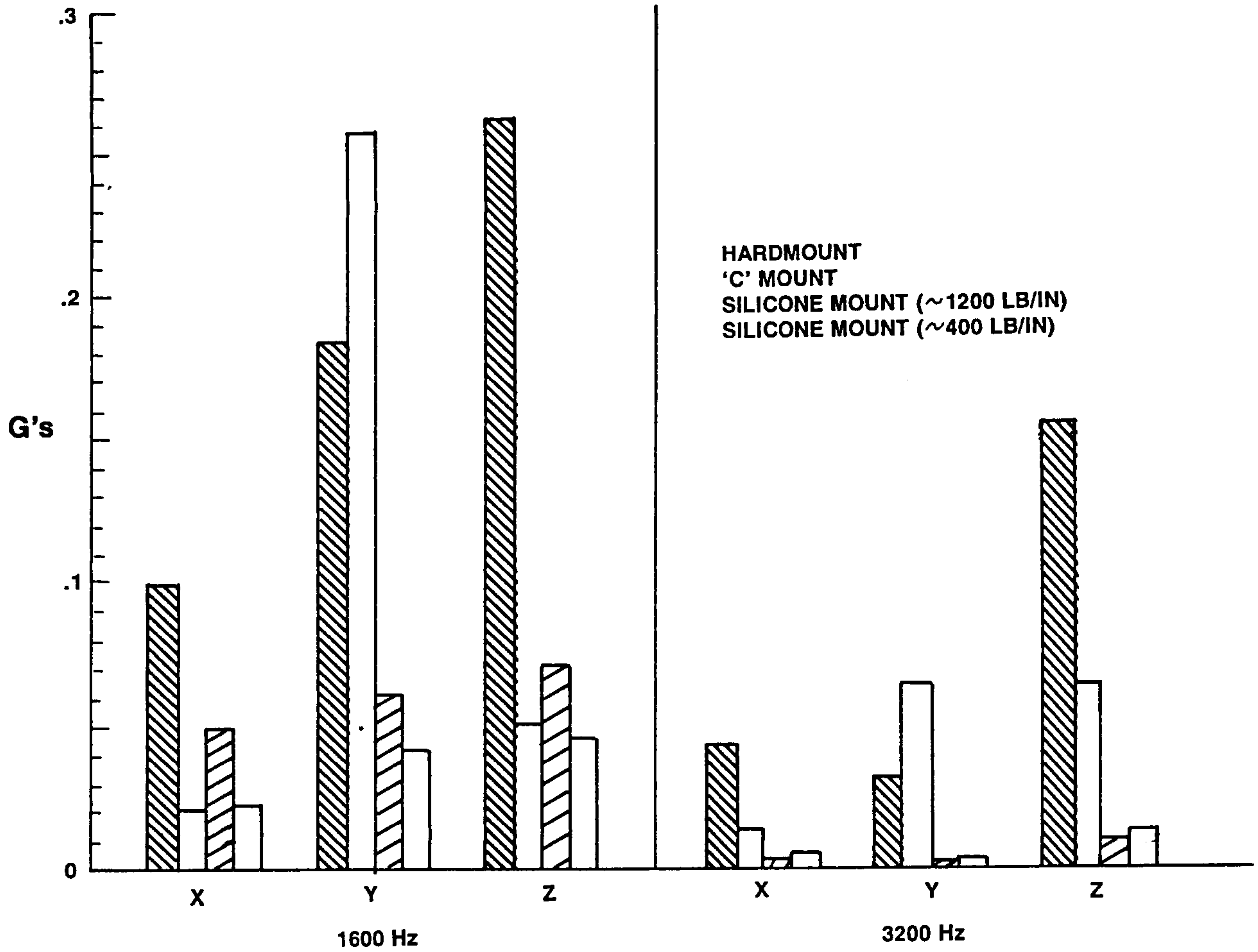

Figure 17. Test Results - Isolators on Centerbody Structure

ANALYTICAL METHODS

PRECEDING PAGE BLANK NOT FILMED

N88-18956

A Superelement Component Dynamic Synthesis Method

M. L. Soni

A method is presented for coupling a broad class of component dynamic models in the manner of direct stiffness assembly and is implemented in a general matrix manipulation program.

INTRODUCTION

A number of methods have been developed in the past to accomplish the basic objectives of the method. These methods are surveyed in detail in [1]. Each of these methods are characterized by the way the component dynamics is input and coupled to adjacent components. Hurty [2,3] proposed that the connect degrees of freedom (DOF) of a component were fixed or had a zero displacement. He then partitioned the modes of the structure into rigid body modes, constraint modes, and normal modes. Craig and Bampton [4] proposed a simplification of Hurty's fixed interface method by dividing component modes into only two groups: constraint modes and normal modes. Bamford [5] added attachment modes to improve the convergence of the method.

Goldman [6] developed the free interface method, employing only rigid body modes and free-free normal modes in component dynamic representation. This technique eliminates the computation of static constraint modes, but their advantage is negated by the poor accuracy of the method. Hou [7] presented a variation of Goldman's free-interface method in which no distinction is made between rigid body modes and free-free normal modes. Gladwell [8] developed "branch mode analysis" by combining free interface and fixed interface methods to reduce the order of the stiffness and mass matrices for individual substructures. The reduction procedure requires the knowledge of topological arrangement and dynamics of all the components in the model. In order to account for adjacent components Benfield and Hruda [9] introduced inertia and stiffness loading of component interfaces. The use of loaded interface modes is shown to have superior convergence characterisics.

MacNeal [10] introduced the use of hybrid modes and inertia relief modes for component mode synthesis. Hybrid modes are substructure normal modes computed with a combination of fixed and free boundary conditions. Inertia relief attachment modes are attachment modes for components with rigid body freedoms. MacNeal also included residual inertia and flexibility to approximate the static contribution of the truncated higher order modes of a component. Rubin [11] extended the residual flexibility approach for free interface method by introducing higher order corrections to account for the truncated modes. Klosterman [12] more fully developed the combined experimental and analytical method introduced by MacNeal. Hintz [13] discussed the implications of truncating various mode sets and developed guidelines for retaining accuracy with a reduced size model.

Recent research has centered on the comparision of the various methods. Baker [14], for example, compares the constrained and free-free approach using experimental techniques and also investigates using mass additive techniques and measured rotational DOF [15]. This investigation was motivated by a need to find the best method for rigidly connected flexible structures. In this connection, the constrained method produced the best result. Klosterman [16] has shown the free-free method to be accurate for relatively stiff structures connected with flexible elements. This supports Rubin's conclusion [11] that the free-free method is at least as accurate when residual effects are accounted for. These conclusions are intuitive because the type of boundary condition imposed in the analysis that best represents the boundary of the assembled structure provides the best accuracy in the modal synthesis.

Meirovitch and Hale [16] have developed a generalized synthesis procedure by broadening the definition of the admissible functions proposed by Hurty [1]. This technique is applicable to both continuous and discrete structural models. The geometric compatibility conditions at connection interfaces are approximately enforced by the method of weighted residuals.

The method due to Klosterman [12] has been implemented in an interactive computer code SYSTAN [17] and that due to Herting [18] is available in NASTRAN. The latter is the most general of the modal synthesis techniques. It allows retention of an arbitrary set of component normal modes, inertia relief modes, and all geometric coordinates at connection boundaries. Both the fixed-interface method of Craig and Bampton, and the MacNeal's residual flexibility method, are special cases of the general method. Other analyses presented in the literature based on modal synthesis techniques are not incorporated into general structural analysis codes.

It is desirable to have a synthesis method to couple different types of component dynamic models in a setting such as that of the finite element method so as to be able to realize the best advantages of both the component synthesis methods and the convenience and generality of the finite element method. The need for a such a capability arises when different types of dynamic models are used to represent the various components of a structure. This variance is dictated by the need to improve accuracy of component dynamic representation, availability of a certain kind of data, etc. Herting's work [18] meets some of these objectives. The procedure presented herein permits a broader class of component models in the manner of direct stiffness finite element assembly and can be implemented in a general matrix manipulation program.

A principal feature of the work developed here is the component dynamic model reduction procedure that leads to an exact and numerically stable synthesis. In order to affect component coupling, neither the specification of external coupling springs nor an user-specified selection of independent coordinate is required. Existing synthesis procedures suffer from these drawbacks. Component dynamic models considered include free-free normal modes with or without interface loading, up to second order stiffness and inertia connections accounting for the effect of modal truncation, fixed interface modes, and also the physical coordinate components. The model reduction procedure involves interior boundary coordinate transformations which explicitly retain connection interface displacement coordinates in the reduced component dynamic representations. Interior coordinates may include physical, modal, or any admissible coordinates. Components in this reduced form are termed "superelement" because they are a generalization of the conventional finite elements of structural mechanics. The problem of component dynamic synthesis is then reduced to the assembly of the superelement. The direct stiffness approach and all subsequent processing operations of the finite element method are then applicable. The formulation, implementation and verification aspects of the superelement component dynamic synthesis method are presented in the following sections.

SUPERELEMENT MODEL REDUCTION

The procedures for reducing component dynamic models to a form involving physical DOFs of the connection interface nodes plus some additional DOFs related to the interior nodes are derived in the following. The component dynamic models in this reduced form possess a structure similar to that of the displacement finite element method and are therefore termed superelements. Four types of component dynamic models are considered: (1) finite element model; (2) fixed interface modal model with static constraint modes; (3) free interface modal model with residual flexibility attachment modes; and (4) free interface model with normal modes. The last type may also include any general admissible shape vectors and corresponding dynamic matrices as long as certain requirements for matrix partitioning and invertibility are satisfied. A system may involve any combination of the above types of component dynamics model since the models are reduced to a common form before assembly.

The finite element and the constrained interface modal models naturally contains the connection interface DOFS and are already in the required superelement form. Constrained interface modal model based superelement synthesis is treated in [19]. The free interface modal model with residual flexibility attachment modes is reduced to the superelement as follows. Expressing component displacements $\underline{X}$ in partitioned form can be witten as

$$\begin{Bmatrix} \underline{X}_O \\ \underline{X}_B \end{Bmatrix} = \begin{bmatrix} \underline{\underline{\Phi}}_{KO} & \underline{\underline{G}}_{OB} \\ \underline{\underline{\Phi}}_{B} & \underline{\underline{G}}_{BB} \end{bmatrix} \begin{Bmatrix} \underline{q}_K \\ \underline{q}_B \end{Bmatrix} \tag{1}$$

where $\underline{\underline{\phi}}$ and $\underline{\underline{G}}$ are respectively the normal mode and residual flexibility attachment mode matrices, $\underline{q}_K$ and $\underline{q}_B$ are the associated generalized coordinates, and the subscripts B and O refer to the boundary and other DOFs. To obtain the superelement reduction transformation, following Martinez [20] solve the lower partition of Eq. (1) for $\underline{q}_B$. Thus,

$$\underline{q}_B = -\underline{\underline{G}}_{BB}^{-1} \underline{\underline{\Phi}}_{KB} \underline{q}_K + \underline{\underline{G}}_{BB}^{-1} \underline{X}_B \tag{2}$$

substituting the above in Eq. (1) leads to the superelement form associated with the residual flexibility attachment model:

$$\begin{Bmatrix} \underline{X}_O \\ \underline{X}_B \end{Bmatrix} = \underline{\underline{T}} \begin{Bmatrix} \underline{q}_K \\ \underline{X}_B \end{Bmatrix} \qquad \text{where,} \qquad T = \left[\begin{array}{c|c} \underline{\underline{\Phi}}_{KO} - \underline{\underline{G}}_{OB} \underline{\underline{G}}_{BB}^{-1} \underline{\underline{\Phi}}_{KB} & \underline{\underline{G}}_{OB} \underline{\underline{G}}_{BB}^{-1} \\ \hline \underline{\underline{0}} & \underline{\underline{I}} \end{array}\right] \tag{3}$$

The generalized coordinates $\underline{q}_K$ are now the participation factors of the modified modes $(\underline{\underline{\Phi}}_{KO} - \underline{\underline{G}}_{OB} \underline{\underline{G}}_{BB}^{-1} \underline{\underline{\Phi}}_{KB})$. The internal partitions of the modified normal modes are in effect free interface normal mode partitions minus a set of constraint modes internal partitions and therefore represent modes constrained at boundary degrees of freedom. The superelement equations of motion are obtained by transforming the component modal equation of motion as

$$\begin{bmatrix} \underline{\underline{M}}_{KK}+\underline{\underline{\phi}}_{KB}^{T}\, \underline{\underline{J}}_{BB}\, \underline{\underline{\phi}}_{KB} & -\underline{\underline{\phi}}_{KB}^{T}\, \underline{\underline{J}}_{BB} \\ \text{sym.} & J_{BB} \end{bmatrix} \begin{Bmatrix} \ddot{\underline{q}}_{K} \\ \ddot{\underline{X}}_{B} \end{Bmatrix} + \begin{bmatrix} \underline{\underline{\Lambda}}_{KK}+ \underline{\underline{\phi}}_{KB}^{T}\, \underline{\underline{G}}_{BB}^{-1}\, \underline{\underline{\phi}}_{KB} & -\underline{\underline{\phi}}_{KB}^{T}\, \underline{\underline{G}}_{BB}^{-1} \\ \text{sym.} & \underline{\underline{G}}_{BB}^{-1} \end{bmatrix} \begin{Bmatrix} \underline{q}_{K} \\ \underline{X}_{B} \end{Bmatrix} = \begin{Bmatrix} \underline{0} \\ \underline{f}_{B} \end{Bmatrix} \tag{4}$$

where $J_{BB} = \underline{\underline{G}}_{BB}^{-1}\, \underline{\underline{H}}_{BB}\, \underline{\underline{G}}_{BB}^{-1}$,and $\underline{\underline{m}}_{KK}$ and $\underline{\underline{\Lambda}}_{KK}$ are generalized mass and stiffness matrices respectively, $\underline{\underline{G}}_{BB}$ and $\underline{\underline{H}}_{BB}$ are the generalized stiffness and mass associated with the residual flexibility attachment modes. The modification of the component generalized mass and stiffness matrices by the contributions from the residual flexibility of the deleted modes is clearly seen in the above equation.

In the event only a truncated set of free interface normal modes is used to represent component displacements, the superelement reduction is obtained from a partial inversion of the modal matrix as described in the following. Consider the free interface normal mode transformation

$$\begin{Bmatrix} \underline{X}_{0} \\ \underline{X}_{B} \end{Bmatrix} = \begin{bmatrix} \underline{\underline{\phi}}_{K0} \\ \underline{\underline{\phi}}_{KB} \end{bmatrix} \underline{q}_{K} \tag{5}$$

where $\underline{\underline{\phi}}_{K0}$ and $\underline{\underline{\phi}}_{KB}$ are $(n_{0} x m_{K})$ and $(n_{B} x m_{K})$size partitions of the component modal matrix corresponding to the interior and boundary degrees of freedom $\underline{X}_{0}$ and $\underline{X}_{B}$, respectively. Consider the lower portion of Eq. (5)

$$\underline{X}_{B} = \underline{\underline{\phi}}_{KB}\, \underline{q}_{K} \tag{6}$$

and partition $\underline{\underline{\phi}}_{KB}$ into a nonsingular invertible square matrix $\underline{\underline{\phi}}_{KB1}$ and remainder $\underline{\underline{\phi}}_{KB2}$. Thus,

$$\underline{X}_{B} = \begin{bmatrix} \underline{\underline{\phi}}_{KB1} & : & \underline{\underline{\phi}}_{KB2} \end{bmatrix} \begin{Bmatrix} \underline{q}_{K1} \\ \underline{q}_{K2} \end{Bmatrix} \tag{7}$$

which requires that the number of kept modes be greater than the number of boundary degrees of freedom. Solving the above equation for $\underline{q}_{K1}$ gives

$$\underline{q}_{K1} = -\underline{\underline{\phi}}_{KB1}^{-1}\, \underline{\underline{\phi}}_{KB2}\, \underline{q}_{K2} + \underline{\underline{\phi}}_{KB1}^{-1}\, \underline{X}_{B} \tag{8}$$

and

$$\underline{q}_K = \left\{\begin{matrix} \underline{q}_{K1} \\ \\ \underline{q}_{K2} \end{matrix}\right\} = \left[\begin{array}{c:c} -\underline{\underline{\Phi}}_{KB1}^{-1}\,\underline{\underline{\Phi}}_{KB2} & \underline{\underline{\Phi}}_{KB1}^{-1} \\ \hdashline \underline{\underline{I}} & \underline{\underline{0}} \end{array}\right] \left\{\begin{matrix} \underline{q}_{K2} \\ \\ \underline{X}_B \end{matrix}\right\}$$

or

$$\underline{q} = \underline{\underline{T}}_2 \left\{\begin{matrix} \underline{q}_{K2} \\ \\ \underline{X}_B \end{matrix}\right\} \tag{9}$$

the generalized coordinates $\underline{q}_{K2}$ are called reduced modal coordinates since they are associated with modified modes as seen in the above equation. Combining transform Eqs. (6) and (9), a net transformation from physical coordinates $\underline{X}$ to free interface normal mode superelement coordinates can be written as

$$\underline{\underline{T}} = \underline{\underline{\Phi}}_K \cdot \underline{\underline{T}}_2 = \left[\begin{array}{c:c} (-\underline{\underline{\Phi}}_{K01}\,\underline{\underline{\Phi}}_{KB1}^{-1}\,\underline{\underline{\Phi}}_{KB2} + \underline{\underline{\Phi}}_{K02}) & \underline{\underline{\Phi}}_{K01}\,\underline{\underline{\Phi}}_{KB1}^{-1} \\ \hdashline \underline{\underline{0}} & \underline{\underline{I}} \end{array}\right] \tag{10}$$

where $\underline{\underline{\Phi}}_{K01}$ and $\underline{\underline{\Phi}}_{K02}$ are partitions of $\underline{\underline{\Phi}}_{K0}$ created using the partitioning information generated in Eq. (8). Analogous to the Ritz transformation for constrained interface modal models, and the transformation of Eq. (4) for residual flexibility model modal, the left and right partitions of the transformation of Eq. (10) may be interpreted as expressing modal matrices of modified normal modes and boundary constraint modes, respectively. The component equations of motion in superelement coordinates $(\underline{q}_2, \underline{X}_B)$ can be obtained using the transform of Eq. (11) as

$$\underline{\underline{T}}^T \begin{bmatrix} \underline{\underline{M}}_{00} & \underline{\underline{M}}_{0B} \\ \\ \underline{\underline{M}}_{B0} & \underline{\underline{M}}_{BB} \end{bmatrix} \underline{\underline{T}} \left\{\begin{matrix} \ddot{\underline{q}}_{K2} \\ \\ \ddot{\underline{X}}_B \end{matrix}\right\} + \underline{\underline{T}}^T \begin{bmatrix} \underline{\underline{K}}_{00} & \underline{\underline{K}}_{0B} \\ \\ \underline{\underline{K}}_{B0} & \underline{\underline{K}}_{BB} \end{bmatrix} \underline{\underline{T}} \left\{\begin{matrix} \underline{q}_{K2} \\ \\ \underline{X}_B \end{matrix}\right\} = \underline{\underline{T}}^T \underline{f} \tag{12}$$

using physical coordinate component model, or

$$T_2^T \begin{bmatrix} \underline{\underline{M}}_{q11} & \underline{\underline{M}}_{q12} \\ \\ \underline{\underline{M}}_{q21} & \underline{\underline{M}}_{q22} \end{bmatrix} \underline{\underline{T}}_2 \left\{\begin{matrix} \ddot{\underline{q}}_{K2} \\ \\ \ddot{\underline{X}}_B \end{matrix}\right\} + \underline{\underline{T}}_2^T \begin{bmatrix} \underline{\underline{K}}_{q11} & \underline{\underline{K}}_{q12} \\ \\ \underline{\underline{K}}_{q21} & \underline{\underline{K}}_{q22} \end{bmatrix} \underline{\underline{T}}_2 \left\{\begin{matrix} \underline{q}_{K2} \\ \\ \underline{X}_B \end{matrix}\right\} = \underline{\underline{T}}_2^T\, \underline{\underline{\Phi}}_K^T\, \underline{f} \tag{12}$$

from modal coordinate model. In the above the generalized mass and stiffness matrices are used to include the case where the columns of the modal matrix in Eq. (12) are not orthogonal. (Mass and stiffness loaded component modes are nonorthogonal with respect to the original unloaded mass and stiffness matrices, for example.). Further, it is to be emphasized again that the reduced modal representation given in Eqs. (9) through (12) is obtainable from any given free interface "modal" representation provided the partitioning conditions leading to Eq. (8) can be met. The columns of modal matrix in Eq. (5) need not be normal modes. The only necessary condition is that they be linearly independent, adequate in number, and be from a complete set, i.e., a linear combination of them should be capable of representing the deformation shapes of the component undergoing motion within the compound of the built-up system.

SUPERELEMENT SYNTHESIS

The reduction procedures described in the preceding section yield component models with a common characteristic: the boundary degrees of freedom are explicitly retained and the internal degrees of freedom are transformed to reduced generalized coordinates. The equations of motion of a superelement component can be expressed as

$$\begin{bmatrix} \underline{\underline{m}}_{qq}^{(\alpha)} & \underline{\underline{m}}_{qB}^{(\alpha)} \\ \text{sym} & \underline{\underline{m}}_{BB}^{(\alpha)} \end{bmatrix} \begin{Bmatrix} \ddot{\underline{q}}^{(\alpha)} \\ \ddot{\underline{X}}_B^{(\alpha)} \end{Bmatrix} + \begin{bmatrix} \underline{\underline{C}}_{qq}^{(\alpha)} & \underline{\underline{C}}_{qB}^{(\alpha)} \\ \text{sym} & \underline{\underline{C}}_{BB}^{(\alpha)} \end{bmatrix} \begin{Bmatrix} \dot{\underline{q}}^{(\alpha)} \\ \dot{\underline{X}}_B^{(\alpha)} \end{Bmatrix} + \begin{bmatrix} \underline{\underline{K}}_{qq}^{(\alpha)} & \underline{\underline{K}}_{qB}^{(\alpha)} \\ \text{sym} & \underline{\underline{K}}_{BB}^{(\alpha)} \end{bmatrix} \begin{Bmatrix} \underline{q}^{(\alpha)} \\ \underline{X}_B^{(\alpha)} \end{Bmatrix} = \begin{Bmatrix} 0 \\ \underline{f}_B^{(\alpha)} \end{Bmatrix} \tag{13}$$

or

$$\underline{\underline{M}}^{(\alpha)} \ddot{\underline{p}}^{(\alpha)} + \underline{\underline{C}}^{(\alpha)} \dot{\underline{p}}^{(\alpha)} + \underline{\underline{K}}^{(\alpha)} \underline{p} = \underline{F}^{(\alpha)}$$

Each component substructure of a given built-up system can be expressed in the above format. Analogous to the matrix equation of a displacement based finite element model, the generalized coordinates may be interpreted as internal DOFs. Assuming that the global structure as partitioned into N components, the assembled global matrices $\underline{\underline{M}}$, $\underline{\underline{C}}$, $\underline{\underline{K}}$ relating the global displacement vector $\underline{X}$ and the global force vector $\underline{F}$ can now be synthesized by the direct stiffness approach from the component matrices of Eq. (13). The direct stiffness approach postulates equal nodal displacement and nodal equilibrium of forces at the connection interfaces of adjacent components, thus

$$\underline{X}_B^{(\alpha)} = \beta_B^{(\alpha)} \underline{X}_B \text{ , and } \underline{f}_B = \sum_{N=1}^{N} \beta_B^{(\alpha)} \underline{f}_B^{(\alpha)} \tag{14}$$

No compatibility conditions exist among the reduced generalized coordinates $\underline{q}^{(\alpha)}$ and remain intact. The coupled system coordinate vector thus becomes

$$\underline{X}^T = \{\underline{q}^{(1)^T}, \underline{q}^{(2)^T}, \ldots, \underline{q}^{(N)^T} \; \underline{X}_B^T\} \tag{15}$$

so that the global mass, damping, and stiffness matrices are given by

$$\underline{\underline{M}} = \sum_{\alpha=1}^{N} \underline{\underline{\beta}}^{(\alpha)^T} \underline{\underline{M}}^{(\alpha)} \beta^{(\alpha)} \quad , \; \underline{\underline{C}} = \sum_{\alpha=1}^{N} \underline{\underline{\beta}}^{(\alpha)^T} \underline{\underline{C}}^{(\alpha)} \beta^{(\alpha)} \; , \; \underline{\underline{K}} = \sum_{\alpha=1}^{N} \underline{\underline{\beta}}^{(\alpha)^T} \underline{\underline{K}}^{(\alpha)} \beta^{(\alpha)} \tag{16}$$

where $\underline{\underline{\beta}}^{(\alpha)}$ is the portion of the component to global transformation matrix $\underline{\underline{\beta}}$ corresponding to the α^{th} component.

$$\underline{Y} = \underline{\underline{\beta}} \, \underline{X} \, , \quad \beta^{(\alpha)} = \left[\begin{array}{cccccccccc} \cdot & \cdot & \cdot & \underline{\underline{I}}^{(\alpha)} & \cdot & \cdot & \cdot & \cdot & \cdot & \cdot \\ \hdashline \cdot & & \cdot & \underline{\underline{0}} & \cdot & \cdot & \cdot & \cdot & \cdot & \underline{\underline{\beta}}^{(\alpha)} \end{array} \right] \tag{17}$$

$\underline{Y}$ being the vector of uncoupled superelement coordinates.

$$\underline{Y}^T = \{\underline{q}^{(1)^T}\ \underline{X}_B^{(1)^T}\quad \underline{q}^{(2)^T}\ \underline{X}_B^{(2)^T}\ \ldots\ldots\ \underline{q}^{(N)^T}\underline{X}_B^{(N)^T}\} \tag{18}$$

and $\underline{\underline{\beta}}_B^{(\alpha)}$ representing the compatibility conditions for the degrees of freedom at the boundaries of the component α.

The built-up system mass, damping, and stiffness matrices are of the following form.

$$\underline{\underline{A}} = \begin{bmatrix} \underline{\underline{a}}_{qq}^{(1)} & \underline{\underline{0}} & \underline{\underline{0}} & \cdot\cdot & \underline{\underline{0}} & \underline{\underline{a}}_{qB}^{(1)} \\ & \underline{\underline{a}}_{qq}^{(2)} & \underline{\underline{0}} & \cdot\cdot & \underline{\underline{0}} & \underline{\underline{a}}_{qB}^{(2)} \\ & & \cdot & & \cdot & \cdot \\ & & & \cdot & \underline{\underline{a}}_{qq}^{(N)} & \underline{\underline{a}}_{qB}^{(N)} \\ & & \text{sym.} & & & \underline{\underline{a}}_{BB} \end{bmatrix} \tag{19}$$

where the coefficients $a_{ij}^{(\alpha)}$ are the mass, damping, or stiffness coefficients matrices given in Eq. (14), and $\underline{\underline{A}}$ is the corresponding global matrix. The diagonal submatrices $\underline{\underline{a}}_{qq}^{(\alpha)}$ in Eq. (19) correspond to the reduced generalized coordinates of the components and are uncoupled from other components.

$$\underline{\underline{a}}_{BB} = \sum_{\alpha=1}^{N} \underline{\underline{\beta}}_B^{(\alpha)^T}\ \underline{\underline{a}}_{BB}^{(\alpha)}\ \underline{\underline{\beta}}_B^{(\alpha)}$$

The submatrices are symmetric and in general fully populated. The system governing equations can be expressed as

$$\underline{\underline{M}}\,\ddot{\underline{X}} + \underline{\underline{C}}\,\dot{\underline{X}} + \underline{\underline{K}}\,\underline{X} = \underline{f} \tag{20}$$

which itself is in a superelement form since the system basis coordinate $\underline{X}$ contains the boundary degrees of freedom explicitly. This is particularly useful from the standpoint of coupling the system of Eq. (20) to a higher level superelement. The recovery of component displacements from the system displacement vector $\underline{X}$ is simply a back substitution and transformation process.

NUMERICAL EXAMPLE AND CONCLUSIONS

The above formulation is implmented as a pre- and post-processor to a general matrix manipulation computer program. The following presents a sample synthesis problem involving free interface and residual flexibility modal models solved using the developed software to demonstrate its working. In Figure 1 the component A represents a lumped parameter model of an aircraft, while that labeled B represents a model of a store to be attached at the tip of the wing. The types of dynamic models employed for each component are as follows. For Aircraft: (1) free interface normal modes followed by a transformation to superelement coordinates, and (2) Free interface normal modes plus a residual flexibility attachment mode followed by a transformation to superelement coordinates. And for the Store: (1) free interface normal modes followed by superelement coordinate transformation, and (2) physical coordinate model. For comparison purposes the problem is also solved using existing MacNeal Method and Rubin Method of synthesis. The results of the synthesis are shown in Table 1. The exact results are obtained by solving the eigenproblem of the built-up system without partitioning. The superelement synthesis using complete mode sets of the components leads to exact system synthesis as expected. Superelement method using severely truncated component mode set along with residual flexibility attachment modes predicts system frequency with an accuracy better than that of the MacNeal method and equal to that of the Rubin's second order method.

It must be noted that in this study different types of component dynamics models are synthesized by virtue of the superelement formulation, and that the accuracy of system synthesis is entirely governed by the type of component dynamic models and not by the coupling procedure.

TABLE 1 DIRECT AND SYNTHESIZED SYSTEM NATURAL FREQUENCIES (RADS./SEC)

MODE NO.	EXACT FREQ.	SUPERELEMENT SYNTHESIS		MACNEAL METHOD (B)	RUBIN METHOD (B)
		A	B		
1	0.	0.	0.	0.	0.
2	52.417	52.417	52.418	52.419	52.418
3	69.348	69.348	69.829	69.886	69.829
4	72.818	72.818	291.697	504.67	291.697
5	418.029	418.03			
6	775.678	775.678			

A: (1 Rigid body + 4 elastic) modes of the aircraft
B: (1 Rigid body + 1 elastic + 1 residual flexibility) mode of the aircraft

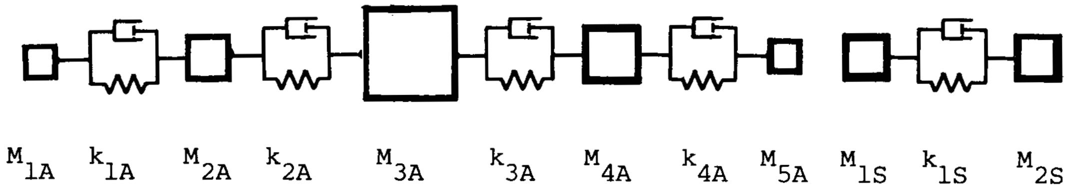

$m_{1A} = m_{5A} = 0.1$, $m_{2A} = 36$, $m_{3A} = 100$, $m_{4A} = 400$
$k_{1A} = 60{,}000$, $k_{2A} = 120{,}000$, $k_{3A} = 100{,}000$, $k_{4A} = 50{,}000$
$m_{1S} = 0.2$, $m_{2S} = 0.4$, $k_{1S} = 2{,}000$

Fig. 1 Lumped Parameter Aircraft-Store System

ACKNOWLEDGEMENT

This work was performed under contract from the University of Cincinnati.

REFERENCES

1. D. Suliscz, "Survey of System Modeling Techniques," M.S. Thesis, University of Cincinnati, 1986.

2. W. Hurty, "Vibrations of Structural Systems by Component Mode Synthesis," Journal of the Engineering Mechanics Division, Vol. 86, Aug. 1960, pp. 51-69

3. W. Hurty, "Dynamic Analysis of Structural Systems Using Component Modes," AIAA Journal, 3(4), 1965, pp. 678-685.

4. R. Craig, and M. Bampton, "Coupling of Structures for Dynamic Analysis," AIAA Journal, July 1968, pp. 1313-1319.

5. R. M. Bamford, "A Modal Combination Program for Dynamic Analysis of Structures," TM-33-290, Jet Propulsion Laboratory, July 1967.

6. R. L. Goldman, "Vibration Analysis by Dynamic Partitioning," AIAA Journal, Vol. 7, No. 6 (1969), pp. 1152-1154.

7. S. Hou, "Review of Modal Synthesis Techniques and a New Approach," Shock and Vibration Bulletin, Vol. 40, No. 4, 1969, pp. 25-39.

8. G. M. L. Gladwell, "Branch Mode Analysis of Vibrating Systems," Journal of Sound and Vibration, Vol. 1, 1964, pp. 41-59.

9. W. A. Benfield, and R. F. Hruda, "Vibrational Analysis of Structures by Component Mode Substitution," AIAA Journal, Vol. 9, 1971, pp. 1255-1261.

10. R. H. MacNeal, "A Hybrid Method of Component Mode Synthesis," Computers and Structures, Vol. 1, 1971, pp. 581-601.

11. S. Rubin. "Improved Component Mode Representation for Structural Dynamic Analysis," AIAA Journal, Vol. 13, 1975, pp. 995-1006.

12. A. L. Klosterman, "A Combined Experimental and Analytical Procedure for Improving Automotive System Dynamics," SAE Paper No. 720093, 1972.

13. R. M. Hintz, "Analytical Methods in Component Modal Synthesis," AIAA Journal, Vol. 13, No. 8, 1975, pp. 1007-1016.

14. M. Baker, "Component Mode Synthesis Methods for Test-Based, Rigidly Connected, Flexible Components," AIAA Journal Paper 84-0943 (1984), pp. 153-13.

15. R. G. Smiley, and B. A. Brinkman, "Rotational Degrees-of-freedom in Structural Modification," Proc. 2nd IMAC, Orlando, FL, 1984, pp. 937-939.

16. A. L. Hale, and L. Meirovitch, "A General Substructure Synthesis Method for Dynamic Simulation of Complex Structures," Journal of Sound and Vibration, Vol. 69, No. 2, 1980, pp. 309-326.

17. J. M. Klahs, J., M. Goldstein, R. Madabusi, and R. Russel, "Assembling Large Scale System Models from Test and Analysis Using Interactive Computing," Proc. 1st IMAC, Orlando, FL, November 1982, pp. 46-52.

18. D. N. Herting, and M. J. Morgan, "A General Purpose Multi-stage Component Modal Synthesis Mehod," Proc. 20th AIAA SDM Conference, St. Louis, MO, 1979.

19. Shu, C. F., and F. H. Chu, "A General Superelement Approach by the Component Mode Synthesis Method," Proc. 2nd IMAC, Orlando, Florida, April 1984.

20. D. R. Martinez, T. J. Carne, and A. K. Miller, "Combined Experimental/ Analytical Modleing Using Component Mode Synthesis," Proc. 25th AIAA Structures, Dynamics & materials Conference, Palm Springs, CA, 1984.

N88-18957

Approximate Method for Predicting the Permanent Set in a Beam in Vacuo and in Water Subject to a Shock Wave

A. L. Stiehl
R. C. Haberman
J. H. Cowles

An approximate method to compute the maximum deformation and permanent set of a beam subjected to a shock wave loading in vacuo and in water was investigated. The method equates the maximum kinetic energy of the beam (and water) to the elastic plastic work done by a static uniform load applied to the beam. Results for the in water case indicate that the plastic deformation is controlled by the kinetic energy of the water. The simplified approach can result in significant savings in computer time or it can expediently be used as a check of results from a more rigorous approach i.e., a finite element solution. The accuracy of the method is demonstrated by various examples of beams with simple support and clamped support boundary conditions.

INTRODUCTION

Computer codes exist today to calculate the elastic-plastic deformation of structures subject to shock wave loading, such as the finite element codes ANSYS reference [1], and STAGS reference [2]. Although these and other codes offer the analyst a large variety of elements and several plasticity theories, the computational effort to calculate the dynamic plastic deformation of a large structure may be substantial. To reduce the computational effort, an approximate method based upon energy considerations was investigated. Calculated quantities of interest are maximum deformation and permanent set. The method equates the maximum kinetic energy to the elastic-plastic work done by a static uniform load applied to the structure. The kinetic energy is calculated from a relatively simple time dependent elastic analysis of the structure and the work is calculated from another relatively simple elastic plastic static analysis. Essential savings in computer time and effort on the part of the analyst can be realized by the simplified method. The method is very similar to approximate energy methods developed over a decade ago for structures in air subjected to impulsive type loadings, references [3], [4] and [5]. The primary differences are, (1) the structure (beam) is in water, and (2) the implementation of the method and validation is carried out with the use of a modern finite element code.

To demonstrate the accuracy of the method, several examples are given. They consist of beams of various lengths and boundary conditions subject to shock wave loadings at normal incidence in vacuo and in water. The shock loading is from an exponentially decaying step wave, with decay time much smaller than the period of vibration. Under these conditions, the loading tends to apply an impulse to (at least) the fundamental mode of the structure, with the maximum kinetic energy occurring primarily in the fundamental mode at very early time and after the shock wave pressure has nearly diminished to zero. These are very important considerations in the energy balance method used herein because the method does not account for the additional external work performed by the shock wave pressure after the peak kinetic energy occurs in the structure. Furthermore, the uniform pressure used in the elastic-plastic static analysis exactly simulates the applied load distribution and approximates the inertia load distribution corresponding to the fundamental mode of the beam. For the case of the beam in water, the fluid reaction force applied back onto the beam is mathematically represented by the doubly asymptotic approximation, DAA reference [6]. This approximation is easily introduced into the dynamic elastic-plastic finite element model.

DESCRIPTION OF ANALYTICAL MODELS

Three analytical models were used in this investigation. They were, (1) an ANSYS dynamic elastic plastic finite element model to calculate the beam's deflection and kinetic energy (and water's kinetic energy) due to a shock wave, (2) an ANSYS static elastic plastic finite element model to calculate the beam's deflection and external work performed by a uniform pressure, and (3) a simplified two degree of freedom model to calculate the elastic plastic response of the beam's fundamental mode to the shock wave.

Fig. 1 shows the dynamic finite element model for the simple support condition. Fixed ends were also considered. The model consisted of eight equal length beam elements with dampers attached and mass elements attached to the opposite end of the dampers. The dampers and masses were used to model fluid-structure interaction effects. The dampers represent the radiation term of the DAA and the masses represent the virtual mass term of the DAA. In the case of the beam's response in vacuo, the damping coefficient and water mass were zero. The applied loading consisted of the time dependent blocked pressure of the shock wave.

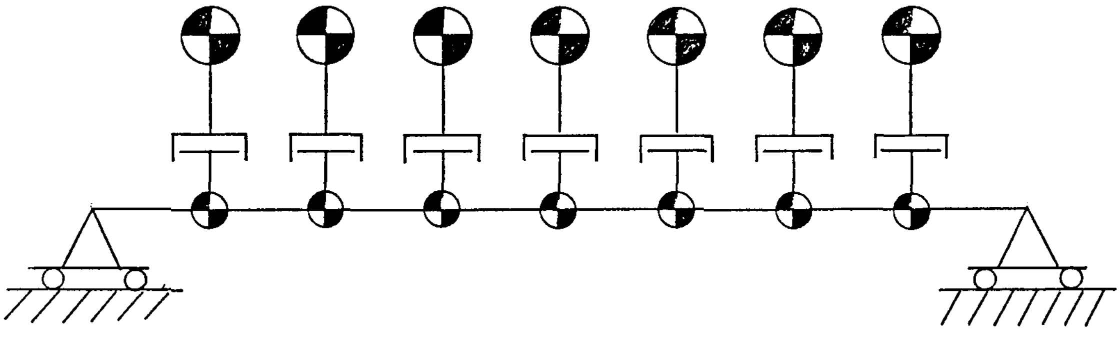

Figure 1. Finite Element Model

The elastic-plastic static finite element model consisted of eight elements also. This beam model was subjected to a statically applied pressure loading. The external work performed by the pressure was calculated with the use of this model by simply integrating the pressure-displacement response.

The simplified spring-mass-damper model is shown in Fig. 2. The spring characteristic is obtained from the elastic-plastic force deflection response of the static model, and the mass, damping, and force terms are obtained by applying Lagrange's equation of motion to the fundamental mode of the beam. This model can be used to calculate the maximum displacement of the beam and the permanent deformation. It will be shown to give very good comparisons with the ANSYS finite element model, thereby demonstrating the dominant contribution of the funadmental mode to the elastic-plastic response.

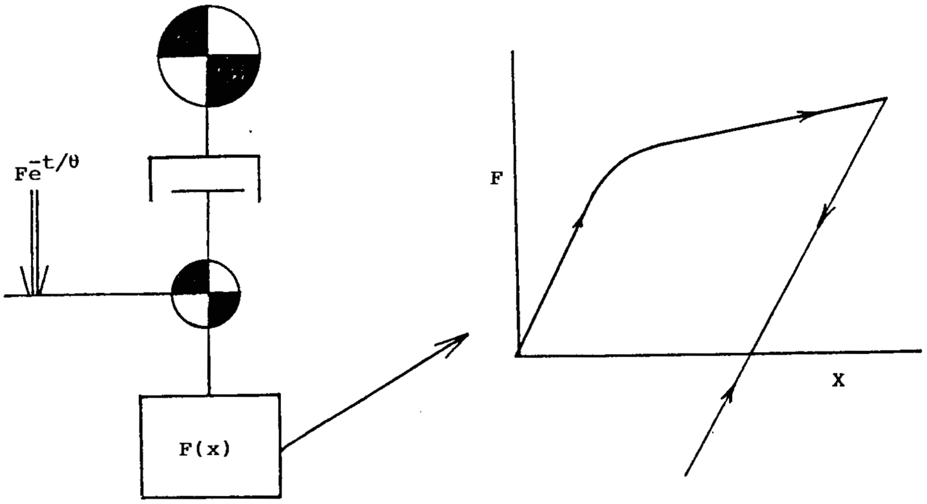

Figure 2. Two DOF Model

RESULTS

Several examples were used to investigate the energy balance method. Beams of 50, 75 and 100 inches long were considered, with simple support and clamped boundary conditions. The width and thickness were 6 inches and 2 inches, respectively. It is to be noted that the width dimension is completely arbitrary. The material was steel with a yield stress of 80000 psi with very little work-hardening. The shock loading pressure on the beam was mathematically expressed as $p = p_o\ e^{t/o}$ where P_o is the blocked pressure. A decay constant of o = .001 seconds was used which for most of the beams was small compared to the fundamental period of vibration. A blocked peak pressure of 2500 psi was used for the water case and for the air case, it was 667 psi. These pressures were chosen for the purpose of producing significant plastic deformation. Cavitation of the water was not accounted for in this investigation.

Fig. 3 illustrates the non-linear force displacement for the simply supported 100 inch long beam, and Fig. 4 illustrates the static work functions for the 100, 75 and 50 inch beams. Similar curves are obtained for clamped support conditions. The beam's dynamic maximum deflection predicted by the energy balance method is obtained by entering into Fig. 4 the peak kinetic energy of the beam (and water) induced by the dynamic load. The peak kinetic energy calculation for this study occurred during the very early time (elastic) response. The permanent deflection is obtained by subtracting from the maximum deflection a recoverable deflection the beam would experience under removal of a static uniform load.

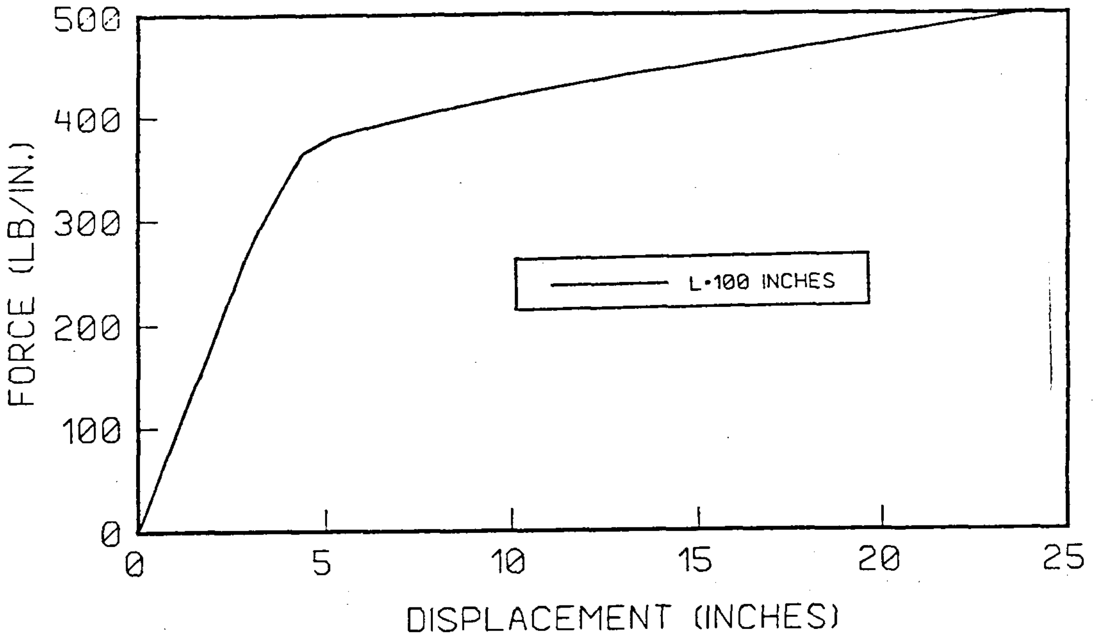

Figure 3. Force-Deflection for S.S. Beam

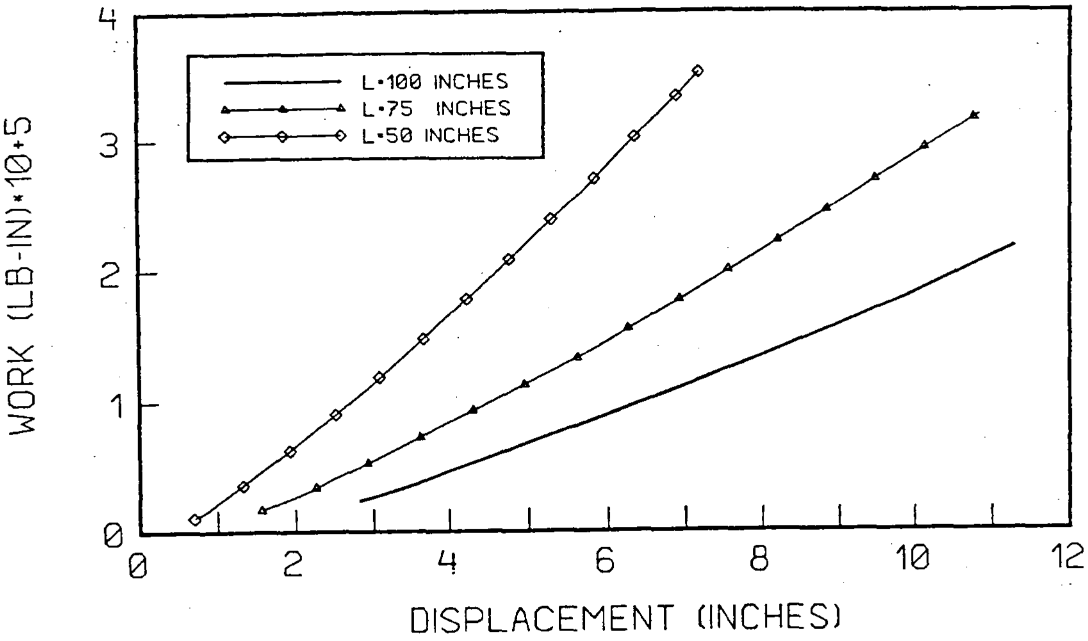

Figure 4. Work Functions for S.S. Beam

Fig. 5 illustrates the actual time dependent in water displacement response at the center of the 100, 75 and 50 inch clamped supported beams. The permanent set was obtained by drawing a mean line through the later time decayed response. The peak kinetic energy occurs at very early time as shown in Fig. 6 for the 100 inch clamped supported beam. This figure also demonstrates that most of the kinetic energy resides in the water (which is primarily converted to plastic work in the beam).

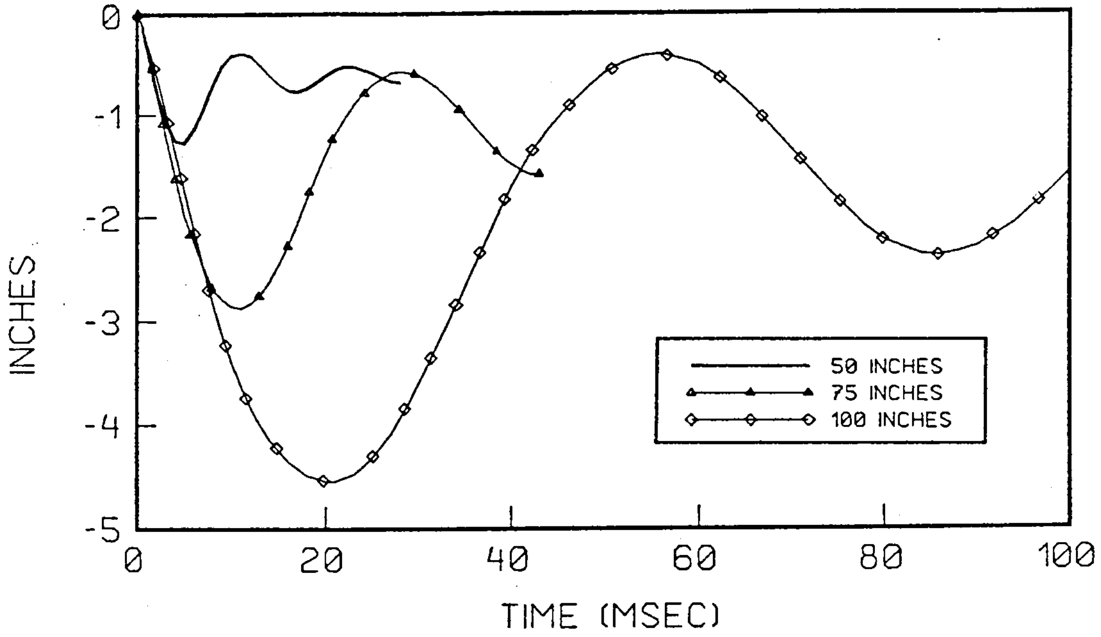

Figure 5. Displacement of C.S. Beam

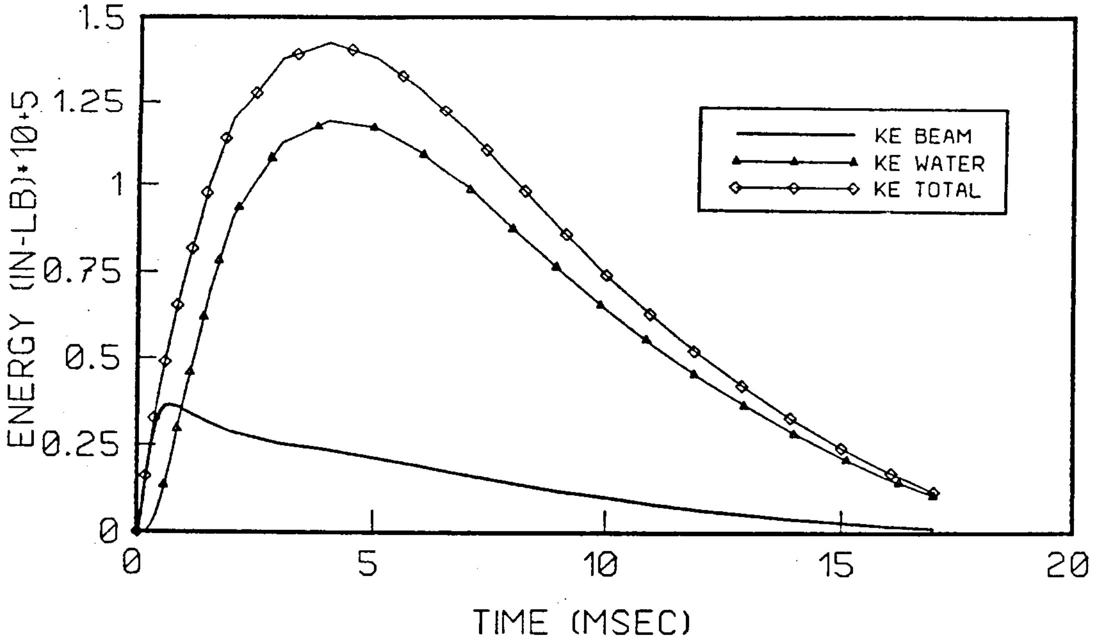

Figure 6. Kinetic Energy of C.S. 100 in. Beam

Table 1 compares the peak deflections and permanent deflections obtained from the ANSYS dynamic response model and the energy balance method, and Table 2 lists the fundamental period of vibration of the six beams. As seen, the comparisons are better for the longer beams. The reason is believed to be the longer period of vibration of the longer beams. As the period approaches, the decay time (.001 seconds), the kinetic energy of the beam reaches a maximum before the shock wave diminishes to zero. Thus there is additional dynamic work performed by the shock wave which is not accounted for in the energy balance method. Another consideration is the influence of higher frequency modes. If they are excited to any appreciable extent, the static work function would therefore not be a good approximation of the strain energy in the dynamically deformed beam. The static work function is only valid for beams responding primarily in their fundamental mode since the work function is based on a uniform pressure applied to the beam. A final consideration is the use of a uniform pressure in the generation of the static work function. A better approximation would have been a distribution corresponding to the fundamental mode of the beam, since it is the kinetic energy associatd with this distribution that is converted to plastic work in the beam.

Fig. 7 compares results of the spring-mass-damper two degree of freedom (DOF) model with the ANSYS finite element model for the clamped supported 50 inch beam in water. As shown, the comparison is reasonably good. Since this simple model is based on the fundamental mode of the beam, it may be concluded that higher order modes do not contribute significantly to the dynamic elastic plastic peak response.

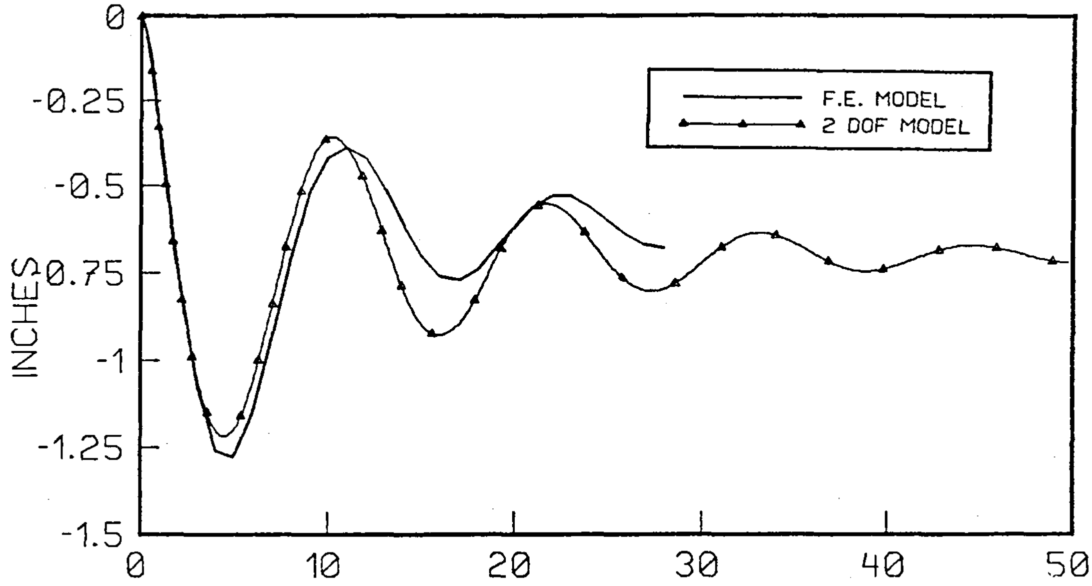

Figure 7. Displacement of 50 in. C.S. Beam

Table 1 Comparison of ANSYS and Simplifed Model

	PEAK DEFLECTION (INCHES)		PERMANENT DEFLECTION (INCHES)	
	ANSYS	ENERGY-BALANCE	ANSYS	ENERGY-BALANCE
Air				
100" Long Beam	5.9	5.9	1.8	2.0
Water				
Simple Support				
100"	10.7	10.3	5.5	5.8
75"	6.60	6.4	4.0	4.7
50"	3.58	2.9	2.0	1.7
Fixed Support				
100"	4.52	4.2	1.5	2.3
75"	2.87	2.4	1.2	1.25
50"	1.28	.8	.60	.29

Table 2 Fundamental Periods of Vibration

Boundary Condition	Length (inches)	Period (seconds)
Simple Support	100	.054
	75	.030
	50	.013
Clamped Support	100	.024
	75	.014
	50	.006

Using the two DOF models, Figs. 8 and 9 compare the kinetic energies for the simply supported long beam and clamped supported short beam with the external work of the applied shock wave, the lost work due to acoustic radiation, and the strain energy of deformation. For the energy balance method to be accurate, the peak kinetic energy should occur after most of the external work has been completed and before there is appreciable strain energy in the beam. This occurs in the case of the long simply support beam but not for the clamped short beam, and therefore helps to illustrate why the energy balance method performed better for the longer beam.

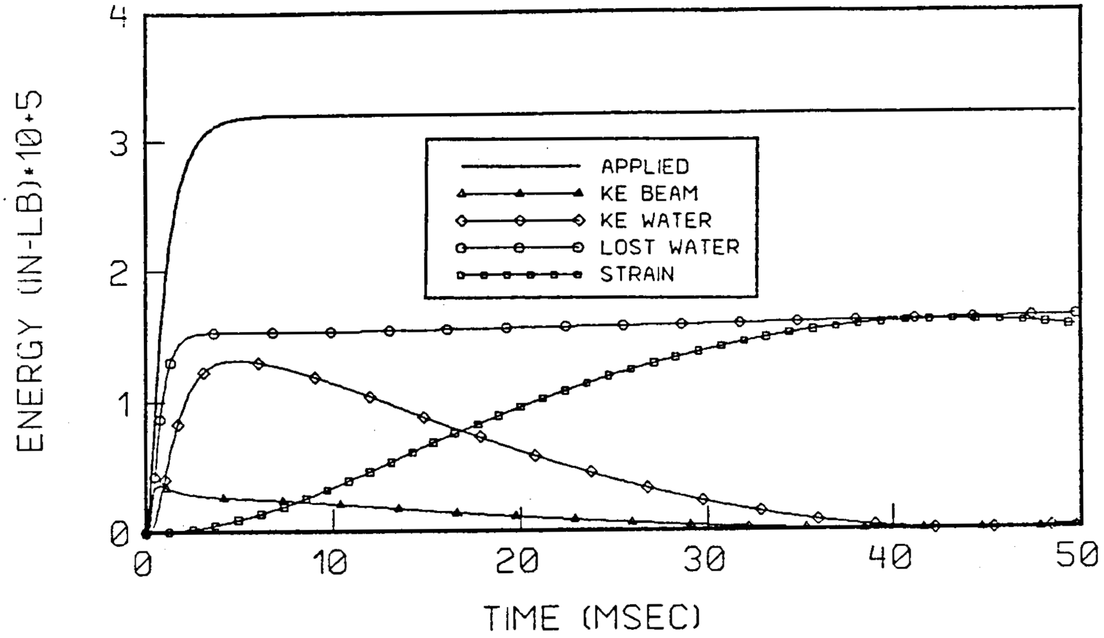

Figure 8. System Energies for 2 DOF Model, S.S. Beam, L = 100 inches

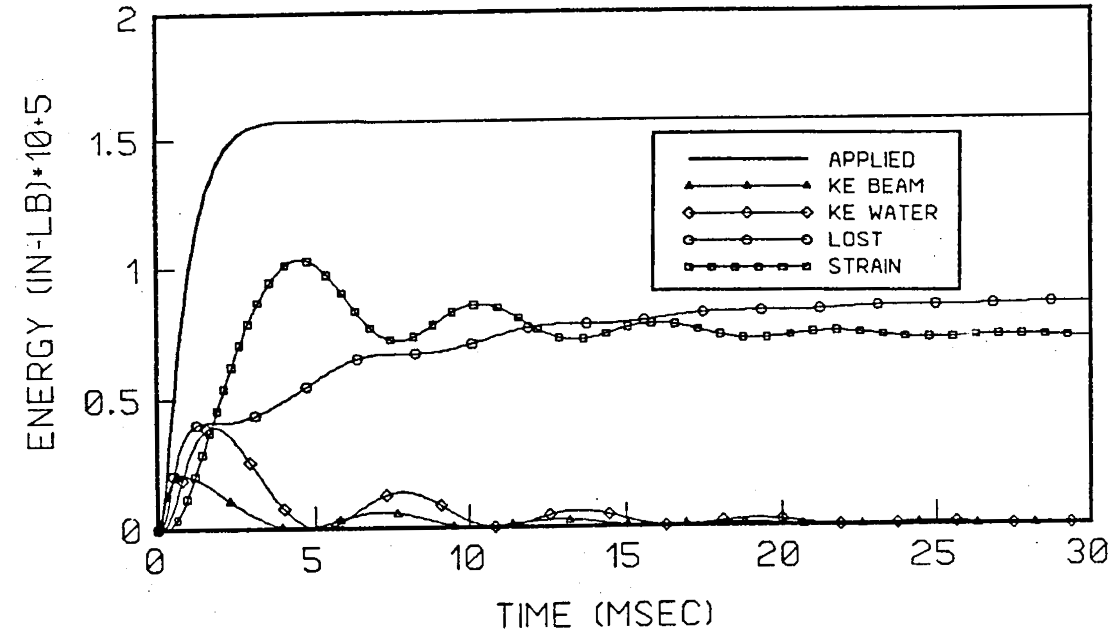

Figure 9. System Energies for 2 DOF Model C.S. Beam, L = 50 inches

CONCLUSION AND RECOMMENDATIONS

The energy balance method has been shown to give reasonably accurate results for the prediction of peak deformation and plastic set in a beam in vacuo and in water subjected to a shock wave whose decay time is small compared to the fundamental period of vibration. Results for the in water case reveal that the plastic deformation is primarily controlled by the kinetic energy of the water. Improvements to the method could be realized by (1) accounting for the actual mode shape in the static work function, and (2) utilizing the improved second order doubly asymptotic approximation, reference [6]. Further validation in predicting the actual in-fluid elastic-plastic response should be carried out by using fluid finite elements to model the fluid. Such a model could also investigate the importance of fluid cavitation. Consideration should also be given to using the energy balance method for other structures, such as plates and cylinders.

REFERENCES

1. "ANSYS FINITE ELEMENT CODE, REVISION 3.2.", Swanson Analysis Systems Inc., Houston, PA

2. B.L. Almroth, F.A. Brogan and G.M. Stanky, Structural Analysis of General Shells Volume II LMSC-D633873, Lockheed Palo Alt-Research Laboratory, January 1983

3. W.E. Baker, "Approximate Techniques for Plastic Deformation of Structures under Impulsive Loading", Shock Vibration Dig, Vol. 7, No. 7, pp 107-117, 1975

4. W.E. Baker, "Approximate Techniques for Plastic Deformation of Structures under Impulsive Loading II", Shock Vibration Dig, Vol. II, No. 7, pp 19-24, 1979

5. W.E. Baker, P.A. Cox, P.S. Westine, J.J. Kulesz, and R.A. Strehlow, Explosion Hazards and Evaluation, pp 300-330. Elsevier Scientific Publishing Co., Amsterdam, 1982.

6. T.L. Geers, "Doubly Asymptotic Approximations for Transient Motions of Submerged Structures", Journal of the Acoustical Society of America, Vol. 64, No. 5, pp 1500-1508, Nov. 1978

N88-18958

Electro-Mechanical Vibratory System

Mario Paz

The problem of predicting the phase angle of two self-synchronized rotors starting from rest, is presented in this paper. It is shown that with insufficient power the rotors may not reach the final operating speed of the motors and stay locked at one of the lower natural frequencies of the vibrating system, thus producing large amplitude and failure of the equipment.

INTRODUCTION

Mechanical vibrators are widely used for producing the motion required in some manufacturing processes such as packing cement mixtures, screening, vibration transportation, vibration pile drivers, etc. The principal component of the mechanical vibratory is an unbalanced mass rotated by an electric motor. In some of these applications, rectilinear vibratory motion is required. This motion may be attained using two synchronized motors having eccentric masses rotating in opposite directions. Synchronization of the rotating masses means coordinating the rotation to maintain a definite phase angle between the rotation of the two motors. Such synchronization may be accomplished by using kinematic coupling such as toothed or chain drivers between the two rotors. However, some years ago, it became apparent the synchronization could be maintained without resorting to any kind of kinematic coupling. It was observed that the angular velocities and phases of the motors automatically kept a definite phase rotation without the use of coupling. Huygens [1] first observed a case of self-synchronization in the seventeenth century. He noticed that two pendulum clocks, regardless of their initial phase angle, came into synchronization if they were mounted on a common resilient support such as a flexible beam. He realized that this phenomenon of self-synchronization could be explained by the small imperceptible motion in the beam transmitted by the pendulums.

At the present time, self-synchronization is finding wider applications in the design of vibrating machines [2]. The use of self-synchronization makes forced synchronization unnecessary. The condition of self-synchronization, as well as the phase angle maintained by the rotors, has been investigated initially by Blekman [3] for one directional motion, by Paz [4,5] for two directional motions and subsequently by others [6,7,8]. Paz investigated analytically and experimentally the problem of predicting the stable phase angle and the direction of the resultant force of any two rotors with parallel axis of rotation. He showed that the phase angle between two rotors, as well as the condition necessary for a stable solution could be predicted with the application of Hamilton's Principle.

These developments gave solutions prescribing the conditions for self-synchronization, but did not focus in the initial transient portion of the motion until it reaches the final steady-state condition. In this transient state, the system may have to transverse some of its natural frequencies at which resonance may occur, locking the motion at a speed lower than the operating speed of the motors, thus, resulting in large amplitudes of motion and failure of the equipment. The electro-mechanical analysis of vibrating equipment during the initial transient motion, is presented in this paper.

CHARACTERISTICS OF INDUCTION MOTOR

The torque capacity of an induction motor is primarily a function of its rotating speed. Fig.1 shows a typical torque-speed curve for this type of motor. The figure also shows an assumed torque-speed curve required to maintain rotation as demanded by the load. In this case, the system will operate in the transient state until it reaches the steady-state condition at which the torque demanded by the load equals the torque of the motor, point P in Fig.1.

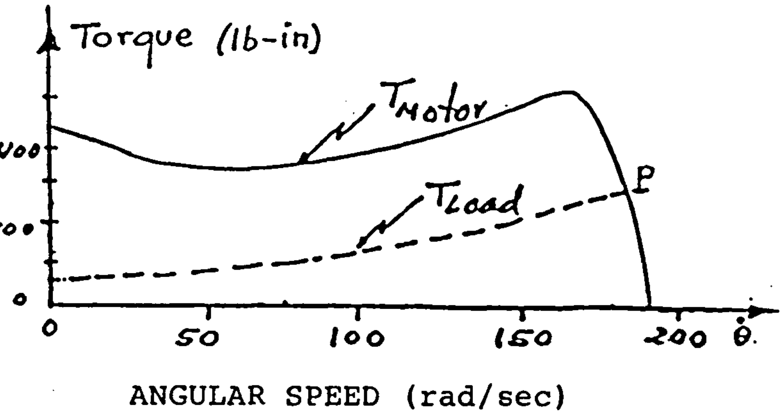

Fig. 1 Speed-Torque Curve For Typical Induction Motor

At any speed $\dot{\theta}$ (rad/sec), the torque differential ΔT between that produced by the motor and the required by the load is available to accelerate the motor. Consequently, applying Newton's second law for a rotating mass, this differential torque is

$$\Delta T = J \cdot \frac{d\dot{\theta}}{dt} \qquad (1)$$

in which J is the mass moment of inertia of the rotating parts of the motor and $\dot{\theta}$ the angular velocity of the rotor.

MECHANICAL VIBRATING SYSTEM

The equations of motions of a mechanical vibrating system my be obtained by direct application of Newton's Law of motion or alternatively by using an energy method such as the application of Lagrange's equation. In any case, the equations of motion for a linear system may, in general, be expressed in matrix notation as

$$[M]\{\ddot{Y}\} + [C]\{\dot{Y}\} + [K]\{Y\} = \{F(t)\} \qquad (2)$$

where [M], [C] and [K] are respectively the mass, damping and stiffness matrices; and $\{Y\}$, $\{\dot{Y}\}$ $\{\ddot{Y}\}$ the displacement, velocity and acceleration vectors of the generalized coordinates.

In the solution of Eq.(2), it is convenient to use modal superposition method to transform these equations to a system of uncoupled equation of the form

$$\ddot{Z}_i + 2\xi_i\omega_i\dot{Z}_i + \omega_i^2 Z_i = P_i(t) \qquad (i=1,2...N) \qquad (3)$$

where Z_i = modal displacement

$\dot{Z}_i$ = modal velocity

$\ddot{Z}_i$ = modal acceleration

ω_i = natural frequency

ξ_i = modal damping ratio

and $P_i(t)$ = modal force

which is given by

$$P_i(t) = \sum_{j=1}^{N} F_j(t)\,\phi_{ji} \qquad (4)$$

where ϕ_{ji} is the j-component of i-th eigenvector.

The solution of the uncoupled equation, Eq.(3) during the transient motion may be obtained by numerical integration in terms of the modal coordinates Z_i.

The motion in function of the generalized coordinates is then given by the transformation

$$\{Y\} = [\Phi]\{Z\} \qquad (5)$$

where $[\Phi]$ is the modal matrix of the system.

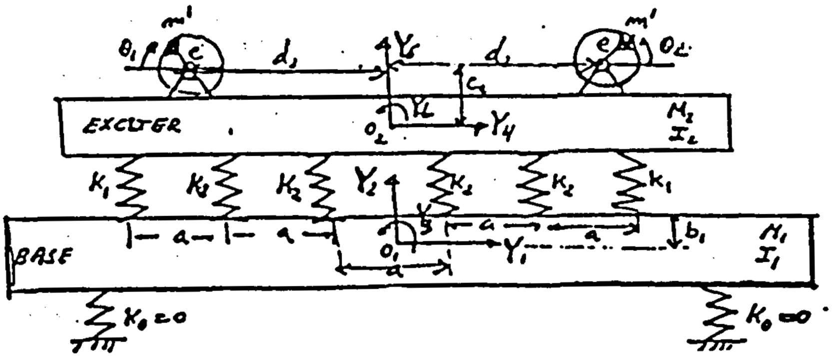

Fig.2 Mathematical model for the example of a vibrating system excited by two self- synchronizing rotors.

TORQUE DEMANDED BY THE LOAD

The torque demanded by the load may be determined from the power consumed by the exciting forces of the rotors. The forces $F_1(t)$ and $F_2(t)$, developed by the two rotors exciting the system are given by

$$F_1(t) = m'e\,\dot{\theta}_1^2 \qquad (6)$$

$$F_2(t) = m'e\,\dot{\theta}_2^2$$

where m' and e are the eccentric mass and its corresponding eccentricity; $\dot{\theta}_1$ and $\dot{\theta}_2$ the angular velocities of the rotors.

The power demanded by the load may be calculated as the product of the rotor forces times the corresponding linear velocities of the points of application of these forces. It is convenient to express this power separately for the two force components in the plane of the rotating forces as

$$F_{11}(t) = F_1(t)\sin\theta_1(t)$$

$$F_{12}(t) = F_1(t)\cos\theta_1(t) \qquad (7)$$

and

$$
\begin{aligned}
F_{21}(t) &= F_2(t)\,\sin\theta_2(t) \\
F_{22}(t) &= F_2(t)\,\cos\theta_2(t)
\end{aligned}
\qquad (8)
$$

where F_{ij} is the j-component of the i-th motor; θ_1 and θ_2 the angular displacements of the rotors.

The power demanded by the load is given by

$$
\begin{aligned}
P_{11}(t) &= F_{11}(t).\dot{X}_{11}(t) \\
P_{12}(t) &= F_{12}(t).\dot{X}_{12}(t)
\end{aligned}
\qquad (9)
$$

and

$$
\begin{aligned}
P_{21}\ (t) &= F_{21}(t).\dot{X}_{21}(t) \\
P_{22}\ (t) &= F_{22}(t).\dot{X}_{22}(t)
\end{aligned}
\qquad (10)
$$

where P_{ij} = Power of j force component of the i-th motor $\dot{X}_{ij}$ = Linear velocity of the force component j of the i-th motor.

Finally, the torque T_L demanded by the load is obtained by simply dividing the power components in Eqs.(9) and (10) by the corresponding angular velocity of the rotors. Consequently, the total torque demanded by the loads is given by

$$T_L = \sum_{k=1}^{2} \frac{1}{\dot{\theta}_k}[P_{k1}(t) + P_{k2}(t)] \qquad (11)$$

ANGULAR VELOCITY OF THE ROTORS

The angular velocity for the rotors is determined by numerical integration of Eq.(1) which expressed in finite differences form may be written as

$$\Delta\,\dot{\theta}(t) = \frac{\Delta T(t)}{J}\,\Delta t \qquad (12)$$

where $\Delta\,\dot{\theta}(t)$ is the incremental angular velocity of the rotors attained in time step Δ t and Δ T(t) is the torque available at accelerate the rotors. As illustrated in Fig.1, this torque is given by the difference between the torque of the motor $T_M(t)$ and the torque $T_L(t)$ demanded by the load; thus for each motor, the differential torque is given by

$$\Delta T(t) = T_M(t) - T_L(t) \qquad (13)$$

The angular velocity for each rotor is then calculated, starting with initial velocity zero ($\dot{\theta}(0)=0$), through the recurrence formula

$$\dot{\theta}(t+\Delta t) = \dot{\theta}(t) + \Delta\dot{\theta}(t) \tag{14}$$

The angular displacement of the rotors, θ_1, and θ_2 is calculated as

$$\begin{aligned} \theta_1(t+\ t) &= \theta_1(t)+\dot{\theta}_1(t) \times \Delta\ (t) \\ \theta_2(t+\ t) &= \theta_2(t)+\dot{\theta}_2(t) \times \Delta\ (t) \end{aligned} \tag{15}$$

starting with the initial displacements of the rotors $\theta_1(t=0)$ and $\theta_2(t=0)$.

The phase angle $\alpha(t)$ between the rotors is then given by the difference between the angular displacements of the rotors. Hence:

$$\alpha(t) = \theta_1(t) - \theta_2(t)$$

NUMERICAL EXAMPLE

Figure 2 shows the mathematical model of a vibrating conveyor, excited by two motors with eccentric masses rotating in opposite directions. The differential equations of motion for the six degrees of freedom in this model were obtained using Lagrange's equation. The numerical values for the components of this system are indicated in Table 1. Discrete values of the torque-speed function for the motors, provided by the manufacture, are given in Table 2.

A time step $\Delta t = 0.01$ sec. was selected and damping in the system was assumed equal to 5% of the critical damping in each mode.

TABLE 1 NUMERICAL VALUES VIBRATING SYSTEM OF FIG.2

BASE:

Mass: $M_1 = 31.863(\text{lb-sec}^2/\text{in})$

Mass moment of inertia:
$I_1 = 42{,}772(\text{lb-sec}^2\text{-in})$

EXCITER:

Mass: $M_2 = 15.236(\text{lb-sec}^2/\text{in})$

Mass moment of inertia:
$I_2 = 4{,}578(\text{lb-sec}^2\text{-in})$

Springs costant:

K_1(axial)= 3k (k = 9,400(lb/in)
K_2(axial)= 9k
K_1(transverse)= 30k
K_2(transverse)= 90k

Distance:

a = 9.0 in
b_1 = 29.0 in
b_2 = 13.25 in
c_2 = 27.0 in
d_2 = 8.0 in

Eccentric rotor:

m'e = 0.1425(lb.sec^2)

TABLE 2 SPEED-TORQUE VALUES

Speed (rad/sec)	0	47.12	162.3	184.3	188.5
Torque (lb-in)	428.4	321.3	616.75	142.8	0

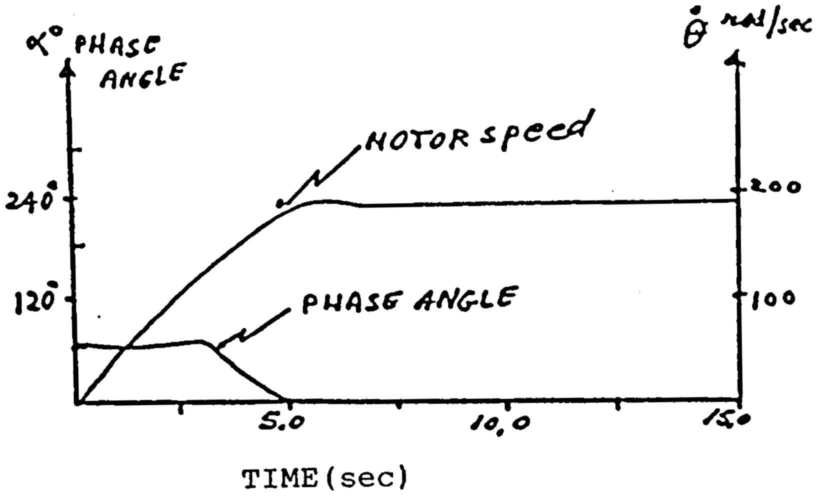

Fig.3 Motor speed and phase angle of the rotors - Motors having full torque.

The analysis of the system modeled as shown in Fig. 2 provided the following three non-zero values for the natural frequencies:

ω_1 =114.7 rad/sec, ω_2 =195.7 rad/sec and ω_3 =783.6 rad/sec.

The solution output includes the motion of the system and of the rotors, as a function of time, during the initial 15 seconds of the transient state. The solution also includes, the torques of the motors and the torques demanded by the load as well as the phase angle between the rotors in the transient state.

For the motors having the speed-torque characteristic depicted in Fig.1 (Numerical values in Table 2), Fig.3 shows the plots of the phase angle between rotors and the angular speed of the motors during the initial 40 seconds motion, while Fig.4 shows these plots assuming that the motors can provide only one-half of the torque indicated in Table 2. The initial phase angle was 60 degrees due to the physical arrangement of the rotors under the effect of gravity.

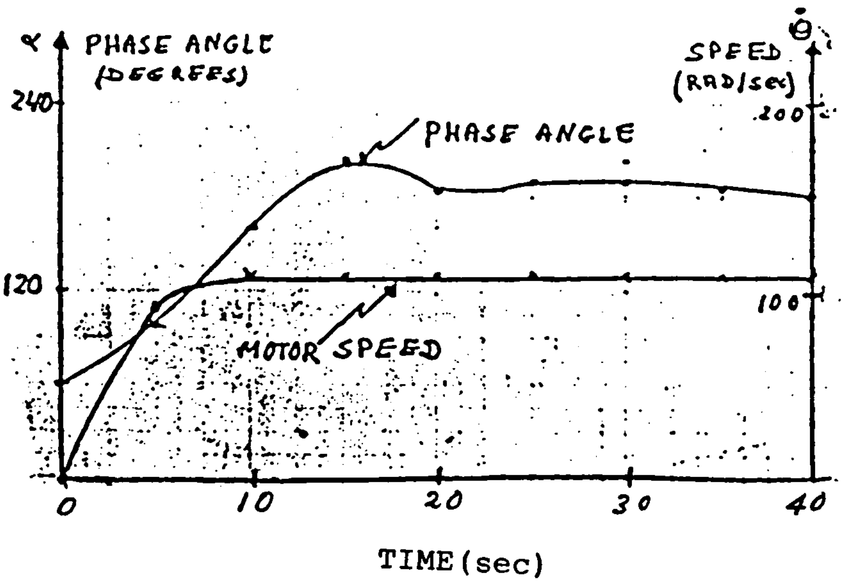

Fig.4 Motor speed and phase angle of the rotors - Motors limited to 50% of the full torque.

DISCUSSION

It may be observed in Fig.3 that for the motors having the speed-torque characteristics of Fig.1, the motors rapidly, in about five seconds reach their operating speed in the neighborhood of $\dot{\theta}$ =185 rad/sec and that rotors attain self-synchronization with a phase angle α=0 degrees. On the other hand, Fig.4 shows that the motors do not have sufficient power to reach the operating speed and become locked in the neighborhood of resonant speed $\omega_r = 114.7$ (rad/sec) attaining out of phase self-synchronization of the rotors $(\alpha=180^\circ)$. In the first case, the self-synchronized machine will perform as intended in the design, while in the second case the system will vibrate erratically at the resonant condition with large amplitudes resulting in failure of the equipment.

REFERENCES

1. Panovko, Y. G. and Gubanova, I. I., "Stability and Oscillations of Elastic Systems," Consultants Bureau, New York, 1965, pp. 234.

2. Paz, Mario and Morris, John, "The Use of Vibration for Material Handling," Journal of Engineering for Industry ASME, Paper No. 73-MH-8, pp. 735-740, August, 1974.

3. Bleckman, I.I., "Rotation of an Unbalanced Rotor Produced by Harmonic Oscillation of the Axis." Bulletin of Academy of Sciences, USSR, Division of Technical Sciences No.8, 1954.

4. Paz, Mario, "Self-Synchronization of Two Eccentric Rotors on Plane Motion." Shock and Vibration, Bulletin 41, Part 6, Naval Research Laboratory, Washington, D.C., Dec. 1970, pp. 159-162.

5. Paz, Mario, "Synchronization and Phase Angle of Two Unbalanced Rotors." Schock and Vibration, Bulletin 44, Part 5, Naval Research Laboratory, Washington, D.C., August 1974, pp. 83-88.

6. Blackman, R.L., Schrader, P.H., and Paz, Mario, "Prediction of Self-Synchronization of Unbalanced Rotors," World Congress on the Theory of Machines and Mechanisms, Vol.2, Part 2, Dublin, Ireland, Sept. 1974, pp. 375-384.

7. Inque, J., Araki, Y., and Wantanabe, Y., "On the Multiple Self-Synchronization of Mechanical Vibrators" Proc. of the World 4th Congress on the Theory of Machines and Mechanisms, University of Newcastle, September 1975, pp. 451-457.

8. Bangchun, Wen, Xiangyang, Lin, "Vibratory Synchronization Transmission," Chinese Journal of Mechanical Engineering, Vol. 20, No. 3, September 1984, pp. 26-42.

1. REPORT NO.
NASA CP-2488

2. GOVERNMENT ACCESSION NO.

3. RECIPIENT'S CATALOG NO.

4. TITLE AND SUBTITLE
58th Shock and Vibration Symposium - Volume II

5. REPORT DATE
February 1988

6. PERFORMING ORGANIZATION CODE

7. AUTHOR(S)
Walter Pilkey and Barbara Pilkey, Compilers

8. PERFORMING ORGANIZATION REPORT #

9. PERFORMING ORGANIZATION NAME AND ADDRESS
George C. Marshall Space Flight Center
Marshall Space Flight Center, Alabama 35812

10. WORK UNIT NO.
M-572

11. CONTRACT OR GRANT NO.

12. SPONSORING AGENCY NAME AND ADDRESS
National Aeronautics and Space Administration
Washington, D.C. 20546 and
The Department of Defense
Washington, D.C.

13. TYPE OF REPORT & PERIOD COVERED
Conference Publication

14. SPONSORING AGENCY CODE

15. SUPPLEMENTARY NOTES
Co-sponsored by the Department of Defense and co-hosted by the Marshall Space Flight Center and the U. S. Army Missile Command. Formerly sponsored by The Shock and Vibration Information Center.

16. ABSTRACT

This NASA Conference Publication contains the proceedings of the 58th Shock and Vibration Symposium, held in Huntsville, Alabama, October 13-15, 1987. Previous Shock and Vibration Symposia were organized by The Shock and Vibration Information Center. The papers are grouped in the categories: mechanical shock, dynamic analysis, space shuttle main engine vibration, isolation and damping, and analytical methods.

17. KEY WORDS
Shock
Vibration
Symposium

18. DISTRIBUTION STATEMENT
Unclassified-Unlimited
Subject Category: 39

19. SECURITY CLASSIF. (of this report)	20. SECURITY CLASSIF. (of this page)	21. NO. OF PAGES	22. PRICE
Unclassified	Unclassified	221	A22

For sale by National Technical Information Service, Springfield, Virginia 22161

NASA-Langley, 1988